DEVELOPMENT AND ANALYSIS OF FINITE STATE MULTI-ROTOR DYNAMIC INFLOW MODELS

A Dissertation
Presented to
The Academic Faculty

By

Feyyaz Guner

In Partial Fulfillment
of the Requirements for the Degree
Doctor of Philosophy in the
School of Aerospace Engineering

Georgia Institute of Technology

May 2021

DEVELOPMENT AND ANALYSIS OF FINITE STATE MULTI-ROTOR DYNAMIC INFLOW MODELS

Approved by:

Dr. J. V. R. Prasad, Advisor
School of Aerospace Engineering
Georgia Institute of Technology

Dr. Lakshmi N. Sankar
School of Aerospace Engineering
Georgia Institute of Technology

Dr. Daniel P. Schrage
School of Aerospace Engineering
Georgia Institute of Technology

Dr. David A. Peters
Mechanical Eng. & Material Science
Washington University in St. Louis

Dr. Chengjian He
Advanced Rotorcraft Technology, Inc.

Date Approved: March 19, 2021

Dedicated to my wife,

Ezgi Melis Dogan Guner, for being my source of happiness in life.

ACKNOWLEDGMENTS

I cannot thank my Ph.D. advisor and mentor, Dr. J. V. R. Prasad, enough for giving me this opportunity to work with him and guiding me through my Ph.D. study. I will treasure our discussions, which were always enlightening and intriguing. I would like to express my heartfelt gratitude to the members of the dissertation committee: Dr. Lakshmi N. Sankar, Dr. Daniel P. Schrage, Dr. David A. Peters, and Dr. Chengjian He for reviewing this dissertation and providing invaluable guidance.

I genuinely appreciate the help received from Dr. Chengjian He and Advanced Rotorcraft Company, Inc. in providing the Viscous Vortex Particle Method and technical support during this study. I am also thankful for comments and suggestions provided by Dr. Hong Xin and Dr. Mark J. S. Lopez at each annual Vertical Lift Research Center of Excellence review. During my Ph.D., I was lucky enough to be part of the NATO AVT-296: Rotorcraft Flight Simulation Model Fidelity Improvement and Assessment research task group and work on the CH-47 helicopter with Mr. David G. Miller from the Boeing Company. I substantially benefited from the discussions made in this task group and extended my knowledge in the rotorcraft simulation area.

I would like to take this opportunity and show my appreciation to Mr. Dogukan Tugberk Karahan, Mrs. Cansu Uzay Karahan, Mr. Emre Yilmaz, Mr. Chams Eddine Mballo, Mr. Robert A. Walters, Dr. Abhishek Mishra, Ms. Avani Gupta, Ms. Auraluck Pichitkul, and Mr. Po-Wei Chen for their support and friendship. My special thanks go to Dr. Yong-Boon Kong for making sure that I had a smooth research transition period before his graduation.

I would like to express my sincere gratitude to my parents: Turgut and Nuran, my sisters: Tugba, Seda, and Eda, my brothers: Sergen and Ali, my father-in-law: Metin, my mother-in-law: Belkis, and my sister-in-law: Ecrin, for their love, encouragement, and support from overseas.

Lastly, I owe a special debt of gratitude to my wife, Ezgi Melis Dogan Guner. Without your unconditional love, kindness, support, and encouragement, I could not have come this far. You are the joy of my life, and I am looking forward to start a new chapter in our life.

This research is partially funded by the U.S. Government, the U.S. Army Technology Development Directorate, CCDC AvMC, under Technology Investment Agreement W911W6-17-2-0002, entitled Georgia Tech Vertical Lift Research Center of Excellence (GT-VLRCOE) with Dr. Mahendra Bhagwat as the Program Manager.

TABLE OF CONTENTS

LIST OF TABLES

LIST OF FIGURES

LIST OF SYMBOLS AND ABBREVIATIONS

Greek Symbols

α_j^{rc}	Cosine part of PPSIM inflow states
α_j^{rs}	Sine part of PPSIM inflow states
χ	Wake skew angle, $\pi/2 - \tan^{-1} \mid \frac{\lambda}{\mu} \mid$, rad
Δ_j^{rc}	Cosine part of costates
Δ_j^{rc}	Sine part of costates
δ_{jn}	Kronecker delta
λ_0	Uniform inflow coefficient
λ_{1c}	Fore-to-aft (longitudinal) inflow coefficient
λ_{1s}	Side-to-side (lateral) inflow coefficient
λ_f	Inflow due to free-stream normalized by ΩR
λ_m	Average inflow at rotor normalized by ΩR
μ	Advance ratio, $V_\infty/\Omega R$
ν, η, ψ	Ellipsoidal coordinates
$\vec{v}$	Induced velocity vector normalized by V_∞
Ω	Rotor rotational speed, rad/s
ϕ	Pressure potential normalized by $\rho\Omega^2 R^2$
$\bar{\psi}_q$	Azimuth angle of q$^{\text{th}}$ blade
Ψ_n^m	PPSIM inflow shaping function
$\hat{\Psi}_n^{mc}$	Cosine part of velocity potentials
$\hat{\Psi}_n^{ms}$	Sine part of velocity potentials
$\tilde{\Psi}_n^{mc}$	Cosine part of velocity shaping function
$\tilde{\Psi}_n^{ms}$	Sine part of velocity shaping function

ρ	Air density, slug/ft^3
$\bar{\tau}$	Reduced time, $V_\infty t/R$
τ_n^{mc}	Cosine part of pressure coefficients
τ_n^{ms}	Sine part of pressure coefficients
ξ	Streamline coordinate

Letter Symbols

a_j^{rc}	Cosine part of VPSIM velocity potential states
a_j^{rs}	Sine part of VPSIM velocity potential states
C_L	Roll moment coefficient
C_M	Pitch moment coefficient
C_T	Thrust coefficient
$\bar{d}, \bar{h}, \bar{l}$	Longitudinal, vertical, and lateral separation distances between rotors normalized by R
$[\tilde{D}]$	Damping matrix
$[L]$	PPSIM inflow influence coefficient matrix
$[\tilde{L}]$	VPSIM inflow influence coefficient matrix
L_q	Blade sectional circulatory lift, lbf/ft
$m,\ r$	Harmonic numbers
$n,\ j$	Polynomial numbers
$[M]$	PPSIM apparent mass matrix
$[\tilde{M}]$	VPSIM apparent mass matrix
M	Total number of harmonics terms
N	Total number of radial terms
$\bar{P}_n^m$	Normalized Legendre function of the first kind
$\bar{Q}_n^m$	Normalized Legendre function of the second kind
Q	Number of blades on one rotor
q	Blade index of the rotor

R	Rotor radius, ft
$\bar{r}$	Blade radial coordinate normalized by R
t	Time, seconds
$\bar{t}$	Nondimensional time, Ωt
$[V_m]$	PPSIM mass flow parameter matrix
$[\tilde{V}_m]$	VPSIM mass flow parameter matrix
V_∞	Free-stream velocity, ft/s
$\vec{v}$	Induced velocity vector normalized by ΩR
$\vec{v}^*$	Adjoint Induced velocity vector normalized by ΩR
v_z	Axial induced velocity normalized by ΩR
$\bar{v}_z$	Average axial induced velocity normalized by ΩR
X	Wake skew function, $\tan(\frac{\chi}{2})$
$\bar{x}, \bar{y}, \bar{z}$	Cartesian coordinates normalized by R

Operator

$\overset{*}{(\,)}$	Derivative with respect to nondimensional time ($\bar{t}$)
$\vec{\nabla}$	Gradient operator

Subscript

$(\,)_1, (\,)_N$	Related to rotor 1 and rotor N, respectively
$(\,)_U, (\,)_L$	Related to upper rotor and lower rotor, respectively

Abbreviations

CMTSVT	Combined Momentum Theory and Simple Vortex Theory
MUAD	Maximum Unnoticeable Added Dynamics
PPSIM	Pressure Potential Superposition Inflow Model
VPSIM	Velocity Potential Superposition Inflow Model
VVPM	Viscous Vortex Particle Method

SUMMARY

Inflow modeling is necessary for accurate performance predictions, aeromechanics analyses, control law development, handling qualities analyses, and flight simulations of single and multi-rotor configurations. Although there are complete inflow theories such as Pitt-Peters and finite state dynamic wake theory (Peters-He) for single rotor configurations, inflow models of multi-rotor configurations still depend on either empirical corrections or data obtained from higher-order wake models to account for the mutual interference effects between the rotors. In this dissertation, an analytical finite state multi-rotor dynamic inflow model known as Velocity Potential Superposition Inflow Model (VPSIM) is formulated from first principles. VPSIM superimposes the velocity potentials of each rotor to account for aerodynamic interactions between the rotors. Along with the recently developed Pressure Potential Superposition Inflow Model (PPSIM), inflow predictions of the VPSIM and PPSIM are compared against a high-fidelity numerical model known as Viscous Vortex Particle Method (VVPM) for various multi-rotor configurations. Inflow predictions show that VPSIM and PPSIM can capture fundamental interference effects with some differences. These differences are attributed to real flow effects such as wake contraction, diffusion, and distortion, which are not included in the analytical rigid wake models, i.e., VPSIM and PPSIM.

To improve correlation with the VVPM, VPSIM and PPSIM must be augmented to include real flow effects. A new system identification methodology is developed to improve VPSIM predictions using the changes in the steady-state inflow components. The developed methodology effectively improves the correlation between VPSIM and VVPM for all flight conditions. Besides, unsteady inflow predictions of the VPSIM are generally improved with the inclusion of real flow effects, especially for the swirl velocity coupling.

Lastly, two quasi-steady approximations are proposed to remove the backward time marching solution of the costates. With approximate methods, interference inflow pre-

dictions become much more efficient and straightforward to acquire. These approximate methods have good agreement with the backward time marching solution at the low frequency range but start to deviate at higher frequencies. In addition to the quasi-steady approximations, costate equation is represented by a convolution integral to remove backward time marching. The convolution integral is much faster to perform than the backward time marching solution; however, it is only applicable to the linear case.

Finite state multi-rotor dynamic inflow models, VPSIM and PPSIM, capture fundamental rotor-on-rotor inflow interference effects for different configurations. Based on the model fidelity requirement, both models can be enhanced using either a higher-order wake model or experimental data. These models can be used in vehicle sizing and performance predictions, aeromechanics analyses, control law development, flight simulations, and handling quality analyses of multi-rotor configurations.

CHAPTER 1
INTRODUCTION

1.1 Background and Motivation

Compared to their fixed-wing counterparts, rotary-wing vehicles operate under the influence of a complex flow field. The downwash (the wake) generated by the fixed-wing vehicle travels downstream and covers large distances in a short amount of time. On the other hand, the wake generated by the rotor blades stays close to the rotor inducing a substantial impact on the overall flow field of the rotor, especially in hover and low speed flights. Inflow reduces the effective angle of attack of the rotor blades; hence, it has a significant influence on the vehicle's response and rotor performance metrics such as thrust generation and power required. The unsteady part of the inflow is also required to capture time histories of the corresponding changes in the rotor aerodynamic loadings [1]. Accurately capturing these aerodynamic loading changes are essential to analyze blade dynamics, dynamic stability of the rotor, and overall vehicle dynamics [2]. Therefore, inflow and its dynamics must be correctly predicted for accurate performance, aeromechanics, flight dynamics, and handling qualities analyses of rotary-wing vehicles.

The simplest inflow model, the momentum theory, assumes uniform inflow across the rotor disk. In hover, momentum theory inflow has good predictions due to flow symmetry, but it has poor performance in forward flight. As speed increases from the hovering flight, the rotor wake gradually loses its symmetry, particularly in the direction of free-stream velocity. It establishes a flow gradient across the rotor with increasing inflow magnitude towards the downstream [3, 4]. This variation of inflow can be added to the momentum theory by expanding the inflow with linear coefficients based on known-wake geometries [5]. However, these extended models are still inadequate in forward flight since magnitudes and

time histories of the first harmonic inflow coefficients solely depend on the aerodynamic thrust and ignore the effects of aerodynamic pitch and roll moments. Although higher-order models such as the Viscous Vortex Particle Method [6, 7] and GT-Hybrid [8, 9] can predict the complex rotor wake in detail, these methodologies are computationally much more demanding than models based on momentum theory, which prevent their usage in real-time simulations. Furthermore, these higher-order models are not in state-space form, and they cannot be readily used for control law developments and stability assessments.

To have an inflow model with adequate accuracy in forward flight, Pitt and Peters developed a three-state dynamic inflow model known as the Pitt-Peters inflow model based on potential flow theory [10, 11]. Pitt-Peters inflow model has a state-space form, where aerodynamic rotor loadings such as thrust, pitch moment, and roll moment are related to the first harmonic inflow variations through an inflow influence coefficient matrix (inflow static gain matrix) [10–12]. In this inflow model, the apparent mass matrix captures the inflow transient response characteristics. In order to have a dynamic inflow model with an arbitrary number of harmonics and radial modes in the inflow expansion, Peters and He have developed a dynamic inflow model known as finite state dynamic wake theory (Peters-He inflow model) [13, 14]. Inflow predictions of this model have been validated with the inflow measurements of an isolated rotor [13, 14]. Pitt-Peters and Peters-He dynamic inflow models are computationally efficient, in state-space form, and reasonably accurate compared to the higher-order models. As a result, these dynamic inflow models are widely used in control law developments, stability assessments, real-time simulations, and handling qualities analyses of rotorcrafts [15–17]. The popularity of these models has led to additional research efforts to improve the accuracy of the dynamic inflow models. For example, the favorable state-space form of these models allows modifications to include wake curvature effects for maneuvering flight [18, 19] and enlarge flight envelope to vortex ring state [20–22], which were neglected in the original formulation.

For conventional main/tail rotor helicopters, several types of inflow models are avail-

able for different rotorcraft applications. However, those models are not applicable to unconventional rotorcraft configurations such as coaxial rotor and tandem rotor helicopters. Current interest in the aerospace industry towards advanced rotorcraft configurations must be supported by novel technologies for safer, quieter, and reliable designs. To achieve such designs, inflow models must take into account rotor-on-rotor inflow interference. Currently, many researchers are working to develop these new sophisticated inflow models using different approaches. The previous success of the finite state dynamic wake theory for conventional main/tail rotor helicopters has recently led its extension to coaxial rotor systems by superimposing the pressure potentials of the rotors [23–32]. Instead of superimposing the pressure potentials of the rotors, one might superimpose the velocity potentials of the rotors to arrive at a similar model. Nevertheless, inflow models that are applicable to generic multi-rotor configurations are still needed for accurate predictions of performance, aeromechanics, control law development, handling qualities analyses, and flight simulation of advanced rotorcraft configurations. For various reasons previously mentioned, new finite state inflow models are essential for supporting the industry's interest towards advanced rotorcraft configurations. The main objective of this dissertation is to develop accurate finite state dynamic inflow models applicable to any generic multi-rotor configuration.

1.2 Literature Review

Most of the published work on the multi-rotor inflow modeling can be mainly categorized into four methods: (1) higher-order wake models such as CFD, free-vortex wake, and hybrid models, (2) augmentation of single rotor inflow models such as Pitt-Peters or Peters-He using free-vortex wake, VVPM, or empirical corrections, (3) extraction of reduced-order models from higher-order models using system identification techniques, and (4) analytical finite state multi-rotor dynamic wake models based on superposition approaches.

Higher-order wake models can model the complex flow field of the advanced rotorcraft configurations in detail. Earlier studies usually used these sophisticated models for per-

formance and wake geometry predictions of the multi-rotor configurations. For example, Kim and Brown [33] utilized the Vorticity Transport Model (VTM) for performance, wake trajectory, and inflow distribution predictions of a coaxial rotor in steady and maneuvering flights. They found that mutual interference between the rotors causes more contraction in the upper rotor wake compared to an equivalent single rotor wake. Furthermore, their study showed that the coaxial rotor has less induced power than the equivalent single rotor in steady hover and forward flight conditions. Instead of using the VTM, Bagai et al. [34, 35] developed a free-vortex wake model and studied wake trajectories of the coaxial, tandem, and tilt-rotor configurations. Similarly, Wachspress and Quackenbush [36] enhanced the free-vortex wake model inside the CHARM software to compare predicted and measured trends in performance, noise, and wake geometry of coaxial rotor configurations with different separation distances. Researchers, for instance, Egolf et al. [37], Kim et al. [38], and Chen et al. [39–42] employed the idea of hybrid CFD and free-vortex wake methods and contributed to development of GT-Hybrid. In Refs. [37–42], Reynolds-Averaged Navier-Stokes (RANS) methodology was used for the near blade solution. The solution switched to free-vortex wake outside of the computational grid to estimate the performance of coaxial and tandem rotor configurations. This hybrid solution approach significantly improved the numerical performance compared to RANS method with a negligible decrease in the accuracy. By a similar token, the source-doublet panel method and free-vortex wake model were coupled by Lee et al. [43, 44] to investigate performance metrics and wake geometries of coaxial and tandem rotor configurations. Instead of focusing on steady flow characteristics, researchers such as Lakshminarayan and Baeder [45] investigated coaxial rotor aerodynamics using a compressible RANS solver to characterize unsteadiness in the flow field in hovering flight.

Although CFD and free-vortex wake methods provide valuable information about the performance estimations and wake geometries, other researchers sought more computationally efficient inflow models in state-space form. They augmented single rotor inflow

models to have better correlations with coaxial rotors. Zhao and He [46] enhanced the Peters-He inflow model using results from the Viscous Vortex Particle Method (VVPM) to account for complex aerodynamic interferences inherent in coaxial rotor configurations. Using VVPM, they modeled the downwash distribution of a coaxial rotor, and then they extracted corrections for the Peters-He inflow influence coefficient and mass flow parameter matrices. Similarly, Xin et al. [47] made use of a free-vortex wake model to calculate interference velocities of a coaxial rotor configuration. Utilizing these velocities, they identified the inflow influence coefficient matrix in the form of the Pitt-Peters inflow model to develop a coaxial rotor inflow model in state-space form. Rather than improving the finite state inflow models, Hackett [48] modified a momentum theory based inflow model to use in flight simulation of the CH-47 helicopter. In this inflow model, some of the correction factors are used to match with the thrust, power, attitudes, and control stick positions of the vehicle in trim, while others are used to improve the transient response characteristics.

A more recent and prominent approach to multi-rotor inflow modeling is the extraction of reduced-order models from the higher-order models such as free-vortex wake or VVPM. Rand et al. [49–51] extracted inflow models in state-space form and performed parametric studies using system identification techniques in conjunction with a free-vortex wake model. Like Rand et al., Keller et al. [52] used a high-fidelity free-vortex wake model to extract linearized inflow models for control law development and flight dynamics simulation of advanced rotorcraft configurations such as compound-coaxial helicopter and multi-rotor vehicle with distributed propulsion. To further improve the fidelity of the extracted model, they included wake distortion effects due to the tip path plane angular rate, off-rotor interference, and mutual interactions to their inflow model without spoiling the favorable state-space form. More recently, Keller et al. [53] introduced another set of dynamic equations in the state-space form to include a far wake response. By coupling the linearized dynamic inflow model and far wake dynamic equation, second-order dynamic responses previously seen in the free-vortex wake analyses were captured. Likewise, He et al. [54]

formulated a state-space inflow model using the Viscous Vortex Particle Method (VVPM) instead of a free-vortex wake model. They employed a unified state-space form, which captures complex aerodynamic interactions such as wake contraction and diffusion to have a more accurate multi-rotor inflow model. Lately, He et al. [55] extended the unified inflow modeling methodology by considering the tip path plane rotation effects and off-rotor interference types such as rotor-on-fuselage, rotor-on-empennage, and other aerodynamic surfaces.

Other researchers have considered analytical multi-rotor inflow modeling methods. They modified the finite state dynamic wake theory by superimposing the pressure potentials of the individual rotors. Prasad et al. [24, 25] conducted initial studies on coaxial rotors to show the viability of this approach. Kong et al. [26, 27, 29, 31] followed the same approach to develop an analytical finite state coaxial rotor inflow model known as the Pressure Potential Superposition Inflow Model (PPSIM). They showed that coaxial rotor PPSIM has good agreement with the VVPM in hover but with some differences in forward flight. These identified differences between the PPSIM and VVPM were attributed to real flow effects such as wake distortion, diffusion, wake contraction/expansions, and wake roll-up. To add these real flow effects into the inflow influence coefficient matrix of the PPSIM, Kong et al. [28, 30, 32] developed an analytical system identification methodology. They also showed that the correlation between PPSIM and VVPM significantly improves with the inclusion of the real flow effects in the PPSIM.

Most of the developed inflow models found in the literature are either specific to a configuration or based on coaxial rotor geometry. Multi-rotor inflow models applicable to generic configurations are still required. Promising PPSIM coaxial rotor results have led its extension to generic multi-rotor configurations [56]. However, apart from the coaxial rotor case, other versions of the PPSIM have not been evaluated against a higher-order wake model such as VVPM. Another approach is to develop an analytical finite state multi-rotor dynamic inflow model based on the superposition of the velocity potentials by considering

the real flow effects and time delay associated with the wake propagation.

1.3 Objective

The literature review showed that most of the developed inflow models are specific to a configuration. These models are generally extracted from the higher-order aerodynamic models in state-space form. Inflow models that are applicable to generic multi-rotor configurations are still required. As such, this dissertation aims to develop an analytical finite state multi-rotor dynamic inflow model from first principles. Specifically, the following objectives are to be studied:

1. Develop a finite state multi-rotor dynamic inflow model from first principles by following the velocity potential superposition approach.

2. Show the connection between the velocity and pressure potential superposition inflow modeling approaches and perform trade-off studies to determine effects of the number of terms used in the inflow expansion on steady and dynamic inflow predictions.

3. Evaluate multi-rotor VPSIM and PPSIM inflow predictions in steady and dynamic conditions against Viscous Vortex Particle Method (VVPM).

4. Identify the real flow effects such as wake contraction/expansion, distortion, diffusion, and wake roll-up, and then incorporate real flow effects into the VPSIM.

5. Improve the computational efficiency of the backward time marching solution of the adjoint equation by finding approximate relations between costates and velocity potential states.

CHAPTER 2

FINITE STATE MULTI-ROTOR DYNAMIC INFLOW MODELS

Velocity and pressure potential finite state dynamic inflow models are derived from first principles. These models assume that flow around the rotor disk is incompressible and inviscid. They assume a rigid cylindrical wake geometry, and their wake skew angles are approximated using the momentum theory. Rigorous derivations of the single rotor velocity [57] and pressure potential [13] inflow models are well documented in the literature; hence, full derivations are not attempted in this dissertation. Instead, modifications applied to the finite state dynamic inflow models are described to arrive at inflow models applicable to multi-rotor configurations.

2.1 Velocity Potential Superposition Inflow Model (VPSIM)

2.1.1 Governing Equations

The continuity and momentum equations are simplified by assuming that flow is incompressible and inviscid. Then, these equations are linearized about a constant free-stream velocity, V_∞. The linearized continuity and momentum equations are given as [57]:

$$\vec{\nabla} \cdot \vec{v} = 0 \tag{2.1}$$

$$\frac{\partial \vec{v}}{\partial \bar{\tau}} - \frac{\partial \vec{v}}{\partial \xi} = -\vec{\nabla} P \tag{2.2}$$

where P is the pressure normalized by ρV_∞^2, $\vec{v}$ is the induced velocity divided by V_∞, and $\bar{\tau}$ is the reduced time, i.e., multiplied by V_∞ / R.

If $\vec{v}$ is represented by the gradient of a scalar function, $\vec{\nabla}\hat{\Psi}$, Eq. (2.1) becomes:

$$\vec{\nabla} \cdot \vec{\nabla}\hat{\Psi} = 0 \tag{2.3}$$

It is clear from Eq. (2.3) that $\hat{\Psi}$ is a potential function and will satisfy the Laplace equation. Pressure (P) can also be expressed in terms of a pressure potential by substituting Eq. (2.3) into Eq. (2.2), and then taking the divergence of the resulting equation [57].

$$\frac{\partial \vec{\nabla} \cdot \vec{\nabla}\hat{\Psi}}{\partial \bar{\tau}} - \frac{\partial \vec{\nabla} \cdot \vec{\nabla}\hat{\Psi}}{\partial \xi} = -\vec{\nabla} \cdot \vec{\nabla} P \tag{2.4}$$

Since the left-hand side of Eq. (2.4) is equal to zero, P can be represented by a pressure potential, Φ. Similar to velocity potential, pressure potential also satisfies the Laplace equation.

$$\vec{\nabla} \cdot \vec{\nabla}\Phi = 0 \tag{2.5}$$

2.1.2 Single Rotor Velocity Potential Dynamic Inflow Model

In order to solve Eqs. (2.1) and (2.2) by the Galerkin method, pressure potentials (Φ) and velocity potentials ($\hat{\Psi}$) are expanded in the ellipsoidal domain (see Appendix A) by the first and second kinds of the Legendre functions (see Appendix B), which satisfy the Laplace equation [57]. By taking advantage of the ellipsoidal domain, where pressure discontinuity across the rotor disk is well represented and the Laplace equation has an analytical solution, a linear velocity potential dynamic inflow model has been established [57]. The nonlinear version of this model has been introduced in Ref. [58] as follows:

$$[\tilde{M}]\{\overset{*}{a}\} + [\tilde{D}][\tilde{V}_m][\tilde{L}]^{-1}[\tilde{M}]\{a\} = [\tilde{D}]\{\tau\} \tag{2.6}$$

In Eq. (2.6), $\{a\}$ and $\{\tau\}$ are column vectors consisting of velocity potential states and pressure coefficients, respectively; $[\tilde{M}]$, $[\tilde{D}]$, $[\tilde{L}]$, and $[\tilde{V}_m]$ are apparent mass, damping, inflow influence coefficient, and mass flow parameter matrices, respectively. Closed-form expressions of these matrices (except for $[\tilde{V}_m]$) are provided in Appendix C.

The velocity potential dynamic inflow model allows calculation of the induced velocity on the rotor and above the rotor once velocity potential states, $\{a\}$, are known. Here, induced velocity is expressed by the gradients of velocity potentials with cosine and sine expansions, as shown in Eq. (2.7).

$$\vec{v} = \sum_{r=0}^{M} \sum_{j=r}^{N} \vec{\nabla}(\hat{\Psi}_j^{rc} + \hat{\Psi}_j^{rs}) \tag{2.7}$$

Each velocity potential consists of time and spatial dependent parts, i.e., velocity potential states (a_j^r) for time dependency and shaping function ($\tilde{\Psi}_j^r$) for spatial dependency. Thus, Eq. (2.7) can be rewritten as:

$$\vec{v} = \sum_{r=0}^{M} \sum_{j=r}^{N} \vec{\nabla}(a_j^{rc}\tilde{\Psi}_j^{rc} + a_j^{rs}\tilde{\Psi}_j^{rs}) \tag{2.8}$$

where

$$\tilde{\Psi}_j^{rc} = \sigma_j^r \Phi_{j+1}^{rc} + \zeta_j^r \Phi_{j-1}^{rc} \tag{2.9}$$

$$\tilde{\Psi}_j^{rs} = \sigma_j^r \Phi_{j+1}^{rs} + \zeta_j^r \Phi_{j-1}^{rs} \tag{2.10}$$

Variables σ_j^r, ζ_j^r, and Φ_j^r are provided in Appendix C.

In order to calculate induced velocity below the rotor disk, another differential equation must be solved to acquire adjoint velocity potential states (costates) [59]. The governing equation of the adjoint velocity potential states (costates) is given in Eq. (2.11). Subse-

quently, adjoint velocities ($\vec{v}^*$) are calculated using the costates and corresponding shaping functions, as shown in Eq. (2.12).

$$-[\tilde{M}]\{\overset{*}{\Delta}\} + [\tilde{D}][\tilde{V}_m][\tilde{L}]^{-1}[\tilde{M}]\{\Delta\} = [\tilde{D}]\{\tau^*\} \tag{2.11}$$

$$\vec{v}^* = \sum_{r=0}^{M}\sum_{j=r}^{N}\vec{\nabla}(\Delta_j^{rc}\tilde{\Psi}_j^{rc} + \Delta_j^{rs}\tilde{\Psi}_j^{rs}) \tag{2.12}$$

Equation (2.11) is unstable in forward time-marching since the derivative term has a minus sign in front of it. To obtain costates (Δ_j^{rc}, Δ_j^{rs}), one must carry out integration backwards in time. Fortunately, $[\tilde{M}]$, $[\tilde{D}]$, $[\tilde{V}_m]$, $[\tilde{L}]$, and $\{\tau\}$ are known from the on-rotor inflow equation. Histories of $[\tilde{V}_m]$, $[\tilde{L}]$, and $\{\tau\}$ are saved and then used in backward time integration. Note that $\{\tau^*\}$ is defined as $\{(-1)^{j+1}\tau\}$.

Induced velocity below the rotor disk can be calculated using the adjoint theorem, which had been rigorously derived earlier in Ref. [59]. The coordinate system, where induced and adjoint induced velocities are defined, is shown in Fig. 2.1. Induced velocity at point *A* ($\vec{v}_A$) is obtained using the velocity at point *B* ($\vec{v}_B$), and the adjoint velocities at points *C* ($\vec{v}_C^*$) and *D* ($\vec{v}_D^*$). When a streamline (ξ) is drawn to point *A*, where it lies inside the rotor wake, point *B* becomes the intersection between the drawn streamline and rotor disk. The distance between the points *A* and *B* is denoted as ξ_0. Point *C* is centrosymmetric to point *B* on the rotor plane, while point *D* is centrosymmetric to point *A* but above the rotor plane. Subsequently, induced velocity at point *A* ($\vec{v}_A$) becomes:

$$\vec{v}_A(r_0, \bar{\psi}_0, \xi_0, t) = \vec{v}_B(r_0, \bar{\psi}_0, 0, t - t_0) + \vec{v}_C^*(r_0, \tilde{\psi}_0, 0, t - t_0) - \vec{v}_D^*(r_0, \tilde{\psi}_0, -\xi_0, t) \tag{2.13}$$

where $t_0 = \xi_0/(\Omega\tilde{V}_T)$, and $\tilde{V}_T$ is the first element in the mass flow parameter matrix (nondimensional net flow passing through the rotor). It should be noted that $\vec{v}_B$ and $\vec{v}_C^*$ require

past values of the velocity potential states ($\{a\}$) and costates ($\{\Delta\}$), respectively. While past values of $\{a\}$ must be saved, Eq. (2.11) must be time-marched backward at each time step until the whole wake is covered. The costate vector from the solution of Eq. (2.11) is used in the calculation of $\vec{v}_C^*$.

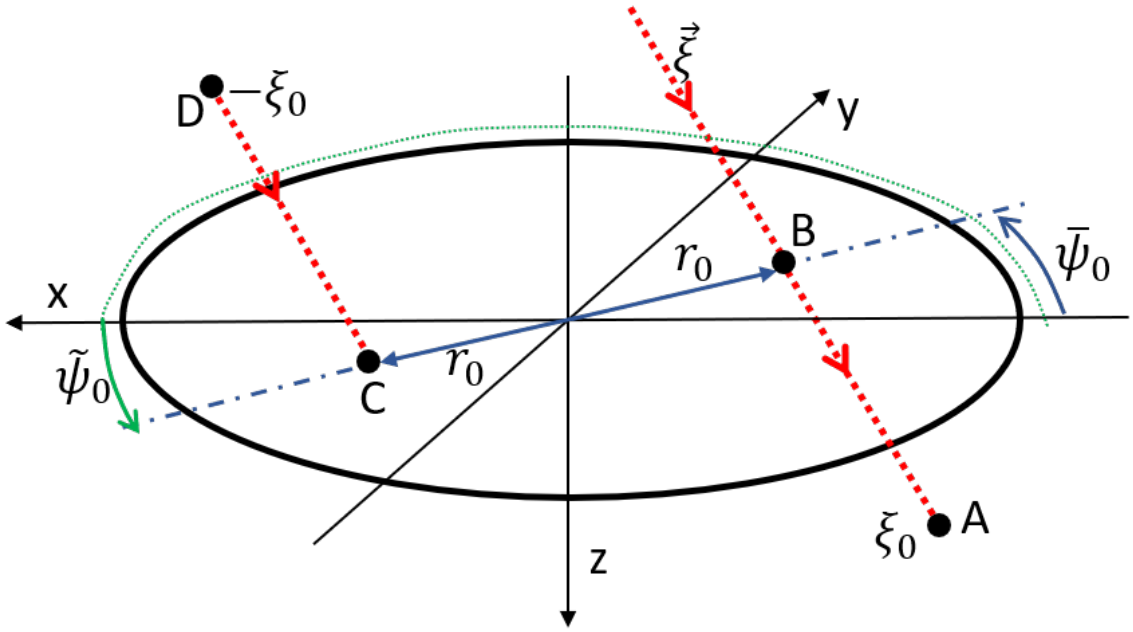

Figure 2.1: Coordinate system for computing induced velocity at point *A*

In summary, inflow below the rotor disk is calculated by first solving Eqs. (2.6) and (2.11). After obtaining velocity potential states and costates, Eq. (2.13) is used along with Eqs. (2.8) and (2.12).

2.1.3 Multi-Rotor Velocity Potential Superposition Inflow Model (VPSIM)

Single rotor velocity potential inflow model is extended to multi-rotor configurations by superimposing the velocity potentials of the rotors to arrive at Velocity Potential Superposition Inflow Model (VPSIM). In VPSIM, each rotor has its own velocity potential, and interference velocities along every direction between the rotors are taken into account by these superimposed velocity potentials. The velocity vector at any point in the flow field can be calculated using Eq. (2.14).

$$\vec{v} = \sum_{r=0}^{M} \sum_{j=r}^{N} \vec{\nabla}[(\hat{\Psi}_j^r)_1 + (\hat{\Psi}_j^r)_2 + ... + (\hat{\Psi}_j^r)_N] \tag{2.14}$$

In Eq. (2.14), $(\hat{\Psi}_j^r)_1$, $(\hat{\Psi}_j^r)_2$, and $(\hat{\Psi}_j^r)_N$ represent velocity potentials (including both sine and cosine parts) of rotor 1, rotor 2, and rotor N, respectively. Note that velocity potentials consist of velocity potential states and shaping functions, i.e., $(\hat{\Psi}_j^r)_N = (a_j^{rc})_N(\tilde{\Psi}_j^{rc})_N + (a_j^{rs})_N(\tilde{\Psi}_j^{rs})_N$. If an induced velocity calculation point is below the rotor disk, then adjoint velocity potential states (costates) of that rotor are also required. In this dissertation, only the z component of the induced velocity is considered. Then, Eq. (2.14) simplifies to:

$$v_z = w = \sum_{r=0}^{M} \sum_{j=r}^{N} \frac{\partial[(\hat{\Psi}_j^r)_1 + (\hat{\Psi}_j^r)_2 + ... + (\hat{\Psi}_j^r)_N]}{\partial z} \tag{2.15}$$

By collecting each rotor's dynamic equations into a single equation set, the most general form of the VPSIM governing equation is established as follows:

$$[\hat{M}]^+ \begin{Bmatrix} \overset{*}{a}_1 \\ \overset{*}{\Delta}_1 \\ \overset{*}{a}_2 \\ \overset{*}{\Delta}_2 \\ \vdots \\ \overset{*}{a}_N \\ \overset{*}{\Delta}_N \end{Bmatrix} + [\hat{D}][\hat{V}_m][\hat{L}]^{-1}[\hat{M}] \begin{Bmatrix} a_1 \\ \Delta_1 \\ a_2 \\ \Delta_2 \\ \vdots \\ a_N \\ \Delta_N \end{Bmatrix} = [\hat{D}] \begin{Bmatrix} \tau_1 \\ \tau_1^* \\ \tau_2 \\ \tau_2^* \\ \vdots \\ \tau_N \\ \tau_N^* \end{Bmatrix} \tag{2.16}$$

where

$$
\begin{aligned}
[\hat{M}]^{+} &= diag(\tilde{M}, -\tilde{M}, \tilde{M}, -\tilde{M}, \cdots, \tilde{M}, -\tilde{M}) \\
[\hat{M}] &= diag(\tilde{M}, \tilde{M}, \tilde{M}, \tilde{M}, \cdots, \tilde{M}, \tilde{M}) \\
[\hat{D}] &= diag(\tilde{D},\ \tilde{D}, \tilde{D},\ \tilde{D}, \cdots, \tilde{D}, \tilde{D}) \\
[\hat{V}_m] &= diag(\tilde{V}_{m1},\ \tilde{V}_{m1},\ \tilde{V}_{m2},\ \tilde{V}_{m2}, \cdots, \tilde{V}_{mN}, \tilde{V}_{mN}) \\
[\hat{L}] &= diag(\tilde{L}(\tilde{X}_1),\ \tilde{L}(\tilde{X}_1), \tilde{L}(\tilde{X}_2),\ \tilde{L}(\tilde{X}_2), \cdots, \tilde{L}(\tilde{X}_N), \tilde{L}(\tilde{X}_N)) \\
\tilde{X}_1 &= \tan(\tilde{\chi}_1/2), \quad \tilde{X}_2 = \tan(\tilde{\chi}_2/2), \quad \tilde{X}_N = \tan(\tilde{\chi}_N/2)
\end{aligned}
$$

As seen from the newly constructed VPSIM governing equation, $[\hat{M}]$, $[\hat{D}]$, $[\hat{V}_m]$, and $[\hat{L}]$ are all block diagonal matrices. This structure is not surprising since interaction among the rotors are considered at the time induced velocity is calculated. Apart from $[\tilde{V}_m]$, all other matrices have analytical expressions identical to the single rotor velocity potential model matrices. Velocity potential inflow influence coefficient matrix of a rotor ($[\tilde{L}]$) depends on the wake skew function ($\tilde{X}$); hence, each rotor might have different values in $[\tilde{L}]$ depending on the loading condition and wake skew angle of that rotor. Because of the wake interference, mass flow parameter matrix ($[\tilde{V}_m]$) and wake skew angle ($\tilde{\chi}$) of each rotor must be corrected. The suggested form of the $[\tilde{V}_m]$ and $\tilde{\chi}$ are provided in the next section.

It is not mandatory to follow the suggested form of the VPSIM governing equation provided in Eq. (2.16) since all matrices are block diagonal and immediate coupling is provided through the mass flow parameter matrices. Therefore, Eq. (2.16) can be decoupled as long as mass flow parameter matrices and wake skew angles are modified to include wake interference effects. In open-loop (prescribed loading) simulations considered in this dissertation, the right-hand side of Eq. (2.16) already has the interference effects. When coupled with a blade element model, inflow interference predictions of VPSIM introduce additional change to the angle of attack of every blade segment resulting in a coupling through loading. Also, the dynamic equation of the adjoint velocity potential states (costates) can

be removed from Eq. (2.16) if desired inflow calculation points are above the corresponding rotor. Note that wake interference is mainly accounted for at the time Eq. (2.15) is used.

In this dissertation, dual-rotor configurations are considered. For these configurations, rotor 1 is always placed above rotor 2 whenever VPSIM is used. As such, Eq. (2.16) can be simplified to the following form:

$$[\hat{M}]^{+}\begin{Bmatrix} \overset{*}{a}_1 \\ \overset{*}{\Delta}_1 \\ \overset{*}{a}_2 \end{Bmatrix} + [\hat{D}][\hat{V}_m][\hat{L}]^{-1}[\hat{M}]\begin{Bmatrix} a_1 \\ \Delta_1 \\ a_2 \end{Bmatrix} = [\hat{D}]\begin{Bmatrix} \tau_1 \\ \tau_1^* \\ \tau_2 \end{Bmatrix} \tag{2.17}$$

where

$$\begin{aligned}
[\hat{M}]^{+} &= diag(\tilde{M}, -\tilde{M}, \tilde{M}) \\
[\hat{M}] &= diag(\tilde{M}, \tilde{M}, \tilde{M}) \\
[\hat{D}] &= diag(\tilde{D},\ \tilde{D}, \tilde{D}) \\
[\hat{V}_m] &= diag(\tilde{V}_{m1},\ \tilde{V}_{m1},\ \tilde{V}_{m2}) \\
[\hat{L}] &= diag(\tilde{L}(\tilde{X}_1),\ \tilde{L}(\tilde{X}_1), \tilde{L}(\tilde{X}_2)) \\
\tilde{X}_1 &= \tan(\tilde{\chi}_1/2), \qquad \tilde{X}_2 = \tan(\tilde{\chi}_2/2)
\end{aligned}$$

2.1.4 Mass Flow Parameter Matrix and Wake Skew Angle in VPSIM

The net flow passing through the rotors must be corrected for multi-rotor configurations due to coupling effects. It has been shown that elements in the mass flow parameter matrix affect the velocity potential states [60]. Aerodynamic interactions not only affect the elements in the mass flow parameter matrix, $\tilde{V}_T$ and $\tilde{V}$, they also affect the momentum theory wake skew angle, $\tilde{\chi}$.

The different modeling structure of VPSIM prevents it from having the same analytical

mass flow parameter matrix as PPSIM [61]. In VPSIM, only the average self-induced velocity of each rotor is analytically known. Thus, average interference velocities are numerically calculated. Sample calculations of $\tilde{V}_T$, $\tilde{V}$, and $\tilde{\chi}$ for rotor 1 are given in Eq. (2.18).

$$\tilde{V}_{T1} = \sqrt{\mu_1^2 + (\lambda_{f_1} + \overline{v}_{z_1} + \overline{v}_{z_{12}} + ... + \overline{v}_{z_{1N}})^2}$$

$$\tilde{V}_1 = \frac{\mu_1^2 + (\lambda_{f_1} + \overline{v}_{z_1} + \overline{v}_{z_{12}} + ... + \overline{v}_{z_{1N}})(\lambda_{f_1} + 2[\overline{v}_{z_1} + \overline{v}_{z_{12}} + ... + \overline{v}_{z_{1N}}])}{\tilde{V}_{T_1}} \tag{2.18}$$

$$\tilde{\chi}_1 = \frac{\pi}{2} - \tan^{-1}\left|\frac{\lambda_{f_1} + \overline{v}_{z_1} + \overline{v}_{z_{12}} + ... + \overline{v}_{z_{1N}}}{\mu_1}\right|$$

where μ_1 is the normalized inplane velocity parallel to the tip path plane of rotor 1, and λ_{f_1} is the normalized velocity perpendicular to it. The variable $\overline{v}_{z_1}$ is the average self-induced velocity rotor 1, whereas $\overline{v}_{z_{12}}$ and $\overline{v}_{z_{1N}}$ are average interference velocities on rotor 1 due to rotor 2 and rotor N, respectively. The average self-induced velocity, $\overline{v}_{z_1}$, is calculated using the classical mass flow parameter equation [62] by transforming the velocity potential states to the Nowak-He variables.

$$\overline{v}_{z_1} = \sqrt{3}a_{1NH}(1) \qquad a_{1NH} = [A]a_1 \tag{2.19}$$

where $[A]$ is the Nowak-He transformation matrix [58].

It is important to note that mass flow parameter matrices of VPSIM and PPSIM are calculated using different approaches [61]. Numerical estimations of the average interference velocities ($\overline{v}_{z_{12}}$ and $\overline{v}_{z_{1N}}$) are slightly different from the one obtained using the analytical expression. Subsequently, mass flow parameter matrices and skew angles of VPSIM and PPSIM show slight differences in some cases and affect the induced inflow distributions of these models.

2.1.5 Backward Time Marching of Costates

Unlike the governing inflow equation, the adjoint equation of costates (adjoint velocity potential states) must be integrated backward in time. Besides, this backward integration is carried out at each time step for a certain wake length. In order to perform this integration, initial values of the costates (Δ_0) and wake length (ξ_0) at each time step are required along with the time histories of the mass flow parameter matrices, wake skew angles (or $[\tilde{L}]$ matrices), and pressure coefficients. The initial costates (Δ_0) can be obtained by solving Eq. (2.11) while setting $\overset{*}{\Delta}_0$ to zero. However, these initial conditions are subject to sudden deviations due to rapid changes in the loading, $\{\tau\}$. Therefore, replacing $\{\tau\}$ with a relation that avoids sudden changes to have a smooth velocity profile is beneficial for practical applications. It is important to note that initial conditions correspond to costates at the current time ($\{\Delta\}_t$) and must be re-calculated at each time step. Chapter 7.1.1 discusses the replacement of $\{\tau\}$ in detail.

2.2 Pressure Potential Superposition Inflow Model (PPSIM)

Similar to Velocity Potential Superposition Inflow Model (VPSIM), Pressure Potential Superposition Inflow Model (PPSIM) is derived from the simplified continuity and momentum equations. A detailed formulation and evaluation of PPSIM for coaxial rotors are provided in Ref. [30]. Therefore, only the governing equation of PPSIM is shown. For N number of rotors, PPSIM has the following form:

$$\begin{bmatrix} M_{11} & \dots & M_{1N} \\ \vdots & \ddots & \vdots \\ M_{N1} & \dots & M_{NN} \end{bmatrix} \begin{Bmatrix} \overset{*}{\alpha}_1 \\ \vdots \\ \overset{*}{\alpha}_N \end{Bmatrix} + [V_m] \begin{bmatrix} L_{11} & \dots & L_{1N} \\ \vdots & \ddots & \vdots \\ L_{N1} & \dots & L_{NN} \end{bmatrix}^{-1} \begin{Bmatrix} \alpha_1 \\ \vdots \\ \alpha_N \end{Bmatrix} = \begin{Bmatrix} \tau_1 \\ \vdots \\ \tau_N \end{Bmatrix} \tag{2.20}$$

where $\{\alpha_1\}$ and $\{\alpha_N\}$ are column vectors of inflow states corresponding to rotor 1 and rotor N, respectively. The variables $\{\tau_1\}$ and $\{\tau_N\}$ are pressure coefficient column vectors of rotor 1 and rotor N, respectively. In Eq. (2.20), subscript $1N$ indicates the effect of rotor N on rotor 1 inflow states, while subscript NN describes the self-induced effect related to rotor N. The pressure coefficients (τ_n^{mc} & τ_n^{ms}) can be calculated from any lifting theory using the following equation [13]:

$$\tau_n^{0c} = \frac{1}{4\pi} \sum_{q=1}^{Q} \int_0^1 \frac{L_q}{\rho \Omega^2 R^3} \Psi_n^0(\bar{r}) d\bar{r}$$

$$\tau_n^{mc} = \frac{1}{2\pi} \sum_{q=1}^{Q} \int_0^1 \frac{L_q}{\rho \Omega^2 R^3} \Psi_n^m(\bar{r}) d\bar{r} \cos(m\psi_q) \tag{2.21}$$

$$\tau_n^{ms} = \frac{1}{2\pi} \sum_{q=1}^{Q} \int_0^1 \frac{L_q}{\rho \Omega^2 R^3} \Psi_n^m(\bar{r}) d\bar{r} \sin(m\psi_q)$$

where L_q represents the sectional lift of q^{th} blade, Q is the total blade number, R is the rotor radius, ρ is the density, Ω is the rotor rotational speed, $\bar{r}$ is the non-dimensional radial blade coordinate, ψ_q is the azimuth angle of q^{th} blade, and Ψ_n^m is the radial shaping function. The analytical formulation of the $\Psi_n^m(\bar{r})$ is provided in Ref. [13]. Note that both PPSIM and VPSIM use the same τ's as the forcing functions.

In PPSIM, aerodynamic rotor-on-rotor coupling effects are captured by off-diagonal blocks in the apparent mass matrix ($[M]$) and the inflow influence coefficient matrix ($[L]$). Although the self-induced effects (diagonal blocks) have closed-form expressions [13], elements in off-diagonal blocks are precalculated using a numerical integration since closed-form expressions are not available. Furthermore, off-diagonal blocks depend on relative separation distances between the rotors. Besides, elements in $[L]$ are a function of the wake skew angle. The equations for the numerical computation of elements in $[M]$ and $[L]$ are

provided in Appendix D.

In Eq. (2.20), free-stream velocity (V_∞) is already replaced by the mass flow parameter matrix ($[V_m]$) to have a nonlinear governing equation, as suggested in Ref. [13]. By having the nonlinear version, total values of $\{\alpha\}$ and $\{\tau\}$ are used instead of the perturbed values $\{\delta\alpha\}$ and $\{\delta\tau\}$. The $[V_m]$ is a block diagonal matrix, i.e., diag($[V_{m1}], ..., [V_{mN}]$). The elements in the mass flow parameter (V_T and V) can be obtained using the uniform inflow state of each rotor, inplane (μ) and normal (λ_f) components of free-stream velocity [62]. For example, the mass flow parameter of rotor N becomes:

$$V_{T_N} = \sqrt{\mu_N^2 + (\lambda_{f_N} + \lambda_{mN})^2}$$

$$V_N = \frac{\mu_N^2 + (\lambda_{f_N} + 2\lambda_{mN})(\lambda_{f_N} + \lambda_{mN})}{V_{T_N}} \tag{2.22}$$

$$\lambda_{mN} = \sqrt{3}\alpha_N(1)$$

where $\alpha_N(1)$ is the uniform inflow state of rotor N.

For coaxial and tandem rotor configurations, Eq. (2.20) is simplified to:

$$\begin{bmatrix} M_{11} & M_{12} \\ M_{21} & M_{22} \end{bmatrix} \begin{Bmatrix} \overset{*}{\alpha}_1 \\ \overset{*}{\alpha}_2 \end{Bmatrix} + \begin{bmatrix} V_{m1} & 0 \\ 0 & V_{m2} \end{bmatrix} \begin{bmatrix} L_{11} & L_{12} \\ L_{21} & L_{22} \end{bmatrix}^{-1} \begin{Bmatrix} \alpha_1 \\ \alpha_2 \end{Bmatrix} = \begin{Bmatrix} \tau_1 \\ \tau_2 \end{Bmatrix} \tag{2.23}$$

Here, diagonal blocks ($M_{11},\ M_{22},\ L_{11},\ L_{22}$) are related to self-induced effects, while off-diagonal blocks ($M_{12},\ M_{21},\ L_{12},\ L_{21}$) capture aerodynamic interference caused by the other rotor. It is crucial to remember that off-diagonal blocks ($M_{12},\ M_{21},\ L_{12},\ L_{21}$) are functions of the relative separation distances between the rotors. These blocks are different for each multi-rotor configuration. The elements in PPSIM off-diagonal blocks are provided for a coaxial and three different tandem rotor configurations in Appendix D.

2.3 Notes on VPSIM and PPSIM: Limitations, Advantages, and Disadvantages

Theoretical formulations of VPSIM and PPSIM follow the same steps as their single rotor counterparts. Common assumptions in both multi-rotor and single rotor inflow models are that flow is incompressible and inviscid. Besides, the wake is assumed to have a rigid cylindrical geometry. In a single rotor configuration, only on-rotor inflow distribution is calculated. Therefore, real flow effects such as wake contraction/expansion, diffusion, and distortion have minimal influence on the single rotor inflow distribution. On the other hand, multi-rotor configurations must consider interactions among the rotors. As such, interference inflow at the other rotor planes must also be calculated to account for mutual interference effects. Once the wake leaves the rotor, real flow effects become more prominent; thus, multi-rotor inflow models suffer more from the assumptions that are made compared to single rotor inflow models. In particular, VPSIM and PPSIM have the following drawbacks.

- As the wake leaves the rotor disk, it starts to contract first to satisfy the continuity equation. Meanwhile, the wake diffuses with air and loses strength as it travels more and more distances. Eventually, the wake ceases contraction, and then it starts to expand until it dies out at the far-stream. Luckily, multi-rotor configurations consist of relatively close rotors. Therefore, they do not suffer much from the wake diffusion and expansion effects. However, wake contraction might be significant for coaxial rotors in hover because the wake starts contracting immediately after leaving the rotor.

- In low speed flight, magnitudes of the induced flow and free-stream velocity are comparable. Due to similar magnitudes, a highly nonlinear (distorted) wake structure is formed, and the validity of the rigid cylindrical wake geometry assumption might become questionable. The wake distortion affects multi-rotor systems more since the wake geometry determines the area of the inflow interference.

Although the governing equations of VPSIM and PPSIM are in state-space form, they have some fundamental differences. In PPSIM, off-diagonal terms in the apparent mass matrix ($[M]$) and the influence coefficient matrix ($[L]$) provide necessary interference effects. In VPSIM, the governing equation consists of block diagonal matrices; thus, the mutual interference effects between the rotors are mainly taken into account at the time inflow is calculated through the superposition of velocity potentials. These differences provide some advantages and disadvantages to both models.

- In VPSIM, another dynamic equation must be solved backward in time to obtain costates. This integration, which starts from the current time, is carried backward in time until the whole wake length is covered. That is why VPSIM has a more complicated form and demands more computational resources due to the additional terms (costates) and bookkeeping. On the other hand, $[M]$ and $[L]$ of PPSIM are precalculated, and PPSIM has the capability of running in real-time.

- As a result of the backward time integration, VPSIM inherently captures the time delay associated with the wake propagation, which PPSIM does not account for. Nevertheless, the time delay effect might be ignored if analyses are limited to low-to-mid frequencies and the separation distances between the rotors are not considerably large.

- PPSIM inflow states are directly related to inflow distribution at each rotor, while this connection is not clear in VPSIM. On the other hand, the induced velocity at any point can be calculated in VPSIM through velocity potentials once the velocity potential states and costates are known. In contrast, PPSIM only provides inflow distributions at rotor planes.

CHAPTER 3
INFLOW COMPARISON METHODOLOGIES AND DESCRIPTION OF SIMULATION SETUP

In order to assess the fidelity of the analytical multi-rotor dynamic inflow models (VPSIM and PPSIM), a higher-order numerical model known as the Viscous Vortex Particle Method (VVPM) is used. VVPM is a wake module inside the FLIGHTLAB comprehensive rotorcraft analysis tool [16]. It is widely used in the multi-rotor flow analyses and extraction of the reduced-order inflow models through the frequency domain system identification techniques [54, 55]. Therefore, VVPM is an ideal candidate for evaluating the fidelity of the VPSIM and PPSIM.

In this chapter, Viscous Vortex Particle Method (VVPM) is briefly introduced. Inflow comparison methodologies and simulation procedures are described.

3.1 Viscous Vortex Particle Method (VVPM)

A brief description of the Viscous Vortex Particle Model (VVPM) and its usage is covered here as details of the model are well documented in Refs. [6, 46, 54]. VVPM solves the vorticity field directly from the vorticity-velocity form of incompressible Navier-Stokes equations using a Lagrangian formulation. It solves governing equations in a convection-diffusion process, which applies to regions with vorticities only. Also, it does not require any grid generation. VVPM captures the fundamental vorticity dominated flow physics for both vorticity stretching and diffusion effects due to air viscosity.

VVPM rotor wake model is coupled with a lifting line based blade element model for vorticity source generation, which is directly related to blade bound circulation from the

Kutta-Joukowski Theorem.

$$
\begin{aligned}
L_{q1}^{0c}(\bar{r},\psi_q) &= \frac{2\pi}{Q}\rho\Omega^2R^3\tau_1^{0c}\bar{r}\sqrt{1-\bar{r}^2}\Psi_1^0 \\
L_{q2}^{1c}(\bar{r},\psi_q) &= \frac{2\pi}{Q}\rho\Omega^2R^3\tau_2^{1c}\bar{r}\sqrt{1-\bar{r}^2}\Psi_2^1\cos(m\psi_q) \\
L_{q2}^{1s}(\bar{r},\psi_q) &= \frac{2\pi}{Q}\rho\Omega^2R^3\tau_2^{1s}\bar{r}\sqrt{1-\bar{r}^2}\Psi_2^1\sin(m\psi_q)
\end{aligned}
\tag{3.1}
$$

where

$$\Psi_n^m(\nu) = \frac{\bar{P}_n^m(\nu)}{\nu}$$

In Eq. (3.1), blade lift distribution ($L_q(\bar{r},\bar{\psi}_q)$) is calculated from rotor pressure coefficients ($\tau_1^{0c},\tau_2^{1c},\tau_2^{1s}$). One can relate aerodynamic thrust (C_T) and moment coefficients (C_M, C_L) to the pressure coefficients in Eq. (3.1) by some constants given in Ref. [13]. This relation allows user-specified airloads distribution ($\tau_1^{0c},\tau_2^{1c},\tau_2^{1s}$) across the rotor disk without a need for airfoil properties such as lift and drag coefficients. Due to the orthogonality of the loading modes in Eq. (3.1), VVPM becomes an ideal candidate for inflow system identification studies since a user can perturb only one loading mode through a selected pressure coefficient without affecting the others. Additionally, VVPM is fully parallelized using both OpenMP on multi-core CPUs and CUDA on compatible GPUs, rendering it an extremely efficient high-fidelity solution for vorticity dominated flow analysis.

Inputs of the VVPM are flight conditions and prescribed rotor loadings. Besides, rotor loadings can be varied during the run time, which is very useful when analyzing transient responses. Minimal post-processing effort is required since VVPM generates the lift distribution and induced velocity field in its output file. It is important to note that VVPM's capabilities are not limited to user-specified airloads. VVPM can be directly coupled with a 6-DOF simulation where airfoil properties are used to compute aerodynamic loadings on the blades.

3.2 Description of Procedures

After establishing FLIGHTLAB definition files for each configuration, simulation parameters such as flight condition and prescribed rotor loadings are specified in a FLIGHTLAB driving script. Then, necessary variables are defined for post-processing. At each time step, induced velocities are sampled at the fixed radial and azimuthal locations of the rotor planes. The procedure to generate VVPM induced velocities is summarized below.

1. Load a multi-rotor model into FLIGHTLAB scope environment.
2. Define advance ratios and prescribed loadings on all rotors.
3. Run the FLIGHTLAB-VVPM model until it achieves a steady-state condition.
4. Define an external input profile to inject perturbation, i.e., step input or sinusoidal frequency sweep.
5. Specify the amount of perturbation and then select a loading component to perturb.
6. Simulate the model for the duration of the perturbation.
7. Save time histories of variables, including blade loadings and induced velocities at pre-defined flow sampling points.

In predicting VPSIM and PPSIM induced flow distributions, blade loadings from the FLIGHTLAB-VVPM are used to ensure that all models have the same loading distribution. Note that VVPM downwash distributions and loadings are time-accurate since blade is moving during the simulation.

3.3 Inflow Comparison Methodologies

Downwash distributions predicted by VPSIM, PPSIM, and VVPM can be directly compared using contour plots. Contour plots provide some qualitative insight into the general

downwash distribution and area of inflow interference. However, they are not suitable for quantitative comparison. Most of the time, three-state inflow models are used in flight simulations, handling qualities analyses, and control law developments. Therefore, uniform (λ_0), fore-to-aft (λ_{1c}), and side-to-side (λ_{1s}) inflow variations are extracted from the on-rotor inflow distributions of PPSIM, VPSIM, and VVPM for quantitative comparison. Figure 3.1 illustrates these fundamental inflow variations.

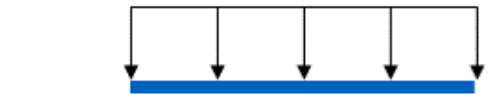

(a) Uniform

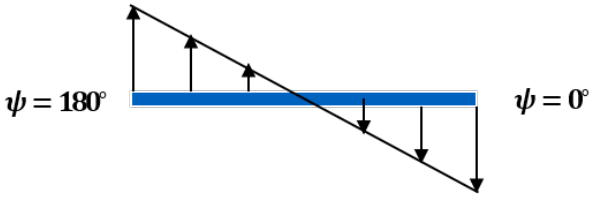

(b) Fore-to-aft (longitudinal)

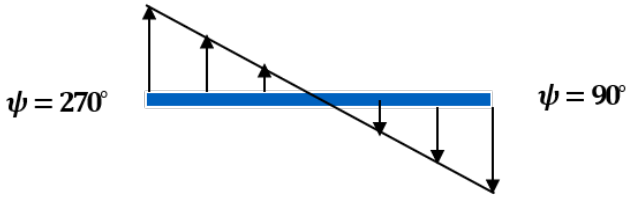

(c) Side-to-side (lateral)

Figure 3.1: Fundamental inflow variations

Induced inflow at the rotor disk due to mean (C_T) and cyclic loadings (C_M, C_L) can be represented by the first harmonic inflow expansion as follows:

$$v_z(\bar{r}, \psi) = \lambda_0 + \lambda_{1c}\bar{r}\cos(\psi) + \lambda_{1s}\bar{r}\sin(\psi) \tag{3.2}$$

By using the orthogonality of trigonometric functions, induced inflow variations in Eq. (3.2) are found to be [19]:

$$\lambda_0 = \frac{1}{\pi} \int_0^{2\pi} \int_0^1 v_z(\bar{r}, \psi) \bar{r} \, d\bar{r} \, d\psi$$

$$\lambda_{1c} = \frac{4}{\pi} \int_0^{2\pi} \int_0^1 v_z(\bar{r}, \psi) \bar{r}^2 \cos(\psi) \, d\bar{r} \, d\psi \tag{3.3}$$

$$\lambda_{1s} = \frac{4}{\pi} \int_0^{2\pi} \int_0^1 v_z(\bar{r}, \psi) \bar{r}^2 \sin(\psi) \, d\bar{r} \, d\psi$$

where $\bar{r}$ and ψ are the rotor radial and azimuthal locations, respectively, of the sampled nondimensional downwash, $v_z(\bar{r}, \psi)$.

Similar to λ_0, λ_{1c}, and λ_{1s} expansion, inflow can also be represented in terms of fundamental three Peters-He inflow states consisting of uniform (α_1^0), fore-to-aft (α_2^{1c}), and side-to-side (α_2^{1s}) variations. These three inflow states (α_1^0, α_2^{1c}, α_2^{1s}) are related to the inflow variations (λ_0, λ_{1c}, λ_{1s}) through radial shaping functions [13]. From any induced flow distribution, α states can be extracted as [54]:

$$\alpha_1^{0c} = \frac{1}{2\pi} \int_0^{2\pi} \int_0^1 v_z(\bar{r}, \psi) \bar{r} \bar{P}_1^0(\bar{r}) \, d\bar{r} \, d\psi$$

$$\alpha_2^{1c} = \frac{1}{\pi} \int_0^{2\pi} \int_0^1 v_z(\bar{r}, \psi) \bar{r} \bar{P}_2^1(\bar{r}) \cos(\psi) \, d\bar{r} \, d\psi \tag{3.4}$$

$$\alpha_2^{1s} = \frac{1}{\pi} \int_0^{2\pi} \int_0^1 v_z(\bar{r}, \psi) \bar{r} \bar{P}_2^1(\bar{r}) \sin(\psi) \, d\bar{r} \, d\psi$$

where $\bar{P}$ is the normalized Legendre function of the first kind.

3.3.1 Steady-State Comparison

Steady values of λ_0, λ_{1c}, λ_{1s} or α_1^{0c}, α_2^{1c}, α_2^{1s} have paramount importance in determining the vehicle performance metrics and trim conditions. Therefore, predictions of these fundamental inflow variations are compared for different flight conditions and configurations. Figure 3.2 summarizes the inflow extraction process in steady-state conditions. Note that only τ_1^{0c}, τ_2^{1c}, and τ_2^{1s} (or C_T, C_M, C_L) are used to drive the simulations of VVPM, VPSIM, and PPSIM. Finite state inflow models can have more than three pressure coefficients depending on the selected harmonic number in the inflow expansion. For every comparison study considered in this dissertation, pressure coefficients except for τ_1^{0c}, τ_2^{1c}, and τ_2^{1s} are always set to zero.

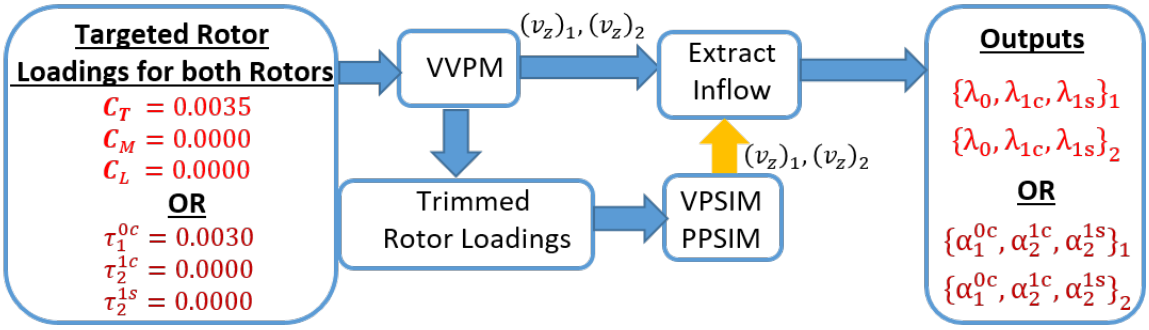

Figure 3.2: Flow chart for acquiring steady-state inflow components

VPSIM and PPSIM are formulated from perturbation theory. These models are linear, although the nonlinear versions of them are widely used. The nonlinear versions are achieved by replacing the free-stream velocity with the mass flow parameter matrix. Thus, it is still instructive to compare perturbed induced inflows from an established flight condition. After inflow reaches the steady-state condition, a step input is introduced to a selected rotor loading component, i.e., $(\Delta C_T)_1$ or $(\Delta\tau_1^{0c})_1$, and simulation is continued until inflow reaches the new steady-state condition. Then, change in the inflow components ($\Delta\lambda$ or $\Delta\alpha$) are computed for comparison.

3.3.2 Frequency Response Comparison

Fidelity of the analytical multi-rotor inflow models is evaluated in the frequency domain by exciting rotor loadings with a sinusoidal frequency sweep. Reference [54] suggests having a frequency range between 0.05 to 4.5 Hz for carrying out inflow dynamic response analysis since VVPM coherence often drops significantly after 4.5 Hz. A normalized chirp (sinusoidal frequency sweep) signal with this frequency range is presented in Fig. 3.3. Frequency responses of VVPM are acquired by the steps described in section 3.2. Figure 3.4 summarizes the procedure further and shows how extracted (actual) VVPM loadings are used to simulate VPSIM and PPSIM. If desired, rotor loadings (C_T, C_M, C_L) and inflow variations (λ_0, λ_{1c}, λ_{1s}) can be replaced by pressure coefficients (τ_1^{0c}, τ_2^{1c}, τ_2^{1s}) and inflow states (α_1^{0c}, α_2^{1c}, α_2^{1s}), respectively. Time histories of the perturbed rotor loadings and extracted fundamental inflow variations of VPSIM, PPSIM, and VVPM, in either form, are supplied as inputs to CIFER® [63] for generating frequency response plots. The results are presented in Bode plots, where inputs are the perturbed rotor loadings (or pressure coefficients) and outputs are the excited induced inflow variations (or inflow states).

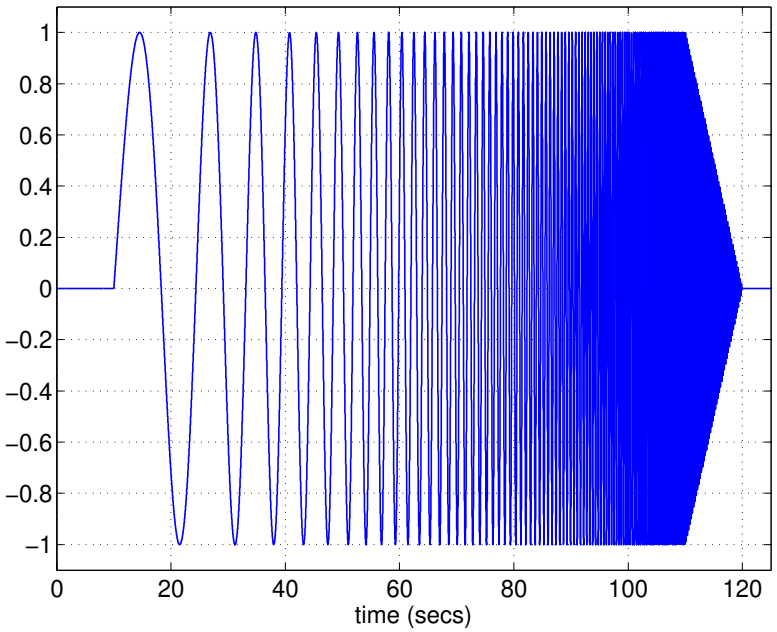

Figure 3.3: Normalized chirp signal used in the frequency sweep

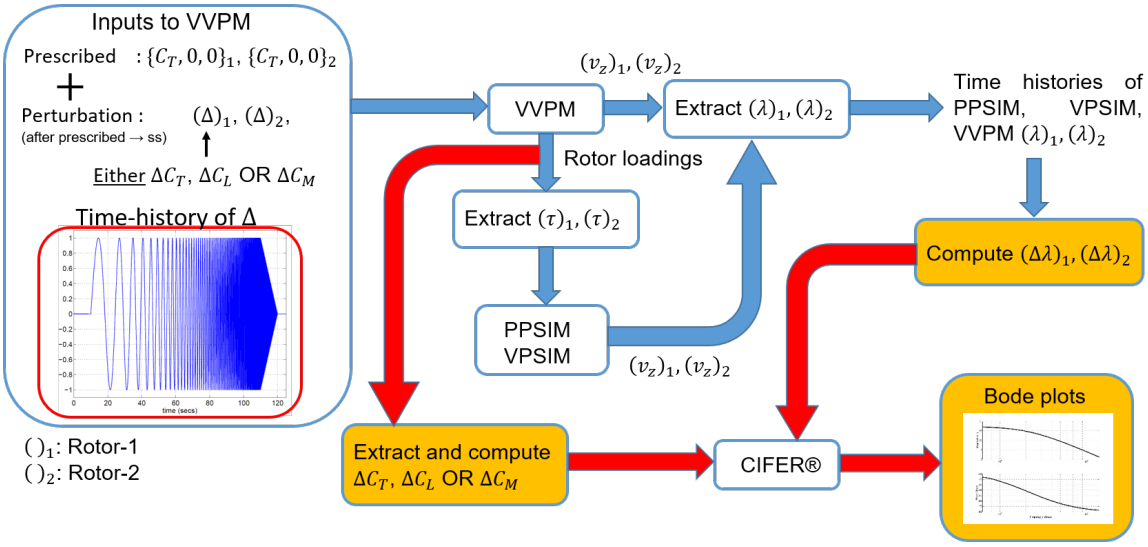

Figure 3.4: Procedure for acquiring frequency response

The following metrics are adopted from the flight dynamics area to quantify frequency responses. Maximum Unnoticeable Added Dynamics (MUAD) Envelopes [64] and frequency response coherence weighted cost function [63] allow direct comparison of the frequency responses of VPSIM, PPSIM, and the truth model. However, it is crucial to recognize that these metrics are invented for comparisons that involve changes in the vehicle attitude angles, angular rates, and accelerations. Inflow dynamics is only one of the factors that affect vehicle dynamics. Although these quantification approaches are not fully applicable to inflow dynamics, they still provide some insight regarding the fidelity of the multi-rotor inflow models.

Maximum Unnoticeable Added Dynamics (MUAD) Envelopes

Maximum Unnoticeable Added Dynamics (MUAD) [64] is used to study differences in frequency responses between VPSIM, PPSIM, and VVPM. The MUAD envelopes examine the quality of the match between the higher-order model (or experiment) and the lower-order model. When a higher-order model is replaced by its lower-order equivalent, certain dynamics are not well captured by the lower-order equivalent model (or reduced-order model), and these mismatches in dynamics cause a loss of fidelity in the simulation model.

The loss of fidelity becomes important when it is perceived by the pilots. This fidelity loss is systematically analyzed with pilots to draw mismatch boundaries. [65]. Observations showed that pilots are sensitive to changes in the dynamics between 1 rad/s and 5 rad/s [64]. Furthermore, pilots are more sensitive to negative changes, as shown in Fig. 3.5.

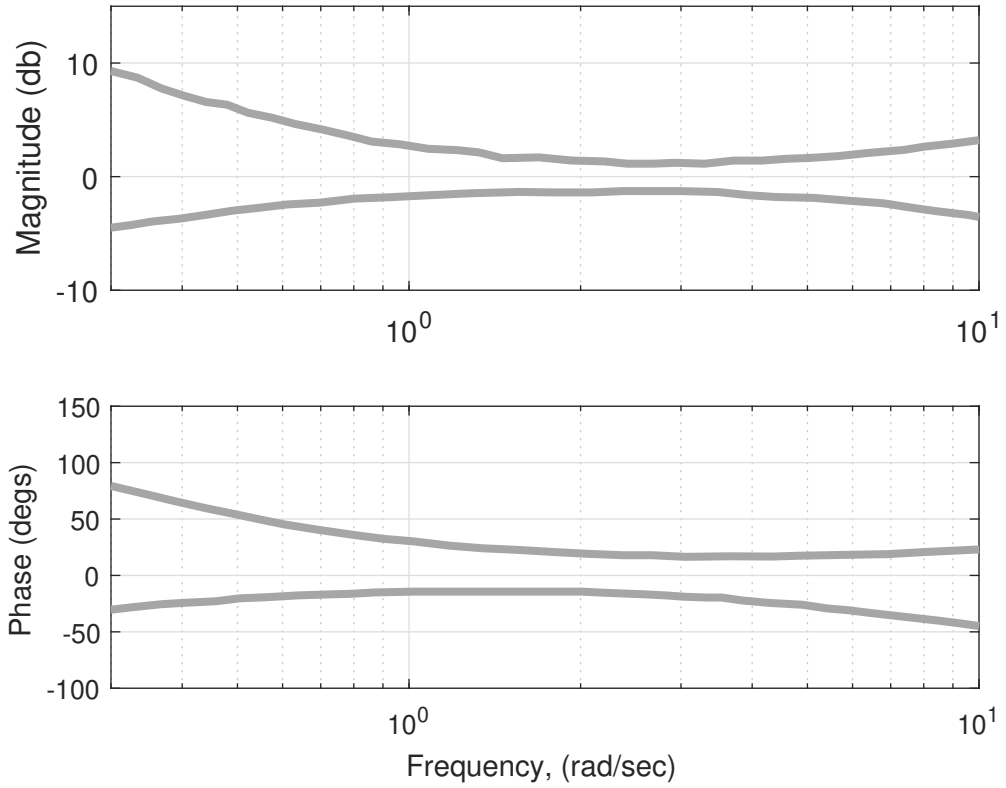

Figure 3.5: Envelopes of Maximum Unnoticeable Added Dynamics

While plotting the MUAD envelopes, the truth model (VVPM or test data, etc.) is taken as reference. Then, mismatches between the truth model and finite state multi-rotor dynamic inflow models are plotted on top of mismatch boundaries (Fig. 3.5).

Computation of cost function from frequency response differences

Frequency responses are quantified using a coherence weighted cost function (J) to determine the differences between the perturbed inflow variations of analytical multi-rotor

dynamic inflow models (VPSIM & PPSIM) and the truth model. The coherence weighted cost function is given as [63]:

$$J = \frac{20}{n_\omega} \sum_{\omega_1}^{\omega_{n_\omega}} W_\gamma [W_g(|\Delta T|)^2 + W_p(\angle \Delta T)^2] \tag{3.5}$$

where $|\Delta T|$ is the magnitude difference in dB between the VVPM and PPSIM or VPSIM for comparison at each frequency, ω. Similarly, $\angle \Delta T$ is the phase difference expressed in degrees at each frequency; n_ω is the number of frequency points; ω_1 and ω_{n_ω} are the starting and ending frequencies of the response, respectively. W_γ is a weighting function dependent on the value of the coherence function of VVPM at each frequency. W_g and W_p are the relative weights for magnitude and phase comparisons, respectively. Reference [63] suggests using $\mathrm{W}_g = 1.0$ and $\mathrm{W}_p = 0.01745$ which sets 1 dB magnitude error equivalent to 7.57 degrees phase error. As a guideline in flight dynamics modeling, a cost function value less than 50 means that differences between the two models are nearly indistinguishable in both frequency and time domains, while a value less than 100 generally reflects a good match between the models [63].

It is important to note that similar threshold values for cost function metrics are not yet established in assessing the fidelity of inflow models. The coherence weighted cost function and Maximum Unnoticeable Added Dynamics (MUAD) error bound envelopes are widely used error metrics in frequency domain analyses. However, designated thresholds in these metrics are defined for body rates, attitudes, and accelerations, etc. Error metrics thresholds for inflow dynamics are still not available. As such, the frequency domain quadratic error metric of Ref. [63] is used only as a qualitative guide for assessing inflow model fidelity. Hence, the use of suggested error thresholds for assessing the rotor inflow models requires caution.

3.4 Scope of Work and Simulation Setup

In this dissertation, mainly two multi-rotor configurations are considered, viz., a coaxial and a tandem rotor configuration. The geometric properties of the Harrington Coaxial Rotor 1 [66] are used to create isolated multi-rotor configurations by changing the separation distances between the rotors. Harrington Coaxial Rotor 1 has a rotor radius of 12.5 ft, and the upper rotor is offset from the lower rotor by 2.38 ft (19 percent of rotor radius). The rotational speed of the upper and lower rotors is 37.5 rad/s. By changing the longitudinal ($\bar{d}$), vertical ($\bar{h}$), and lateral ($\bar{l}$) separation distances of Harrington Coaxial Rotor 1, a tandem rotor configuration is created. Here, vertical and lateral separation distances are fixed to 0.19 and 0, respectively, while longitudinal separation distance is changed from 0 (coaxial) to 1.5 (tandem). Figure 3.6 presents a generic configuration of two rotors where separation distances are normalized by the rotor radius, R.

Comparisons of contour plots and steady-state inflow components among the VPSIM, PPSIM, and VVPM are carried out as advance ratio is varied from hover to 0.2 for each configuration. Steady-state perturbation and frequency response cases are considered for hover and low speeds conditions. The wake distortion effect is maximum at low speeds and has a significant contribution to the inflow interference. Often, rotor 1 (upper/front rotor) aerodynamic loadings are perturbed since the wake of rotor 1 has a substantial impact on rotor 2 (lower/rear rotor) because some portion of rotor 2 always operates inside the wake of rotor 1. By placing rotor 1 deliberately above rotor 2, the effect of the wake interference can be studied for different flight conditions. Moreover, the wake of rotor 2 (lower/rear rotor) moves further away from rotor 1 as speed increases. As a consequence, interference effects on rotor 1 significantly diminish.

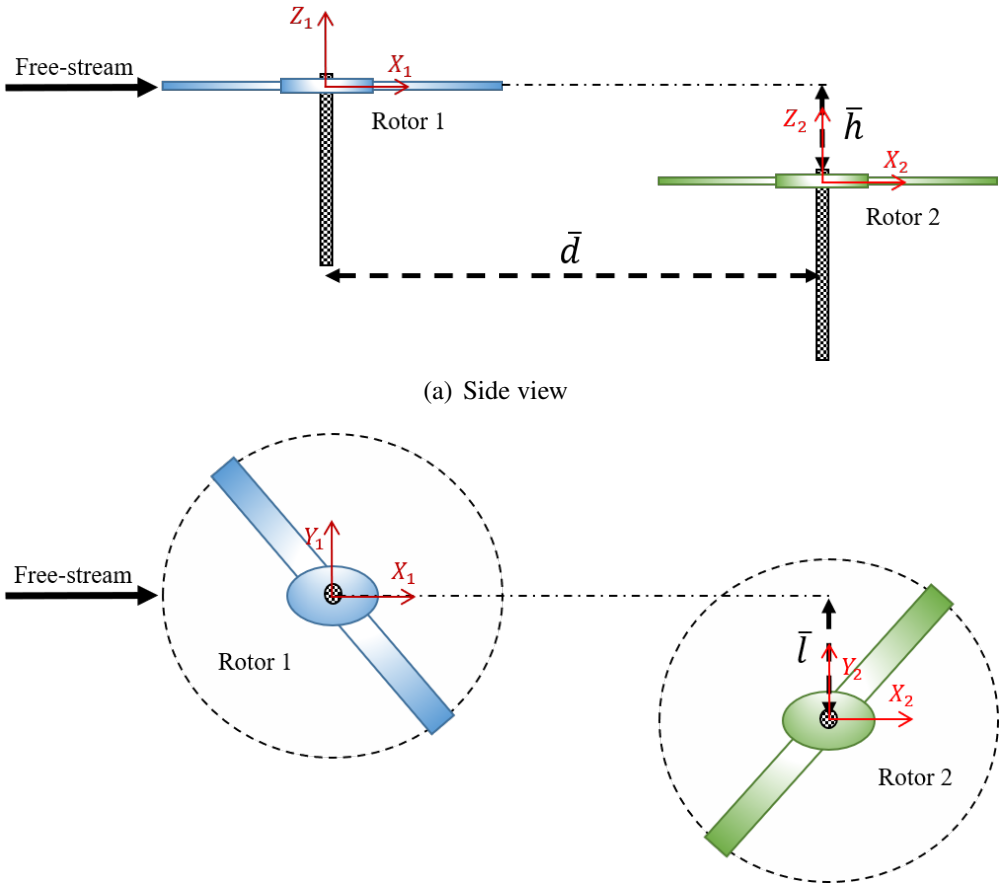

(a) Side view

(b) Top view

Figure 3.6: A generic dual-rotor configuration

3.5 Extraction of PPSIM Inflow Influence Coefficient Matrix

The inflow influence coefficient matrix ($[L]$) provides a direct relation between the rotor aerodynamic loadings and inflow states. By applying a system identification technique [30], inflow influence coefficient matrices of VVPM and VPSIM can be identified from their downwash distributions in the form of PPSIM $[L]$. By comparing the identified inflow influence coefficient matrices, PPSIM $[L]$ can be corrected using the $[L]$ of the reference wake model, i.e., VVPM, to improve the correlation. This is a potent technique applicable to any rotor configuration. Reference [30] demonstrates its application to a coaxial rotor. In this section, identification of the PPSIM $[L]$ is briefly described as the entire process is provided in Ref. [30].

In VVPM, loading distribution consists of an orthogonal set of loading modes, which are predetermined by prescribing the pressure coefficients using Eq. (3.1). This prescription provides a clear advantage to VVPM since inflow responses are directly related to the single excited pressure mode without exciting the other loading modes. Equation (3.6) describes the identification process [30]. In this equation, perturbed rotor 1 and rotor 2 pressure coefficients are expressed as $\{\Delta\tau_1\}$ and $\{\Delta\tau_2\}$, respectively. Variables $\{\Delta\alpha_{11}\}$ and $\{\Delta\alpha_{21}\}$ represent the changes in rotor 1 and rotor 2 inflow states due to applied step input on rotor 1 pressure coefficients. Similarly, $\{\Delta\alpha_{12}\}$ and $\{\Delta\alpha_{22}\}$ are the changes in rotor 1 and rotor 2 inflow states due to applied step input on rotor 2 pressure coefficients.

$$
\begin{aligned}
[L_{11}]_{\text{Identified}} &= 2V_1\{\Delta\alpha_{11}\}\{\Delta\tau_1\}^+ \\
[L_{12}]_{\text{Identified}} &= 2V_2\{\Delta\alpha_{12}\}\{\Delta\tau_2\}^+ \\
[L_{21}]_{\text{Identified}} &= 2V_1\{\Delta\alpha_{21}\}\{\Delta\tau_1\}^+ \\
[L_{22}]_{\text{Identified}} &= 2V_2\{\Delta\alpha_{22}\}\{\Delta\tau_2\}^+
\end{aligned}
\tag{3.6}
$$

where

$$
\begin{aligned}
\{\Delta\tau_1\}^+ &= [\{\Delta\tau_1\}^T\{\Delta\tau_1\}]^{-1}\{\Delta\tau_1\}^T \\
\{\Delta\tau_2\}^+ &= [\{\Delta\tau_2\}^T\{\Delta\tau_2\}]^{-1}\{\Delta\tau_2\}^T
\end{aligned}
$$

$$
\{\alpha\} = \begin{Bmatrix} \alpha_1^{0c} \\ \alpha_2^{1c} \\ \alpha_2^{1s} \end{Bmatrix} \qquad \{\tau\} = \begin{Bmatrix} \tau_1^{0c} \\ \tau_2^{1c} \\ \tau_2^{1s} \end{Bmatrix}
$$

In Eq. (3.6), the mass flow parameter matrix ($[V_m]$) is replaced by a scalar value, V. Using V and small perturbations from an established flight condition, the inflow influence coefficient matrix can be identified from the inflow distribution of any wake model.

CHAPTER 4

CONNECTION BETWEEN THE VPSIM AND PPSIM

VPSIM and PPSIM are formulated from first principles and in state-space form. However, their final forms have some differences due to approaches taken in the derivation processes. In PPSIM, off-diagonal blocks of the apparent mass matrix ($M_{12},\ M_{21}$) and influence coefficient matrix ($L_{12},\ L_{21}$) depict the flow interactions between the rotors. Besides, PPSIM states are directly related to on-rotor inflow distribution. This form of the PPSIM is desirable since coupling between the rotors is immediately available from off-diagonal blocks. In VPSIM, the governing inflow equation consists of block diagonal matrices, and velocity potential states are related to the whole flow field. Mutual interference effects between the rotors are taken into account at the time inflow is calculated through the superposition of velocity potentials. In this form, it is often hard to see how interference effects are included in VPSIM. Therefore, an inflow influence coefficient matrix ($[L]$) is extracted from the downwash distribution of VPSIM and then compared against the $[L]$ of PPSIM. Note that $[L]$ is defined for PPSIM and should not be confused by the $[\tilde{L}]$ of VPSIM.

Inflow simulations of Harrington coaxial rotor [66] configuration are used to portray the connection between the VPSIM and PPSIM. Figure 4.1 shows the coaxial rotor configuration. Inflow influence coefficient matrices of VPSIM and PPSIM are compared in hover and at the advance ratio of 0.07 for this rotor. In VPSIM, the number of odd and even velocity potential sates are varied to explore their effects on the extracted $[L]$ of VPSIM. Also, a chirp input is applied one at a time to upper rotor uniform (τ_1^{0c}), fore-to-aft (τ_2^{1c}), and side-to-side (τ_2^{1s}) pressure coefficients to analyze the effect of selected odd and even velocity potential states on transient inflow response. Finally, steady-state inflow predictions from Viscous Vortex Particle Method (VVPM) are compared against the inflow predictions from PPSIM and VPSIM for this coaxial rotor as advance ratio is varied from hover to 0.2.

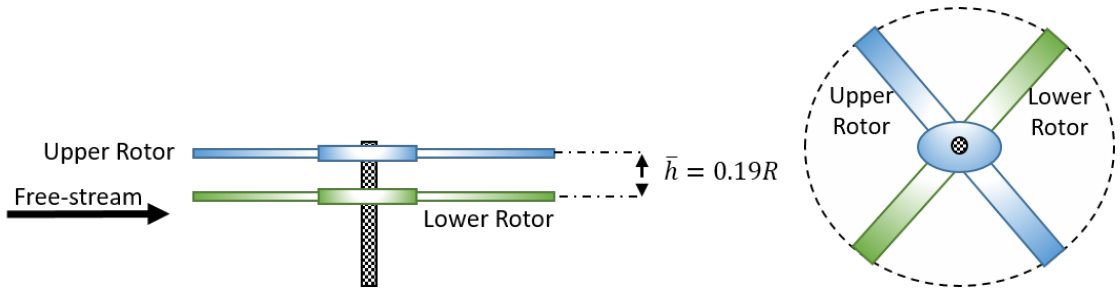

(a) Side view (b) Top view

Figure 4.1: Harrington coaxial rotor configuration

4.1 Inflow Influence Coefficient Matrix Comparison

Before extracting the VPSIM $[L]$, the overall extraction methodology (Eq. (3.6)) is validated. For this purpose, inflow distributions of the three-state, six-state, and fifteen-state PPSIM are used, and extracted inflow influence coefficient matrices are compared against the theoretical $[L]$ obtained by using Eqs. (D.4)–(D.6). Table 4.1 shows that extracted inflow influence coefficient matrices agree well with the theoretical $[L]$ in hover. Small differences between the theoretical and extracted inflow influence coefficient matrices are attributed to the lower and upper limits of the radial integral defined in Eq. (3.4). In practical applications, the lower limit starts from the root-cutout, and the upper integration limit ends at the last aerodynamics calculation point just before the blade tip. Despite this difference, extracted inflow influence coefficient matrices have good agreement with the theoretical $[L]$. Since VPSIM is subject to the same radial integration limits, the extracted $[L]$ of PPSIM is used as a reference in comparisons. The number of odd and even velocity potential states are varied in VPSIM to understand their effects on steady and transient inflow response. Table 4.2 displays the number of odd and even velocity potential states and costates that are considered in VPSIM.

Tables 4.3 and 4.4 compare extracted inflow influence coefficient matrices from inflow distributions of VPSIM with different number of odd and even velocity potential states. In hover (Table 4.3), every VPSIM case shows a good correlation with PPSIM. At the ad-

vance ratio of 0.07 (Table 4.4), the element corresponds to the lower rotor self-uniform inflow ($L_{22}(1,1)$) is slightly under-predicted by the VPSIM for all cases compared to PP-SIM. In contrast, elements in L_{21} show that VPSIM predicts slightly more interference than the PPSIM. In addition, the effect of the even velocity potential states on interference calculation becomes more evident since off-diagonal blocks ($L_{12},\ L_{21}$) of VPSIM slightly differ from each other. Although there are some differences between PPSIM and VPSIM at the advance ratio of 0.07, extracted inflow influence coefficient matrices of VPSIM show that superposition of the velocity potentials is a viable approach for capturing mutual interference effects between the rotors like PPSIM.

Table 4.1: Validation of the extracted inflow influence coefficient matrices using PPSIM coaxial rotor downwash distribution in hover

Elements [a]	PPSIM-T[b]	PPSIM-3[c]	PPSIM-6[d]	PPSIM-15[e]
$L_{11}(1,1)$	0.750	0.748	0.748	0.749
$L_{11}(2,2)$	0.625	0.621	0.621	0.623
$L_{11}(3,3)$	0.625	0.622	0.622	0.623
$L_{12}(1,1)$	0.529	0.528	0.528	0.528
$L_{12}(2,2)$	0.338	0.336	0.336	0.337
$L_{12}(3,3)$	0.338	0.336	0.336	0.338
$L_{21}(1,1)$	0.971	0.969	0.969	0.970
$L_{21}(2,2)$	0.912	0.906	0.906	0.908
$L_{21}(3,3)$	0.912	0.907	0.907	0.909
$L_{22}(1,1)$	0.750	0.748	0.748	0.749
$L_{22}(2,2)$	0.625	0.621	0.621	0.623
$L_{22}(3,3)$	0.625	0.622	0.622	0.623
$\|\| x \|\|_2$ [f]	0	0.009	0.008	0.005

[a] $L_{ij}(m,n)$ subscript ij indicates the effect of j^{th} rotor on i^{th} rotor while (m,n) indicates an element in L_{ij} corresponding to m^{th} row and n^{th} column

[b] Theoretical $[L]$

[c] Extracted $[L]$ from 3-state PPSIM downwash distribution

[d] Extracted $[L]$ from 6-state PPSIM downwash distribution

[e] Extracted $[L]$ from 15-state PPSIM downwash distribution

[f] l^2-norm

Table 4.2: Number of odd and even velocity potential states (v. p. states) used for a rotor in VPSIM

VPSIM	Odd v. p. states	Even v. p. states	Total v. p. states
V-mO1	3	0	3 (+3)[a]
V-mO1E1	3	3	6 (+6)
V-mO2	6	0	6 (+6)
V-mO2E2	6	6	12 (+12)
V-mO4	15	0	15 (+15)
V-mO4E4	15	15	30 (+30)

[a](+Number) indicates number of additional terms (costates) required for the upper rotor

Table 4.3: Comparison of coaxial rotor extracted inflow influence coefficient matrices in hover

Elements	V-mO1	V-mO1E1	V-mO2	V-mO2E2	V-mO4	V-mO4E4	PPSIM
$L_{11}(1,1)$	0.749	0.749	0.749	0.749	0.749	0.746	0.748
$L_{11}(2,2)$	0.623	0.623	0.623	0.623	0.623	0.623	0.621
$L_{11}(3,3)$	0.624	0.624	0.624	0.624	0.624	0.624	0.622
$L_{12}(1,1)$	0.528	0.528	0.528	0.528	0.528	0.525	0.528
$L_{12}(2,2)$	0.337	0.337	0.337	0.337	0.337	0.337	0.336
$L_{12}(3,3)$	0.337	0.337	0.337	0.337	0.337	0.338	0.336
$L_{21}(1,1)$	0.970	0.970	0.970	0.970	0.970	0.970	0.969
$L_{21}(2,2)$	0.910	0.910	0.910	0.910	0.910	0.909	0.906
$L_{21}(3,3)$	0.911	0.911	0.911	0.911	0.911	0.911	0.907
$L_{22}(1,1)$	0.749	0.749	0.749	0.749	0.749	0.746	0.748
$L_{22}(2,2)$	0.623	0.623	0.623	0.623	0.623	0.623	0.621
$L_{22}(3,3)$	0.624	0.624	0.624	0.624	0.624	0.624	0.622

Table 4.4: Comparison of coaxial rotor extracted inflow influence coefficient matrices at the advance ratio of 0.07

Elements	V-mO1	V-mO1E1	V-mO2	V-mO2E2	V-mO4	V-mO4E4	PPSIM
$L_{11}(1,1)$	0.749	0.749	0.749	0.749	0.749	0.749	0.749
$L_{11}(1,2)$	-0.170	-0.170	-0.169	-0.169	-0.170	-0.170	-0.170
$L_{11}(2,1)$	0.340	0.340	0.340	0.339	0.340	0.339	0.339
$L_{11}(2,2)$	0.550	0.550	0.550	0.550	0.550	0.550	0.548
$L_{11}(3,3)$	0.697	0.697	0.697	0.697	0.697	0.698	0.695
$L_{12}(1,1)$	0.528	0.528	0.528	0.528	0.528	0.528	0.528
$L_{12}(1,2)$	-0.097	-0.089	-0.098	-0.094	-0.097	-0.089	-0.089
$L_{12}(2,1)$	0.149	0.149	0.149	0.178	0.146	0.177	0.177
$L_{12}(2,2)$	0.311	0.311	0.311	0.311	0.311	0.311	0.310
$L_{12}(3,3)$	0.363	0.363	0.363	0.363	0.363	0.363	0.362
$L_{21}(1,1)$	1.043	1.041	1.039	1.039	1.041	1.030	0.921
$L_{21}(1,2)$	-0.275	-0.261	-0.278	-0.267	-0.278	-0.271	-0.259
$L_{21}(2,1)$	0.528	0.533	0.512	0.556	0.505	0.525	0.516
$L_{21}(2,2)$	0.789	0.795	0.798	0.793	0.795	0.788	0.659
$L_{21}(3,3)$	1.091	1.091	1.095	1.091	1.092	1.094	0.952
$L_{22}(1,1)$	0.719	0.720	0.720	0.721	0.720	0.719	0.748
$L_{22}(1,2)$	-0.132	-0.132	-0.131	-0.132	-0.132	-0.132	-0.137
$L_{22}(2,1)$	0.266	0.264	0.269	0.267	0.270	0.262	0.273
$L_{22}(2,2)$	0.577	0.577	0.577	0.577	0.576	0.578	0.574
$L_{22}(3,3)$	0.672	0.672	0.672	0.672	0.672	0.672	0.669

4.2 Frequency Response Comparison

The effect of the number of odd and even velocity potential states on inflow dynamics is studied in the frequency domain by exciting upper rotor pressure coefficients (τ_1^{0c}, τ_2^{1c}, τ_2^{1s}) with a sinusoidal frequency sweep. Note that only τ_1^{0c}, τ_2^{1c}, and τ_2^{1s} are utilized to drive the simulations while other pressure coefficients, even if they exist, are set to zero. A normalized chirp (sinusoidal frequency sweep) signal with a frequency range between 0.05 to 4.5 Hz (see Fig. 3.3) is used during simulations. After applying the frequency sweep

to a selected pressure coefficient, changes in the inflow distributions are saved, and then inflow states (α_1^{0c}, α_2^{1c}, α_2^{1s}) are extracted using Eqs. (3.4). Time histories of the perturbed pressure coefficient and extracted fundamental inflow states of VPSIM and PPSIM are supplied as inputs to CIFER® [63]. The results are presented in Bode plots where input is the perturbed upper rotor pressure coefficient, and outputs are the excited inflow states. It is essential to recognize that PPSIM inflow expansion is established by a set of orthogonal inflow states ($\{\alpha\}$) [30]. In PPSIM, even if a different number of states is used in the inflow expansion, uniform (α_1^{0c}), fore-to-aft (α_2^{1c}), and side-to-side (α_2^{1s}) inflow variations, which are extracted using Eq. (3.4), are same and independent of the selected terms in the inflow expansion due to this orthogonality. Therefore, while only one PPSIM case is shown, the number of VPSIM velocity potential states is varied in the following results.

Figures 4.2 and 4.3 show uniform and fore-to-aft inflow responses in hover due to perturbations of the upper rotor uniform and fore-to-aft pressure coefficients, respectively. At the upper rotor, magnitude and phase plots indicate that VPSIM predictions with only odd velocity potential states have responses similar to PPSIM predictions in hover (Figs. 4.2(a)–4.3(a)), whereas VPSIM cases with both odd and even velocity potential states (except for the case V-mO1E1 in Fig. 4.3) predict an earlier decrease in magnitude towards the high frequency range. At the lower rotor, every VPSIM case differs from the PPSIM as the time delay effect, which is inherently included in VPSIM, becomes more prominent at the higher frequencies, as shown in Figs. 4.2(b)–4.3(b).

Figures 4.4, 4.5, and 4.6 present uniform, side-to-side, and fore-to-aft inflow responses with respect to perturbed uniform, side-to-side, and fore-to-aft pressure coefficients. Like the hover case, VPSIM cases with only odd velocity potential states have responses like PPSIM cases at the upper rotor. While inflow responses of VPSIM with odd and even velocity potential states display a slightly earlier decrease in magnitude compared to VPSIM cases with only odd velocity potential states, their phase predictions have good agreement at both upper and lower rotors. Similar to hover, every VPSIM case displays the effect of

time delay at the lower rotor inflow response, whereas PPSIM does not have such an effect, as shown in Figs. 4.4(b), 4.5(b), and 4.6(b). Fig. 4.6 presents that VPSIM with 15 odd and 15 even velocity potential states case (V-mO4E4) predicts slightly less fore-to-aft inflow (α_2^{1c}) magnitude at both rotors compared to other VPSIM cases. In forward flight, uniform and fore-to-aft inflow components are coupled due to the wake skew. The coupling is more severe in this case because 15 odd and 15 even velocity potential states populate the $[L]$, and this large number of even velocity potential states mostly affects the interference inflow predictions. Therefore, VPSIM fore-to-aft inflow prediction is more sensitive to changes in the number of even velocity potential states.

4.3 Steady-State Inflow Components and Contour Plot Comparisons Against Viscous Vortex Particle Method

Isolated Harrington coaxial rotor model (Fig. 4.1) with only aerodynamic forces (without consideration of blade dynamics) is modeled in FLIGHTLAB. The targeted steady-state pressure coefficients of both rotors are set to $\{\tau\} = \{0.003,\ 0.0,\ 0.0\}^T$. The detailed acquisition of the steady-state inflow states follows the procedure provided in chapter 3. The procedure is also summarized in Fig. 3.2.

Figure 4.7 shows predicted values of the upper rotor steady-state uniform and fore-to-aft (longitudinal) inflow components as advance ratio is varied from hover to 0.2. PPSIM and all VPSIM cases have a good match with VVPM in $(\alpha_1^{0c})_U$ prediction. At the low advance ratio region, PPSIM and VPSIM slightly underestimate the fore-to-aft inflow component $(\alpha_2^{1c})_U$ compared to the VVPM prediction. At low speed, the wake is highly nonlinear since distortion effects alter the wake structure. On the other hand, both PPSIM and VPSIM assume a rigid wake geometry. Therefore, rigid wake models under-predict the fore-to-aft inflow component at the low advance ratio region. This mismatch is not specific to the multi-rotor case since single rotor finite state dynamic inflow models also under-predict the fore-to-aft inflow component at low advance ratio region.

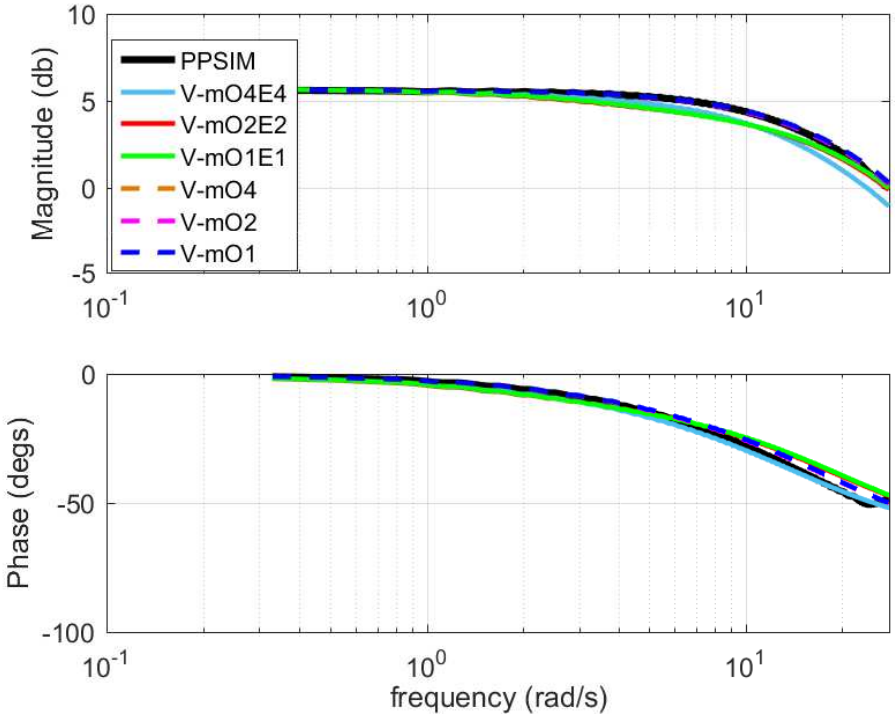

(a) Upper rotor uniform inflow

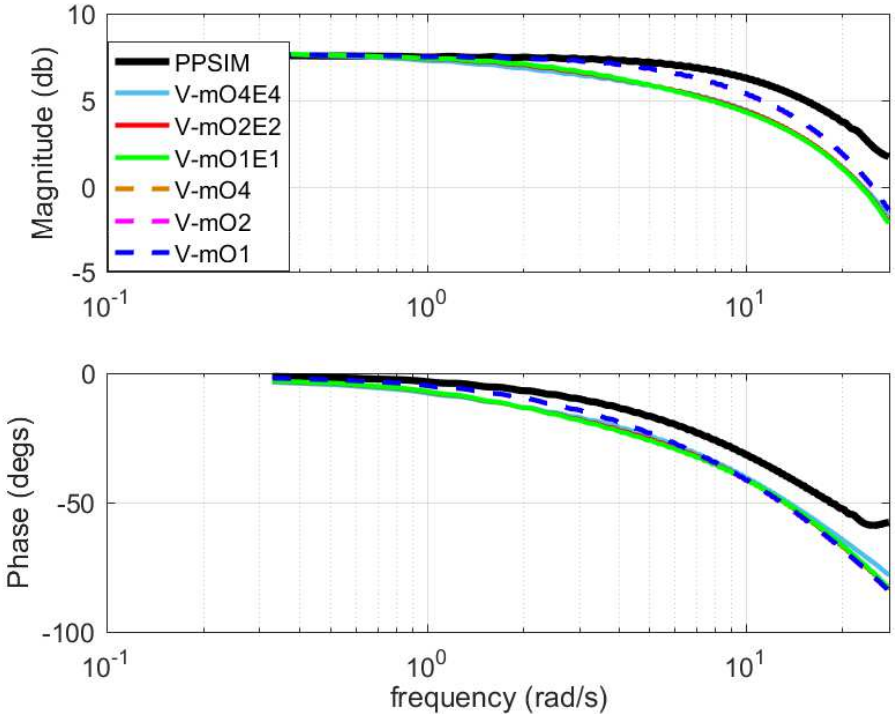

(b) Lower rotor uniform inflow

Figure 4.2: Comparison of coaxial rotor uniform (α_1^{0c}) inflow response due to τ_1^{0c} excitation in hover

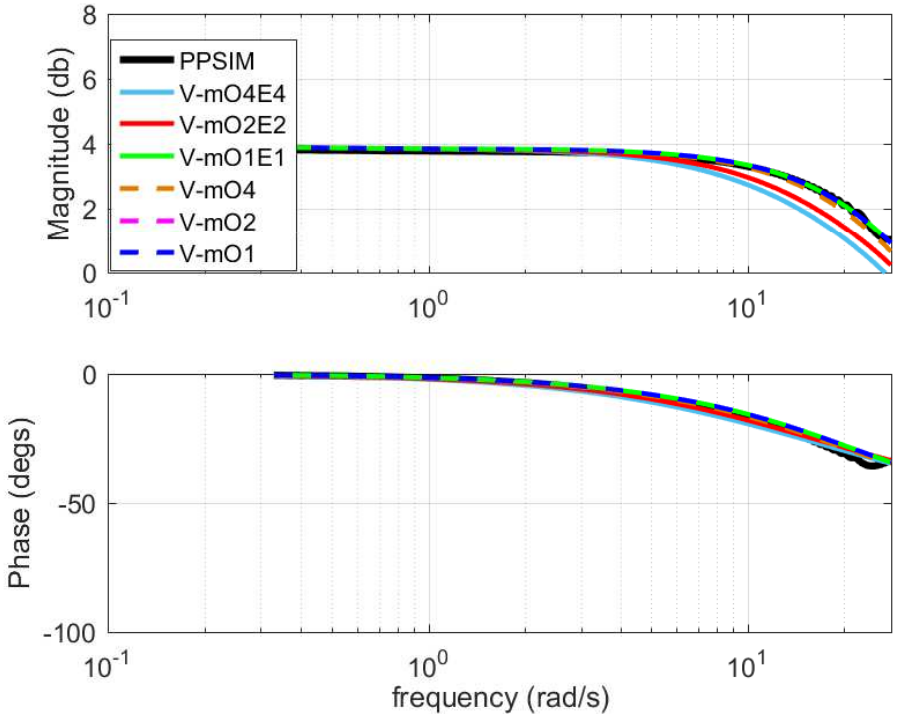

(a) Upper rotor fore-to-aft (longitudinal) inflow

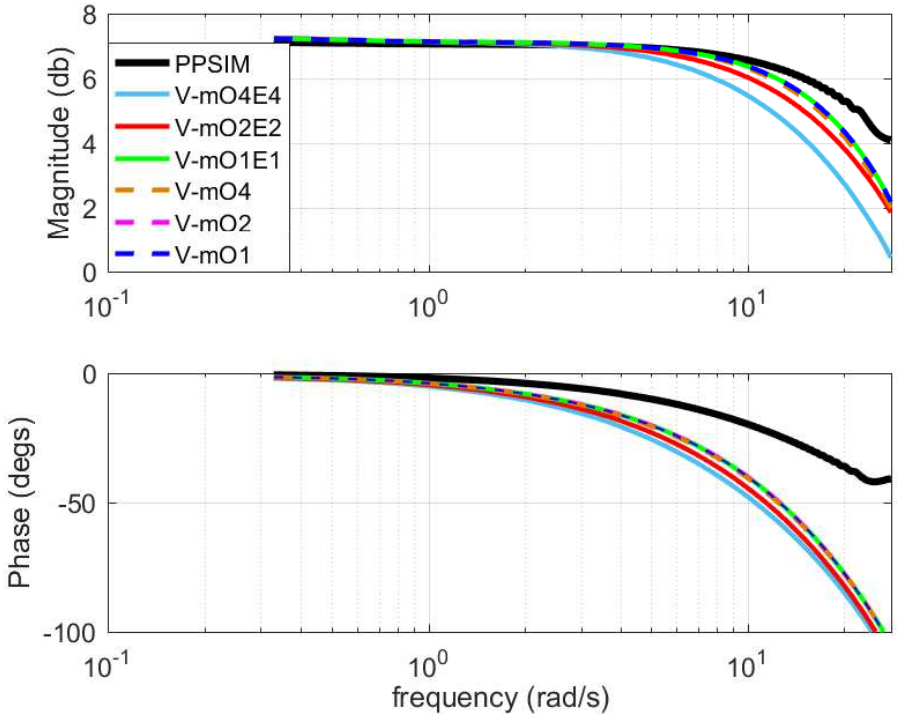

(b) Lower rotor fore-to-aft (longitudinal) inflow

Figure 4.3: Comparison of coaxial rotor fore-to-aft (α_2^{1c}) inflow response due to τ_2^{1c} excitation in hover

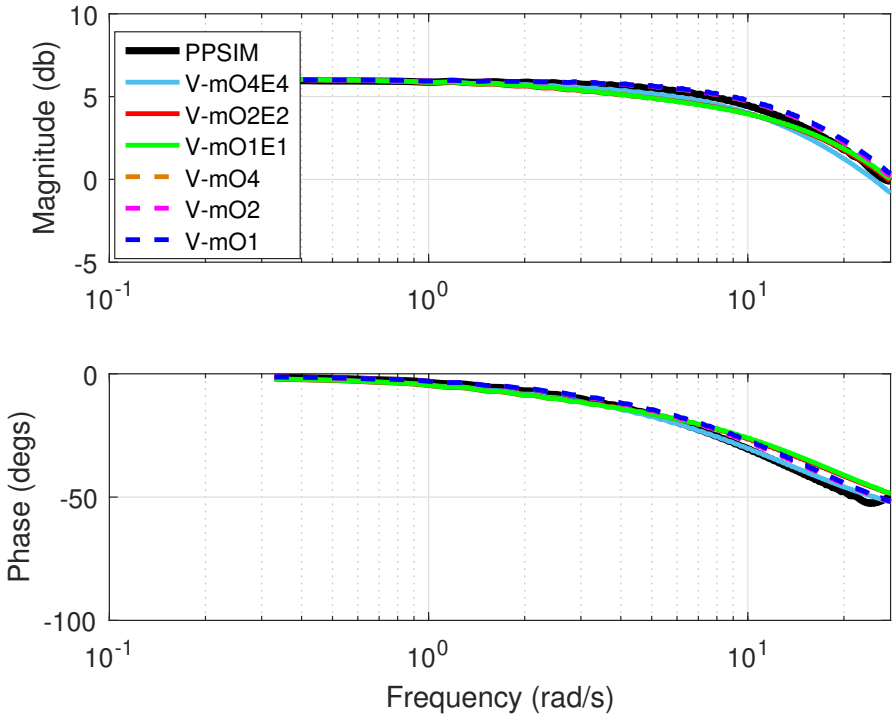

(a) Upper rotor uniform inflow

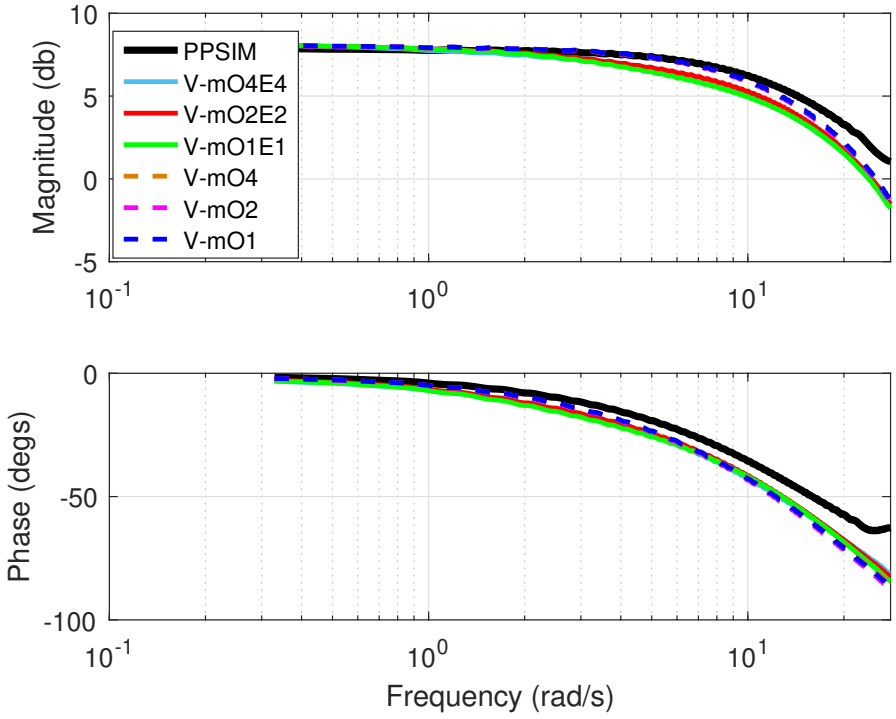

(b) Lower rotor uniform inflow

Figure 4.4: Comparison of coaxial rotor uniform (α_1^{0c}) inflow response due to τ_1^{0c} excitation at $\mu = 0.07$

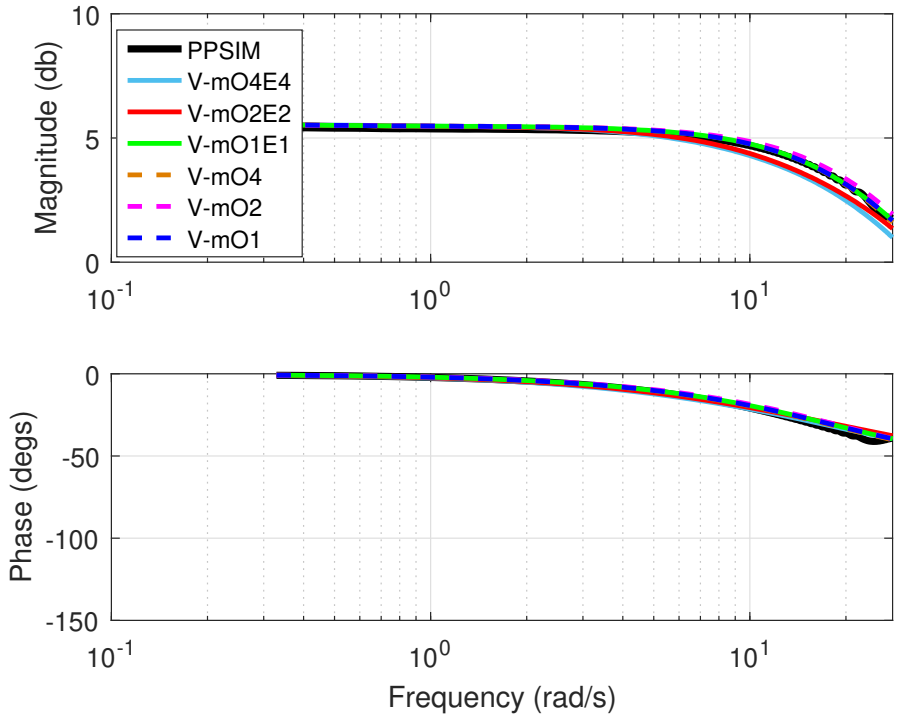

(a) Upper rotor side-to-side (lateral) inflow

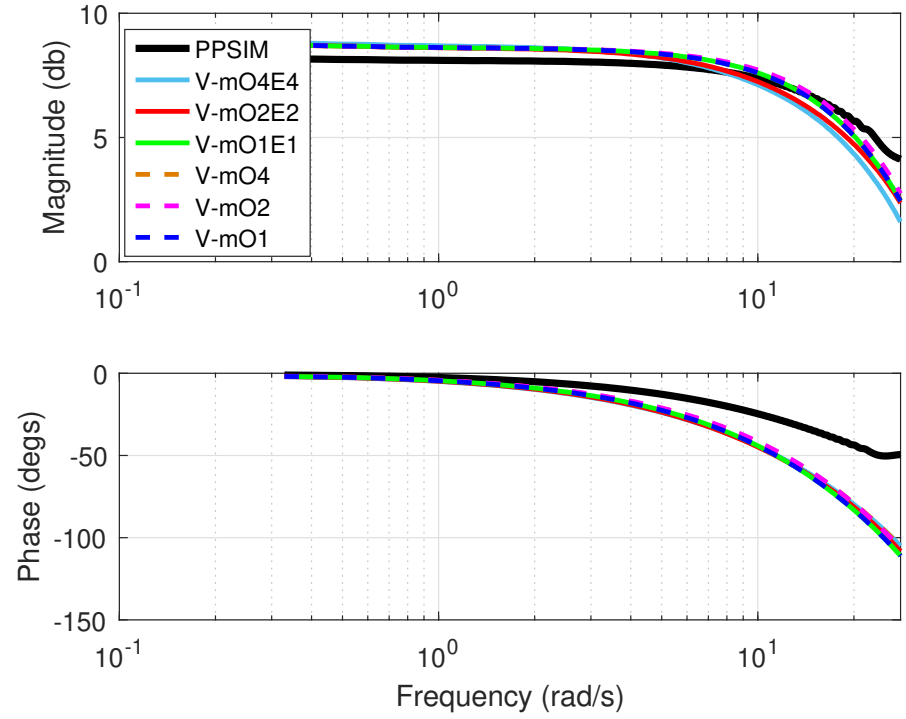

(b) Lower rotor side-to-side (lateral) inflow

Figure 4.5: Comparison of coaxial rotor side-to-side (α_2^{1s}) inflow response due to τ_2^{1s} excitation at $\mu = 0.07$

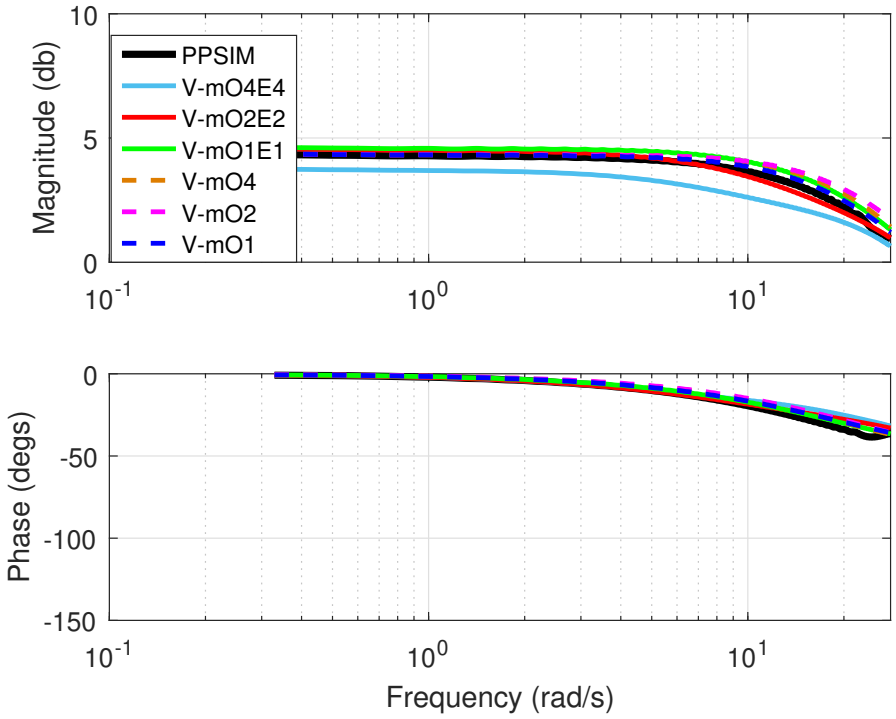

(a) Upper rotor fore-to-aft (longitudinal) inflow

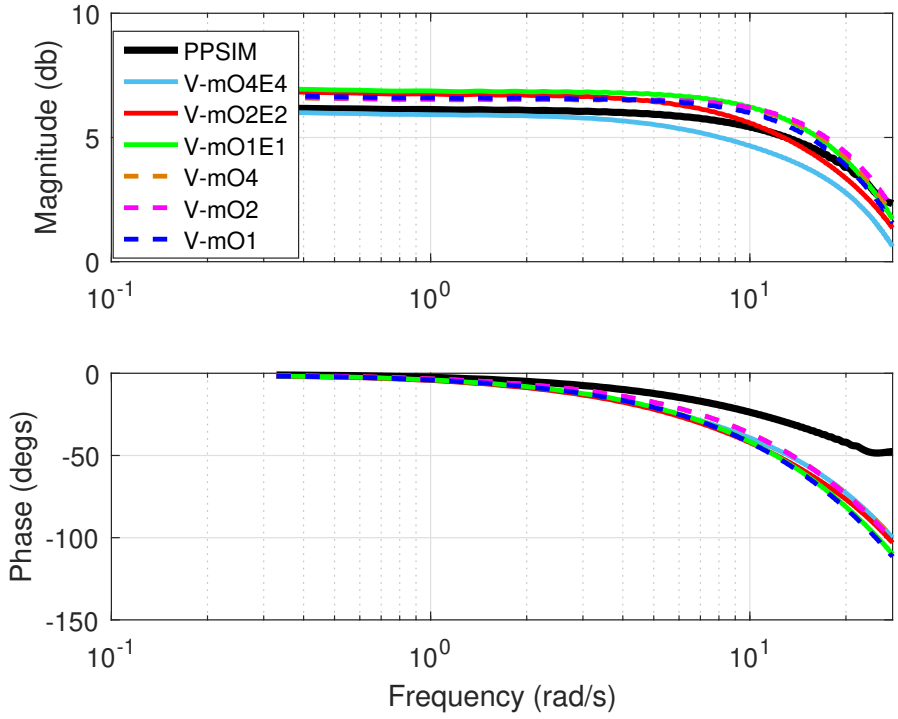

(b) Lower rotor fore-to-aft (longitudinal) inflow

Figure 4.6: Comparison of coaxial rotor fore-to-aft (α_2^{1c}) inflow response due to τ_2^{1c} excitation at $\mu = 0.07$

Figure 4.8 presents the predicted values of the lower rotor steady-state uniform and fore-to-aft (longitudinal) inflow components. At low speed, PPSIM and all VPSIM cases have a good match with each other in both uniform and fore-to-aft inflow predictions. In uniform inflow prediction, PPSIM slightly overestimates the predictions of VVPM. On the other hand, VPSIM cases (except for the V-mO4E4 at the advance ratio of 0.16) underestimate the uniform inflow component after the advance ratio of 0.07. Fore-to-aft inflow predictions of PPSIM and VPSIM show good correlations with VVPM at the lower rotor. Compared to the upper rotor, lower rotor fore-to-aft inflow component ($(\alpha_2^{1c})_L$) peak is moved from advance ratio of 0.07 to 0.04 due to interference effects. It is important to note that the skew angle (χ) is larger than 85 degrees (close to edgewise flow) when the advance ratio is greater than or equal to 0.16. It is previously shown that the adjoint theorem requires "downstream blending method" for correctly converging to an analytical solution [58]. Even though downstream blending is not considered in this study, VPSIM still has satisfactory steady-state uniform and fore-to-aft inflow predictions, as shown in Fig. 4.8.

Figures 4.9 and 4.10 present inflow distributions of the upper and lower rotors, respectively, at the advance ratio of 0.07. While PPSIM 3-state case shows linear inflow distributions at both rotors, VPSIM 3-state case (only odd velocity potential states) has nonlinear inflow distributions because VPSIM uses a different shaping function than the PPSIM. As numbers of PPSIM inflow states and VPSIM velocity potential states increase, their inflow distributions become closer to the inflow distributions obtained from the VVPM.

In VPSIM, inflow predictions of the upper rotor are somewhat insensitive to changes in the number of odd and even velocity potential states. These states mainly affect the interference inflow calculations below the rotor disk, especially the effects of even velocity potential states are noticeable at the high frequency range. For steady-state predictions, VPSIM with 15 odd and 15 even velocity potential states case has a slightly better correlation with VVPM at the lower rotor. Therefore, VPSIM with 15 odd and 15 even velocity potential states case is subsequently used in the comparison studies that involve the VVPM.

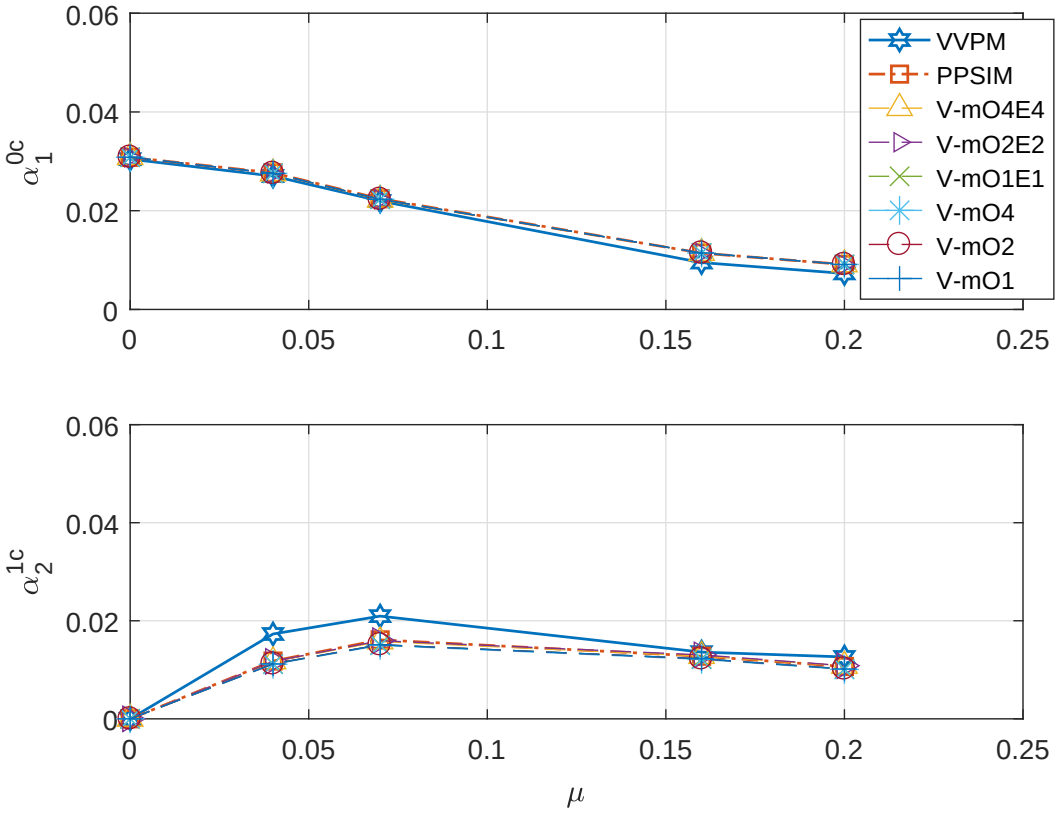

Figure 4.7: Comparison of upper rotor uniform and fore-to-aft inflow variations

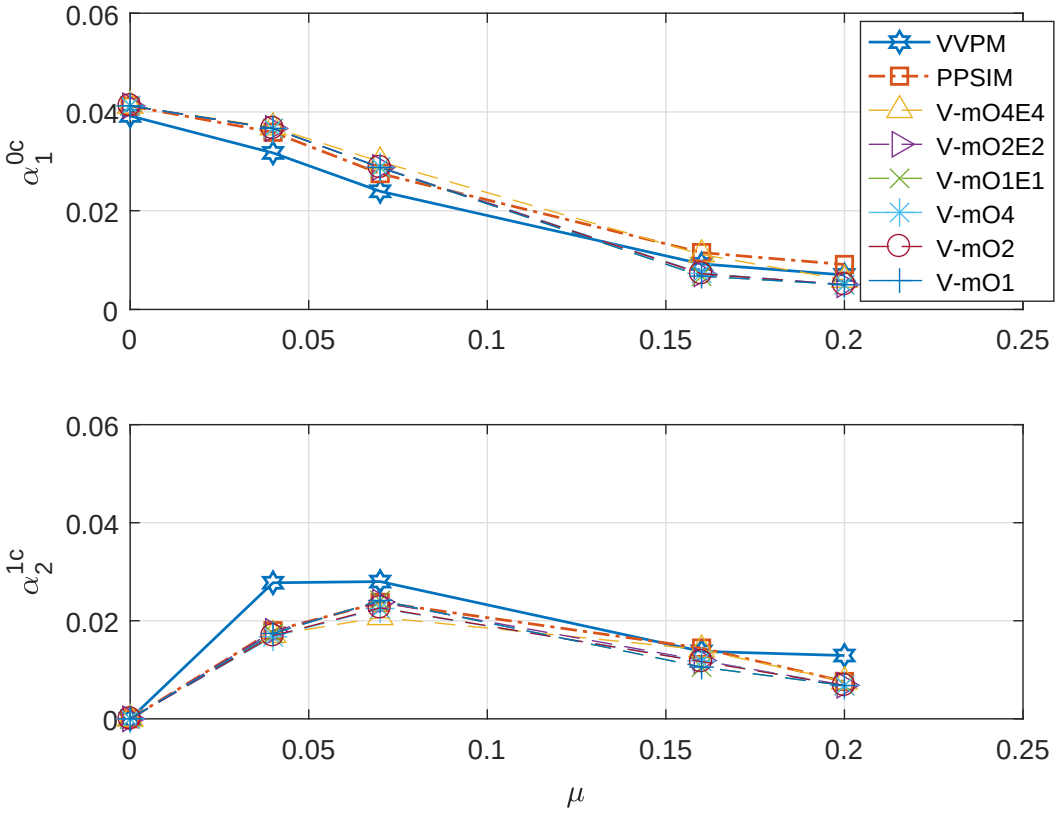

Figure 4.8: Comparison of lower rotor uniform and fore-to-aft inflow variations

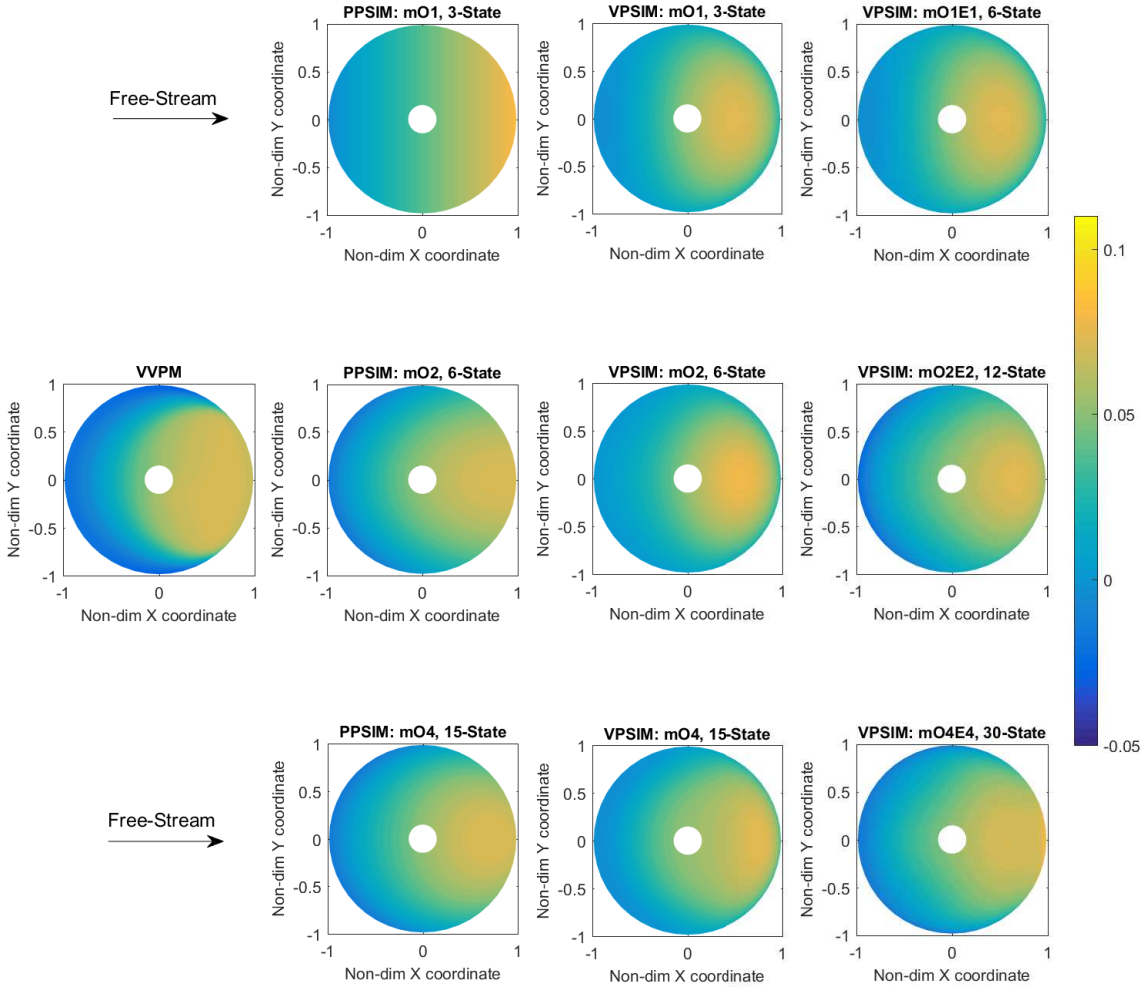

Figure 4.9: Comparison of upper rotor inflow distributions for various PPSIM inflow states and VPSIM velocity potential states at $\mu = 0.07$

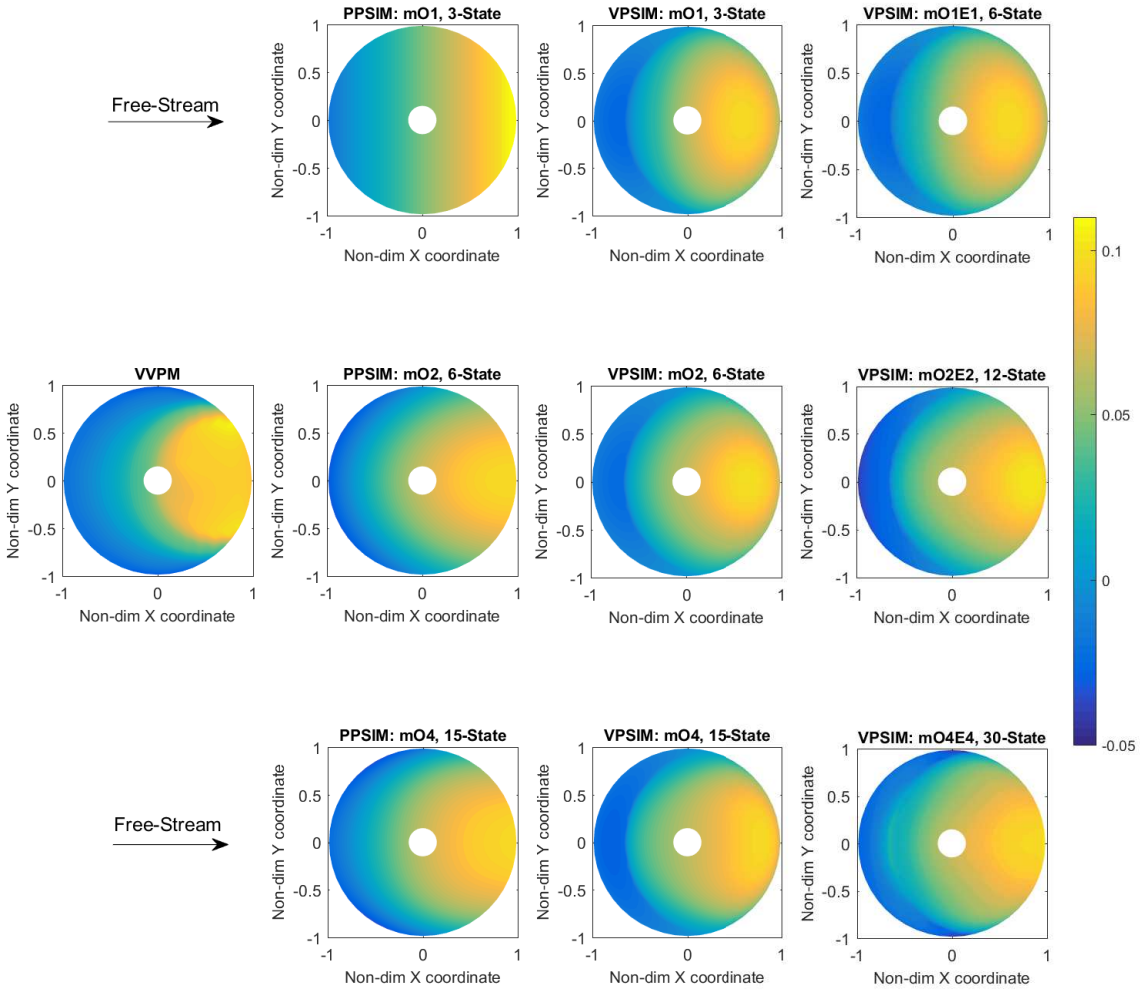

Figure 4.10: Comparison of lower rotor inflow distributions for various PPSIM inflow states and VPSIM velocity potential states at $\mu = 0.07$

The findings of this chapter indicate that VPSIM can capture coaxial rotor rotor-on-rotor inflow interference effects, although its governing equation consists of block diagonal matrices. The mass flow parameters and skew angles of the rotors in this equation are modified to account for the rotor-on-rotor interference effects. These modifications to governing equation alter the magnitudes of the velocity potential states and costates (if applicable) of each rotor. Using these altered velocity potential states and costates (if needed), both self-induced and interference inflow velocities on a rotor are computed.

Another steady-state coaxial rotor inflow comparison for VPSIM is available in chapter 8. Along with the VPSIM inflow predictions, predictions of the recently developed Combined Momentum Theory and Simple Vortex Theory (CMTSVT) [67] multi-rotor inflow model are compared against the VVPM and GT-Hybrid predictions (Ref. [42]). Description of this new multi-rotor inflow model, CMTSVT, is also available in chapter 8.

CHAPTER 5

EVALUATION OF THE FINITE STATE MULTI-ROTOR DYNAMIC INFLOW MODELS

In a coaxial rotor configuration, the lower rotor directly operates under the influence of the upper rotor wake, especially for the hovering flight. When there is a longitudinal or a lateral separation distance between the rotors, a challenging problem arises due to the partially overlapping interference area. In order to understand the effect of this overlapping area on rotor-on-rotor inflow interference in hover, the longitudinal separation distance of the Harrington coaxial rotor is gradually increased from 0.0R (coaxial) to 2.0R with the increment of 0.25R. All configurations have a vertical separation distance of 0.19R. The lateral separation distance is fixed to 0.0R since flow is symmetric in hover. Because of this symmetry, configurations with a lateral separation distance or a longitudinal separation distance have similar inflow distributions. For the longitudinal separation distance study, only Velocity Potential Superposition Inflow Model (VPSIM) is compared against the Viscous Vortex Particle Method (VVPM) since VPSIM and Pressure Potential Superposition Inflow Model (PPSIM) have good agreement in hover for steady-state inflow predictions. Another study for the varying longitudinal separation distance is given in chapter 8.4.1, which provides additional validation case for the VPSIM using the recently developed Combined Momentum Theory and Simple Vortex Theory (CMTSVT) multi-rotor inflow model [67].

Next, a tandem rotor configuration is evaluated in detail using Velocity Potential Superposition Inflow Model (VPSIM), Pressure Potential Superposition Inflow Model (PPSIM), and Viscous Vortex Particle Method (VVPM). In this case, the longitudinal separation distance is fixed to 1.5R. The results of this configuration are provided in terms of extracted steady-state inflow components and contour plots for the advance ratios that are varied from

0.0 to 0.2. In all simulations (including the varying longitudinal separation distance study), both rotors have a thrust coefficient (C_T) of 0.0035, whereas roll moment (C_L) and pitch moment (C_M) coefficients are fixed to zero. Throughout sections 5.2 and 5.3, PPSIM uses 15 odd inflow states, while VPSIM uses 15 odd and 15 even velocity potential states to have downwash distributions comparable to those obtained from the VVPM. After achieving a steady-state condition, 10%, i.e., 0.00035, a step change to each loading component is applied to analyze perturbed inflow variations. Finally, frequency responses of the PPSIM and VPSIM are compared against those acquired by using the VVPM.

In this section, Rotor 1 in Fig. 3.6 refers to the upper/front rotor for tandem rotor configurations. Similarly, Rotor 2 in Fig. 3.6 refers to the lower/back rotor for tandem rotor configurations. Subscripts $(\ )_U$ and $(\ )_L$ represent the upper/front rotor and the lower/back rotor, respectively. Furthermore, throughout the dissertation, subscripts $(\ )_U$ and $(\ )_L$ are used interchangeably with subscripts $(\ )_1$ and $(\ )_2$, respectively.

5.1 Effect of the Longitudinal Separation Distance on the Rotor-on-Rotor Inflow Interference in Hover

Rotor-on-rotor interference is greatly affected by the relative separation distances between the rotors. Inflow interference region determines the overall inflow distributions of the rotors and the first harmonic inflow components. Capturing this phenomenon is crucial as it affects vehicles' stability and control characteristics [68, 69]. Multi-rotor configurations may have different separation distances between the rotors. Thus, finite state multi-rotor dynamic inflow models should capture the rotor-on-rotor inflow interference for generic multi-rotor configurations. In order to study the longitudinal separation distance effect on the rotor-on-rotor inflow interference in hover, the longitudinal separation distance of the Harrington coaxial rotor is varied from zero (coaxial) to 2.0R with the increment of 0.25R.

Figures 5.1 and 5.2 present extracted upper rotor and lower rotor steady-state inflow components, respectively, for various longitudinal separation distances in hover. To provide

further insight into this effect, contour plots of the VPSIM and VVPM are also provided in Figs. 5.3–5.6 for separation distances of 0.0R, 0.5R, 1.0R, and 1.5R.

VPSIM upper rotor extracted uniform inflow components ($(\lambda_0)_U$) are slightly larger than the VVPM $(\lambda_0)_U$ for every longitudinal separation distance case (Fig. 5.1). This slight overestimation is mostly related to the inflow distribution near the blade tip. VVPM inflow distribution has more upwash near the blade tip than the VVPM inflow distribution, as shown in Figs. 5.3–5.6. In finite state inflow models, inflow distribution near the blade root and tip regions requires many radial shaping functions to converge. Reference [13] provides a great discussion about this topic. VPSIM upper rotor extracted fore-to-aft (longitudinal) inflow components ($(\lambda_{1c})_U$) are similar to those obtained from the VVPM, as shown in Fig. 5.1. Especially, the agreement between the VPSIM $(\lambda_{1c})_U$ and VVPM $(\lambda_{1c})_U$ is good for separation distances of 0.0R, 1.0R, 1.5R, and 2.0R. Again, most of the small differences between the VPSIM and VVPM are related to the inflow distribution near the blade tip. VPSIM upper rotor extracted side-to-side (lateral) inflow components ($(\lambda_{1s})_U$) are zero for every longitudinal separation distance case, while VVPM predicts non-zero $(\lambda_{1s})_U$ for every case apart from the coaxial rotor configuration. It is important to recognize that both aerodynamic pitch and roll moments are set to zero in these simulations. The reason why finite state multi-rotor dynamic inflow models have zero $(\lambda_{1s})_U$ is related to the rigid cylindrical wake geometry assumption. In reality, the wake has a helical geometry that couples cosine and sine components of the inflow. Thus, VVPM has non-zero $(\lambda_{1s})_U$ when there is non-zero $(\lambda_{1c})_U$ due to the cosine and sine coupling.

Next, VPSIM and VVPM lower rotor extracted uniform inflow components ($(\lambda_0)_L$) are shown in Fig. 5.2. VPSIM $(\lambda_0)_L$ predictions have overall good agreement with the VVPM $(\lambda_0)_L$ predictions. The largest difference is seen for the coaxial rotor case, where the wake contraction effect is dominant. VPSIM lower rotor extracted fore-to-aft (longitudinal) inflow components ($(\lambda_{1c})_L$) have a good correlation with the VVPM $(\lambda_{1c})_L$ predictions except for the case where the longitudinal separation distance is 2.0R. In this case, VPSIM

has zero $(\lambda_{1c})_L$ because there is no area of interference. On the other hand, in VVPM, the wake geometry is altered by the presence of other rotor's wake. Therefore, even without an area of interference, VVPM can predict non-zero $(\lambda_{1c})_L$. The contour plots in Figs. 5.3–5.6 show that VPSIM is able to capture qualitatively correct rotor-on-rotor inflow interference for different multi-rotor configurations. VPSIM lower rotor extracted lateral inflow components are similar to the upper rotor lateral inflow components.

Although VPSIM has some limitations (see chapter 2.3), it can capture essential inflow interference effects in hover for different multi-rotor configurations in terms of both extracted inflow components and contour plots.

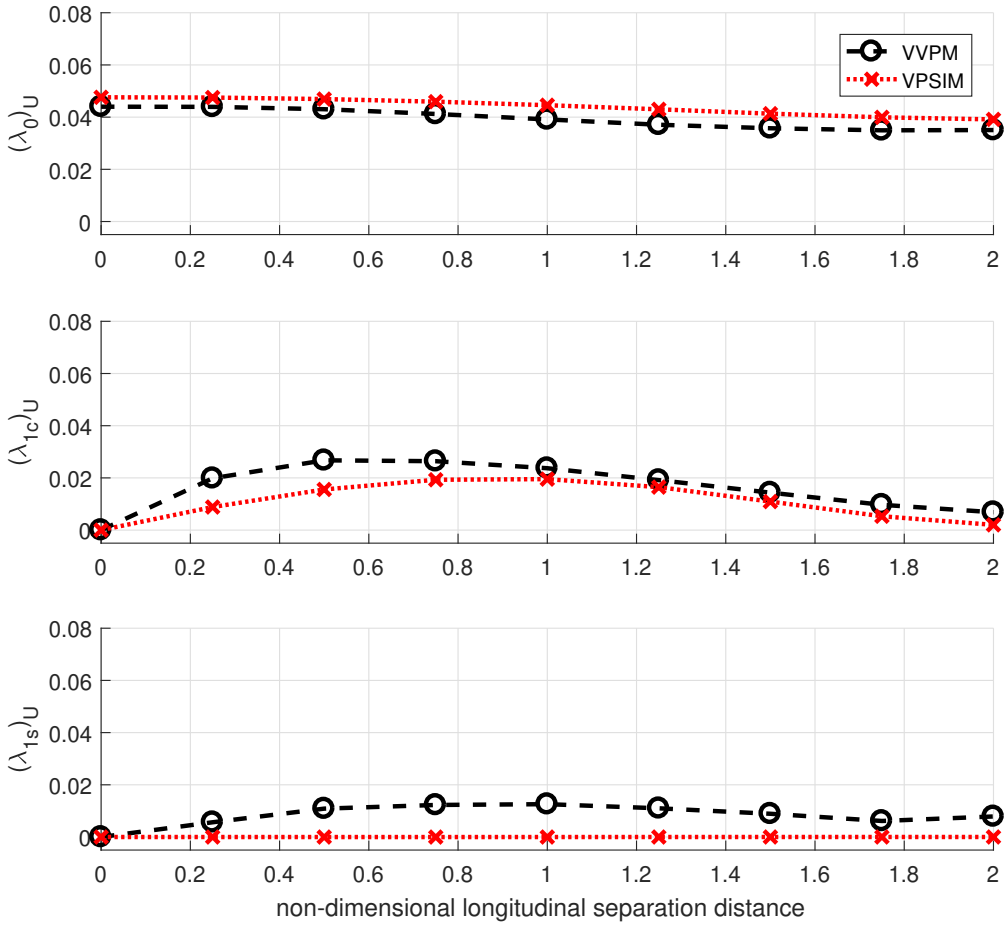

Figure 5.1: Upper (rotor 1) rotor extracted inflow components for various longitudinal separation distances in hover, vertical separation distance is fixed to 0.19R

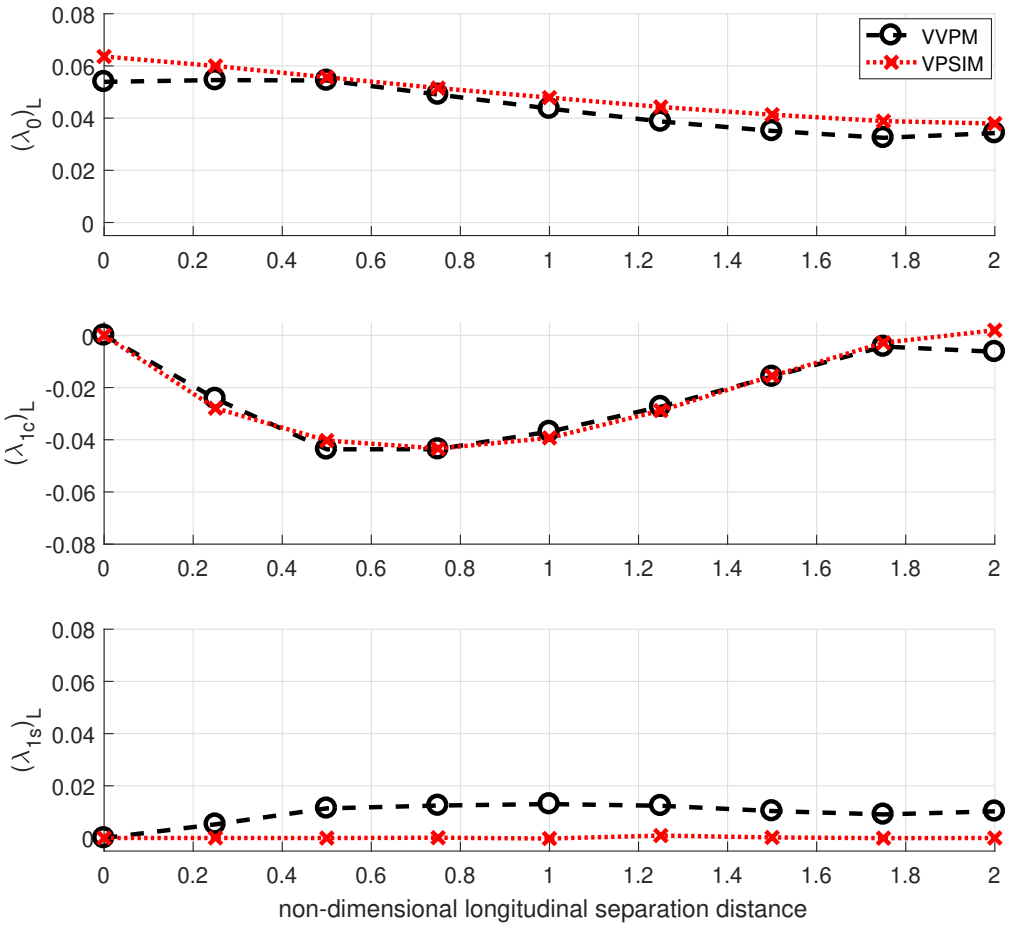

Figure 5.2: Lower (rotor 2) rotor extracted inflow components for various longitudinal separation distances in hover, vertical separation distance is fixed to 0.19R

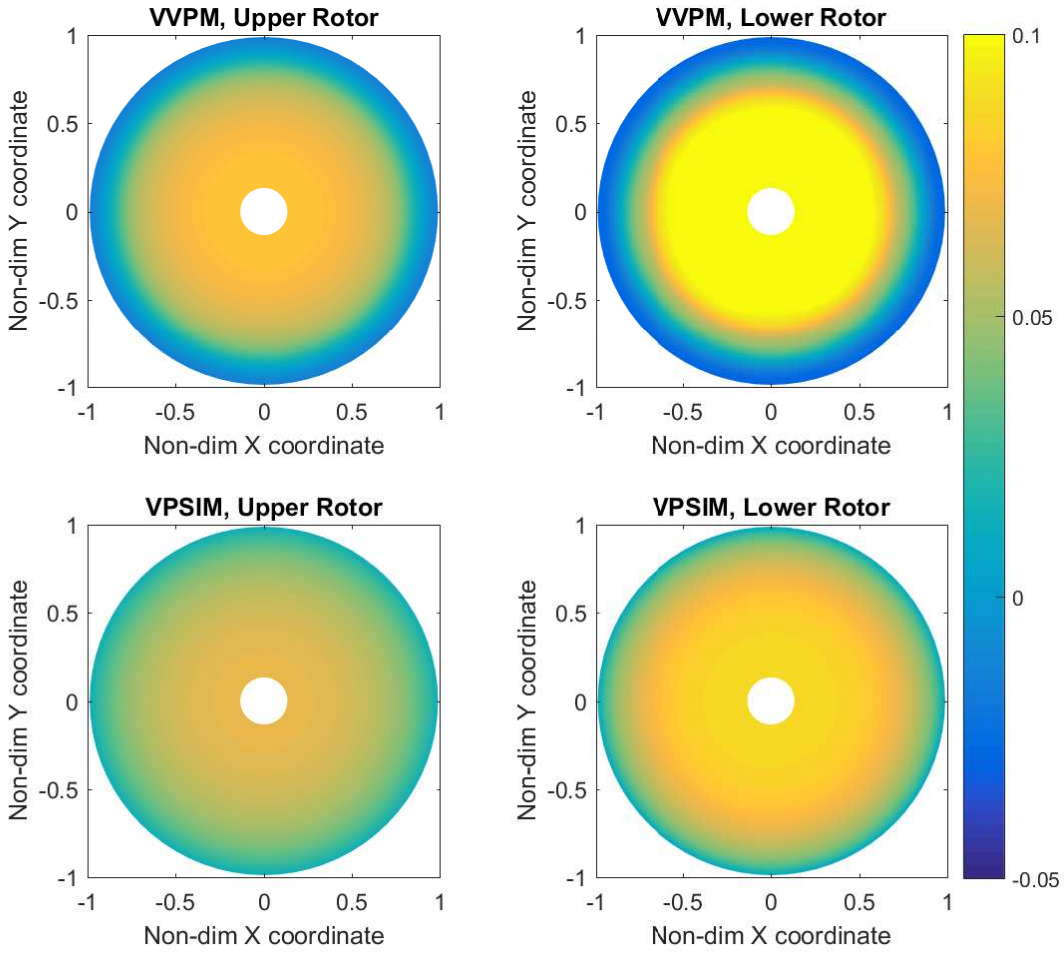

Figure 5.3: Comparison of inflow distributions for the longitudinal separation distance of 0.00R and vertical separation distance of 0.19R in hover

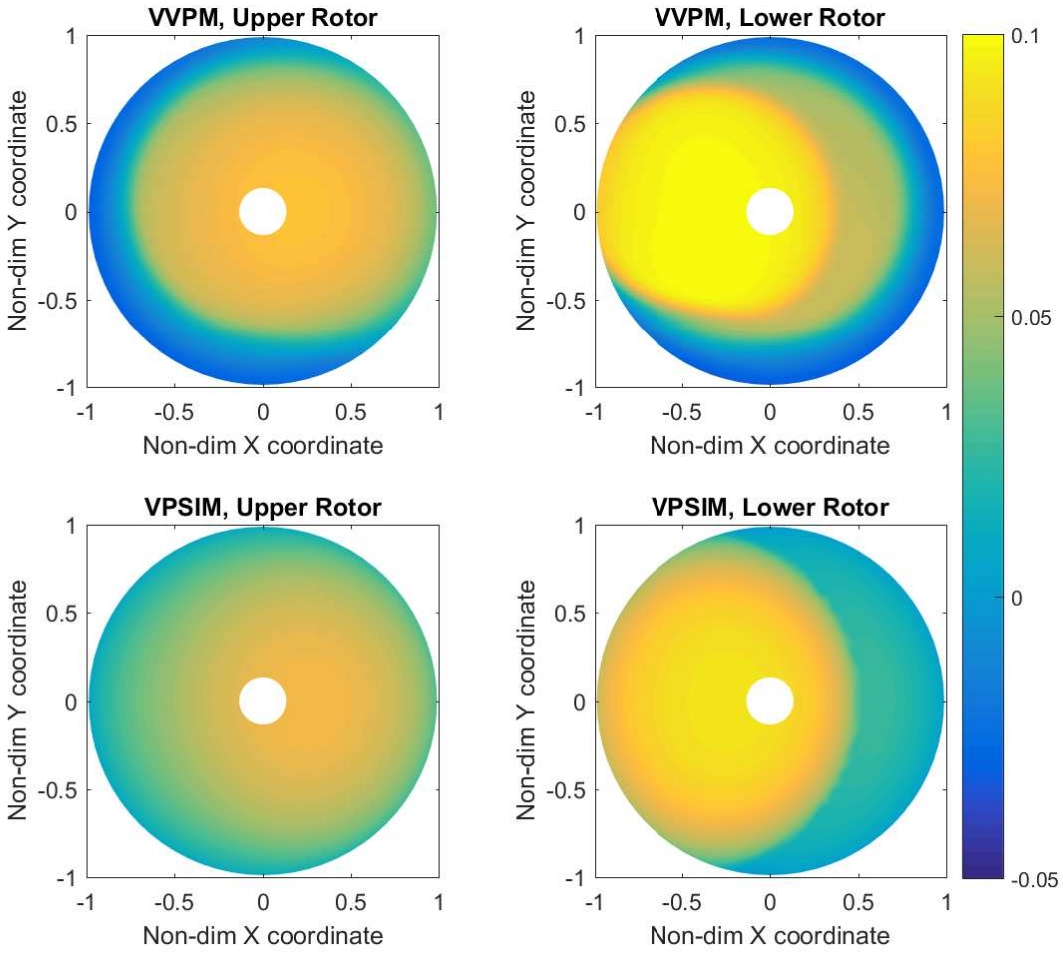

Figure 5.4: Comparison of inflow distributions for the longitudinal separation distance of 0.50R and vertical separation distance of 0.19R in hover

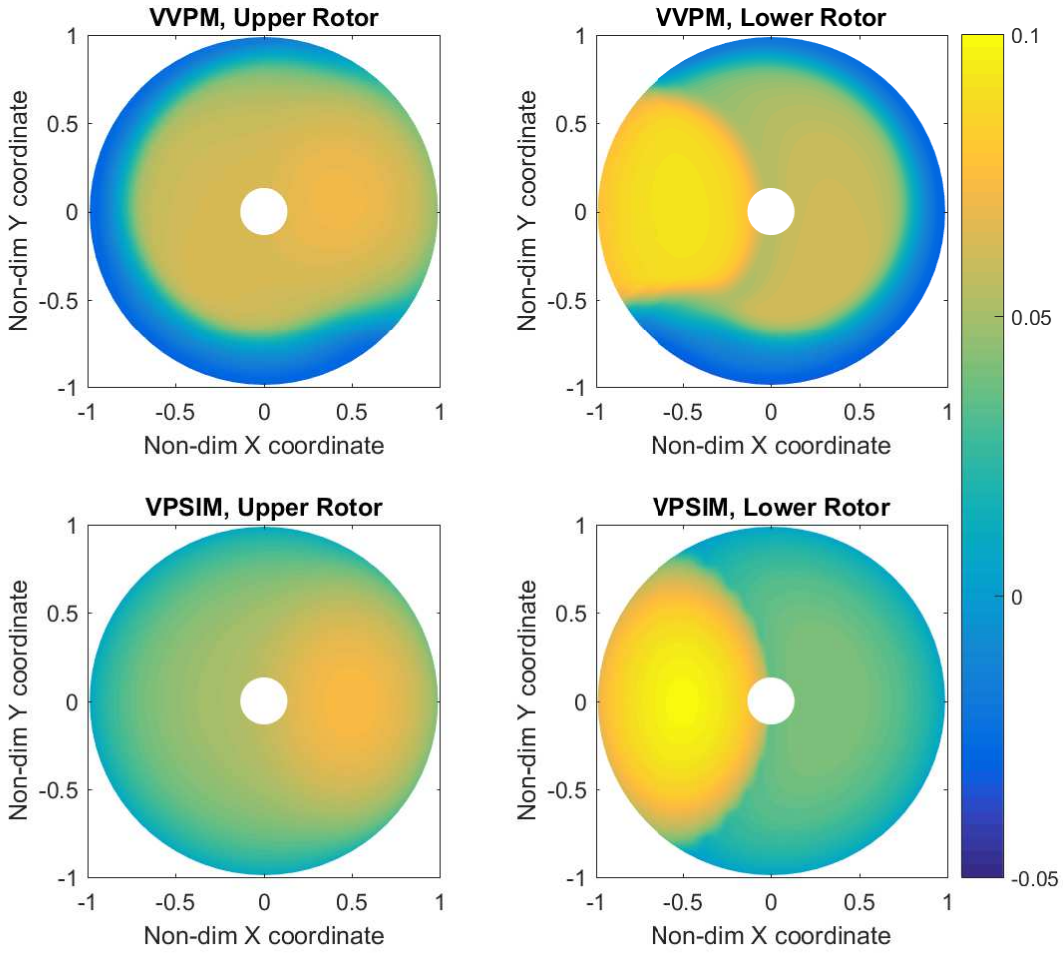

Figure 5.5: Comparison of inflow distributions for the longitudinal separation distance of 1.00R and vertical separation distance of 0.19R in hover

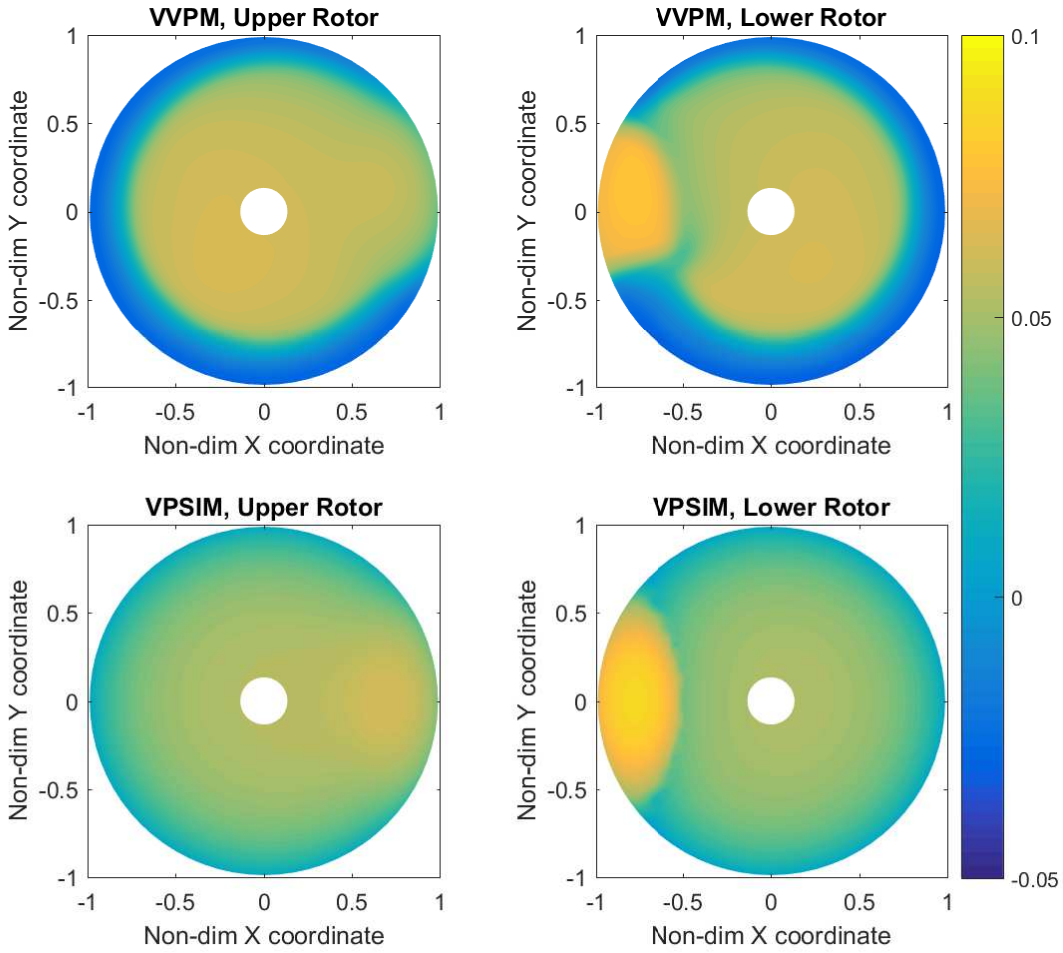

Figure 5.6: Comparison of inflow distributions for the longitudinal separation distance of 1.50R and vertical separation distance of 0.19R in hover

5.2 Evaluation of VPSIM and PPSIM Steady-State Inflow Predictions

Inflow predictions of the VPSIM and PPSIM are evaluated in detail against the VVPM in chapters 5.2 and 5.3 for a tandem rotor configuration. Figure 5.7 represents the selected tandem rotor configuration. The rotors are separated from each other vertically by 0.19R and horizontally by 1.5R.

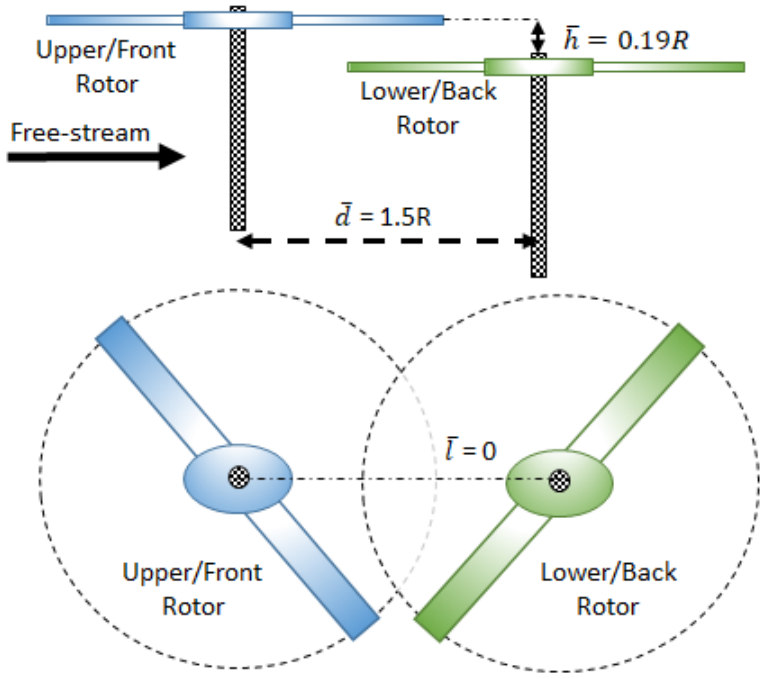

Figure 5.7: Tandem rotor configuration

Comparison of the upper/front rotor and lower/back rotor steady-state extracted inflow variations (the first harmonic inflow coefficients) are given in Figs. 5.8 and 5.9, respectively. Figure 5.8 shows that models have a good correlation at the upper/front rotor $(\lambda_0)_U$ except for the hover case. VPSIM and PPSIM slightly overestimate the hover value of $(\lambda_0)_U$. In hover, VVPM has a large upwash region near the tip region, as shown in Fig. 5.10. Because of this large upwash region, VVPM has a smaller $(\lambda_0)_U$ than those obtained from the VPSIM and PPSIM. As speed increases, $(\lambda_0)_U$ of each model rapidly decreases like a single rotor momentum theory inflow (Figs. 5.8 & 5.10). This decrement is expected since the upper/front rotor is not under the direct influence of the lower/back rotor wake.

The predictions of $(\lambda_{1c})_U$ indicate that VPSIM and PPSIM are able to follow the trend of VVPM $(\lambda_{1c})_U$ throughout all flight conditions. VPSIM and PPSIM have a good correlation with VVPM at higher speeds while having some differences at lower speeds. At lower flight speeds, magnitude of the wake is comparable to the flight speed; thus, wake structure becomes highly nonlinear. The wake travels a longer distance along the front region of the rotor due to wake distortion effects before it convects the downstream. These nonlinear wake distortion effects are not included in both VPSIM and PPSIM formulation since their wake geometries are based on a rigid cylindrical wake structure. Furthermore, the front and rear sides of the rotor have the same wake skew angle calculated from the momentum theory. Figure 5.10 qualitatively presents that VVPM has a broader upwash region (causing more fore-to-aft inflow gradient) than the VPSIM and PPSIM at the advance ratios of 0.04 and 0.07. As speed increases, differences between the VVPM and finite state multi-rotor dynamic inflow models diminish quickly.

The $(\lambda_{1s})_U$ results show that there is an almost constant difference between the VVPM and finite state multi-rotor dynamic inflow models. This difference is due to the swirl velocity that is only considered in the VVPM. In VPSIM and PPSIM, cosine and sine terms are not coupled; consequently, the effect of the swirl velocity is excluded in the modeling.

Figure 5.9 presents extracted inflow components of the lower/back rotor. The $(\lambda_0)_L$ predictions of the VPSIM and PPSIM have overall good agreement with the VVPM data. Unlike the upper/front rotor case, $(\lambda_0)_L$ first increases up to the advance ratio of 0.07, then decreases as speed increases further. Although the magnitude of the upper/front rotor inflow rapidly decreases with speed, the increase in the interference area at the lower/back rotor compensates for this reduction, as shown in Fig. 5.11. VPSIM and PPSIM accurately capture this increase in the interference area. At the highest advance ratio where skew angle is close to 90°, VPSIM underestimates the value of $(\lambda_0)_L$ compared to VVPM and PPSIM. It is because off-rotor induced velocity estimations of the VPSIM converge poorly towards the pure edgewise flow condition ($\chi \geq 85^\circ$), although this problem can be avoided by using

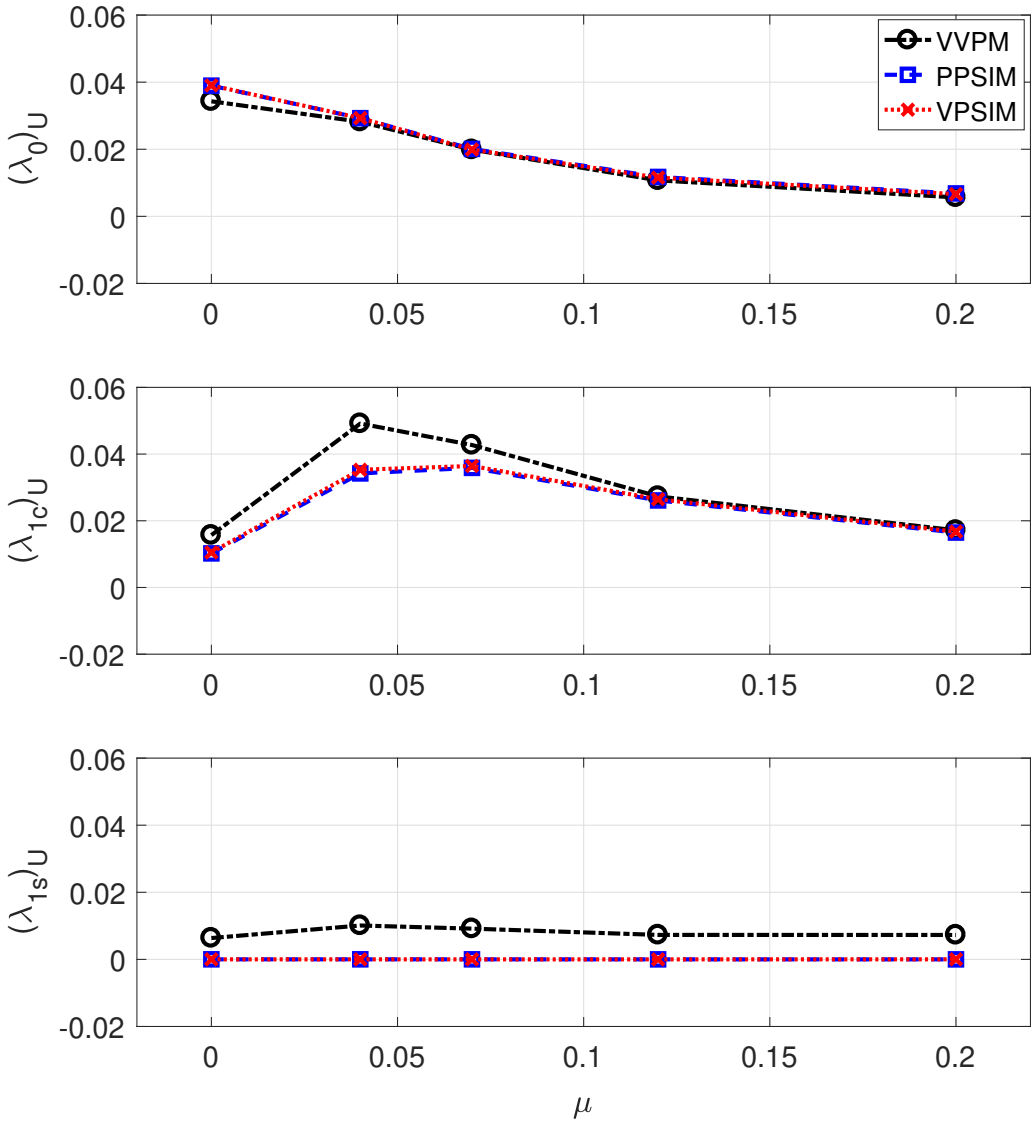

Figure 5.8: Upper/front rotor extracted inflow components

the so-called "downstream blending method" [58].

Results of $(\lambda_{1c})_L$ show an entirely different trend than the $(\lambda_{1c})_U$. Here, the lower/back rotor's front region partially overlaps with the upper/front rotor's rear at low speeds and operates under the wake of the upper/front rotor even in hover. The downwash received from the upper/front rotor creates a $(\lambda_{1c})_L$ with the opposite sign of $(\lambda_{1c})_U$. The change in the $(\lambda_{1c})_L$ is insignificant as speed increases from hover to advance ratio of 0.04 (Fig. 5.9).

Then, $(\lambda_{1c})_L$ starts to increase again and becomes comparable to $(\lambda_{1c})_U$ after the advance ratio of 0.12. Both VPSIM and PPSIM can capture the variation in the $(\lambda_{1c})_L$ and are similar to VVPM throughout the flight envelope. The only noticeable difference is spotted at the advance ratio of 0.07, where $(\lambda_{1c})_L$ is about to change its sign.

Similar to the upper/front rotor case, VPSIM and PPSIM do not show any variation in $(\lambda_{1s})_L$, as presented in Fig. 5.9.

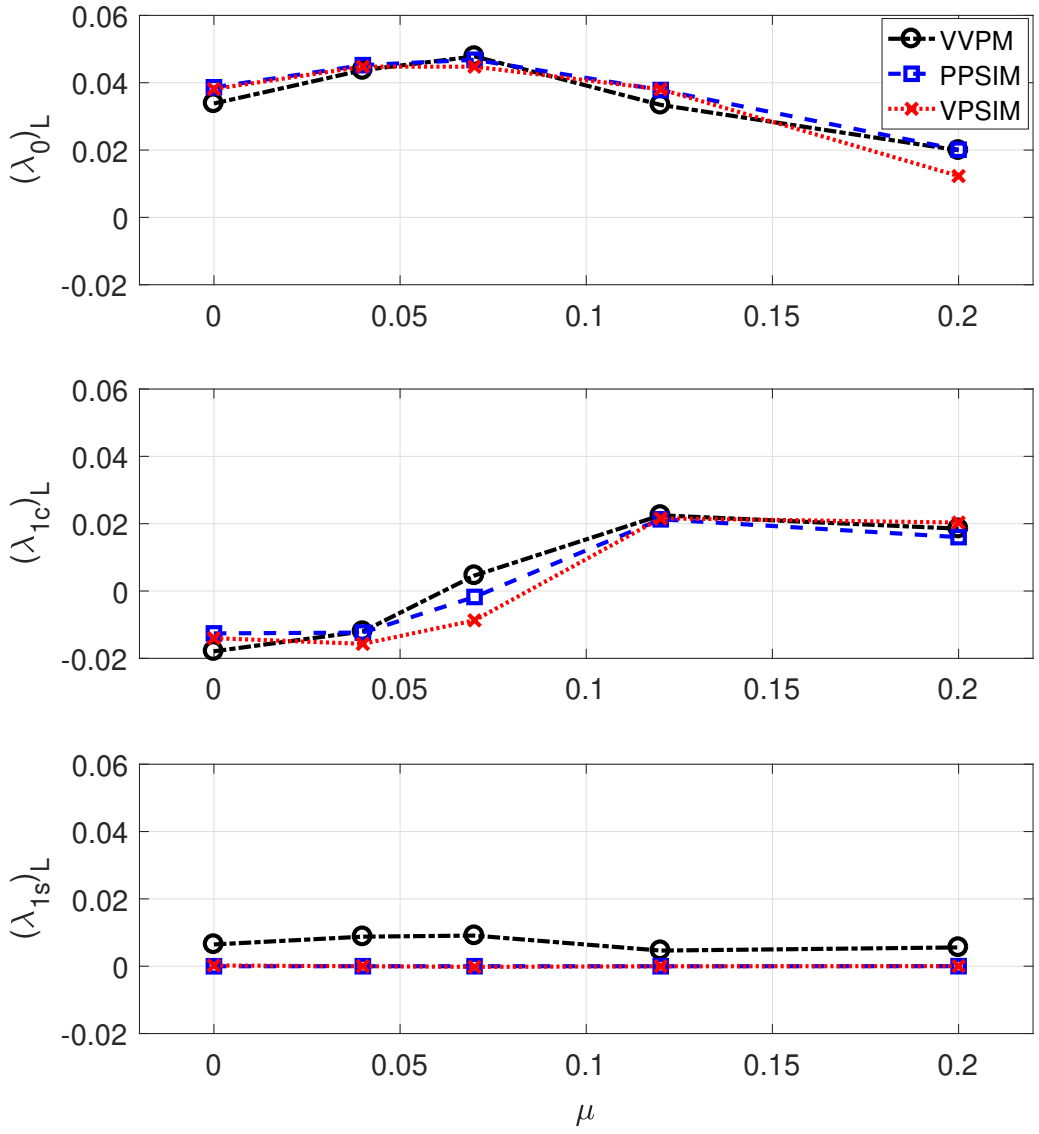

Figure 5.9: Lower/back rotor extracted inflow components

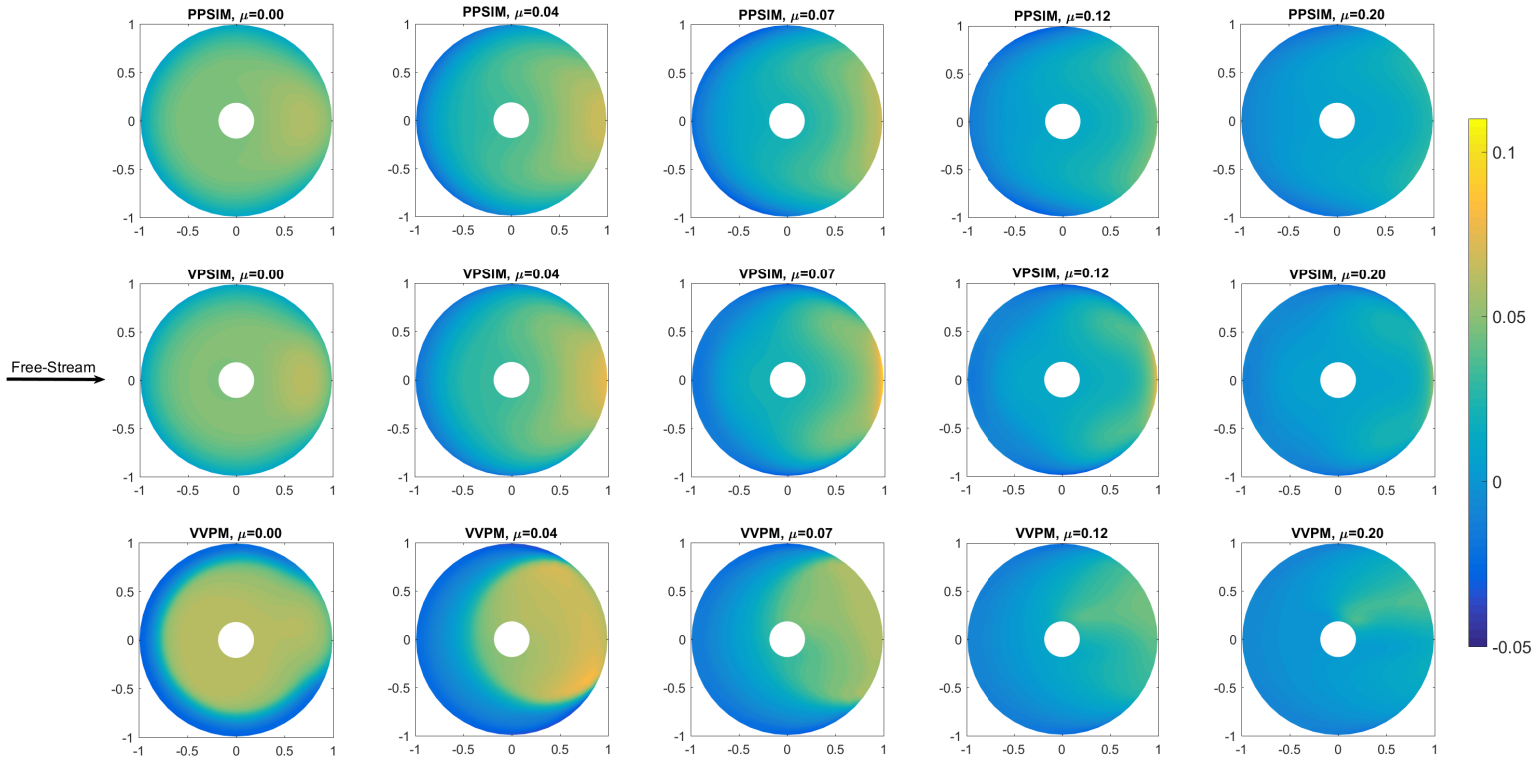

Figure 5.10: Upper/front rotor inflow distributions vs. advance ratio

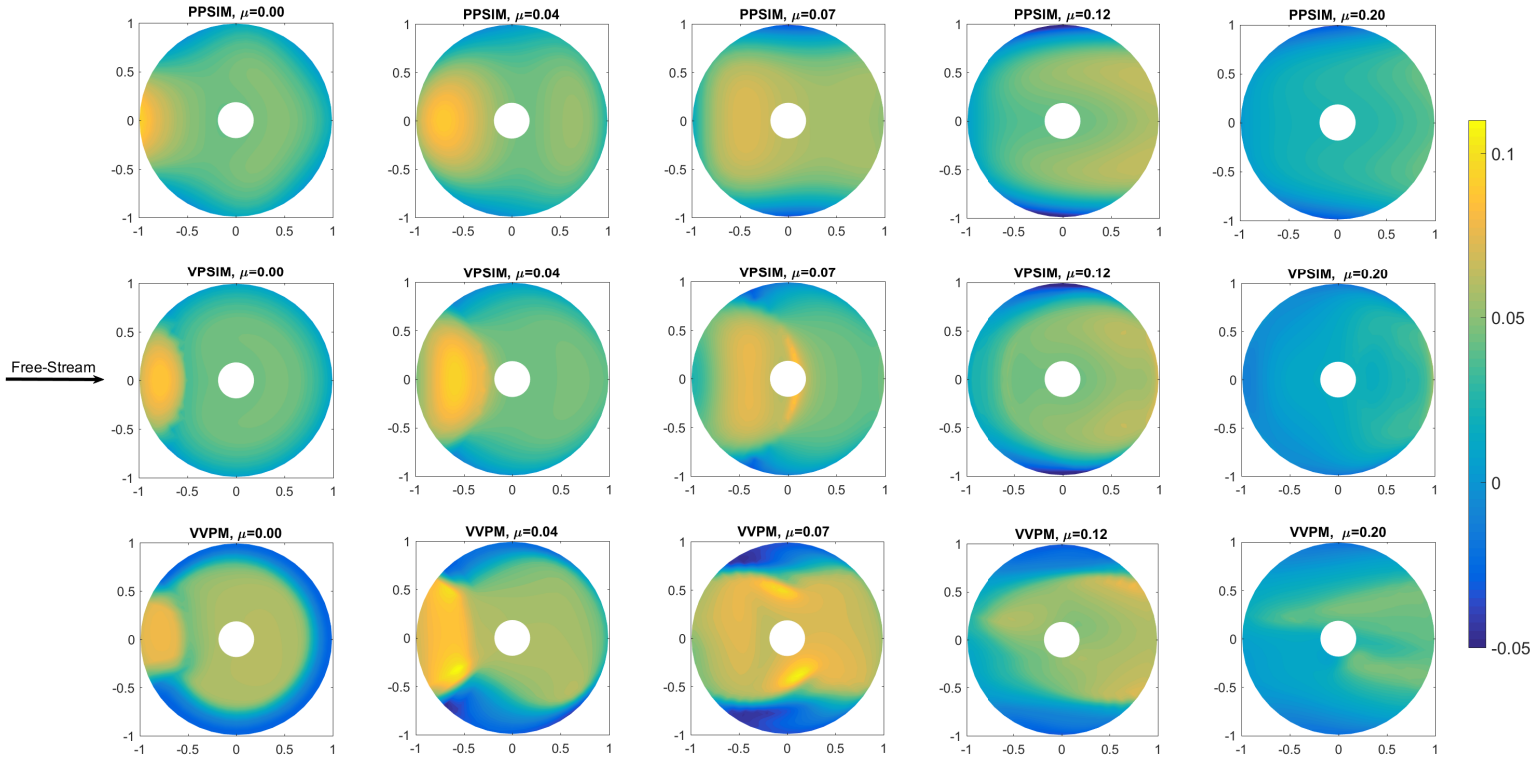

Figure 5.11: Lower/back rotor inflow distributions vs. advance ratio

Steady-state inflow perturbations in hover and at the advance ratio of 0.04 due to the applied step inputs are presented in Tables 5.1 and 5.2. For ease of comparison, changes in the uniform ($\Delta\lambda_0$), longitudinal ($\Delta\lambda_{1c}$), and lateral ($\Delta\lambda_{1s}$) inflow variations are scaled by 10^3 to increase readability, i.e., $\Delta\hat{\lambda}_0 = \Delta\lambda_0 \times 10^3$. Besides, if the magnitude of the inflow response is two orders of magnitude less than the inflow response with the highest order of magnitude, that inflow response is set to zero to avoid overshadowing the important inflow components.

Table 5.1 shows that VPSIM and PPSIM underestimate the uniform inflow perturbation ($\Delta\hat{\lambda}_0$) due to $(C_T)_U$ at the upper/front rotor. At the lower/back rotor, fore-to-aft inflow components are significantly affected instead of the uniform inflow as a result of the partially overlapping region. In VVPM, $(\Delta\hat{\lambda}_{1c})_U$ affects $\Delta\hat{\lambda}_{1s}$ of both rotors due to the effect of the swirl velocity, while such an effect is absent from the VPSIM and PPSIM results. When $(C_M)_U$ is perturbed, trends of $(\Delta\hat{\lambda}_{1c})_U$ and $(\Delta\hat{\lambda}_{1c})_L$ are captured by the VPSIM and PPSIM. After applying $(C_L)_U$ perturbation, it is observed that the change in the upper/front rotor $(\hat{\lambda}_{1s})_U$ is predicted well by both VPSIM and PPSIM. When lower rotor loadings are perturbed, similar predictions with smaller magnitude changes are observed compared to the upper/front rotor perturbation cases.

At the advance ratio of 0.04, $(C_T)_U$ perturbation affects uniform and fore-to-aft inflow variations of the upper/front and lower/back rotors, as shown in Table 5.2. VVPM has a larger $(\Delta\hat{\lambda}_{1c})_U$ indicating that uniform to fore-to-aft inflow coupling is weaker in the VPSIM and PPSIM. When $(C_M)_U$ is perturbed, VPSIM and PPSIM correctly follow the direction of the inflow response. The lower/back rotor perturbations show that changes in the upper/front rotor inflow variations are smaller than the lower/back rotor inflow variations.

Table 5.1: Comparison of the perturbed extracted inflow components for the tandem rotor configuration in hover

Perturbation[a]	Models	$(\Delta\hat{\lambda}_0)_U$	$(\Delta\hat{\lambda}_0)_L$	$(\Delta\hat{\lambda}_{1c})_U$	$(\Delta\hat{\lambda}_{1c})_L$	$(\Delta\hat{\lambda}_{1s})_U$	$(\Delta\hat{\lambda}_{1s})_L$
	VPSIM	1.86	0.13	0.00	-0.77	0.00	0.00
$(\Delta C_T)_U$	PPSIM	1.86	0.14	0.00	-0.80	0.00	0.00
	VVPM	1.97	0.00	0.25	-0.55	-0.33	0.60
	VPSIM	0.00	0.18	2.32	-0.98	0.00	0.00
$(\Delta C_M)_U$	PPSIM	0.00	0.19	2.34	-1.02	0.00	0.00
	VVPM	0.00	0.12	2.51	-1.05	-1.83	-0.67
	VPSIM	0.00	0.00	0.00	0.00	2.34	0.11
$(\Delta C_L)_U$	PPSIM	0.00	0.00	0.00	0.00	2.37	0.00
	VVPM	-0.16	0.20	1.12	-0.31	1.83	-0.51
	VPSIM	0.14	1.85	0.54	0.00	0.00	0.00
$(\Delta C_T)_L$	PPSIM	0.14	1.86	0.55	0.00	0.00	0.00
	VVPM	0.16	2.20	0.33	-0.16	1.22	0.00
	VPSIM	-0.12	0.00	-0.47	2.38	0.00	0.00
$(\Delta C_M)_L$	PPSIM	-0.12	0.00	-0.48	2.38	0.00	0.00
	VVPM	0.12	0.07	-0.02	1.77	-1.01	0.70
	VPSIM	0.00	-0.02	0.00	0.00	0.00	2.39
$(\Delta C_L)_L$	PPSIM	0.00	0.00	0.00	0.00	0.00	2.42
	VVPM	0.05	-0.27	-0.28	-1.49	0.00	1.80

[a]Bracket subscripts *U* and *L* correspond to upper (rotor 1) and lower (rotor 2) rotors, respectively

Table 5.2: Comparison of the perturbed extracted inflow components for the tandem rotor configuration at advance ratio of 0.04

Perturbation[a]	Models	$(\Delta\hat{\lambda}_0)_U$	$(\Delta\hat{\lambda}_0)_L$	$(\Delta\hat{\lambda}_{1c})_U$	$(\Delta\hat{\lambda}_{1c})_L$	$(\Delta\hat{\lambda}_{1s})_U$	$(\Delta\hat{\lambda}_{1s})_L$
	VPSIM	2.12	0.25	0.65	-1.50	0.00	0.00
$(\Delta C_T)_U$	PPSIM	2.12	0.18	0.66	-1.57	0.00	0.00
	VVPM	2.04	0.43	2.14	-1.30	0.51	0.00
	VPSIM	-0.49	0.52	2.23	-1.78	0.00	0.00
$(\Delta C_M)_U$	PPSIM	-0.27	0.90	2.80	-2.33	0.00	0.00
	VVPM	-0.13	0.38	1.70	-1.06	-1.00	-0.28
	VPSIM	-0.01	-0.03	0.01	0.12	3.41	1.15
$(\Delta C_L)_U$	PPSIM	0.00	-0.04	0.02	0.11	3.43	1.45
	VVPM	-0.56	-0.01	-0.39	0.24	3.16	1.76
	VPSIM	0.00	1.84	0.33	0.79	0.00	0.00
$(\Delta C_T)_L$	PPSIM	0.00	1.82	0.32	0.78	0.00	0.00
	VVPM	-0.17	1.62	0.26	1.60	0.93	1.42
	VPSIM	-0.06	-0.27	-0.26	1.78	0.00	0.00
$(\Delta C_M)_L$	PPSIM	-0.07	-0.15	-0.25	1.90	0.00	0.00
	VVPM	0.04	-0.06	-0.11	1.38	-0.22	0.41
	VPSIM	0.00	-0.02	0.00	0.00	0.00	2.30
$(\Delta C_L)_L$	PPSIM	0.00	0.00	0.00	0.00	0.00	2.25
	VVPM	0.15	-0.13	0.13	-0.97	0.00	1.88

[a]Bracket subscripts *U* and *L* correspond to upper (rotor 1) and lower (rotor 2) rotors, respectively

5.3 Evaluation of VPSIM and PPSIM Frequency Responses

Velocity Potential Superposition Inflow Model (VPSIM) and Pressure Potential Superposition Inflow Model (PPSIM) are evaluated against Viscous Vortex Particle Method (VVPM) in the frequency domain for the tandem rotor configuration, which has longitudinal, vertical, and lateral separation distances of 1.5R, 0.19R, and 0.0R, respectively. The methodology for obtaining the frequency response results is provided in chapter 3. It is important to recognize that frequency domain error metrics such as coherence weighed cost function and Maximum Unnoticeable Added Dynamics (MUAD) envelopes are not defined for the inflow dynamics. However, these metrics are still valuable in terms of understanding the overall inflow dynamics and assessing the models. Thus, in this dissertation, they are used as a guideline. For example, MUAD envelopes in Fig. 3.5 show that pilots are highly sensitive to changes in the dynamics between 1.0 and 5.0 rad/s. In addition, Ref. [70] indicated that speed derivatives in flight dynamics analyses are related to the low frequency excitation ($0.1 \sim 1.0$ rad/s). Reference [30] also analyzed the VVPM frequency responses for a single rotor and a coaxial rotor in detail. It showed that the coherence of the VVPM is usually above 0.95 for frequencies between 0.35 and 5 rad/s. Therefore, the coherence weighted cost function (Eq. (3.5)) is computed for frequencies between 0.35 and 5.0 rad/s.

The changes in the steady-state inflow variations in Tables 5.1 and 5.2 showed that the upper/front rotor loading changes have more impact on the overall behavior of the multi-rotor inflow variations. Especially in forward flight, the lower/back rotor loading changes have little effect on the upper/front rotor inflow since wake skewed backward. This backward skew is the reason why upper/front rotor inflow components are not usually shown when a loading change is introduced to the lower/back rotor. Furthermore, cases with low coherence and cases with relatively low magnitude responses compared to the primary input-output cases are not shown.

Frequency response differences between the VPSIM, PPSIM, and VVPM in hover are

provided in terms of the coherence weighted cost function in Table 5.3 for each loading excitation. In addition to the total cost function, the magnitude and phase cost functions are also provided for further insight. The cost functions are generally below 100 (except for the cases 6, 8 for both models, and case 2 for PPSIM in Table 5.3), which indicate good correlations between finite state multi-rotor dynamic inflow models and VVPM. The cost functions of both PPSIM and VPSIM are close to each other and have the same order of magnitude.

Table 5.3: Frequency response differences between the VPSIM, PPSIM, and VVPM for the tandem rotor configuration in hover

				Cost function[a] (0.35 $\sim$ 5 rad/s)		
Case No.	Input[b]	Output	Model	Magnitude	Phase	Total
1	$(\Delta C_T)_U$	$(\Delta\lambda_0)_U$	PPSIM	5.0	1.7	6.7
			VPSIM	22.4	2.7	25.1
2		$(\Delta\lambda_{1c})_L$	PPSIM	103.8	18.3	122.1
			VPSIM	41.8	41.8	83.6
3	$(\Delta C_M)_U$	$(\Delta\lambda_{1c})_U$	PPSIM	9.0	3.7	12.7
			VPSIM	16.5	1.3	17.8
4		$(\Delta\lambda_{1c})_L$	PPSIM	76.7	9.7	86.4
			VPSIM	47.3	30.2	77.5
5	$(\Delta C_L)_U$	$(\Delta\lambda_{1s})_U$	PPSIM	6.7	3.7	10.5
			VPSIM	16.3	2.8	19.1
6	$(\Delta C_T)_L$	$(\Delta\lambda_{1c})_U$	PPSIM	50.0	182.5	232.4
			VPSIM	58.9	191.7	250.6
7		$(\Delta\lambda_0)_L$	PPSIM	6.6	6.3	12.9
			VPSIM	23.8	3.0	26.8
8	$(\Delta C_M)_L$	$(\Delta\lambda_{1c})_U$	PPSIM	145.1	36.0	181.1
			VPSIM	110.3	23.1	133.4
9		$(\Delta\lambda_{1c})_L$	PPSIM	1.1	6.2	7.4
			VPSIM	1.4	2.2	3.5
10	$(\Delta C_L)_L$	$(\Delta\lambda_{1s})_L$	PPSIM	2.0	6.8	8.8
			VPSIM	7.0	2.8	9.8

[a]Computed using Eq. (3.5)
[b]Bracket subscripts *U* and *L* correspond to upper (rotor 1) and lower (rotor 2) rotors, respectively

Frequency responses of $(\Delta\lambda_0)_U$ and $(\Delta\lambda_{1c})_L$ in hover due to the upper/front rotor thrust excitation are shown in Fig. 5.12. Figure 5.13 shows Maximum Unnoticeable Added Dynamics (MUAD) envelopes (or error boundaries) for the same case for the frequency range of 0.35 and 5.0 rad/s. VPSIM and PPSIM have good agreement with each other for $(\Delta\lambda_0)_U$ prediction, while VVPM phase response starts to deviate after 6 rad/s. This phase drop is also observed in single rotor configurations [54, 60]; thus, this mismatch between the VVPM and analytical multi-rotor inflow models cannot be traced back to the interference effects. Figure 5.13(a) exhibits that $(\Delta\lambda_0)_U$ predictions of the VPSIM and PPSIM are inside the MUAD boundaries, although VPSIM prediction continues along the lower magnitude boundary for frequencies between 3 and 5 rad/s. In $(\Delta\lambda_{1c})_L$ response, the coherence is usually high between the frequencies of 2.0 and 8.0 rad/s where VVPM data is reliable. VPSIM and PPSIM show good matches with the VVPM, while VPSIM has a slightly better match towards the high frequency range. Figure 5.13(b) shows that phase predictions of the VPSIM and PPSIM are usually inside the MUAD envelopes, whereas magnitude predictions are slightly above the upper magnitude limit of the MUAD envelope.

Next, frequency response differences between the VPSIM, PPSIM, and VVPM at the advance ratio of 0.04 are provided in terms of the coherence weighted cost function in Table 5.4 for each loading perturbation. Compared to the hover case, computed cost functions are generally higher at low speeds because of the large wake distortion effects. Finite state single and multi-rotor inflow models assume a rigid cylindrical wake structure; thus, these distortion effects are not considered in their formulation. The wake distortion effects also alter the inflow interference area between the rotors by changing the wake structure. At this advance ratio, VPSIM and PPSIM average cost functions are equal to 213 and 235, respectively. Table 5.4 shows that VPSIM, PPSIM, and VVPM phase differences are usually small compared to the magnitude differences. It is important to recognize that the cost function and MUAD metrics are defined for flight dynamics analyses. In this dissertation, these metrics are used as a guideline to gain some insight into the fidelity of the models.

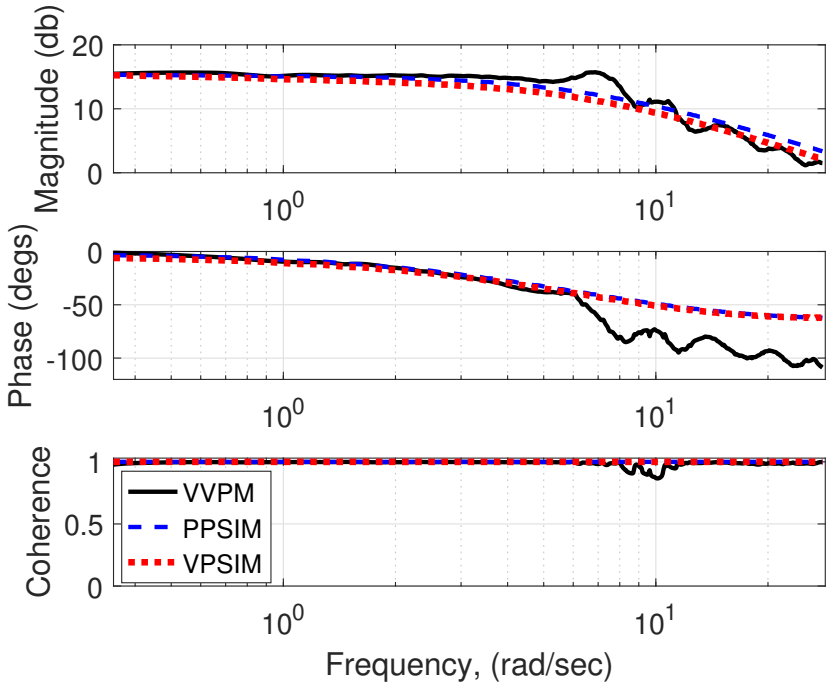

(a) $(\Delta\lambda_0)_U$ due to $(\Delta C_T)_U$, case 1 in Table 5.3

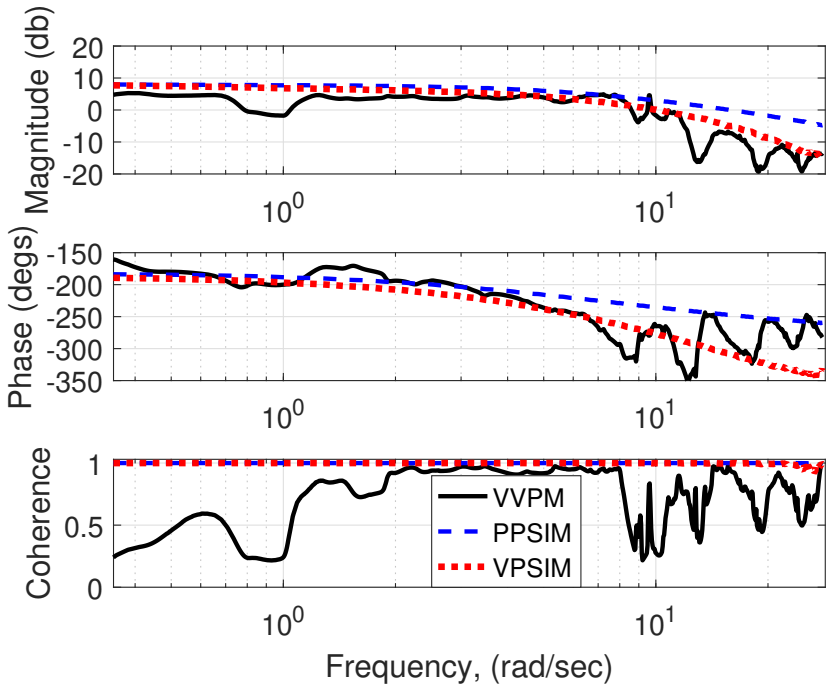

(b) $(\Delta\lambda_{1c})_L$ due to $(\Delta C_T)_U$, case 2 in Table 5.3

Figure 5.12: Comparison of the tandem rotor configuration frequency responses due to the upper rotor thrust coefficient excitation in hover

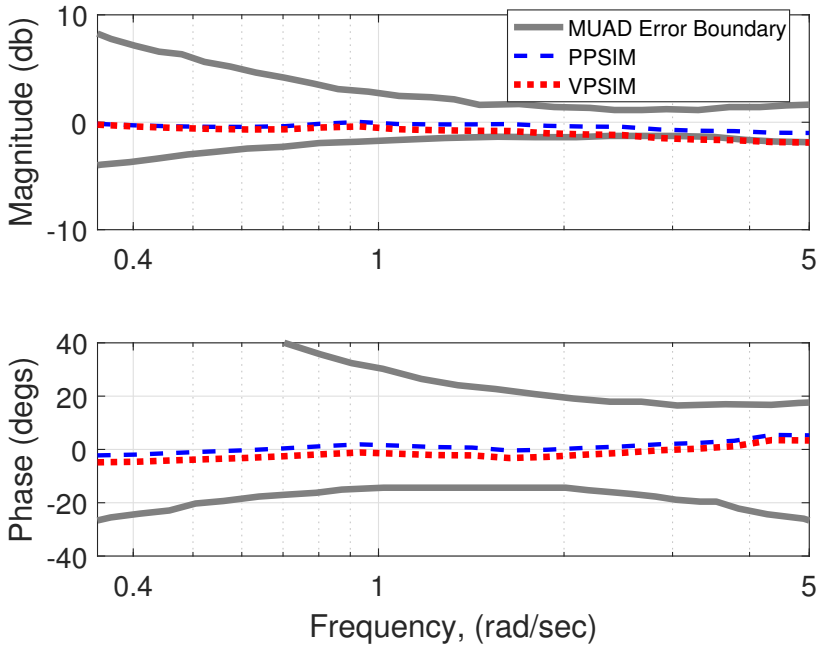

(a) $(\Delta\lambda_0)_U$ due to $(\Delta C_T)_U$, case 1 in Table 5.3

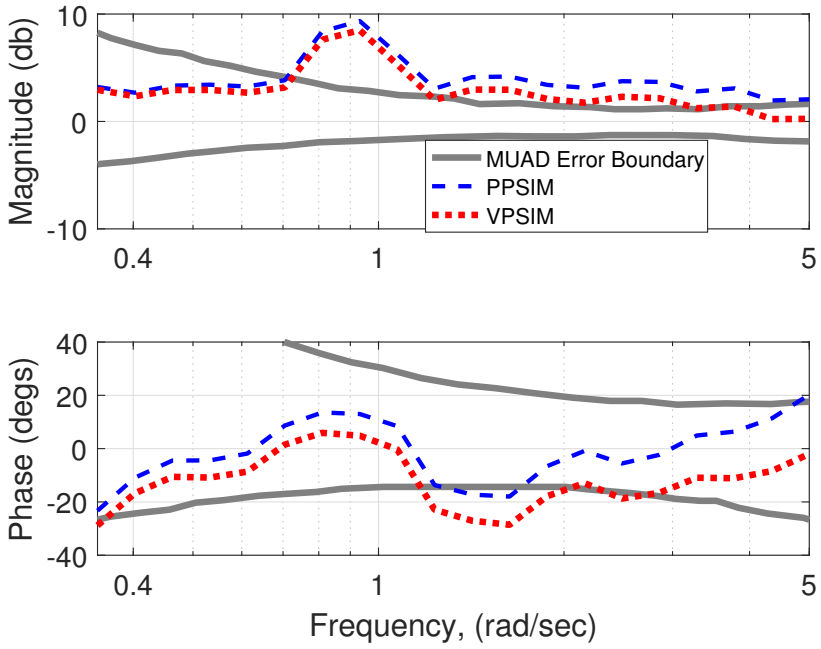

(b) $(\Delta\lambda_{1c})_L$ due to $(\Delta C_T)_U$, case 2 in Table 5.3

Figure 5.13: Comparison of the tandem rotor configuration frequency responses due to the upper rotor thrust coefficient excitation in hover

Table 5.4: Frequency response differences between the VPSIM, PPSIM, and VVPM for the tandem rotor configuration at advance ratio of 0.04

				Cost function[a] (0.35 $\sim$ 5 rad/s)		
Case No.	Input[b]	Output	Model	Magnitude	Phase	Total
1	$(\Delta C_T)_U$	$(\Delta\lambda_0)_U$	PPSIM	24.1	17.8	41.9
			VPSIM	54.9	23.4	78.3
2		$(\Delta\lambda_{1c})_L$	PPSIM	122.1	37.3	159.4
			VPSIM	338.6	46.7	385.3
3	$(\Delta C_M)_U$	$(\Delta\lambda_0)_U$	PPSIM	326.9	100.9	427.7
			VPSIM	217.1	83.5	300.6
4		$(\Delta\lambda_{1c})_U$	PPSIM	209.8	7.9	217.8
			VPSIM	34.7	7.7	42.5
5		$(\Delta\lambda_0)_L$	PPSIM	339.9	203.4	543.3
			VPSIM	70.4	272.0	342.3
6		$(\Delta\lambda_{1c})_L$	PPSIM	442.5	21.1	463.6
			VPSIM	90.4	53.0	143.4
7	$(\Delta C_L)_U$	$(\Delta\lambda_{1s})_U$	PPSIM	4.6	5.7	10.3
			VPSIM	11.5	3.5	15.0
8		$(\Delta\lambda_{1s})_L$	PPSIM	47.8	640.5	688.3
			VPSIM	36.4	110.1	146.5
9	$(\Delta C_T)_L$	$(\Delta\lambda_0)_L$	PPSIM	48.0	9.2	57.2
			VPSIM	47.7	13.1	60.7
10		$(\Delta\lambda_{1c})_L$	PPSIM	529.3	11.8	541.1
			VPSIM	896.1	4.0	900.2
11	$(\Delta C_M)_L$	$(\Delta\lambda_{1c})_L$	PPSIM	194.3	1.0	195.3
			VPSIM	125.8	1.4	127.2
12	$(\Delta C_L)_L$	$(\Delta\lambda_{1s})_L$	PPSIM	8.8	3.6	12.4
			VPSIM	12.9	2.5	15.5

[a]Computed using Eq. (3.5)
[b]Bracket subscripts *U* and *L* correspond to upper (rotor 1) and lower (rotor 2) rotors, respectively

At the advance ratio of 0.04, all models have similar variations in $(\Delta\lambda_0)_U$ predictions like the hover case, as shown in Fig. 5.14(a). The MUAD plot in Fig. 5.15(a) shows that VPSIM and PPSIM phase responses are inside the designated envelopes. Their magnitude responses slightly cross the lower MUAD envelope between the frequencies of 2 and

4 rad/s. At the lower/back rotor, VVPM exhibits significant phase and coherence drops in $(\Delta\lambda_{1c})_L$ prediction towards the high frequency range, as shown in Fig. 5.14(b). Figure 5.14(b) illustrates that VPSIM and PPSIM have good agreement with each other in the magnitude response even though their phase responses deviate after 7 rad/s as expected. PPSIM does not contain the time delay effect, whereas VPSIM inherently includes the time delay effect associated with the wake propagation. As a result, VPSIM inflow predictions often have more phase drop at higher frequencies than the PPSIM inflow predictions. In $(\Delta\lambda_{1c})_L$ magnitude prediction, VVPM slightly differs from the finite state multi-rotor dynamic inflow results after 1.0$\sim$2.0 rad/s. Figure 5.15(b) exhibits that magnitude predictions of finite state multi-rotor dynamic inflow models are outside of the MUAD envelopes after 1.0$\sim$2.0 rad/s. On the other hand, VPSIM and PPSIM $(\Delta\lambda_{1c})_L$ phase predictions are usually inside the MUAD envelopes.

The frequency response of $\Delta\lambda_{1c}$ due to the upper/front rotor pitch moment perturbation is presented in Fig. 5.16. In terms of magnitude, VPSIM and PPSIM (slightly worse) have larger $(\Delta\lambda_{1c})_U$ than the one predicted by the VVPM. MUAD plot in Fig. 5.17(a) illustrates that VPSIM is inside the MUAD envelopes for $(\Delta\lambda_{1c})_U$ magnitude and phase predictions, whereas PPSIM $(\Delta\lambda_{1c})_U$ magnitude prediction crosses the MUAD magnitude boundary after the frequency of 1 rad/s. Figure 5.16(b) shows $(\Delta\lambda_{1c})_L$ predictions at the lower/back rotor. The models have similar trends with some magnitude differences. As a result of the coherence drop near 10 rad/s, sudden jumps in VVPM magnitude and phase predictions are observed. In this case, VPSIM has better agreement with the VVPM for the entire frequency range. Figure 5.17(b) exhibits MUAD envelopes for the low frequency range (0.35$\sim$5.0). As seen, VPSIM has a better $(\Delta\lambda_{1c})_L$ magnitude prediction than the PPSIM and usually stays inside the MUAD envelopes. On the other hand, PPSIM phase prediction is slightly better than the VPSIM phase prediction for frequencies between 3.0 and 5 rad/s.

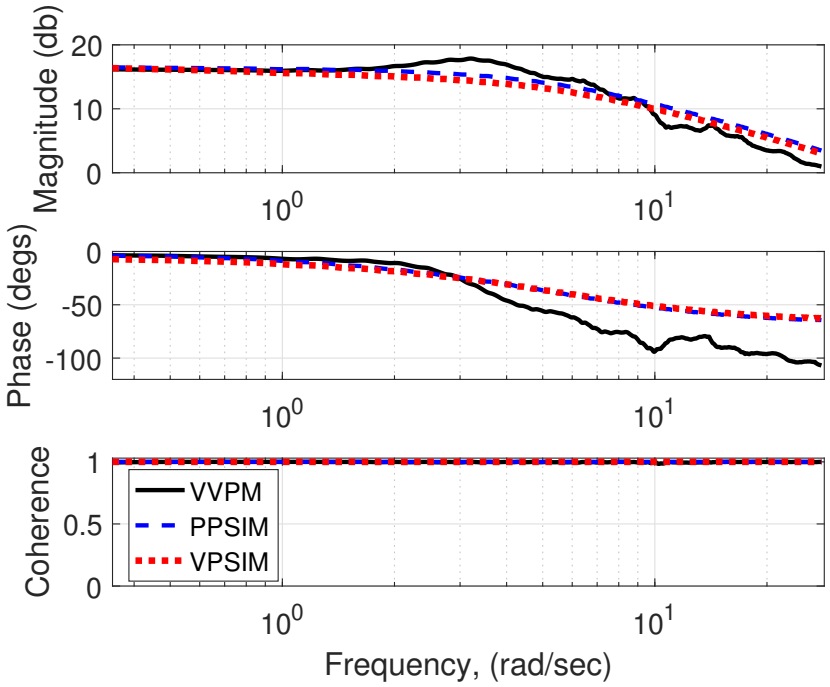

(a) $(\Delta\lambda_0)_U$ due to $(\Delta C_T)_U$, case 1 in Table 5.4

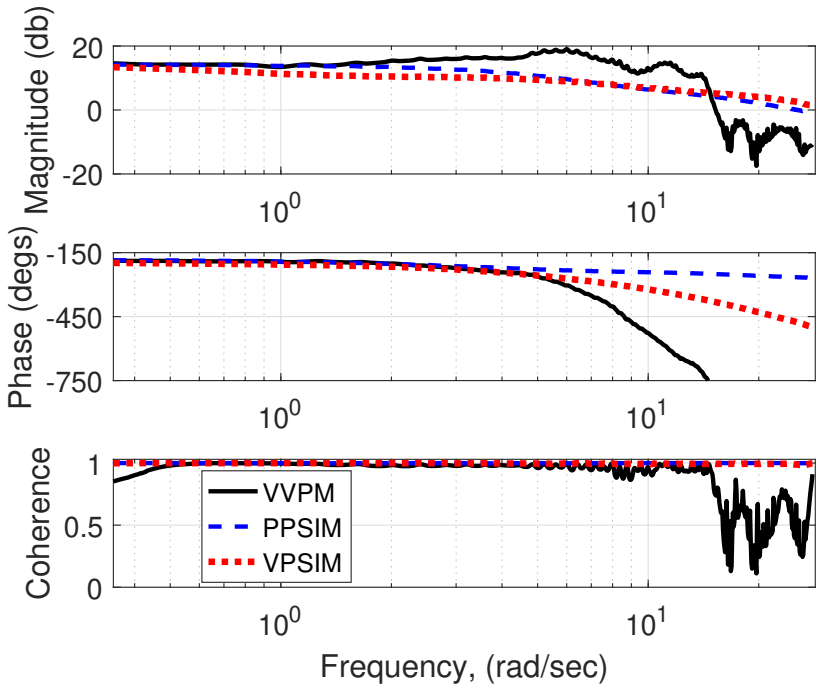

(b) $(\Delta\lambda_{1c})_L$ due to $(\Delta C_T)_U$, case 2 in Table 5.4

Figure 5.14: Comparison of the tandem rotor configuration frequency responses due to the upper rotor thrust coefficient excitation at $\mu = 0.04$

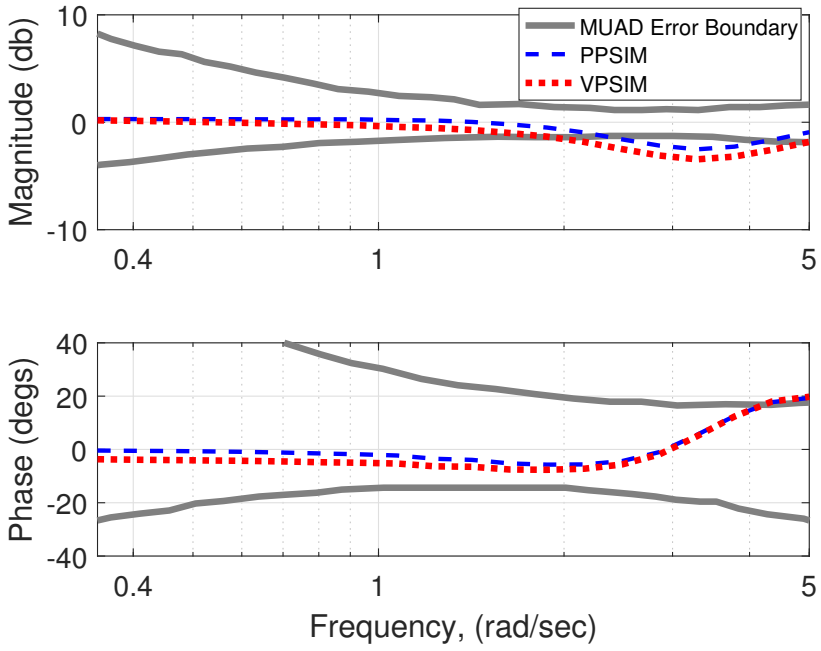

(a) $(\Delta\lambda_0)_U$ due to $(\Delta C_T)_U$, case 1 in Table 5.4

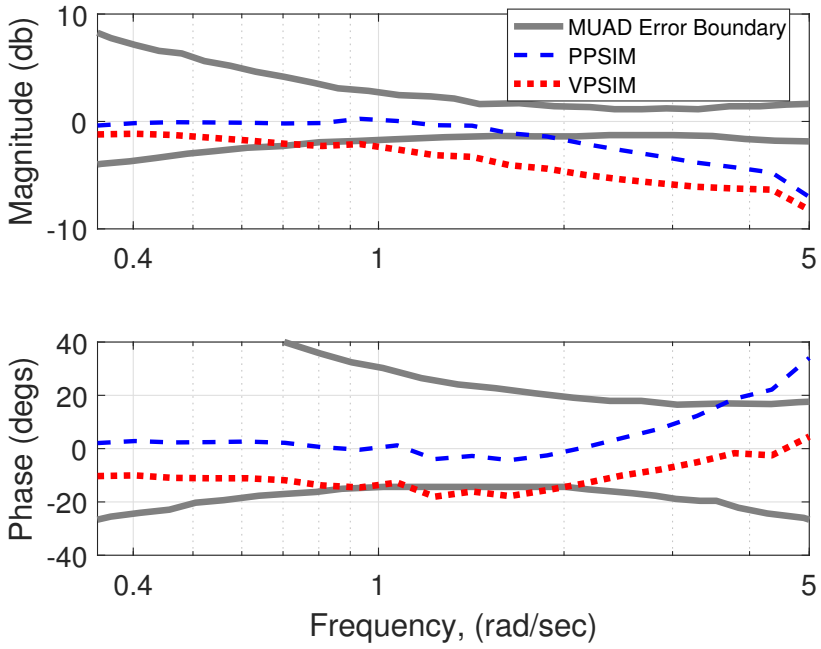

(b) $(\Delta\lambda_{1c})_L$ due to $(\Delta C_T)_U$, case 2 in Table 5.4

Figure 5.15: Comparison of tandem rotor configuration frequency responses due to upper rotor thrust coefficient excitation at $\mu = 0.04$

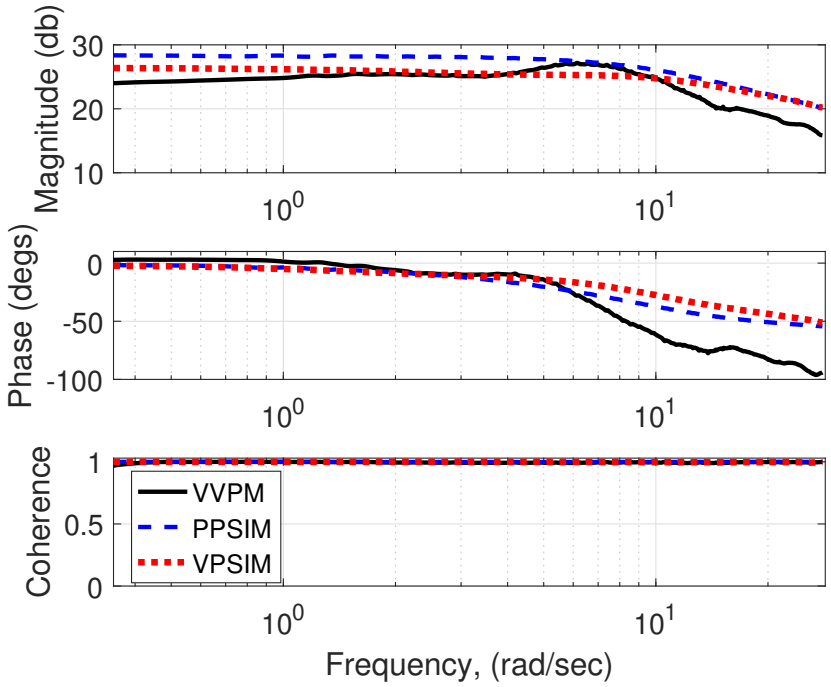

(a) $(\Delta\lambda_{1c})_U$ due to $(\Delta C_M)_U$, case 4 in Table 5.4

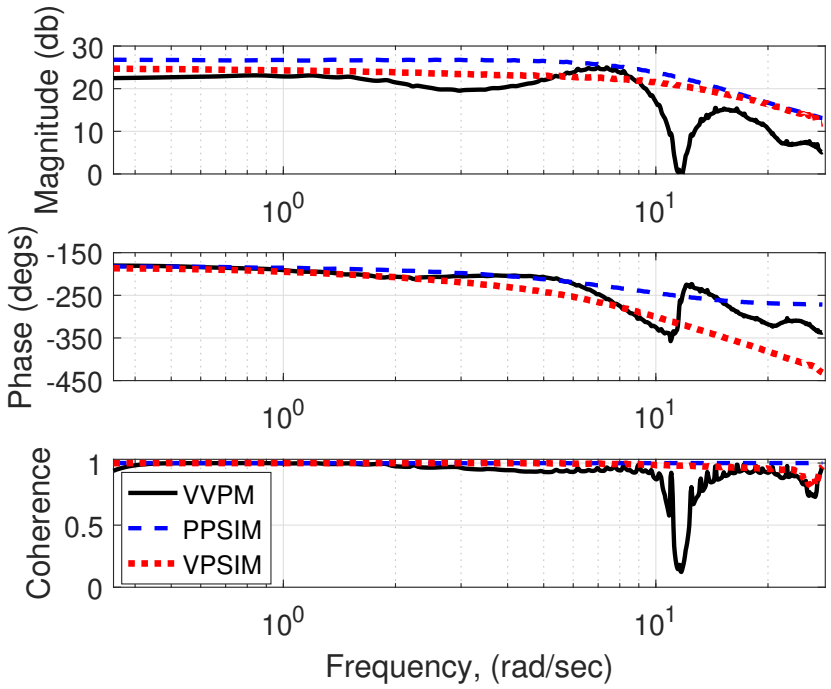

(b) $(\Delta\lambda_{1c})_L$ due to $(\Delta C_M)_U$, case 6 in Table 5.4

Figure 5.16: Comparison of the tandem rotor configuration frequency responses due to the upper rotor pitch moment coefficient excitation at $\mu = 0.04$

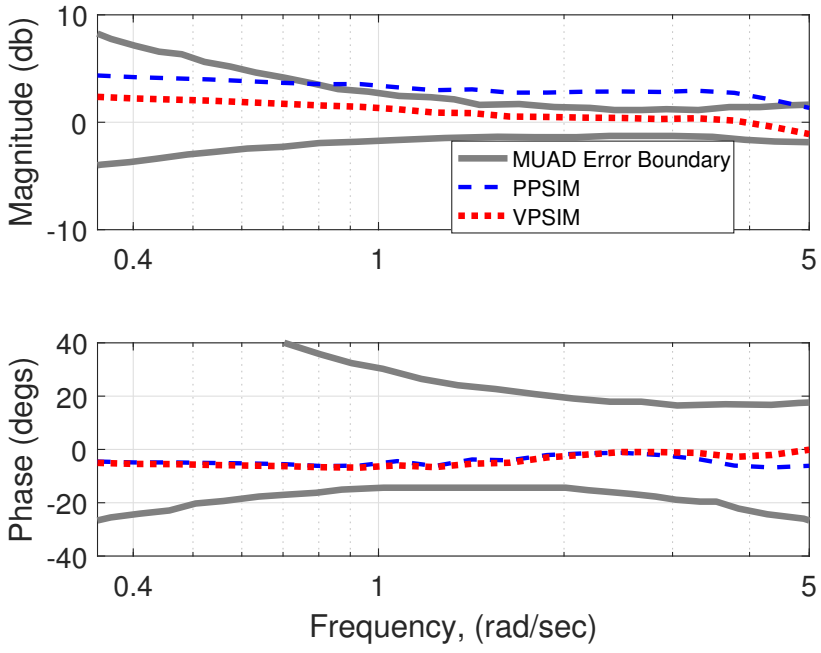

(a) $(\Delta\lambda_{1c})_U$ due to $(\Delta C_M)_U$, case 4 in Table 5.4

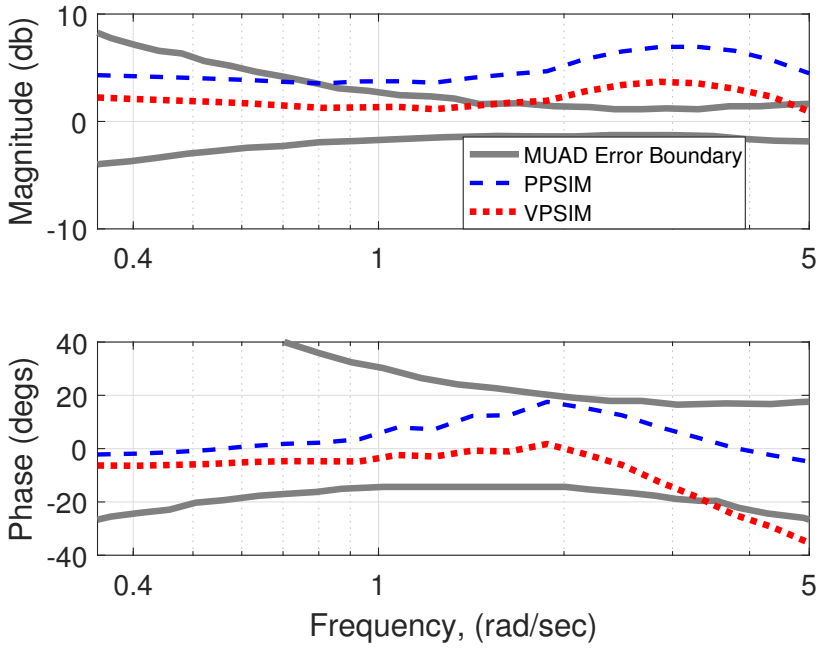

(b) $(\Delta\lambda_{1c})_L$ due to $(\Delta C_M)_U$, case 6 in Table 5.4

Figure 5.17: Comparison of the tandem rotor configuration frequency responses due to the upper rotor pitch moment coefficient excitation at $\mu = 0.04$

CHAPTER 6
INCLUSION OF THE REAL FLOW EFFECTS IN THE VELOCITY POTENTIAL SUPERPOSITION INFLOW MODEL

Comparisons against the Viscous Vortex Particle Method (VVPM) in chapter 4 and chapter 5 show that Velocity Potential Superposition Inflow Model (VPSIM) and Pressure Potential Superposition Inflow Model (PPSIM) capture some of the fundamental interference effects for different multi-rotor configurations at various flight conditions. Some of the identified differences between the VVPM and finite state multi-rotor dynamic inflow models are related to real flow effects such as wake contraction/expansion, wake distortion, wake diffusion (due to air viscosity), wake roll-up, and wake swirl velocity. These real flow effects are not taken into account in the VPSIM and PPSIM since they are based on the potential flow theory.

For single rotor configurations, finite state dynamic inflow models, i.e., Pitt-Peters [10–12] and Peters-He [13, 14], have been used widely for flight dynamics analyses and real-time flight simulations. These models provide adequate accuracy and excellent computational performance. In addition, inflow states are directly available in these models, which are required for control law development and stability analyses. On the other hand, finite state multi-rotor dynamic inflow models suffer more from the potential flow assumption compared to their single rotor counterparts since wake vortices from the rotors affect each other or even may coalesce and change the overall wake structure of the rotors [30, 32]. In particular, effects of the wake vortices are strong during hover and low speed flight, where vortices remain close to rotors. These vortex interactions alter the overall wake structure/geometry of the rotors and affect both self-induced inflow and interference inflow components of all rotors. Furthermore, wake contraction/expansion, wake distortion, diffusion effects become more important once the wake leaves the rotor. After all, these effects

determine the area of interference and strength of the interference inflow. Therefore, these real flow effects should be included in the finite state multi-rotor dynamic inflow models to provide more accurate multi-rotor inflow predictions, especially when loading changes are introduced to the rotors.

Kong et al. [28, 32] developed an analytical system identification methodology to include real flow effects in the inflow influence coefficient matrix of the PPSIM ($[L]$) using the steady changes in the inflow states due to perturbed rotor loadings. In PPSIM, an analytical methodology is possible for two reasons: (1) PPSIM is an example of state-coupled model, where coupling between the rotors is provided through off-diagonal blocks of the $[L]$, and inflow states already include the interference effects, (2) instead of the first harmonic inflow components (Pitt-Peters λ states), inflow states (α) are extracted from the VVPM inflow distribution. On the other hand, VPSIM is an output-coupled model, where interference is mainly taken into consideration at the time induced velocity is calculated. In VPSIM, the inflow influence coefficient matrix ($[\tilde{L}]$) connects velocity potential states to the whole flow field. In contrast, PPSIM inflow states are only used in the determination of on-rotor inflow calculations. Besides, unlike the PPSIM, VPSIM requires costates for calculating the induced velocity below the rotor disk. Costates are obtained by solving another ordinary differential equation through backward time marching. For these reasons, a different system identification methodology is needed for inclusion of real flow effects in VPSIM.

In this chapter, only Harrington coaxial rotor configuration is considered. The developed system identification methodology is applicable to any configuration. Also, PPSIM results are not shown here as PPSIM is already compared against the VVPM in detail for Harrington coaxial rotor configuration [30]. Similar to the previous PPSIM studies in Refs. [30, 32], the flow field is represented by six states (three odd velocity potential states for each rotor) in VPSIM simulations. Note that additional three costates are necessary for the VPSIM to predict interference inflow at the lower rotor due to the upper rotor.

6.1 System Identification Methodology

VPSIM is considered as an output-coupled model where interference effects are primarily considered in the induced velocity calculation. The inflow influence coefficient matrix ($[\tilde{L}]$) of the VPSIM connects velocity potential states to the whole flow field. Thus, correcting $[\tilde{L}]$ will affect the induced velocity not only for the on-rotor flow field but also for the off-rotor flow field. However, representation of the whole flow field of a multi-rotor configuration only with velocity potentials might not be possible due to existing strong rotor-on-rotor wake interactions. Some correction terms other than the $[\Delta\tilde{L}]$ are needed to fully represent the flow field of a multi-rotor configuration. In Ref. [54], some gains are introduced for the interference inflow computation, which is typical for an output-coupled model. The same approach is followed for the VPSIM since it has a similar model structure.

In order to incorporate the real flow effects into the VPSIM for the changes in the steady-steady inflow components ($\Delta\lambda_0$, $\Delta\lambda_{1c}$, $\Delta\lambda_{1s}$), the governing inflow equation of the VPSIM for the coaxial rotor (see Eq. (2.17)) is modified as follows:

$$[\hat{V}_m][\hat{L}]^{-1}[\hat{M}] \begin{Bmatrix} a_1 \\ \Delta_1 \\ a_2 \end{Bmatrix} = \begin{Bmatrix} \tau_1 \\ \tau_1^* \\ \tau_2 \end{Bmatrix} \tag{6.1}$$

where

$$\begin{aligned}
[\hat{M}] &= diag(\tilde{M}, \tilde{M}, \tilde{M}) \\
[\hat{V}_m] &= diag(\tilde{V}_{m1},\ \tilde{V}_{m1},\ \tilde{V}_{m2}) \\
[\hat{L}] &= diag(\tilde{L}(\tilde{X}_1) + \Delta\tilde{L}_1(\tilde{X}_1),\ \tilde{L}(\tilde{X}_1) + \Delta\tilde{L}_1(\tilde{X}_1), \tilde{L}(\tilde{X}_2) + \Delta\tilde{L}_2(\tilde{X}_2)) \\
\tilde{X}_1 &= \tan(\tilde{\chi}_1/2), \quad \tilde{X}_2 = \tan(\tilde{\chi}_2/2)
\end{aligned}$$

Note that Eq. (6.1) represents the steady-state governing inflow equation. In this equation, inflow influence coefficient matrices of the upper and lower rotors are modified by $\Delta\tilde{L}_1(\tilde{X}_1)$ and $\Delta\tilde{L}_2(\tilde{X}_2)$ to include real flow effects. Both $\Delta\tilde{L}_1(\tilde{X}_1)$ and $\Delta\tilde{L}_2(\tilde{X}_2)$ are 3×3 matrices since the flow field of each rotor is represented by three velocity potential states. After obtaining velocity potential states of both rotors ($\{a\}_1$ & $\{a\}_2$) and costates of the upper rotor ($\{\Delta\}_1$), self-induced inflow and interference inflow of both rotors are computed. Equations (6.2) and (6.3) are used for the self-induced inflow computation of the upper rotor (rotor 1) and lower rotor (rotor 2), respectively.

$$w_1^{self} = \frac{\partial}{\partial z}\sum_{r=0}^{M}\sum_{j=r}^{N}\left[(a_j^{rc})_1(\tilde{\Psi}_j^{rc})_1 + (a_j^{rs})_1(\tilde{\Psi}_j^{rs})_1\right] \tag{6.2}$$

$$w_2^{self} = \frac{\partial}{\partial z}\sum_{r=0}^{M}\sum_{j=r}^{N}\left[(a_j^{rc})_2(\tilde{\Psi}_j^{rc})_2 + (a_j^{rs})_2(\tilde{\Psi}_j^{rs})_2\right] \tag{6.3}$$

Equation (6.4) computes the interference inflow at the upper rotor due to the lower rotor. Here, gain *H* introduces real flow effects into the interference inflow. Similarly, Eq. (6.5) with the correction term *G* computes the interference inflow at the lower rotor due to the upper rotor. For calculating the induced velocity below the rotor disk, costates are required, and adjoint theorem (see Eq. (2.13)) must be used. That is why Eq. (6.5) is different from Eqs. (6.2), (6.3), and (6.4).

$$w_1^{int} = \frac{\partial}{\partial z}\sum_{r=0}^{M}\sum_{j=r}^{N}\left[H_j^{rc}(\tilde{X}_2)(a_j^{rc})_2(\tilde{\Psi}_j^{rc})_2 + H_j^{rs}(\tilde{X}_2)(a_j^{rs})_2(\tilde{\Psi}_j^{rs})_2\right] \tag{6.4}$$

$$w_2^{int} = \frac{\partial}{\partial z} \sum_{r=0}^{M} \sum_{j=r}^{N} \begin{bmatrix} G_j^{rc}(\tilde{X}_1)(a_j^{rc})_1(\tilde{\Psi}_j^{rc}(r_0, \bar{\psi}, 0))_1 \; + \; G_j^{rs}(\tilde{X}_1)(a_j^{rs})_1(\tilde{\Psi}_j^{rs}(r_0, \bar{\psi}, 0))_1 + \\ G_j^{rc}(\tilde{X}_1)(\Delta_j^{rc})_1(\tilde{\Psi}_j^{rc}(r_0, \tilde{\psi}, 0))_1 \; + \; G_j^{rs}(\tilde{X}_1)(\Delta_j^{rs})_1(\tilde{\Psi}_j^{rs}(r_0, \tilde{\psi}, 0))_1 - \\ G_j^{rc}(\tilde{X}_1)(\Delta_j^{rc})_1(\tilde{\Psi}_j^{rc}(r_0, \tilde{\psi}, -\xi_0))_1 - G_j^{rs}(\tilde{X}_1)(\Delta_j^{rs})_1(\tilde{\Psi}_j^{rs}(r_0, \tilde{\psi}, -\xi_0))_1 \end{bmatrix} \tag{6.5}$$

It is important to recognize that shaping function ($\tilde{\Psi}$) is a spatial function consisting of the first and second kind of the Legendre functions. Although this function is the same for both rotors, subscripts 1 and 2, i.e., $(\tilde{\Psi})_1$, are kept to represent the reference frame of the corresponding rotor (see Fig. 3.6). For example, Eq. (6.4) computes the interference inflow at the upper rotor due to the lower rotor. In this computation, locations of the upper rotor aerodynamic calculation points are determined with respect to the lower rotor reference frame. Similarly, to compute self-induced inflow at the lower rotor, aerodynamic calculation points are determined with respect to the lower rotor reference frame.

Kong et al. [27, 28] showed that PPSIM inflow influence coefficient matrix corrections are less sensitive to changes in flight conditions if perturbed quantities are used. In other words, rotor loadings are perturbed to find corresponding changes in the steady-state inflow components. A similar approach is adopted for the VPSIM. The following simulation process is used to find correction terms ($\Delta\tilde{L}_1(\tilde{X}_1)$, $\Delta\tilde{L}_2(\tilde{X}_2)$, $G(\tilde{X}_1)$ & $H(\tilde{X}_2)$):

1. Set initial thrust coefficient to 0.0035 ($\tau_1^{0c} = 0.0030$) for both upper and lower rotors.

2. Set initial aerodynamic roll moment (C_L) and pitch moment (C_M) coefficients to zero for all rotors.

3. Find the steady-state condition corresponding to initial loading and flight conditions.

4. Linearize the VPSIM by replacing the mass flow parameter matrix of each rotor ($\tilde{V}_m$) with the scalar parameter $\tilde{V}$ of each rotor at the corresponding steady-state condition.

5. Introduce a step change of 0.000175 (%5 of C_T) to a single rotor loading mode, and then simulate till the new steady-state condition is reached.

6. Subtract the initial steady-state inflow components from the new steady-state inflow components resulting from the applied step change to a rotor loading mode to find the changes in the inflow components ($\Delta\lambda_0$, $\Delta\lambda_{1c}$, $\Delta\lambda_{1s}$).

7. Repeat the process for each rotor's loading mode (three for the upper rotor and three for the lower rotor).

Changes in the Viscous Vortex Particle Method (VVPM) inflow components are obtained by following the same simulation process except for the linearization step. In this simulation process, an applied step change to a single loading mode results in six perturbed inflow components (three for each rotor). Since there are six loading modes (three for each rotor), 36 perturbed inflow components are obtained in total after the simulations. Using the VVPM perturbed inflow components, it is possible to identify the correction terms $\Delta\tilde{L}_1(\tilde{X}_1)$, $\Delta\tilde{L}_2(\tilde{X}_2)$, $G(\tilde{X}_1)$, and $H(\tilde{X}_2)$ by minimizing the differences between the VPSIM and VVPM perturbed inflow components. To start the system identification process, these differences in the perturbed inflow components must be accurately quantified to describe the objective function. Reference [32] quantified the changes in the inflow states with a quadratic function. The same approach is followed here except that inflow states ($\{\alpha\}$) are replaced by inflow components in $\{\lambda\}$ form. Equation (6.6) represents the 2-norm of all perturbed inflow components corresponding to the chosen inflow model. In addition, 2-norm of the perturbed inflow component differences between the inflow models are calculated using Eq. (6.7). Lastly, differences between the VPSIM and VVPM perturbed inflow components are defined as a single percentage error using Eq. (6.8).

$$|| A ||_2 = \sqrt{\sum_{i=1}^{36} | \Delta\lambda_i |^2} \tag{6.6}$$

$$|| \Delta A ||_2 = \sqrt{\sum_{i=1}^{36} | \Delta\lambda_{i,VPSIM} - \Delta\lambda_{i,VVPM} |^2} \tag{6.7}$$

$$J_q = \frac{|| \Delta A ||_2}{|| A ||_{2,VVPM}} \times 100 \tag{6.8}$$

In the system identification process, J_q is minimized by a quasi-Newton unconstrained optimization algorithm to identify $\Delta\tilde{L}_1(\tilde{X}_1)$, $\Delta\tilde{L}_2(\tilde{X}_2)$, $G(\tilde{X}_1)$, and $H(\tilde{X}_2)$. Note that by using the linearized VPSIM, simulation steps only from 5 to 7 are repeated in the optimization process, which significantly reduces the overall simulation time. Table 6.1 presents the identified correction terms for the VPSIM. The nominal values of the *H* and *G* correction terms are equal to 1.0. These terms are multiplied with velocity potential states (*G* is also multiplied with costates) to improve interference inflow predictions. These terms, especially *H*, are generally close to 1.0, indicating that VPSIM captures some of the fundamental interference effects. The initial values of every element inside the $\Delta\tilde{L}_1(\tilde{X}_1)$ and $\Delta\tilde{L}_2(\tilde{X}_2)$ are equal to zero. The identified values in Table 6.1 indicate that correction terms are usually small for advance ratios of 0.00, 0.07, and 0.12. The only exception is seen in the cosine-sine (fore-to-aft to side-to-side) coupling elements of the lower rotor, $\Delta\tilde{L}_2(2,3)$ and $\Delta\tilde{L}_2(3,2)$, in hover. In VVPM, the lower rotor has a strong self-induced fore-to-aft to side-to-side coupling in hover for the coaxial rotor configuration. The same phenomenon is also reported in Ref. [32]. The lower rotor directly operates within the upper rotor wake, which alters the flow field of the lower rotor. That is why $\Delta\tilde{L}_2(2,3)$ and $\Delta\tilde{L}_2(3,2)$ are larger than other identified terms in hover. In forward flight, the mutual fore-to-aft to side-to-side coupling disappears for both rotors. Now, instead of the mutual interference, only the fore-to-aft inflow component affects the side-to-side inflow component, although its effect is smaller compared to the hover case.

Next, changes in the inflow components are analyzed in detail for the original VPSIM, VPSIM with correction terms, and VVPM. From now on, VPSIM with correction terms is referred to as *improved VPSIM*, whereas VPSIM without correction terms is referred to as *original VPSIM* or simply *VPSIM*. Figures 6.1 and 6.2 show changes in the steady-state inflow components in hover due to perturbations of the upper and lower rotor loading modes,

Table 6.1: Identified correction terms for the VPSIM

Correction	$\mu = 0.00$			$\mu = 0.07$			$\mu = 0.12$		
	-0.02	-0.02	-0.01	-0.04	0.22	-0.09	-0.10	0.31	-0.05
$\Delta\tilde{L}_1$	0.00	-0.22	0.11	0.03	-0.18	0.01	0.06	-0.13	-0.01
	0.00	-0.21	-0.22	0.18	-0.24	-0.30	0.22	-0.26	-0.36
G	0.75	0.61	0.72	0.78	0.93	0.91	1.04	0.65	1.24
	0.10	0.01	0.01	0.00	0.07	0.14	-0.08	0.27	0.10
$\Delta\tilde{L}_2$	0.01	-0.02	-1.34	0.29	-0.29	-0.08	0.17	-0.18	-0.06
	-0.01	1.61	-0.09	0.32	0.44	0.13	-0.07	0.35	-0.29
H	1.02	1.01	1.08	0.94	0.73	0.92	1.00	1.01	1.02

respectively. Figure 6.1 illustrates that VPSIM over-estimates the changes in the inflow components for every upper rotor loading mode compared to the VVPM and improved VPSIM. The magnitude of the over-estimation is relatively higher at the lower rotor. The original VPSIM does not include the real flow effects such as wake contraction/expansion, diffusion, and other rotor wake interactions since it is based on the potential flow theory. The absences of these modeling details explain why agreement between the original VPSIM and VVPM further deteriorate at the lower rotor. Since a small vertical distance separates the rotors in Harrington coaxial rotor configuration, diffusion (or wake decay) effect is smaller than other effects. The swirl coupling is another effect that is missing in the original VPSIM, as shown in Figs. 6.1(b) and 6.1(c). For example, perturbation of the upper rotor aerodynamic pitch moment changes both fore-to-aft and side-to-side inflow components. The primary inflow response, the fore-to-aft inflow component, is larger than the secondary response (side-to-side inflow) as expected (Figs 6.1(b)) for both rotors. For the upper rotor aerodynamic roll moment perturbation, the secondary response (fore-to-aft inflow) is smaller than the secondary response of the previous case, although primary responses have similar magnitudes. Inflow predictions related to lower rotor loading perturbation cases are provided in Fig. 6.2. In these perturbation cases, VPSIM primary inflow

predictions have better agreement with VVPM predictions than the upper rotor perturbation cases. Figure 6.2 also shows that changes at the upper rotor inflow components are less than the inflow changes observed at the lower rotor. This phenomenon is expected since lower rotor pressure loading effects propagate upstream (against the upper rotor downwash) while substantially diffusing [32]. Although original VPSIM captures primary responses well, it completely ignores the secondary responses related to the swirl coupling. In fact, the swirl coupling effect due to the lower rotor aerodynamic pitch or roll moment perturbation is considerably higher than the swirl coupling effect seen at the upper rotor perturbation cases. The lower rotor always operates inside the downwash of the upper rotor in hover, which alters the flow field at the lower rotor [32]. These differences between the VPSIM and VVPM are significantly reduced after including the real flow effects in the VPSIM. The improved VPSIM is able to capture primary and secondary responses for both upper and lower inflow predictions for every loading perturbation case. The wake contraction/diffusion and wake swirl effects embedded into correction terms reduce the cost function (J_q) from 88.3 to 8.6 for the improved VPSIM. This reduction in the cost function confirms the effectiveness of the introduced system identification method for capturing the real flow effects in hover.

Figures 6.3 and 6.4 show changes in the steady-state inflow predictions at the advance ratio of 0.07. Figure 6.3 illustrates changes in the inflow components due to upper rotor loading perturbation cases. In forward flight, a new inflow coupling (uniform-to-sine) arises because the change in the rotor thrust creates side-to-side inflow components at both rotors in addition to uniform and fore-to-aft inflow components (Fig. 6.3(a)). This thrust change probably influences the wake roll-up effect resulting in uniform-to-sine inflow coupling. On the other hand, swirl coupling in forward flight is slightly different than the hover case. Observations of Figs. 6.3(b) and 6.3(c) show that only aerodynamic pitch moment perturbation alters both fore-to-aft and side-to-side inflow components. The perturbation of the aerodynamic roll moment solely alters the side-to-side inflow component. Similar to the upper rotor case, these new inflow interference effects are also seen in the lower

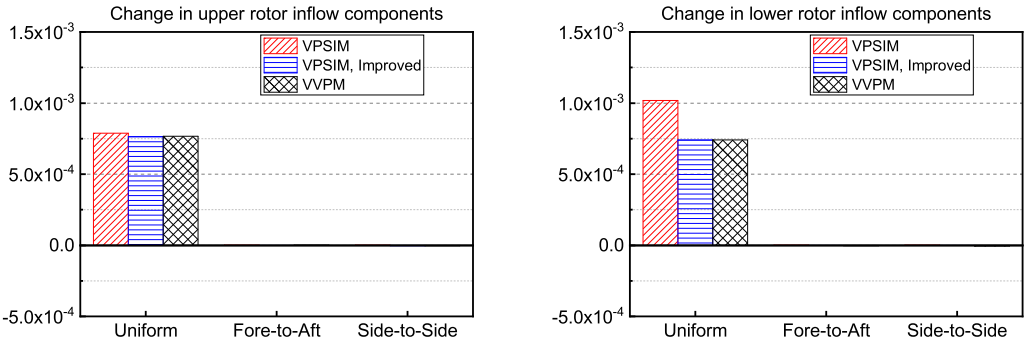

(a) Perturbation of upper rotor thrust coefficient

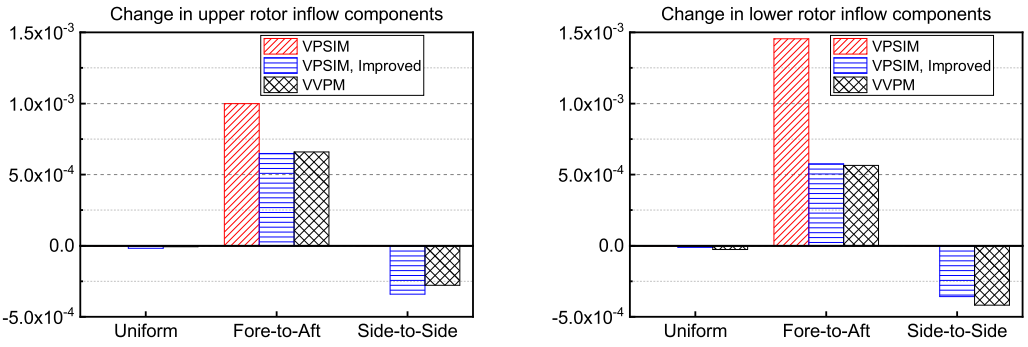

(b) Perturbation of upper rotor aerodynamic pitch moment coefficient

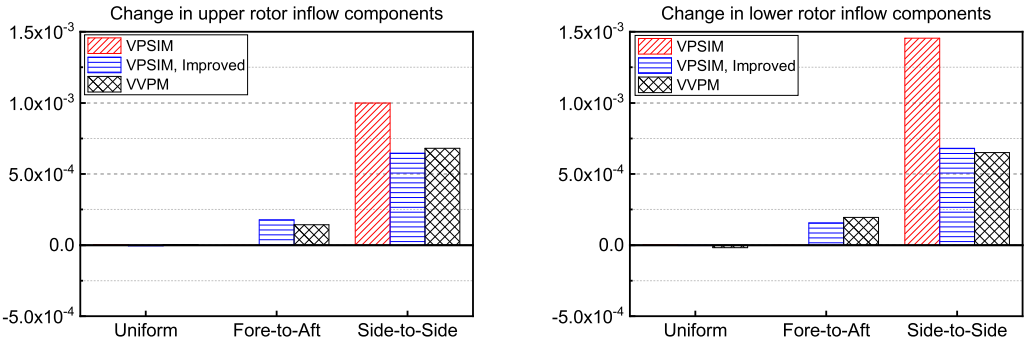

(c) Perturbation of upper rotor aerodynamic roll moment coefficient

Figure 6.1: Changes in steady-state inflow components due to upper rotor loading perturbations in hover

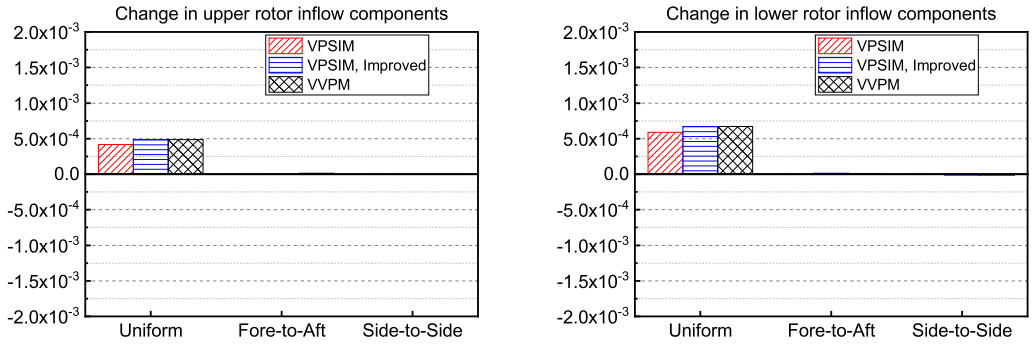

(a) Perturbation of lower rotor thrust coefficient

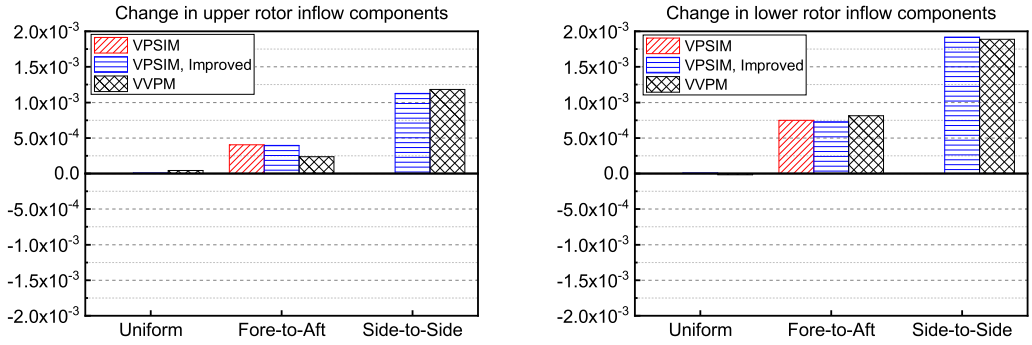

(b) Perturbation of lower rotor aerodynamic pitch moment coefficient

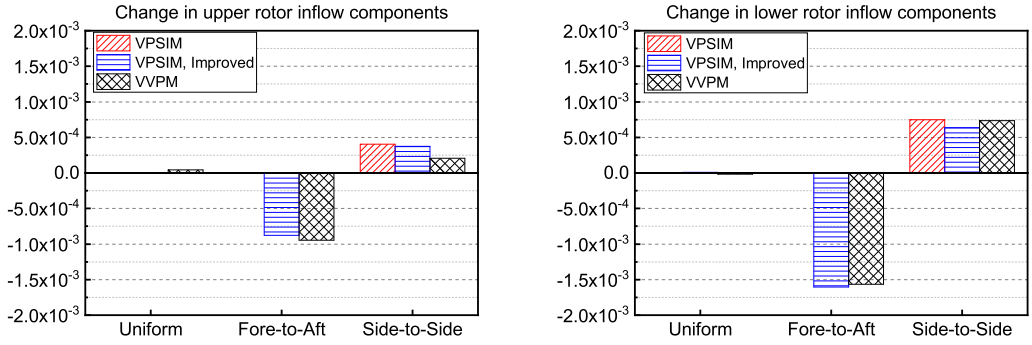

(c) Perturbation of lower rotor aerodynamic roll moment coefficient

Figure 6.2: Changes in steady-state inflow components due to lower rotor loading perturbations in hover

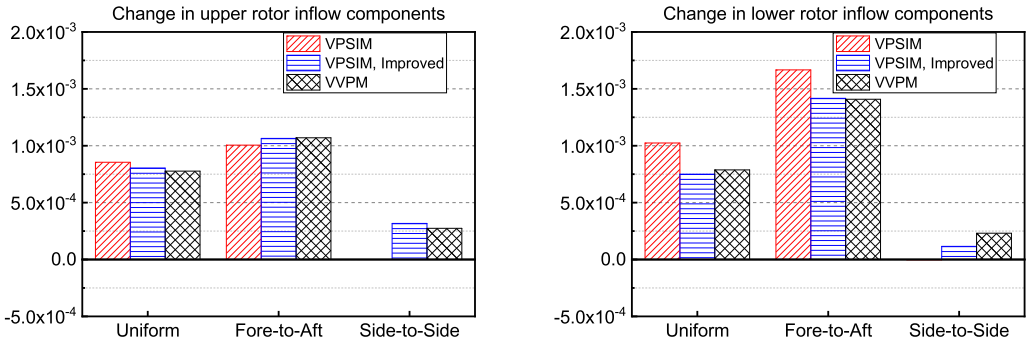

(a) Perturbation of upper rotor thrust coefficient

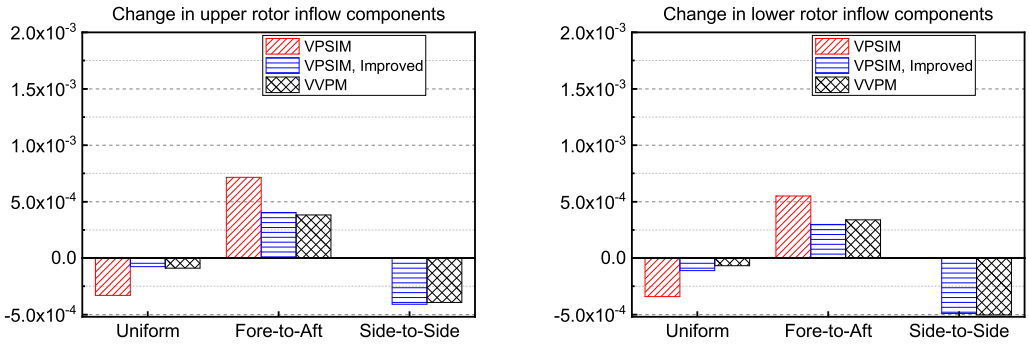

(b) Perturbation of upper rotor aerodynamic pitch moment coefficient

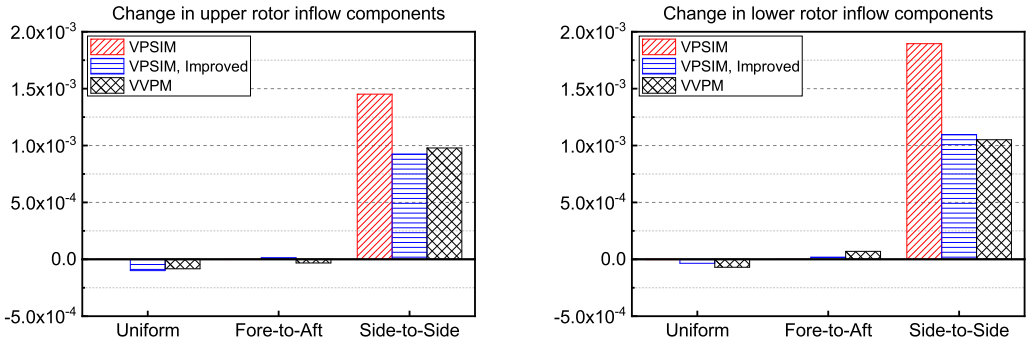

(c) Perturbation of upper rotor aerodynamic roll moment coefficient

Figure 6.3: Changes in steady-state inflow components due to upper rotor loading perturbations at advance ratio of 0.07

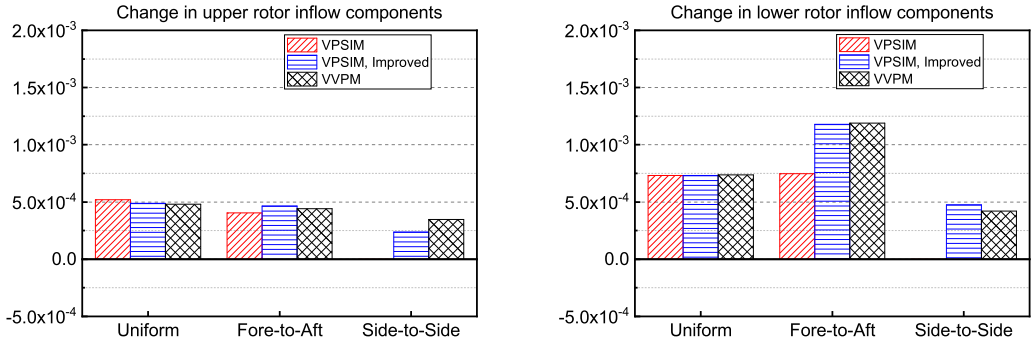

(a) Perturbation of lower rotor thrust coefficient

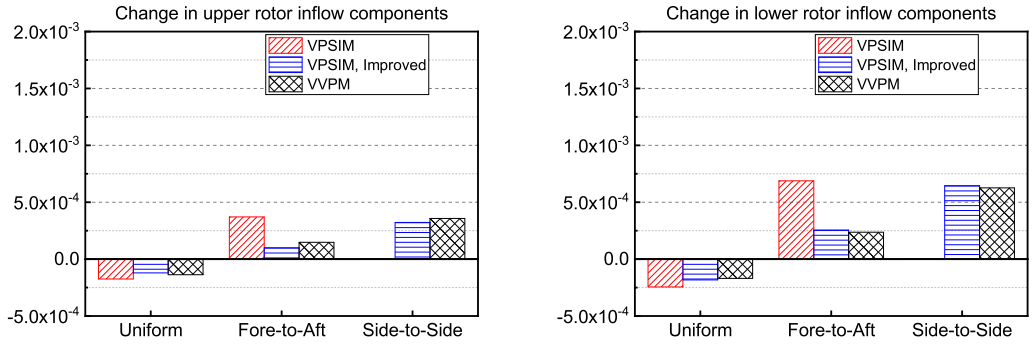

(b) Perturbation of lower rotor aerodynamic pitch moment coefficient

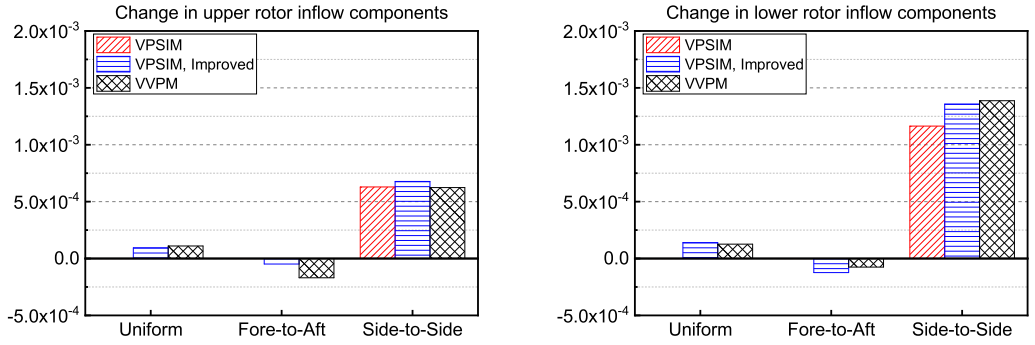

(c) Perturbation of lower rotor aerodynamic roll moment coefficient

Figure 6.4: Changes in steady-state inflow components due to lower rotor loading perturbations at advance ratio of 0.07

rotor perturbation cases with some magnitude differences (Fig. 6.4). For lower rotor loading perturbation cases, changes in the upper rotor inflow components are smaller than the changes in the lower rotor inflow components. The opposite is generally true for the upper rotor perturbation cases. This outcome is expected since the lower rotor's influence on the upper rotor gradually decreases as wake skews backward in forward flight. All real flow effects omitted in the original VPSIM are identified and used to improve the correlation between the VPSIM and VVPM. The addition of these effects into the VPSIM considerably improves the correlation with VVPM at both rotors for every loading perturbation case. The cost function (J_q) is reduced from 50.5 to 7.6 also confirming the effectiveness of the developed system identification methodology for forward flight conditions.

6.2 Sensitivity of Identified Correction Terms to Different Initial Rotor Loading

The results shown in chapter 6.1 are based on a single initial loading condition where the thrust sharing ratio between the upper and lower rotors is unity ($C_{T,1}/C_{T,2} = 1.0$), and rotors have initial uniform loading (thrust coefficient) of 0.0035. For all simulations, aerodynamic roll moment and pitch moment coefficients of both rotors are set to zero. The upper rotor and lower rotor thrust coefficients are represented as $C_{T,1}$ and $C_{T,2}$, respectively. In flight simulations, rotors might have different initial loading conditions due to torque balancing, flight conditions, etc. Thus, a sensitivity study should be conducted to determine changes in the identified correction terms due to initial rotor loading and flight conditions. A similar study has been performed for the PPSIM by Kong et al. [32] to investigate sensitivity of the extracted inflow influence coefficient matrix ($[L]$). Similar to the study of Kong et al. [32], thrust sharing ratios of $C_{T,1}/C_{T,2} = 1.2$ and $C_{T,1}/C_{T,2} = 0.8$ are used in the simulations along with $C_{T,1}/C_{T,2} = 1.0$.

After obtaining the VVPM coaxial rotor model inflow responses for the new thrust sharing cases, correction terms of the VPSIM ($\Delta\tilde{L}_1(\tilde{X}_1)$, $\Delta\tilde{L}_2(\tilde{X}_2)$, $G(\tilde{X}_1)$, and $H(\tilde{X}_2)$) are identified with the same procedure described earlier. Elements in $\Delta\tilde{L}_1(\tilde{X}_1)$ and $\Delta\tilde{L}_2(\tilde{X}_2)$

blocks are plotted with respect to skew function ($\tilde{X}$) of the corresponding rotor in Figs. 6.5 and 6.6, respectively. Similarly, elements in $G(\tilde{X}_1)$ and $H(\tilde{X}_2)$ are plotted in Fig. 6.7. In these figures, each cluster of points corresponds to a single flight condition, while each point in a cluster represents a single thrust sharing ratio condition. Curve-fitted correlations corresponding to elements of the correction terms are also provided in Figs. 6.5, 6.6, and 6.7 as solid lines. For ease of application, second order polynomial functions are used in the fitting process. The measure of the quality of fit is provided in Table 6.2 in terms of goodness-of-fit (R^2) for each element. The goodness-of-fit describes the discrepancy between data points and expected values from the curve-fitted functions. The goodness-of-fit can take any value between 0 and 1, where values close to 1 are considered as a good fit since a greater proportion of the variance is taken into account. Most of the R^2 values provided in Table 6.2 are larger than 0.8, indicating that fitted-curves capture the large portion of the variance in the data associated with the thrust sharing ratio and flight conditions.

Next, curve-fitted corrections are included in VPSIM for improving correlations with the VVPM. Note that these correction terms are identified from a linearized version of the VPSIM. However, in flight simulations, nonlinear versions of the finite state dynamic inflow models are used. Here, curve-fitted corrections are implemented to the nonlinear version of the VPSIM for achieving a practical model that can be directly used in flight simulations. Table 6.3 shows comparisons of $||A||_2$ and J_q between the VVPM, improved VPSIM (curve-fitted), and VPSIM for various advance ratios and thrust sharing conditions. Especially in hover, significant improvement is achieved, as indicated by J_q values. At the advance ratio of 0.12, where skew angles of both rotors are close to 85°, smaller improvements are achieved. Although improvements seem to be small, one should consider that the free-stream velocity dominates the flow fields of the rotors at this advance ratio. Therefore, at this advance ratio, the effect of the inflow on rotor dynamics will be relatively small compared to the effect of the inflow in hover and low speeds. In view of this, the addition of curve-fitted corrections into the nonlinear VPSIM proves the feasibility of the approach

for improving the inflow model fidelity.

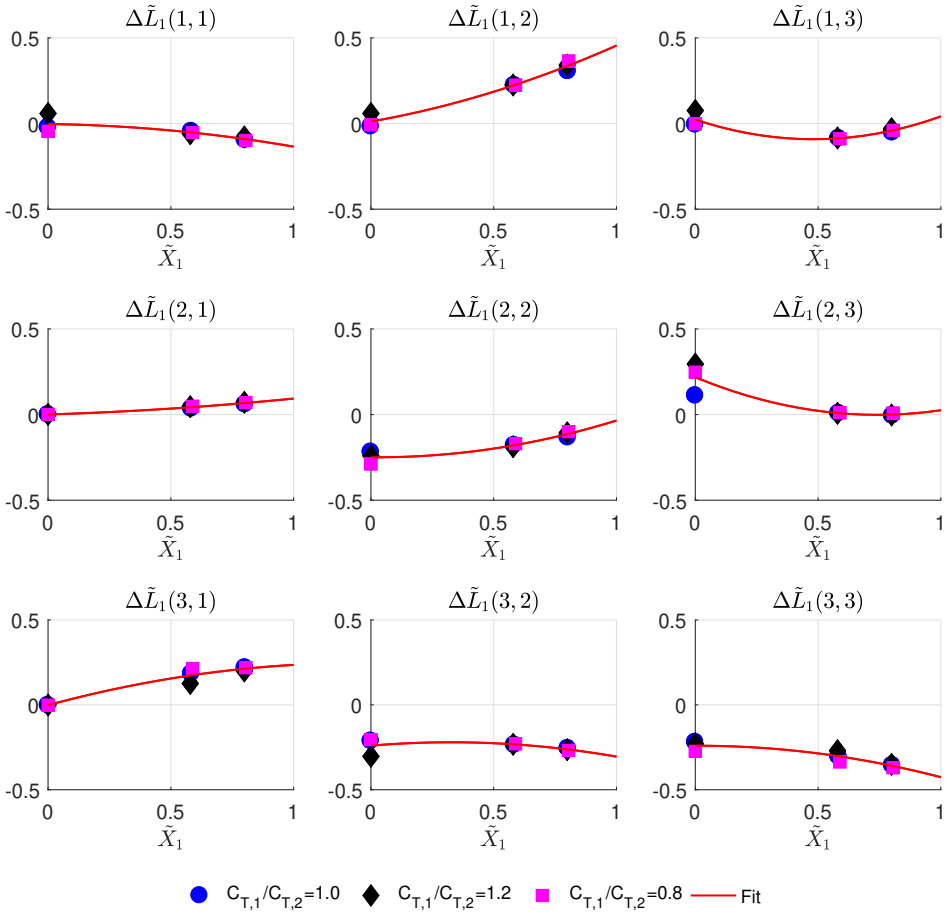

Figure 6.5: Curve-fitted correlations between elements in $\Delta\tilde{L}_1$ and rotor 1 wake skew function

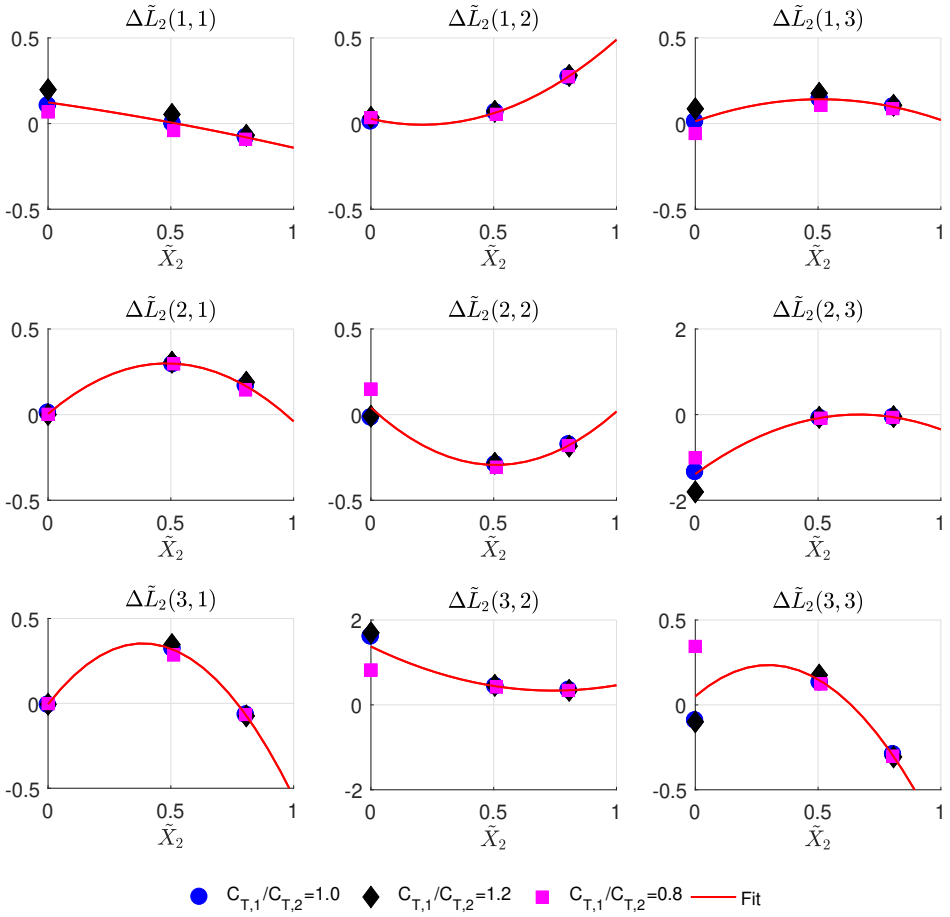

Figure 6.6: Curve-fitted correlations between elements in $\Delta\tilde{L}_2$ and rotor 2 wake skew function

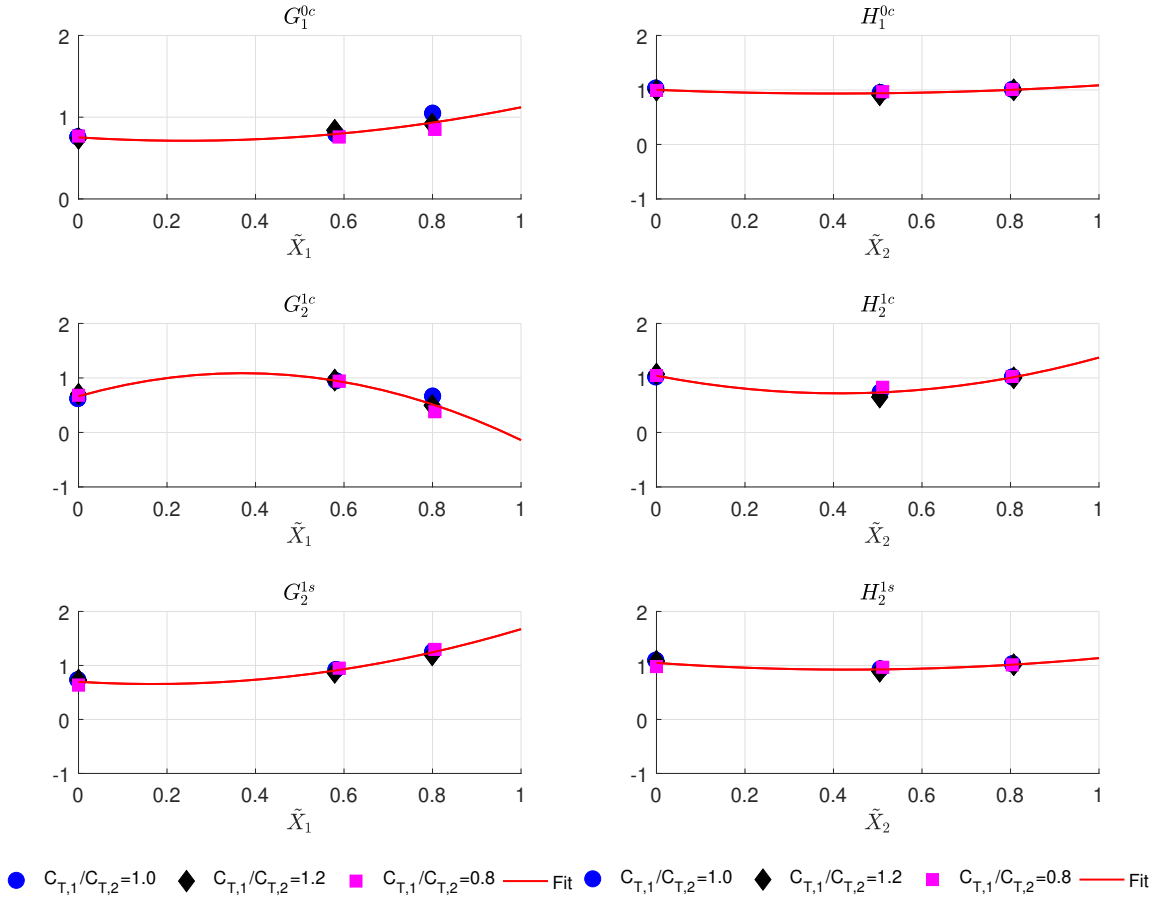

(a) Elements in G term

(b) Elements in H term

Figure 6.7: Curve-fitted correlations between elements in $G(\tilde{X}_1)$ & $H(\tilde{X}_2)$ and corresponding wake skew function

Table 6.2: Goodness-of-fit (R^2) for cure-fitted correlations between elements in the correction terms and corresponding skew function

Correction	R^2			Correction	R^2		
	0.6479	0.9697	0.8000		0.8237	0.9943	0.6618
$\Delta\tilde{L}_1$	0.9724	0.8948	0.8321	$\Delta\tilde{L}_2$	0.9907	0.9063	0.9161
	0.9504	0.1917	0.8450		0.9936	0.8068	0.7156
G	0.7059	0.8804	0.9767	H	0.7964	0.9050	0.7104

Table 6.3: Comparisons of $||A||_2$ and J_q between VVPM, improved VPSIM (curve-fitted), and VPSIM at selected flight conditions

		$\|\|A\|\|_2$			$J_q = \frac{\|\|\Delta A\|\|_2}{\|\|A\|\|_{2,\text{VVPM}}} \times 100\%$	
μ	$\frac{C_{T,1}}{C_{T,2}}$	VVPM	VPSIM, Imp[a]	VPSIM	VPSIM, Imp	VPSIM
	0.8	0.00312	0.00378	0.00319	39.5	81.5
Hover	1.0	0.00366	0.00378	0.00313	17.0	88.3
	1.2	0.00419	0.00379	0.00309	19.1	90.2
	0.8	0.00361	0.00358	0.00383	24.5	64.1
0.07	1.0	0.00360	0.00357	0.00379	21.3	62.7
	1.2	0.00365	0.00357	0.00376	20.4	61.2
	0.8	0.00302	0.00322	0.00358	29.1	50.8
0.12	1.0	0.00304	0.00329	0.00364	32.5	51.9
	1.2	0.00307	0.00324	0.00367	28.7	52.0

[a]VPSIM, Improved

6.3 Evaluation of VPSIM and Improved VPSIM Frequency Responses

Frequency responses of the VPSIM and improved VPSIM are evaluated against the VVPM for Harrington coaxial rotor configuration. The initial steady-state rotor thrust coefficient is set to 0.0035 for both rotors, while aerodynamics pitch moment and roll moment coefficients are set to zero for both rotors. At each flight condition, a chirp input is introduced to each loading condition one at a time to obtain frequency responses. The coherence weighted cost function is calculated for the frequency range of 0.35$\sim$5.0 rad/s. Cost functions due to the magnitude and phase differences are provided along with the total cost function for gaining further insight. Here, improved VPSIM uses curve-fitted correction terms. Besides, nonlinear versions of the original VPSIM and improved VPSIM are used in simulations.

Table 6.4 shows frequency response differences between the VPSIM, improved VPSIM, and VVPM in hover. Both original VPSIM and improved VPSIM have small cost functions for the thrust excitation cases. For every upper rotor perturbation case, improved VPSIM has a lower cost function than the VPSIM. Most of the improvement is due to the corrected magnitude response. For lower rotor aerodynamic roll moment and pitch moment perturbation cases, primary inflow responses of the improved VPSIM have higher cost functions than the original VPSIM. These increase in the cost functions are related to added cosine-sine coupling into the improved VPSIM. The cosine-sine coupling alters the frequency response of the primary inflow component. For example, Fig. 6.8 shows frequency response comparison between the VPSIM, improved VPSIM, and VVPM for the lower rotor fore-to-aft inflow component due to the lower rotor pitch moment perturbation in hover (case 12 in Table 6.4). As seen, improved VPSIM frequency response has the same trend as the VVPM frequency response, but its magnitude and phase deviate approximately after 1.0 rad/s. On the other hand, frequency response of the original VPSIM stays flat almost for entire frequency range and does not follow the VVPM frequency response

at the high frequency range. Although the primary inflow response cost function of the improved VPSIM is larger than the original VPSIM primary inflow response cost function for lower rotor perturbation cases, improved VPSIM captures coupling effects and provides a greater improvement in the secondary inflow responses, as shown in cases 13 and 15 in Table 6.4. As an example, the upper rotor fore-to-aft inflow component due to the lower rotor roll moment perturbation in hover (case 13 in Table 6.4) is provided in Fig. 6.9. In this secondary inflow response, improved VPSIM has much better agreement with VVPM than the original VPSIM because improved VPSIM captures cosine-sine coupling, unlike the original VPSIM. Figures 6.10 and 6.11 are other examples of inflow responses related to cosine-sine coupling. In these figures, improved VPSIM exhibits a good correlation with VVPM, whereas magnitude plots of the original VPSIM are significantly different.

Figure 6.12 shows the frequency response of the upper rotor uniform inflow component due to the upper rotor thrust perturbation in hover (case 1 in Table 6.4). Corresponding Maximum Unnoticeable Added Dynamics (MUAD) plot is also shown in Fig. 6.13 for the frequency range of 0.35$\sim$5.0 rad/s. Both VPSIM and improved VPSIM virtually have the same response and stay inside the MUAD envelopes for both magnitude and phase responses.

Frequency response comparison between VPSIM, improved VPSIM, and VVPM for the lower rotor uniform inflow component due to the lower rotor thrust perturbation in hover (case 10 in Table 6.4) is shown in Fig. 6.14. The improved VPSIM magnitude response has better agreement with the VVPM magnitude response than the VPSIM magnitude response up to 1.0 rad/s. In addition, the improved VPSIM has a slightly better phase response than the original VPSIM. Figure 6.15 shows that both improved VPSIM and VPSIM are inside the MUAD envelopes.

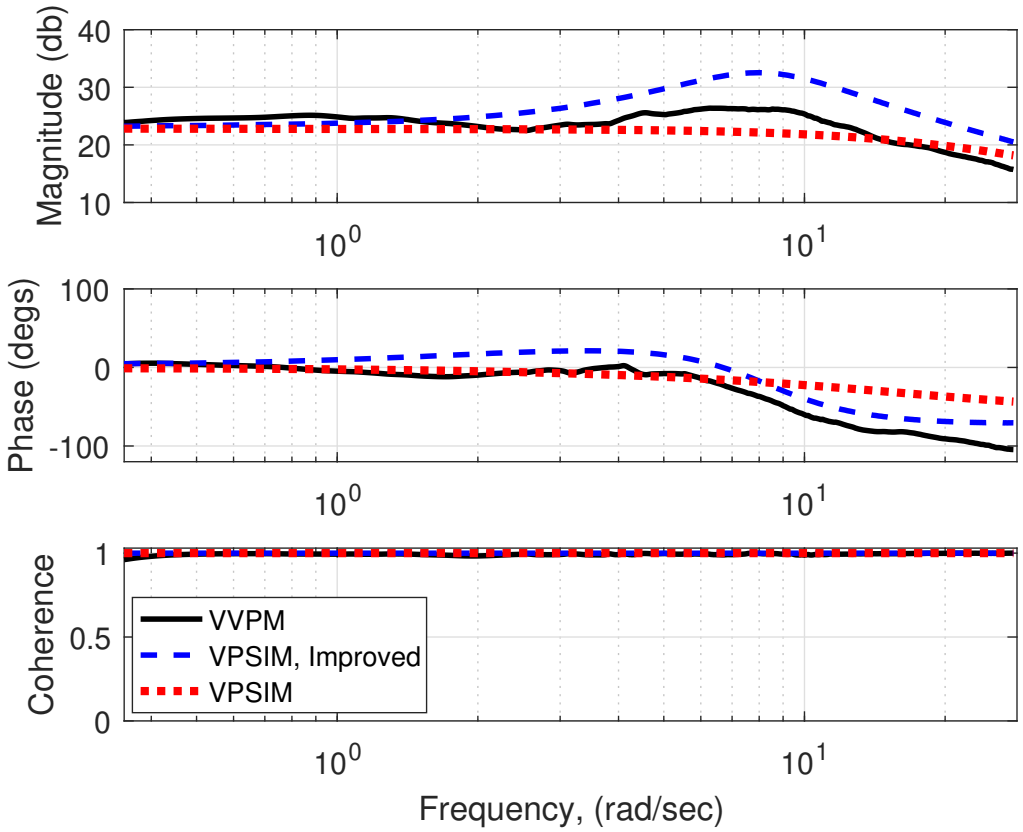

Figure 6.8: Frequency response comparison between VPSIM, improved VPSIM, and VVPM for lower rotor fore-to-aft inflow component due to lower rotor pitch moment perturbation in hover, i.e., case 12 in Table 6.4

Table 6.4: Frequency response differences between VPSIM, improved VPSIM, and VVPM for Harrington coaxial rotor configuration in hover

Case No.	Input[b]	Output	Model	Cost function[a] (0.35∼5.0 rad/s) Magnitude	Phase	Total
1	$(\Delta C_T)_U$	$(\Delta\lambda_0)_U$	VPSIM, Improved	2.9	4.9	7.8
			VPSIM	4.0	3.5	7.5
2		$(\Delta\lambda_0)_L$	VPSIM, Improved	35.8	5.6	41.4
			VPSIM	102.2	4.6	106.8
3	$(\Delta C_M)_U$	$(\Delta\lambda_{1c})_U$	VPSIM, Improved	108.0	33.8	141.9
			VPSIM	124.5	46.4	170.8
4		$(\Delta\lambda_{1c})_L$	VPSIM, Improved	30.0	230.6	260.6
			VPSIM	739.5	235.1	974.5
5	$(\Delta C_L)_U$	$(\Delta\lambda_{1c})_U$	VPSIM, Improved	92.9	18.0	110.9
			VPSIM	27051.3	22.8	27074.1
6		$(\Delta\lambda_{1s})_U$	VPSIM, Improved	101.7	28.5	130.1
			VPSIM	130.6	40.3	170.9
7		$(\Delta\lambda_{1c})_L$	VPSIM, Improved	21.7	48.2	69.8
			VPSIM	26693.4	49.2	26742.6
8		$(\Delta\lambda_{1s})_L$	VPSIM, Improved	54.5	245.8	300.2
			VPSIM	819.3	253.1	1072.4
9	$(\Delta C_T)_L$	$(\Delta\lambda_0)_U$	VPSIM, Improved	44.2	20.8	65.0
			VPSIM	19.7	21.8	41.5
10		$(\Delta\lambda_0)_L$	VPSIM, Improved	10.3	6.6	16.9
			VPSIM	16.8	10.9	27.8
11	$(\Delta C_M)_L$	$(\Delta\lambda_{1c})_U$	VPSIM, Improved	498.8	42.2	541.0
			VPSIM	119.6	58.5	178.1
12		$(\Delta\lambda_{1c})_L$	VPSIM, Improved	94.2	121.4	215.6
			VPSIM	54.6	8.3	62.9
13	$(\Delta C_L)_L$	$(\Delta\lambda_{1c})_U$	VPSIM, Improved	608.4	38.8	647.2
			VPSIM	54416.4	9115.5	63531.9
14		$(\Delta\lambda_{1s})_U$	VPSIM, Improved	517.6	42.4	560.0
			VPSIM	120.3	46.5	166.8
15		$(\Delta\lambda_{1c})_L$	VPSIM, Improved	750.7	67.9	818.5
			VPSIM	51318.2	8622.0	59940.2
16		$(\Delta\lambda_{1s})_L$	VPSIM, Improved	101.8	125.1	226.8
			VPSIM	66.5	7.6	74.1

[a]Computed using Eq. (3.5)

[b]Bracket subscripts *U* and *L* correspond to upper (rotor 1) and lower (rotor 2) rotors, respectively

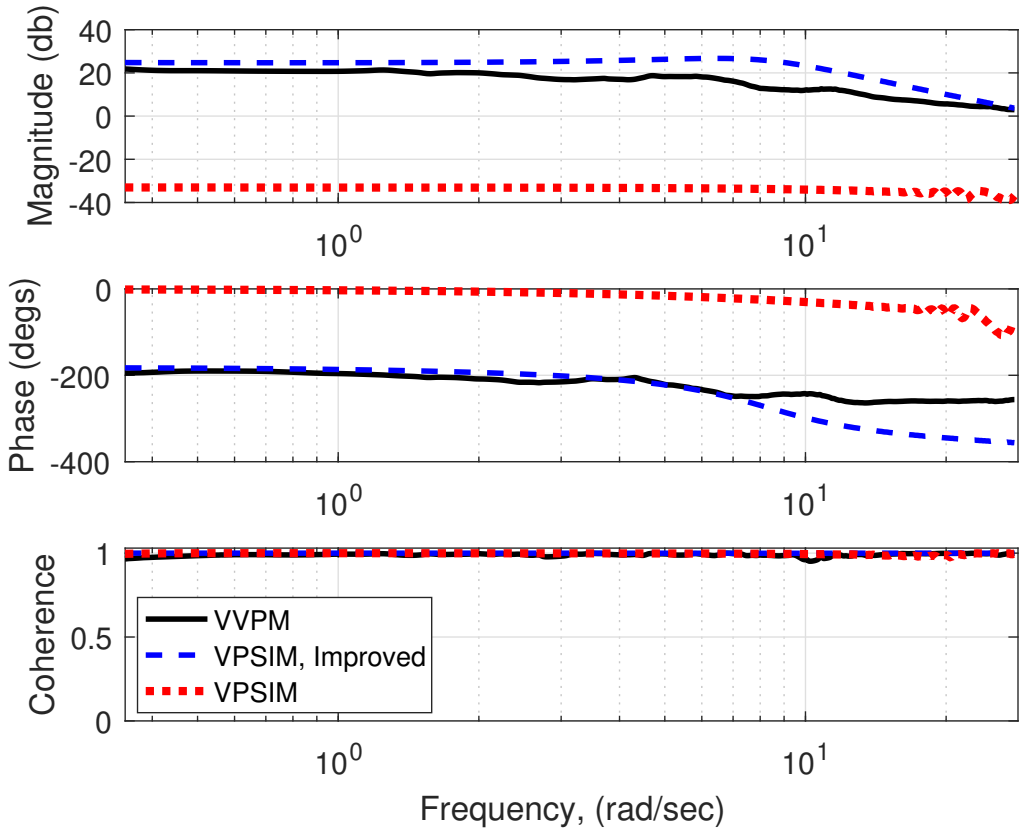

Figure 6.9: Frequency response comparison between VPSIM, improved VPSIM, and VVPM for upper rotor fore-to-aft inflow component due to lower rotor roll moment perturbation in hover, i.e., case 13 in Table 6.4

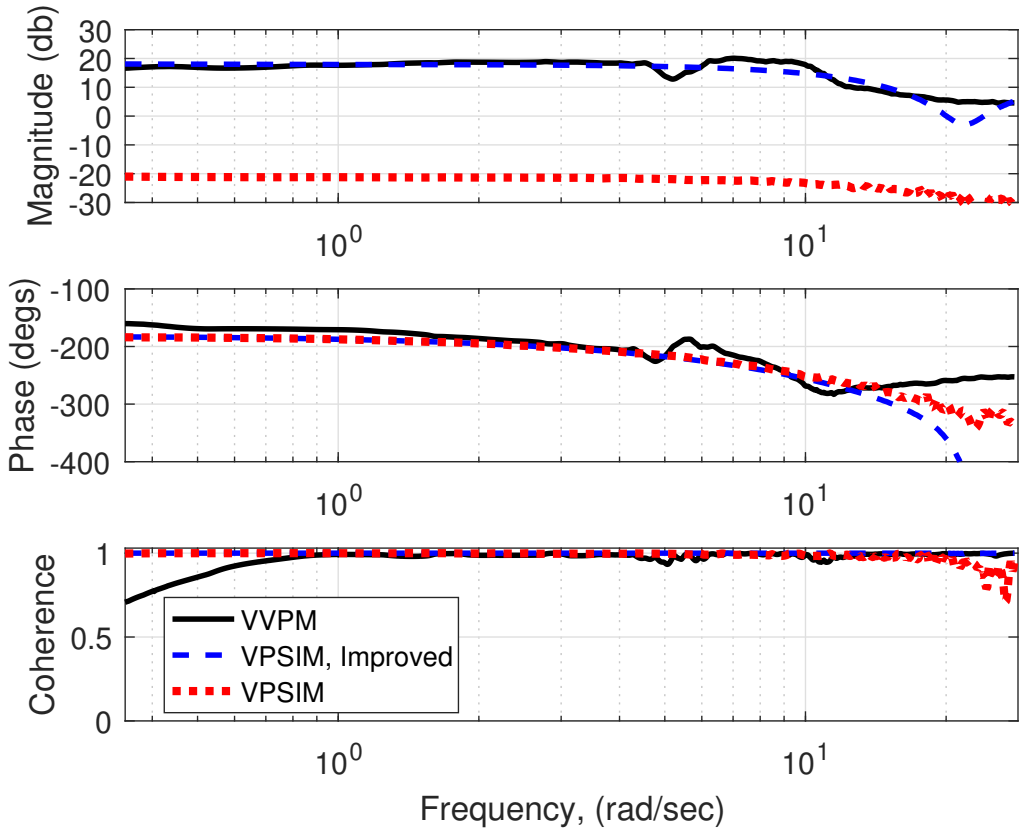

Figure 6.10: Frequency response comparison between VPSIM, improved VPSIM, and VVPM for lower rotor fore-to-aft inflow component due to upper rotor roll moment perturbation in hover, i.e., case 7 in Table 6.4

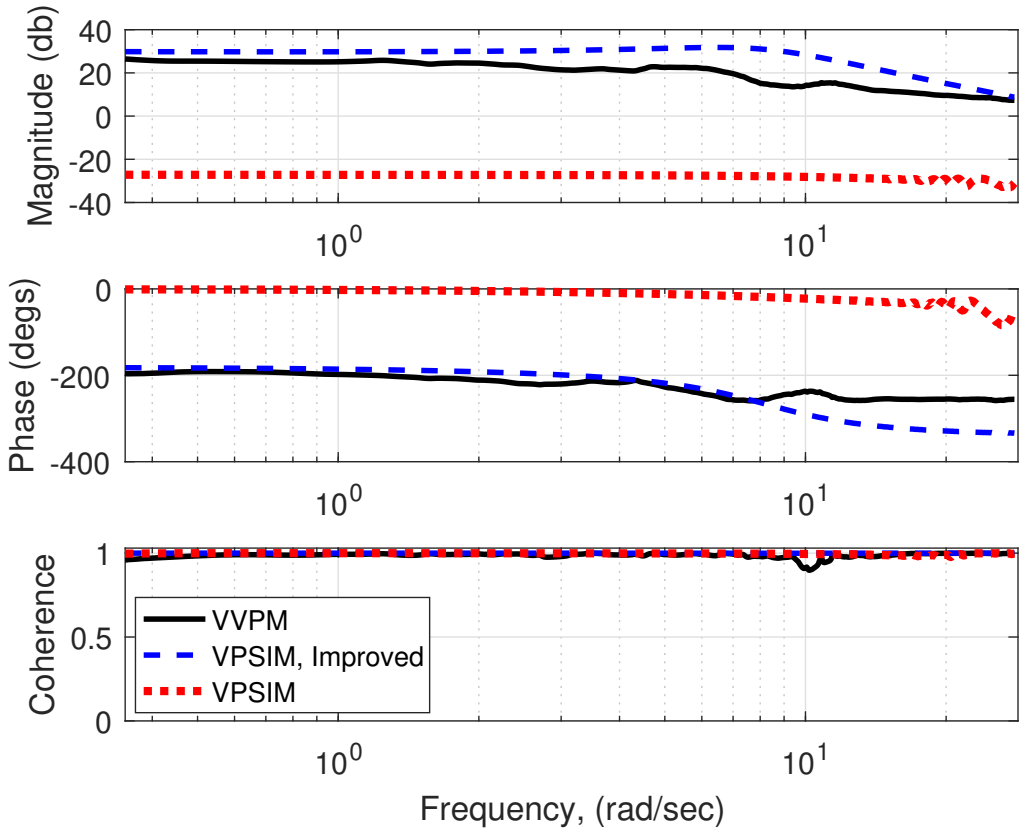

Figure 6.11: Frequency response comparison between VPSIM, improved VPSIM, and VVPM for lower rotor fore-to-aft inflow component due to lower rotor roll moment perturbation in hover, i.e., case 15 in Table 6.4

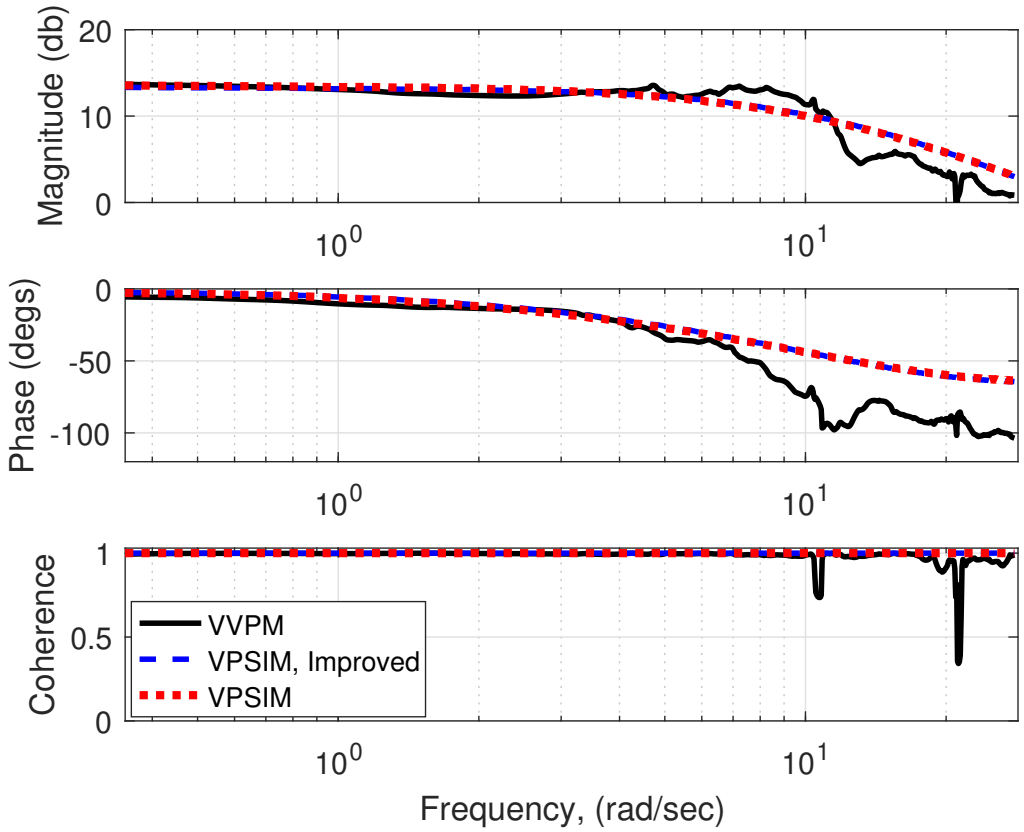

Figure 6.12: Frequency response comparison between VPSIM, improved VPSIM, and VVPM for upper rotor uniform inflow component due to upper rotor thrust perturbation in hover, i.e., case 1 in Table 6.4

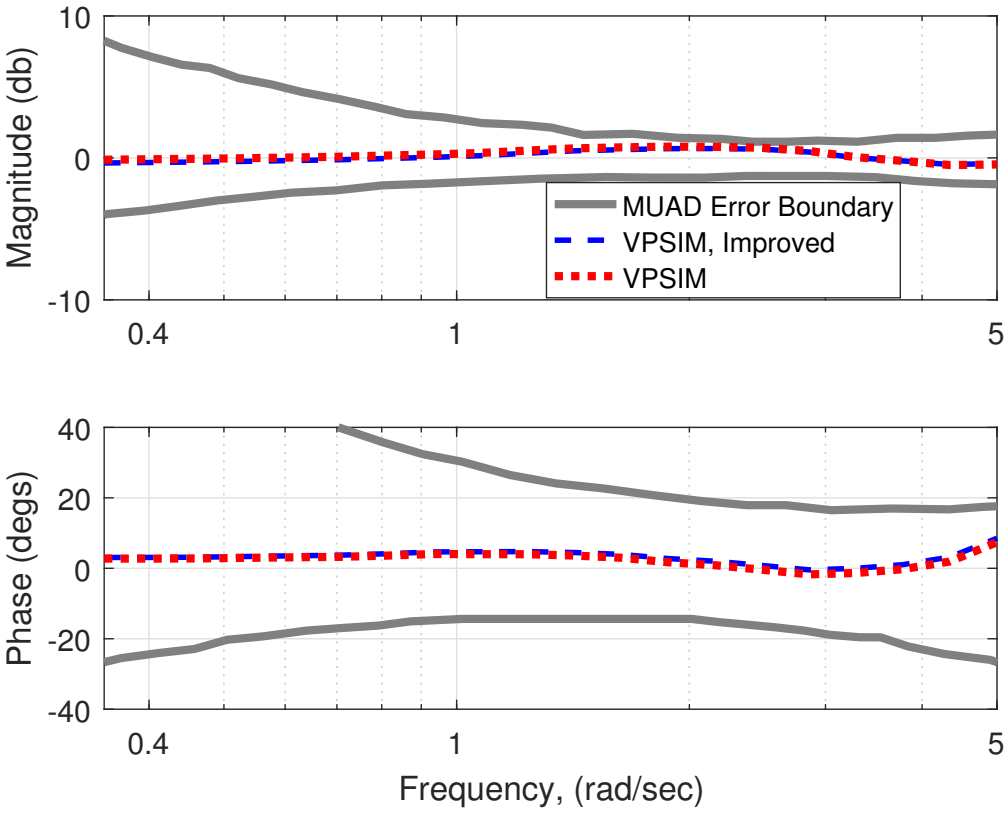

Figure 6.13: Frequency response differences (0.35∼5.0 rad/s) between VPSIM, improved VPSIM, and VVPM for case 1 in Table 6.4

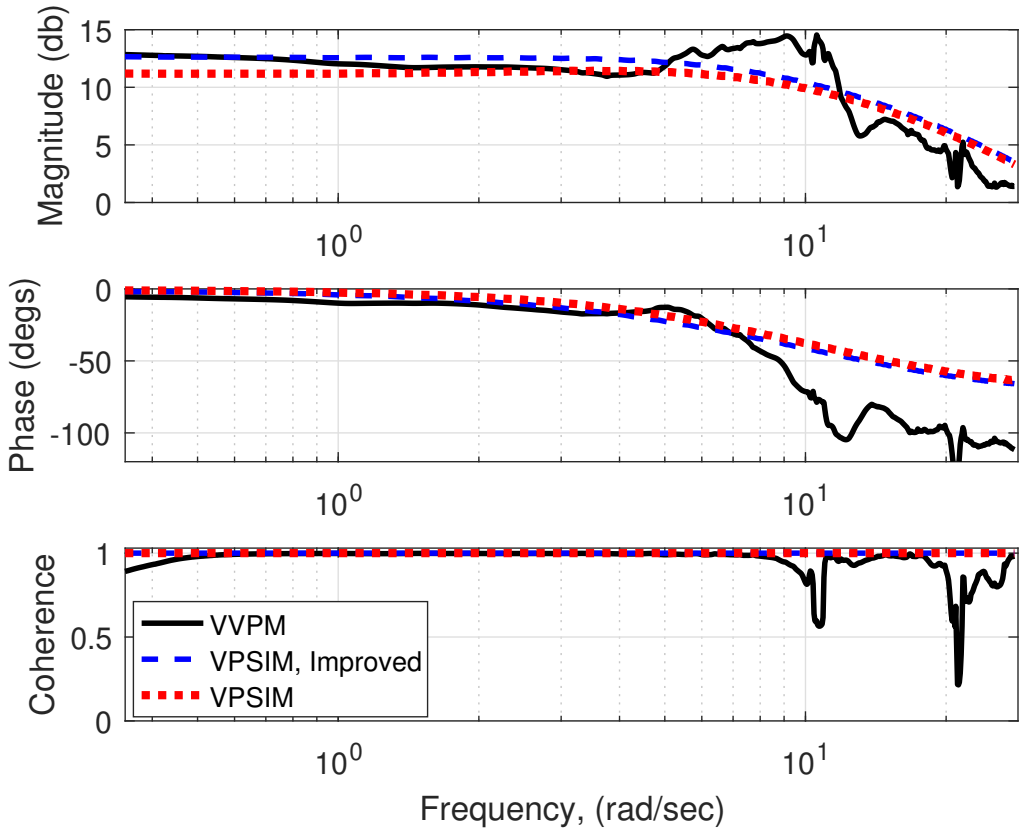

Figure 6.14: Frequency response comparison between VPSIM, improved VPSIM, and VVPM for lower rotor uniform inflow component due to lower rotor thrust perturbation in hover, i.e., case 10 in Table 6.4

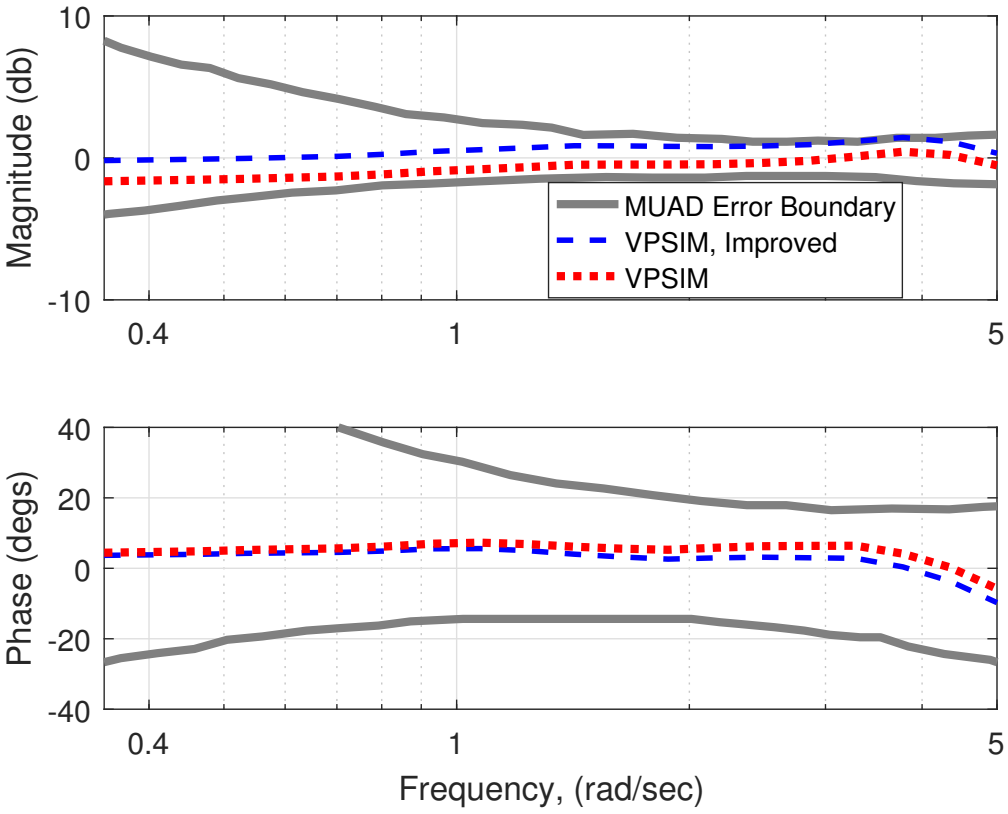

Figure 6.15: Frequency response differences (0.35∼5.0 rad/s) between VPSIM, improved VPSIM, and VVPM for case 10 in Table 6.4

Next, frequency response differences between the VPSIM, improved VPSIM, and VVPM for Harrington coaxial rotor configuration at the advance ratio of 0.07 are provided in terms of cost functions in Table 6.5. Here, inflow responses with small magnitudes and low coherences are not taken into consideration. Reference [30] performed extensive frequency response analyses using PPSIM and VVPM for Harrington coaxial rotor configuration and determined the inflow frequency response cases suitable for the analyses. A similar approach is followed, and cases with a good coherence and relatively larger magnitude response are analyzed. Although both original VPSIM and improved VPSIM usually have good agreements with the VVPM, cost functions of the improved VPSIM are lower than the cost functions of the original VPSIM except for case 6 in Table 6.5. While the only large difference between the improved VPSIM and VVPM is seen in the upper rotor fore-to-aft inflow response due to the lower rotor thrust coefficient perturbation (case 8 in Table 6.5), original VPSIM has broad disagreement at fore-to-aft inflow responses of both rotors due to the lower rotor thrust coefficient perturbation (case 8 & 10 in Table 6.5). It is challenging for rigid wake models to capture fore-to-aft inflow responses at this advance ratio since the wake is highly nonlinear and wake distortion effects alter the overall wake geometry.

Figure 6.16 presents a frequency response comparison between the VPSIM, improved VPSIM, and VVPM for the upper rotor side-to-side inflow component due to the upper rotor roll moment perturbation at the advance ratio of 0.07 (case 7 in Table 6.5). Improved VPSIM has a good correlation with VVPM for the magnitude response compared to the VPSIM. In contrast, the VPSIM phase response is slightly better than the improved VPSIM phase response after the frequency of 2.0 rad/s. MUAD envelope plot (Fig. 6.17) shows that improved VPSIM predictions are inside the MUAD envelopes for both magnitude and phase responses. On the other hand, the original VPSIM inflow magnitude response crosses the upper magnitude response envelope after the frequency of 1.0 rad/s.

Frequency response of the upper rotor uniform inflow component due to the lower rotor thrust perturbation (case 9 in Table 6.5) is shown in Fig. 6.18. Frequency responses of

both original VPSIM and improved VPSIM are virtually identical in this case. Figure 6.19 presents the MUAD plot of this case. Both original VPSIM and improved VPSIM phase responses are inside the MUAD phase envelope. On the other hand, their magnitude responses deviate from the VVPM and slightly cross the MUAD magnitude envelope after the frequency of 4 rad/s.

Table 6.5: Frequency response differences between VPSIM, improved VPSIM, and VVPM for Harrington coaxial rotor configuration at advance ratio of 0.07

				Cost function[a] (0.35∼5.0 rad/s)		
Case No.	Input[b]	Output	Model	Magnitude	Phase	Total
1	$(\Delta C_T)_U$	$(\Delta\lambda_0)_U$	VPSIM, Improved	7.0	5.2	12.2
			VPSIM	4.9	8.5	13.4
2		$(\Delta\lambda_{1c})_U$	VPSIM, Improved	358.1	38.8	396.8
			VPSIM	520.7	14.1	534.7
3		$(\Delta\lambda_0)_L$	VPSIM, Improved	46.3	4.2	50.5
			VPSIM	94.4	3.1	97.4
4		$(\Delta\lambda_{1c})_L$	VPSIM, Improved	230.9	22.4	253.3
			VPSIM	243.5	15.8	259.3
5	$(\Delta C_L)_U$	$(\Delta\lambda_{1s})_U$	VPSIM, Improved	2.4	10.1	12.5
			VPSIM	171.2	0.7	171.9
6		$(\Delta\lambda_{1s})_L$	VPSIM, Improved	213.7	308.5	522.2
			VPSIM	22.6	249.7	272.4
7	$(\Delta C_T)_L$	$(\Delta\lambda_0)_U$	VPSIM, Improved	16.3	5.5	21.8
			VPSIM	16.1	5.2	21.3
8		$(\Delta\lambda_{1c})_U$	VPSIM, Improved	2455.1	49.4	2504.5
			VPSIM	3928.4	68.5	3996.9
9		$(\Delta\lambda_0)_L$	VPSIM, Improved	12.1	10.0	22.0
			VPSIM	15.4	12.7	28.1
10		$(\Delta\lambda_{1c})_L$	VPSIM, Improved	125.7	49.9	175.6
			VPSIM	3267.1	65.1	3332.2
11	$(\Delta C_L)_L$	$(\Delta\lambda_{1s})_U$	VPSIM, Improved	0.9	26.2	27.1
			VPSIM	107.4	3.4	110.8
12		$(\Delta\lambda_{1s})_L$	VPSIM, Improved	1.4	18.7	20.0
			VPSIM	132.1	1.5	133.5

[a]Computed using Eq. (3.5)
[b]Bracket subscripts *U* and *L* correspond to upper (rotor 1) and lower (rotor 2) rotors, respectively

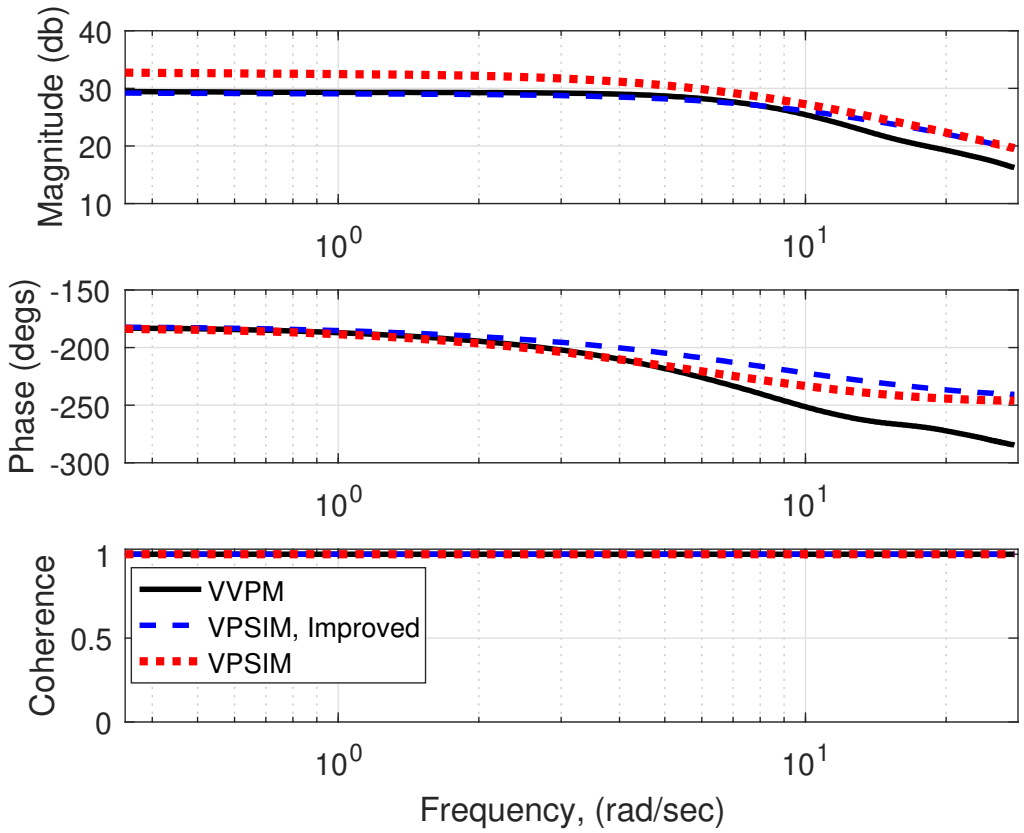

Figure 6.16: Frequency response comparison between VPSIM, improved VPSIM, and VVPM for upper rotor side-to-side inflow component due to upper rotor roll moment perturbation at the advance ratio of 0.07, i.e., case 7 in Table 6.5

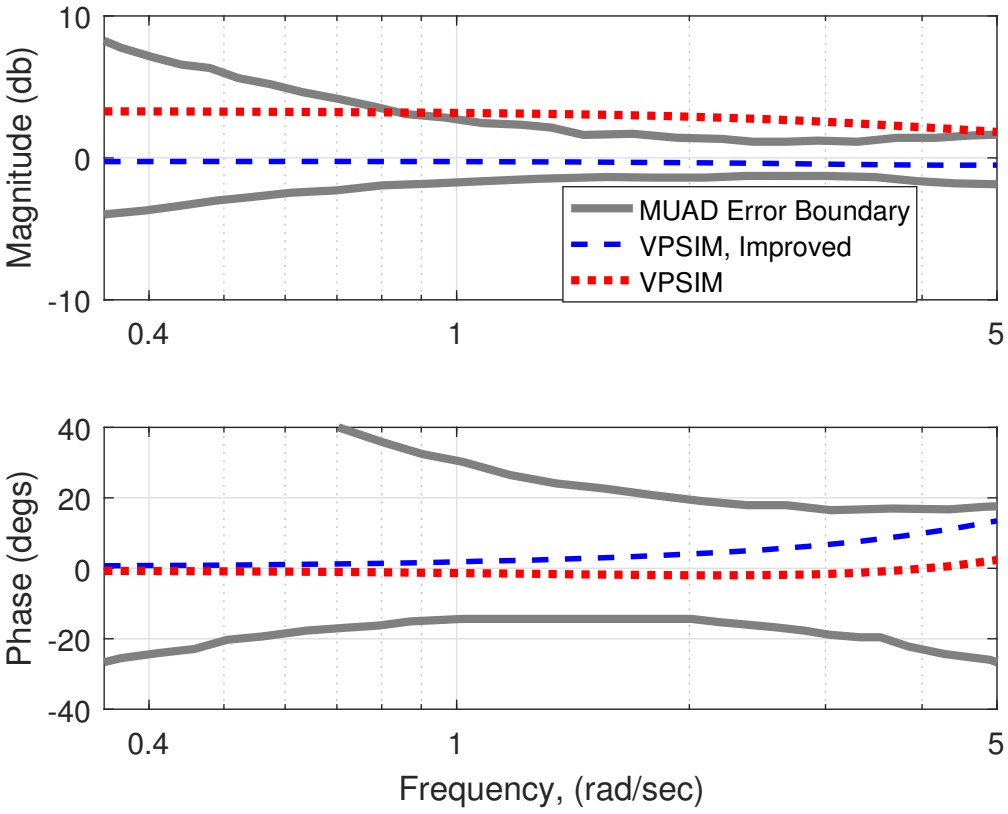

Figure 6.17: Frequency response differences (0.35∼5.0 rad/s) between VPSIM, improved VPSIM, and VVPM for case 7 in Table 6.5

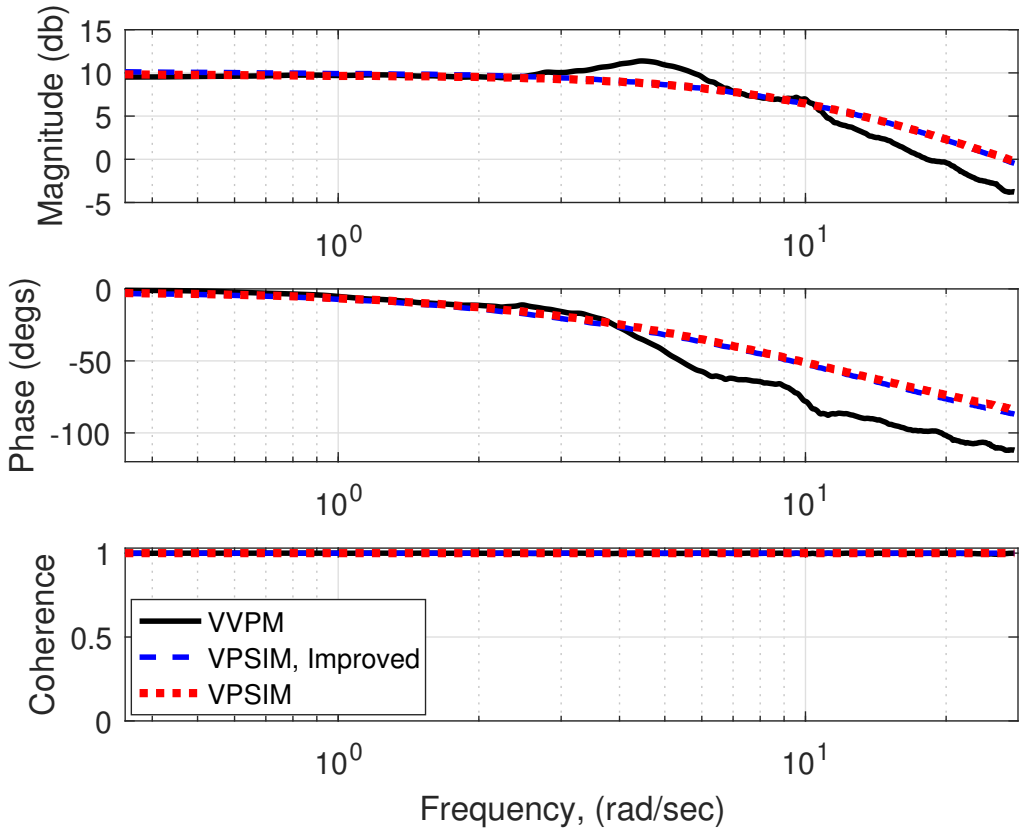

Figure 6.18: Frequency response comparison between VPSIM, improved VPSIM, and VVPM for upper rotor uniform inflow component due to lower rotor thrust perturbation at the advance ratio of 0.07, i.e., case 9 in Table 6.5

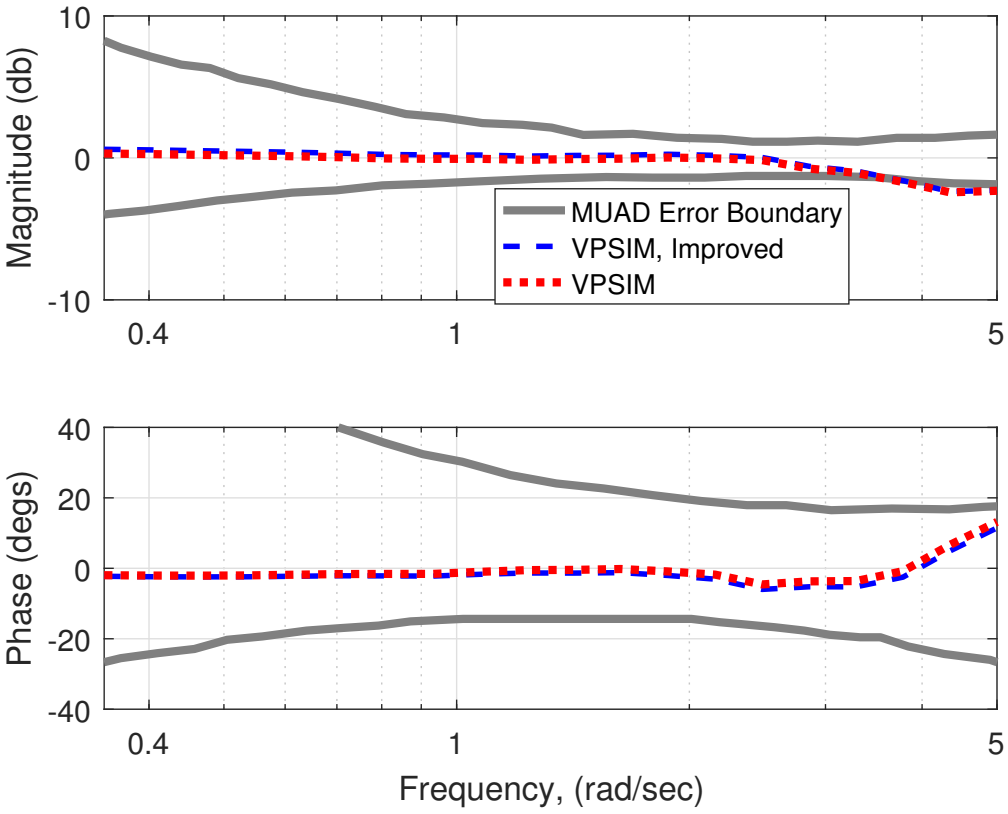

Figure 6.19: Frequency response differences (0.35∼5.0 rad/s) between VPSIM, improved VPSIM, and VVPM for case 9 in Table 6.5

Next, frequency response comparison between the VPSIM, improved VPSIM, and VVPM for the upper rotor side-to-side inflow component due to the lower rotor roll moment perturbation at the advance ratio of 0.07 (case 15 in Table 6.5) is shown in Fig. 6.20. Improved VPSIM inflow magnitude response has much better agreement with the VVPM than the VPSIM up to the frequency of 8.0 rad/s. Wake roll-up effects, which alter the side-to-side inflow components, are successfully added to improved VPSIM. Maximum Unnoticeable Added Dynamics (MUAD) envelope plot in Fig. 6.21 also confirms the good correlation between the improved VPSIM and VVPM magnitude responses.

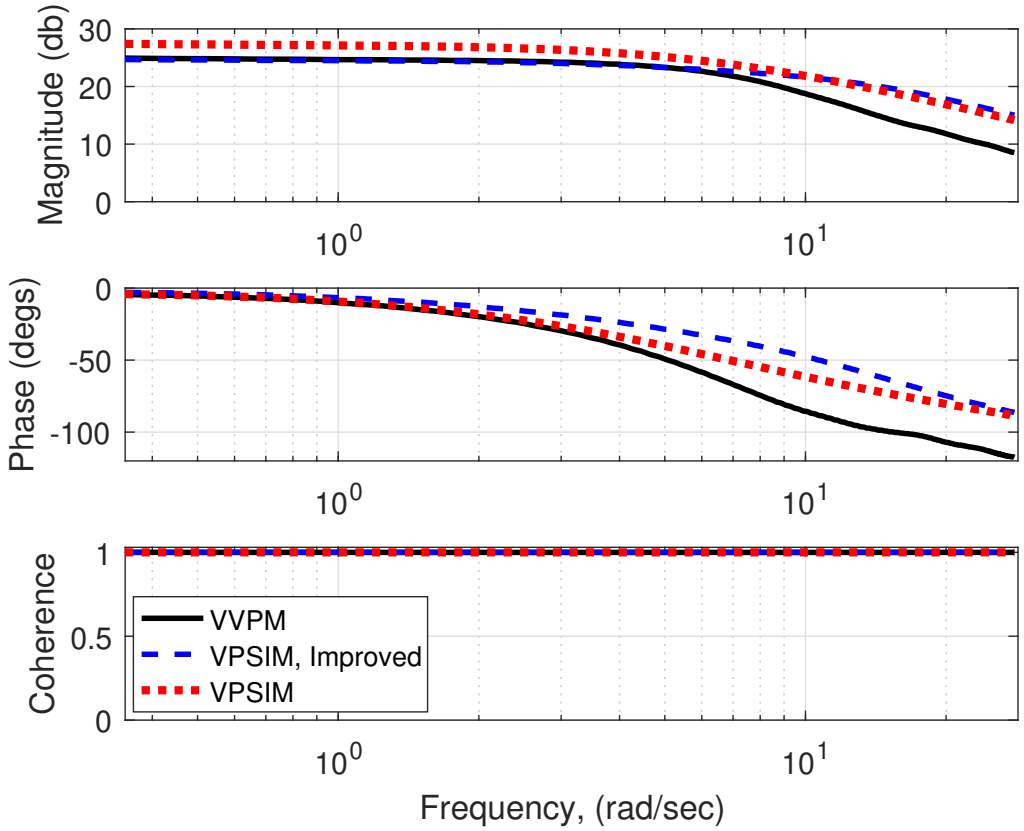

Figure 6.20: Frequency response comparison between VPSIM, improved VPSIM, and VVPM for upper rotor side-to-side inflow component due to lower rotor roll moment perturbation at the advance ratio of 0.07, i.e., case 15 in Table 6.5

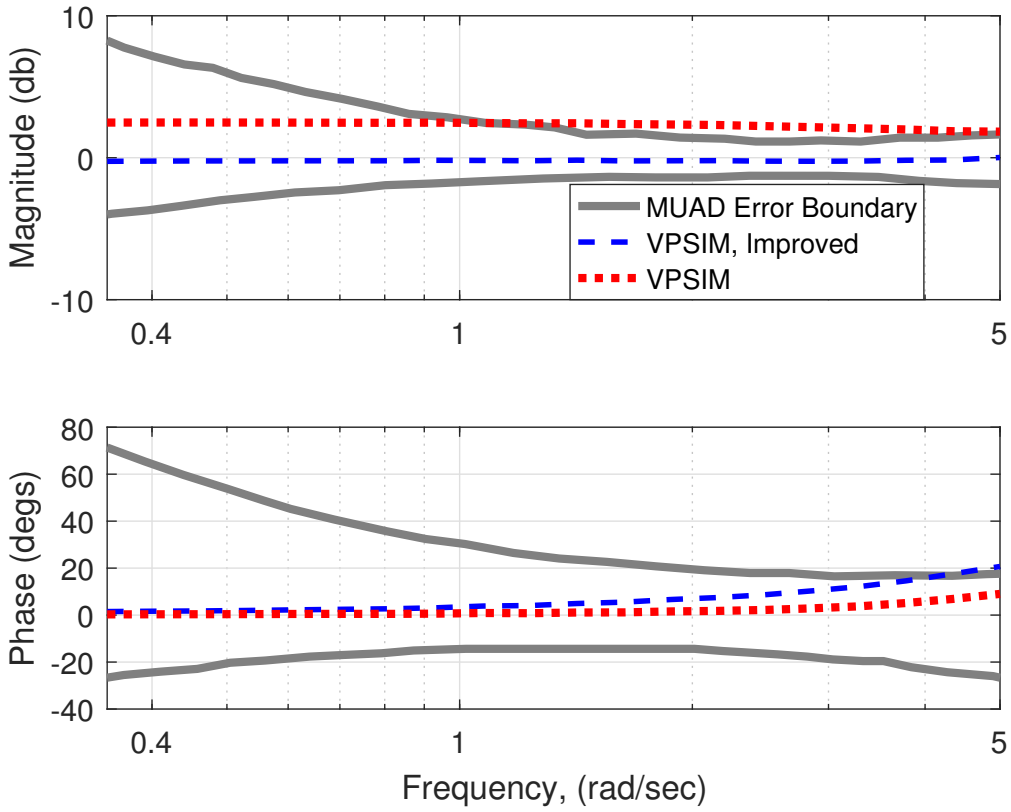

Figure 6.21: Frequency response differences (0.35∼5.0 rad/s) between VPSIM, improved VPSIM, and VVPM for case 15 in Table 6.5

Wake roll-up, wake distortion, wake contraction, wake diffusion, and swirl velocity effects are introduced to the VPSIM through a system identification methodology. These corrections are identified at zero frequency (steady-state perturbation cases). Although improved VPSIM significantly enhances the frequency response correlations with the VVPM for most cases, these corrections might introduce some unintended phase errors after the low frequency region. These deteriorations in the phase correlations are also reported in Ref. [30]. Compared to the improvements achieved in the magnitude part of the frequency responses, these slight deteriorations seen in the phase responses are found to be negligible.

6.4 Reduction of the Number of Correction Terms in the Improved VPSIM

In this chapter, correction terms are identified for the equal thrust sharing ratio case to include real flow effects in the VPSIM for a coaxial rotor configuration. The flow field of each rotor is represented by three odd velocity potential states in VPSIM. In addition, three costates are used to consider inflow interference at the lower rotor due to the upper rotor. During the system identification process, differences between the VPSIM's and VVPM's perturbed uniform ($\Delta\lambda_0$), longitudinal ($\Delta\lambda_{1c}$), lateral ($\Delta\lambda_{1s}$) inflow components are minimized for the step inputs individually applied to six loading modes (see Eq.(6.8)). Each rotor has uniform (C_T), longitudinal (C_M), and lateral (C_L) loading modes. Since perturbation of each loading mode results in changes in six inflow components (three per rotor), 36 outputs are created in total for six loading perturbations. Using the approach explained in chapter 6.1, it is shown that the addition of correction terms significantly improves the coaxial rotor VPSIM inflow predictions compared to the original VPSIM.

In order to have the best match between the VPSIM's and VVPM's perturbed uniform, longitudinal, and lateral inflow predictions, 36 correction terms must be identified since predictions involve 36 total outputs. Utilizing the least-squares-fit method, it is possible to use fewer terms during the identification. In fact, in chapter 6.1, 24 correction terms are identified instead of 36 to have a more straightforward implementation and avoid over-parametrization. The identified correction terms in Table 6.1 show that some of the terms are small enough to be neglected. Besides, removal of the small correction terms is necessary to pinpoint important missing real flow effects in the VPSIM.

Instead of directly removing the small terms in Table 6.1, derivatives of the cost function (J_q) with respect to each correction term are calculated and tabulated in Table 6.6. Terms with smaller gradients are eliminated for the next identification process and marked with the † symbol. Comparisons of Tables 6.1 and 6.6 show that if the magnitude of an identified correction term is small, the gradient of the J_q corresponding to that term is also small.

Table 6.6: Gradients of the cost function for the equal thrust sharing ratio case

Gradient	$\mu = 0.00$			$\mu = 0.07$			$\mu = 0.12$		
$\frac{\partial J_q}{\partial \Delta \tilde{L}_1}$	-1.2†[a]	0.2†	0.1†	-4.2	-8.9	3.6†	-29.1	-10.2	2.5†
	-0.1†	-33.9	5.8	-4.7†	7.4	0.0†	-5.8†	-0.3	0.7†
	-0.1†	-13.2	-32.9	-7.9	0.5†	-23.3	-10.5	6.5†	5.1
$\frac{\partial J_q}{\partial \mathrm{G}}$	0.2†	6.6	7.3	1.8†	-1.5	-10.2	-4.7†	-9.0	-6.1
$\frac{\partial J_q}{\partial \Delta \tilde{L}_2}$	-0.8†	-0.1†	-0.1†	0.5†	-2.4	-4.9†	3.4†	-12.8	-4.7†
	-0.1†	0.0	11.5	-12.8	15.6	4.6†	-4.9	5.7	2.1†
	0.1†	-14.0	0.6	-16.7	-22.5	-6.0	2.5	-11.6	7.8
$\frac{\partial J_q}{\partial \mathrm{H}}$	-0.2†	-2.0†	-3.5†	0.6†	1.5†	-0.8†	1.8†	-0.6†	-0.7†

[a]Terms eliminated for the next identification process

After removing the correction terms with small gradients, the remaining terms are re-identified using the same process explained in chapter 6.1. The number of correction terms is reduced from 24 to 10 for the hover case, whereas the number of correction terms is reduced to 13 for the forward flight cases, as shown in Table 6.7. The identified reduced-order terms in Table 6.7 are almost the same as the terms that are identified in Table 6.1. This similarity shows that every correction term affects a specific inflow mode as expected from the state-space modeling structure. With this information, every inflow prediction mismatch between the VPSIM and VVPM can be isolated to pinpoint missing real flow effects in the VPSIM, causing the difference. For example, swirl coupling correction terms for the self-induced inflow ($\Delta \tilde{L}_1$ and $\Delta \tilde{L}_2$) are retained for the hover case. As explained earlier, VPSIM is based on the potential flow theory and does not account for the swirl coupling. The lower rotor swirl coupling terms, $\Delta \tilde{L}_2(2,3)$ and $\Delta \tilde{L}_2(3,2)$, are significantly larger than the upper rotor swirl coupling terms since the lower rotor directly operates within the downwash of the upper rotor in hover. The existence of this large coupling is also reported in Ref. [32]. Correction terms (or gains) for the interference inflow predic-

tions on the upper rotor due to the lower rotor (H) are entirely neglected for all flight cases since $\partial J_q/\partial$H terms are considerably smaller than the other terms. Neglecting these terms means that VPSIM is able to capture interference effects due to the lower rotor reasonably well. On the other hand, interference inflow predictions on the lower rotor due to the upper rotor require corrections (G) for both cosine and sine terms for all flight conditions. It is worth emphasizing that wake geometry is significantly altered by the wake distortion, contraction/expansion, and wake interaction effects. This geometry change further violates another assumption that VPSIM use: rigid cylindrical wake geometry. The first harmonic cosine and sine inflow components establish gradients on the rotor disk and alter the overall wake geometry. Depending on the strength of these terms, the path followed by the wake can be notably changed. This change in the wake geometry reshapes the area of interference and modifies the corresponding inflow interference predictions. For the forward flight self-induced corrections ($\Delta\tilde{L}_1$ and $\Delta\tilde{L}_2$), more terms are required than the hover case since rotors operate within the more complex flow field. While rotors are mainly subject to wake contraction/expansion and diffusion effects in hover, additional wake interaction effects such as wake roll-up and wake distortion affect the rotors, especially in low speed flight. For instance, terms related to the lateral inflow component due to the lateral loading perturbation ($\Delta\tilde{L}_1(3,3)$ and $\Delta\tilde{L}_2(3,3)$) are larger in the forward flight case due to the wake roll-up effect. Moreover, uniform-to-sine inflow coupling terms at both rotors ($\Delta\tilde{L}_1(3,1)$ and $\Delta\tilde{L}_2(3,1)$) are required to capture the effect of thrust on the lateral inflow component, which was neglected in the hover case. In forward flight, while sine terms lose their effectiveness to influence cosine terms of both rotors ($\Delta\tilde{L}_1(2,3)$ and $\Delta\tilde{L}_2(2,3)$), the cosine term of the lower rotor still alters the sine term of the lower rotor ($\Delta\tilde{L}_2(3,2)$). The uniform inflow components of both rotors also require correction terms from the longitudinal inflow ($\Delta\tilde{L}_1(1,2)$ and $\Delta\tilde{L}_2(1,2)$) to account for some of the wake distortion effects in forward flight. Lastly, uniform-to-cosine coupling term, $\Delta\tilde{L}_2(2,1)$, is added to the lower rotor to account for the wake distortion effect.

Table 6.7: Identified reduced-order correction terms for the equal thrust sharing ratio case

Correction	$\mu = 0.00$			$\mu = 0.07$			$\mu = 0.12$		
	†	†[a]	†	-0.14	0.24	†	-0.10	0.31	†
$\Delta\tilde{L}_1$	†	-0.22	0.11	†	-0.19	†	†	-0.13	†
	†	-0.21	-0.22	0.18	†	-0.31	0.22	†	-0.35
G	†	0.61	0.72	†	1.01	0.93	†	0.63	1.22
	†	†	†	†	0.07	†	†	0.27	†
$\Delta\tilde{L}_2$	†	-0.02	-1.35	0.24	-0.30	†	0.17	-0.18	†
	†	1.64	-0.08	0.32	0.43	0.11	-0.07	0.35	-0.29
H	†	†	†	†	†	†	†	†	†

[a]Terms removed from the identification process compared to Table 6.1

Next, improved VPSIM with the reduced-order correction terms (*VPSIM, Reduced-Order Improved* or *VPSIM, ROI*) is compared against the original VPSIM and improved VPSIM (with 24 terms). Table 6.8 shows the cost functions (J_q) of the models for the equal thrust sharing ratio case. The reduced-order improved VPSIM has a significantly lower cost function than the original VPSIM and close to improved VPSIM, especially for the hover case. In hover, the cost function difference between the reduced-order improved VPSIM and improved VPSIM is only 3.5, although the former version of the VPSIM has 10 correction terms rather than 24. This difference increases to 13.5 and 11.0 at advance ratios of 0.07 and 0.12, respectively. In forward flight, more terms are needed to match with the improved VPSIM as additional interference effects arise and inflow loses its symmetry.

Table 6.8: Comparison of J_q for original and improved VPSIM models at selected flight conditions for $\frac{C_{T,1}}{C_{T,2}} = 1.0$

μ	VPSIM	VPSIM, Reduced Order Improved	VPSIM, Improved
Hover	88.3	12.1	8.6
0.07	50.5	21.1	7.6
0.12	41.2	17.1	6.1

Detailed inflow response comparisons between the VPSIM, reduced-order improved VPSIM, improved VPSIM, and VVPM are provided in Figs. 6.22, 6.23 for the hover case, and 6.24, 6.25 for the forward flight case. Aerodynamic phenomena seen in these figures are already explained in chapter 6.1 (see Figs. 6.1, 6.2, 6.3, 6.4); thus, the focus is shifted to the reduced-order improved VPSIM and its performance compared to the improved VPSIM and original VPSIM. The reduced-order improved VPSIM is generally close to the improved VPSIM. In the worst-case scenario, its predictions are equal to the original VPSIM. The model with reduced-order correction terms can capture most of the interference effects, including the large swirl couplings seen in the hover case. The accuracy of the reduced-order improved VPSIM can be easily improved by adding additional terms. For example, the lower rotor uniform inflow prediction due to the upper rotor uniform loading perturbation in hover (Fig. 6.22(a)) of the reduced-order improved model can be further improved by adding a single G term corresponding to the uniform inflow interference prediction.

In this chapter, a new system identification methodology is developed to incorporate real flow effects into the VPSIM. With the inclusion of the real flow effects via the identified correction terms ($\Delta\tilde{L}_1$, G, $\Delta\tilde{L}_2$, and H), changes in the VPSIM steady-state inflow components become much closer to the changes in the VVPM steady-state inflow components. These identified correction terms not only improve the steady-state inflow components perturbations but also usually improve the unsteady inflow predictions of the VPSIM. The number of correction terms is roughly reduced to half to highlight the essential interference effects. While inflow predictions are mainly affected by swirl velocity and wake contraction/expansion effects in hover, wake distortion and wake roll-up effects are also important in forward flight on top of the interference effects seen in the hover. The improved VPSIM with the reduced-order correction terms can capture these strong interference effects without losing too much accuracy. One may always include/remove more terms to reach the desired accuracy to capture/neglect specific effects since one correction term only affects

the specific inflow component.

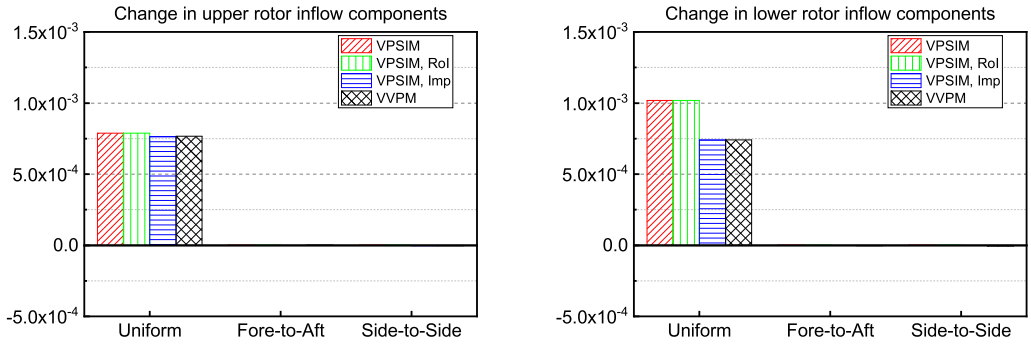

(a) Perturbation of upper rotor thrust coefficient

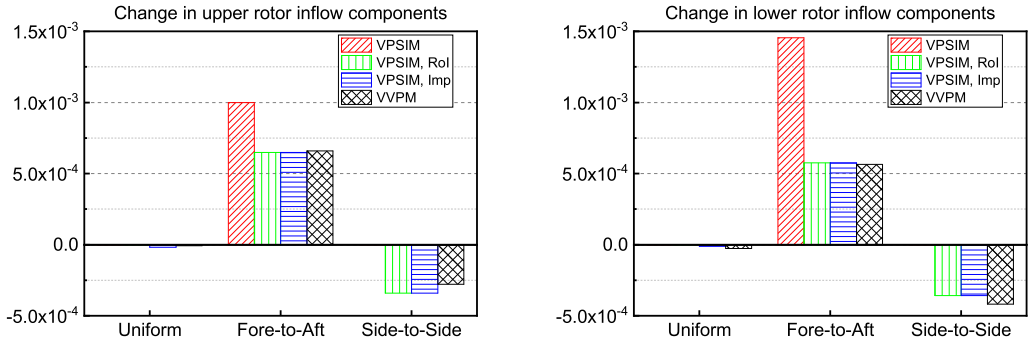

(b) Perturbation of upper rotor aerodynamic pitch moment coefficient

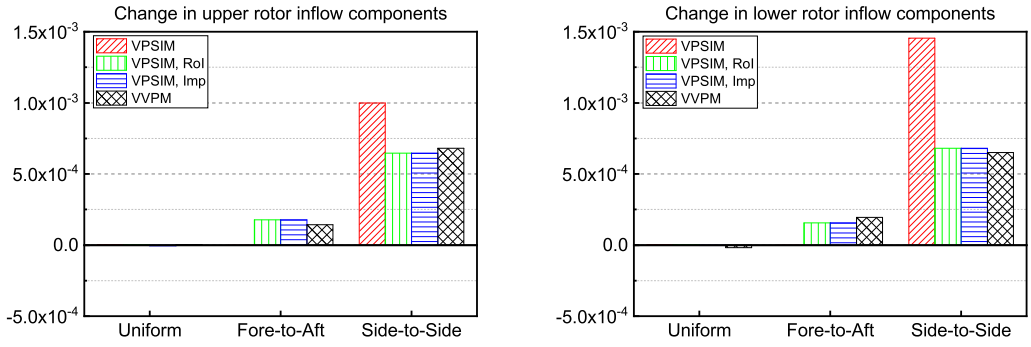

(c) Perturbation of upper rotor aerodynamic roll moment coefficient

Figure 6.22: Changes in steady-state inflow components due to upper rotor loading perturbation in hover with reduced-order improved VPSIM

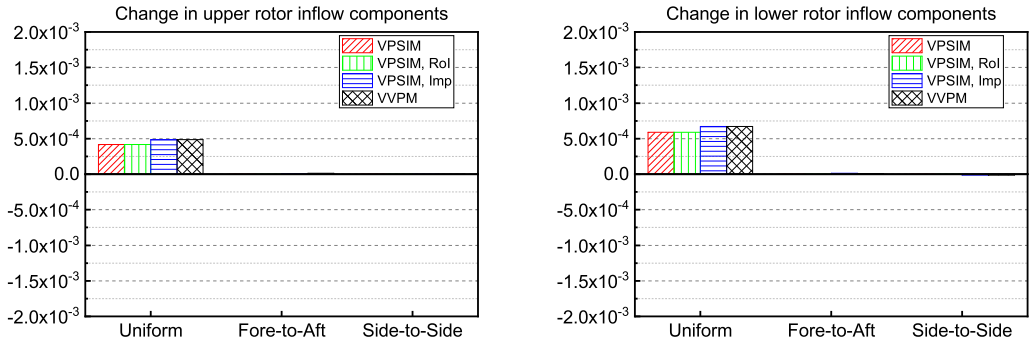

(a) Perturbation of lower rotor thrust coefficient

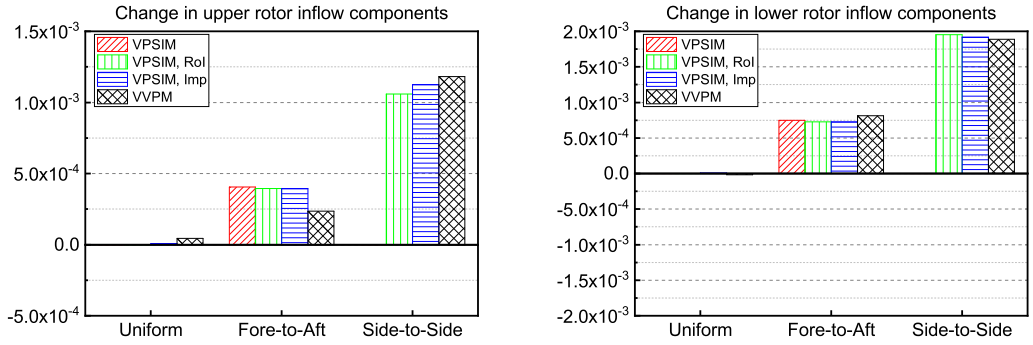

(b) Perturbation of lower rotor aerodynamic pitch moment coefficient

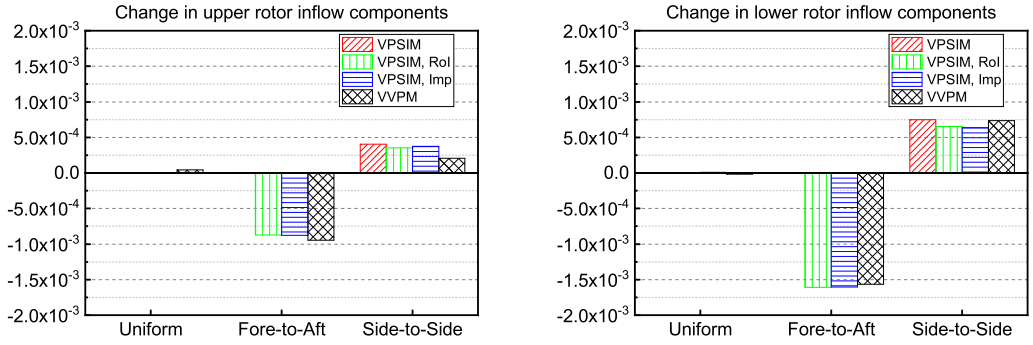

(c) Perturbation of lower rotor aerodynamic roll moment coefficient

Figure 6.23: Changes in steady-state inflow components due to lower rotor loading perturbation in hover with reduced-order improved VPSIM

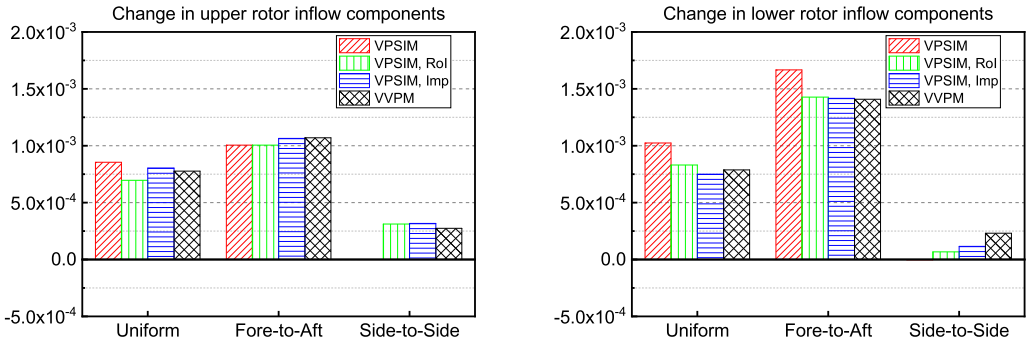

(a) Perturbation of upper rotor thrust coefficient

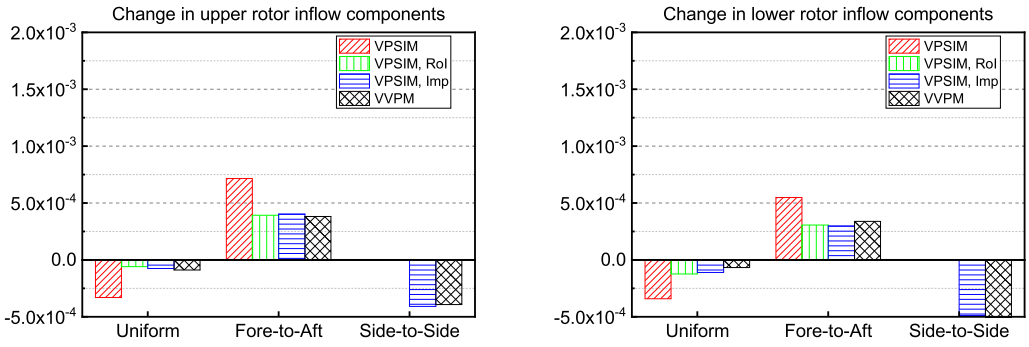

(b) Perturbation of upper rotor aerodynamic pitch moment coefficient

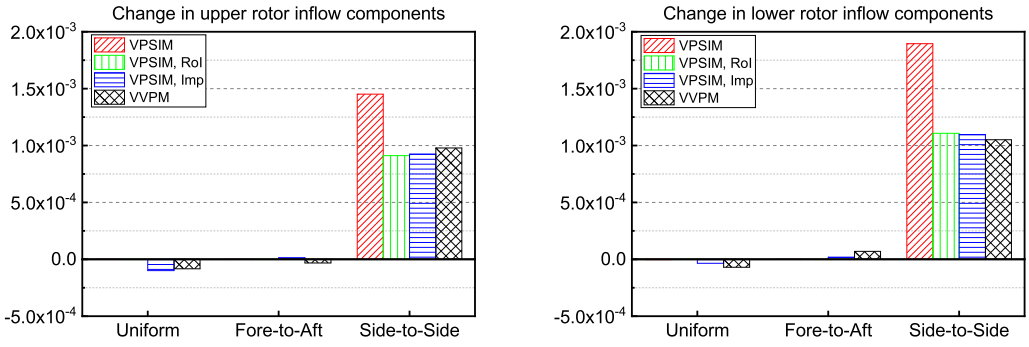

(c) Perturbation of upper rotor aerodynamic roll moment coefficient

Figure 6.24: Changes in steady-state inflow components due to upper rotor loading perturbation at advance ratio of 0.07 with reduced-order improved VPSIM

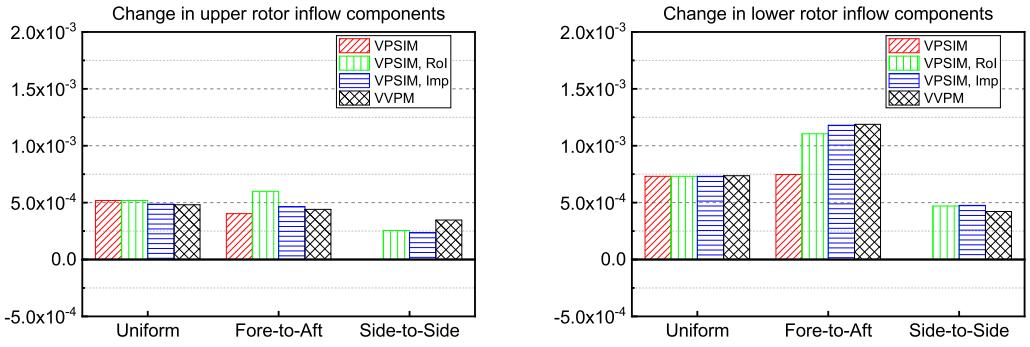

(a) Perturbation of lower rotor thrust coefficient

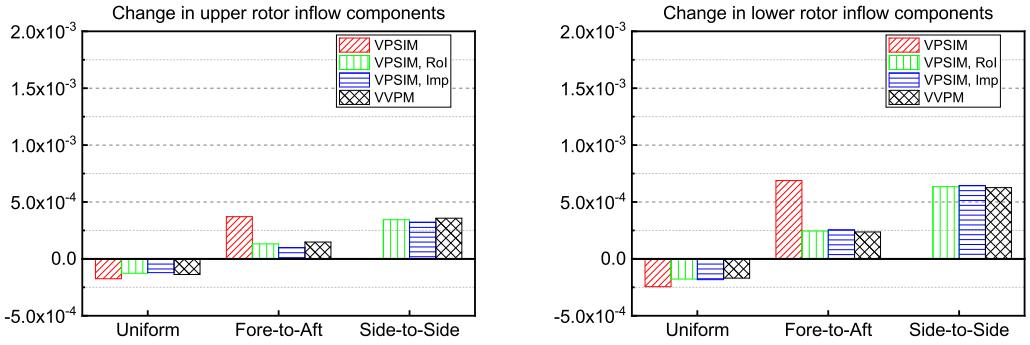

(b) Perturbation of lower rotor aerodynamic pitch moment coefficient

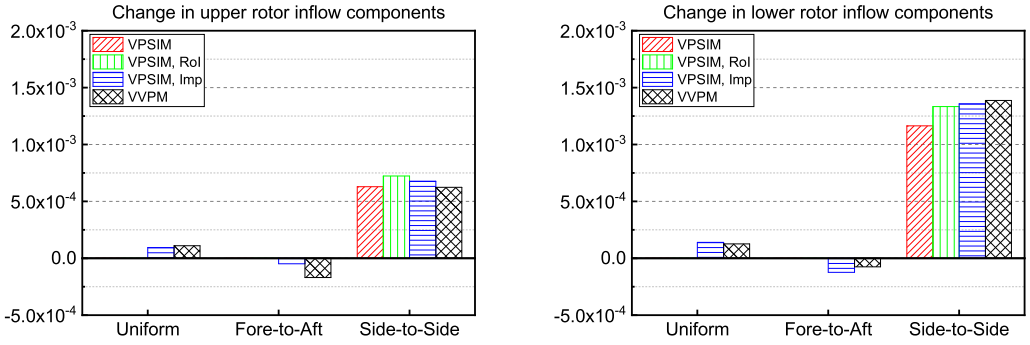

(c) Perturbation of lower rotor aerodynamic roll moment coefficient

Figure 6.25: Changes in steady-state inflow components due to lower rotor loading perturbation at advance ratio of 0.07 with reduced-order improved VPSIM

CHAPTER 7
QUASI-STEADY APPROXIMATIONS TO COSTATE EQUATION: ELIMINATION OF THE BACKWARD TIME INTEGRATION

Modeling and simulation of compound helicopters and electric vertical take-off and landing vehicles (eVTOLs) require not only accurate inflow modeling of the rotors but also modeling of the inflow interference on any aerodynamic surface. Therefore, off-rotor inflow interference predictions have become much more critical than in the past as newer designs are subject to interferences such as rotor-on-rotor, rotor-on-wing, rotor-on-propeller, etc. Using the Peters-He model, it is possible to obtain steady-state off-rotor inflow using integral of the distributed pressure functions of the flow field, albeit at the expense of computational complexity [71]. On the other hand, velocity potential finite state dynamic inflow model can capture the time-varying inflow anywhere in the flow field almost without an additional step after obtaining the velocity potential states and costates [57, 59]. Nevertheless, the velocity potential based inflow model has not become common for flight simulation as the solution of the costate equation requires integration backward in time, making it incompatible for real-time simulations. Thus, approximations to the costate equation are explored to remove the need for its integration backward in time. Approximations can simplify the process of obtaining flow velocities below the rotor disk, especially for real-time simulations. As such, the fidelity of the approximated inflow models is assessed using example simulation cases.

7.1 Quasi-Steady Approximations

Velocity potential finite state dynamic inflow model captures inflow dynamics below the rotor disk compared to an analytical solution [58, 59]. This model is computationally more expensive than the pressure potential based finite state dynamic inflow model due to back-

ward time integration. Besides, backward time integration increases the overall simulation complexity. On the other hand, once backward time integration is carried out, calculation of the inflow anywhere in the flow field becomes straightforward. In the proposed approach, the adjoint equation (Eq. (2.11)) is approximated using its quasi-steady solution. Then, approximate relations are established between the velocity potential states and costates.

It is evident from Eqs. (2.6) and (2.11) that both equations have the same matrices. Nevertheless, there are two differences: (1) pressure coefficients of Eq. (2.11) are modified $\{\tau^*\} = [T]\{\tau\}$ where $[T] = diag((-1)^{j+1})$, (2) the derivative term of Eq. (2.11) has a minus sign in front of it. Since both equations have the same matrices, an approximate relation between the velocity potential states and costates is made using a quasi-steady representation of Eqs. (2.6) and (2.11). After dropping the derivative term, Eq. (2.11) can be solved for costates, $\{\Delta\}$, as follows:

$$\{\Delta\} = [\tilde{M}]^{-1}[\tilde{L}][\tilde{V}_m]^{-1}[T]\{\tau\} \tag{7.1}$$

In Eq. (7.1), $\{\tau\}$ is replaced by the following relation:

$$\{\tau\} = [\tilde{V}_m][\tilde{L}]^{-1}[\tilde{M}]\{a\} \tag{7.2}$$

Although Eq. (7.2) is not strictly valid for the transient part of the solution, the idea is to use the dynamics of velocity potential states in order to obtain the costates. Hence, Eq. (7.1) becomes:

$$\{\Delta\} = [\tilde{M}]^{-1}[\tilde{L}][\tilde{V}_m]^{-1}[T][\tilde{V}_m][\tilde{L}]^{-1}[\tilde{M}]\{a\} \tag{7.3}$$

The relation between $\{a\}$ and $\{\Delta\}$ is exact in steady-state. Thus, the new approach

converges to the Costate model (backward time marching solution of Eq. (2.11)) in steady flight condition. The value of $\{\Delta\}$ is approximated using the value of $\{a\}$ in Eq. (7.3) and subsequently used in Eqs. (2.12) and (2.13).

7.1.1 Costates at the current time and past time

Costates at the current time ($\{\Delta\}_t$) are obtained by inserting velocity potential states at the current time ($\{a\}_t$) into Eq. (7.3).

$$\{\Delta\}_t = [\tilde{M}]^{-1}[\tilde{L}][\tilde{V}_m]^{-1}[T][\tilde{V}_m][\tilde{L}]^{-1}[\tilde{M}]\{a\}_t \tag{7.4}$$

Equation (7.4) is also used for the calculation of initial condition of the adjoint equation (Eq. (2.11)) to start backward time integration. Use of Eq. (7.4) in place of Eq. (7.1) as an initial condition for backward time marching eliminates sudden jumps in velocity from impulsive load changes on the rotor. Note that Eq. (7.4) is used in the calculation of $\vec{v}_D^*$ for both the Costate model (exact model) and quasi-steady approximation (approximate model). For calculation of $\vec{v}_C^*$ in Eq. (2.13), costates at the past time ($\{\Delta\}_{t-t_0}$) are needed. The Costate model uses the backward time marching solution of Eq. (2.11) to obtain $\{\Delta\}_{t-t_0}$, whereas the quasi-steady approximation uses the following equation:

$$\{\Delta\}_{t-t_0} = [\tilde{M}]^{-1}[\tilde{L}][\tilde{V}_m]^{-1}[T][\tilde{V}_m][\tilde{L}]^{-1}[\tilde{M}]\{a\}_{t-t_0} \tag{7.5}$$

Because of the quasi-steady approximation, the difference between the Costate model and the proposed approximation is expected to grow at high frequencies. Therefore, an alternate approximation is also explored for reducing some of this expected difference at higher frequencies. In the second approximation, average values for the velocity potential states ($\{\bar{a}\}$) over the wake propagation time (t_0) are used in Eq. (7.5) instead of $\{a\}_{t-t_0}$.

$$\{\Delta\}_{t-t_0} = [\tilde{M}]^{-1}[\tilde{L}][\tilde{V}_m]^{-1}[T][\tilde{V}_m][\tilde{L}]^{-1}[\tilde{M}]\{\bar{a}\} \tag{7.6}$$

where

$$\{\bar{a}\} = \frac{1}{K}\sum_{t_i=t}^{t-t_0}\{a\}_{t_i} \tag{7.7}$$

The variable K represents the number of time steps from the current time (t) to the past time ($t - t_0$). From now on, the first approximation is referred to as Model–1 if Eq. (7.5) is used to obtain $\{\Delta\}_{t-t_0}$. Instead, if Eq. (7.6) is used, the second approximation is referred to as Model–2.

7.2 Fidelity of Inflow Model with Approximations

In order to assess the impact of the proposed approximations, off-rotor inflow dynamics below the rotor disk are examined by using an isolated UH-60 main rotor. Two spatial locations below the rotor disk that correspond to fuselage aerodynamic reference point and horizontal tail aerodynamic center are considered. Main rotor geometry and locations of fuselage aerodynamic reference point and horizontal tail aerodynamic center are taken from Ref. [72]. Figure 7.1 shows the setup used in simulations. Here, advance ratios from hover to 0.3 are considered. The thrust coefficient is also varied from 0.0066 to 0.0102 for identifying the effect of the main rotor loading on the proposed approximations. As both on-disk and off-disk inflow predictions are influenced by both even and odd numbered terms in the potential function expansion, it is essential to determine how many even and odd numbered terms one must use depending on the actual application. For real-time flight simulations, a trade-off between computational performance and accuracy should be performed to determine the needed number of odd and even velocity potential states in the velocity potential expansion. Reference [73] shows that predictions using velocity poten-

tial inflow model with six odd numbered velocity potential states match well with off-rotor inflow measurements. When even terms are included in the velocity potential expansion, both on-disk and off-disk inflow dynamics at high frequency range are affected. However, even terms degrade the stability of the velocity potential based inflow model. As such, the present study uses six odd numbered terms in the velocity potential expansion.

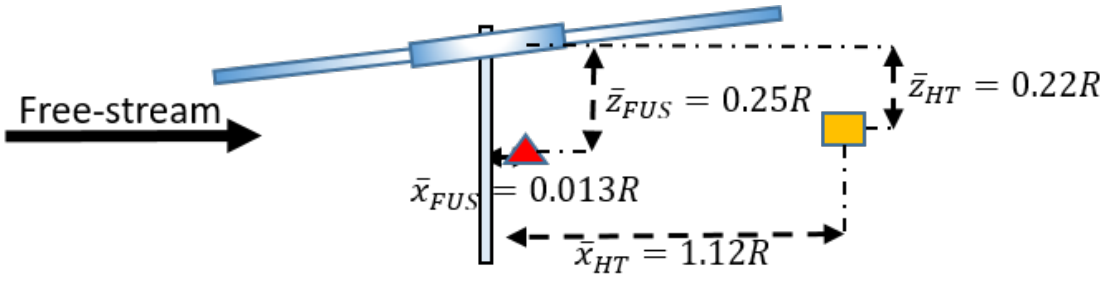

Figure 7.1: Isolated UH-60 main rotor (triangle: fuselage location, rectangle: horizontal tail location)

Off-rotor inflow dynamics is studied in the frequency domain by exciting rotor uniform (τ_1^{0c}) and fore-to-aft (τ_2^{1c}) pressure coefficients with a sinusoidal frequency sweep. A normalized chirp (sinusoidal frequency sweep) signal with a frequency range between 0.4 to 20 rad/s is used as an input profile (Fig. 7.2). Time histories of the chosen pressure coefficient perturbations and predictions of the resulting rotor inflow changes at the selected locations below the rotor are provided as inputs to CIFER® [63] for generating frequency response plots. The results are presented as Bode magnitude and phase plots, which can be used for model fidelity assessment in the frequency domain.

Figure 7.3 shows the comparison of inflow predictions at the fuselage aerodynamic reference point for hovering flight. When uniform loading is perturbed (Fig. 7.3(a)), phase predictions of quasi-steady approximations start to deviate after 3∼4 rad/s, while magnitude predictions of Model–1 and Model–2 have good agreement up to 7 rad/s compared to predictions acquired from the Costate model. For the fore-to-aft loading perturbation case (Fig. 7.3(b)), Model–2 has good agreement with the Costate model, whereas Model–1 shows some differences at high frequency region of the magnitude prediction.

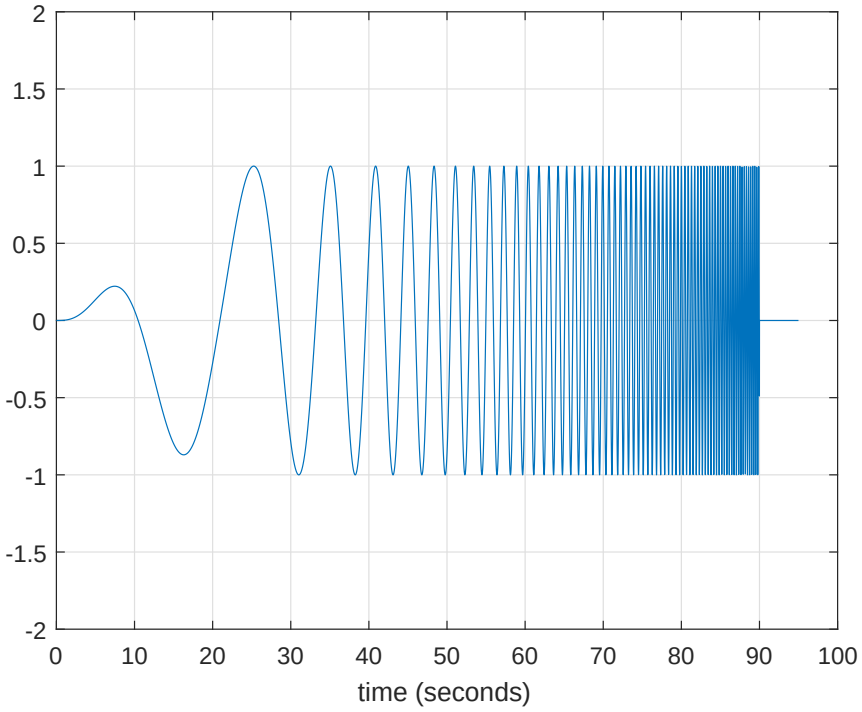

Figure 7.2: Normalized chirp signal used in the frequency sweep

Inflow predictions acquired from the Costate model and the approximate models at the horizontal tail aerodynamic center are compared in Fig. 7.4. These approximate models exhibit good correlations with the Costate model for both uniform and fore-to-aft loading perturbations. For these cases, execution times of Costate model (Eq. (2.11)), Model–1 (Eq. (7.5)), and Model–2 (Eq. (7.6)) are recorded. The average execution time of Model–1 is 20 times shorter than the average execution time of the Costate model, whereas 15 times shorter average execution time is achieved using Model–2. The quasi-steady approximations of costates significantly reduce the computational cost making these models feasible for real-time simulations.

The errors seen at high frequencies in magnitude and phase responses for both Model–1 and Model–2 approximations shown in Figs. 7.3 and 7.4 are a consequence of the quasi-steady approximations of the costate dynamics in the transfer functions of the inflow velocities at the selected locations computed using Eq. (2.13). While the overall transfer function,

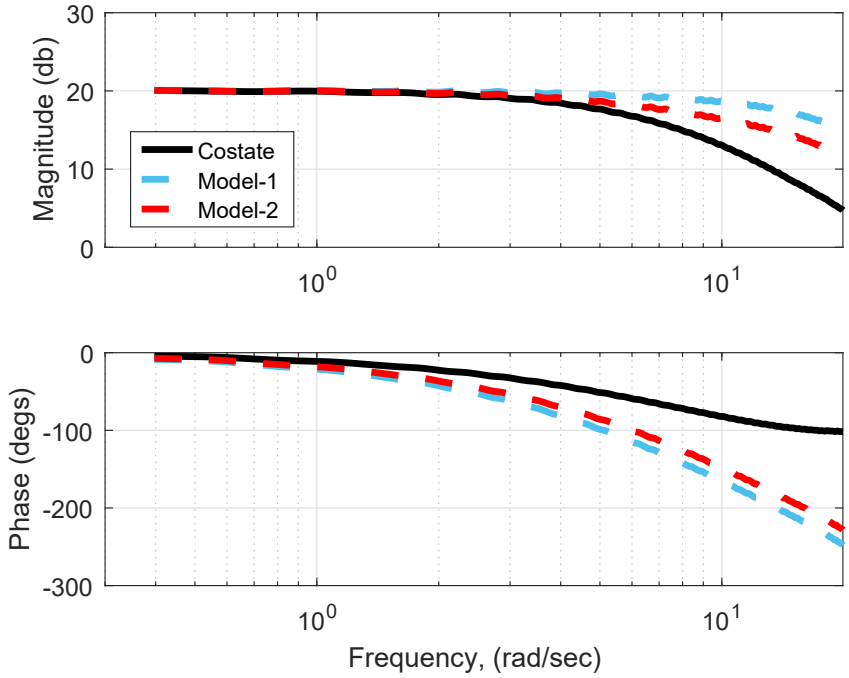

(a) Uniform loading (τ_1^{0c}) sweep

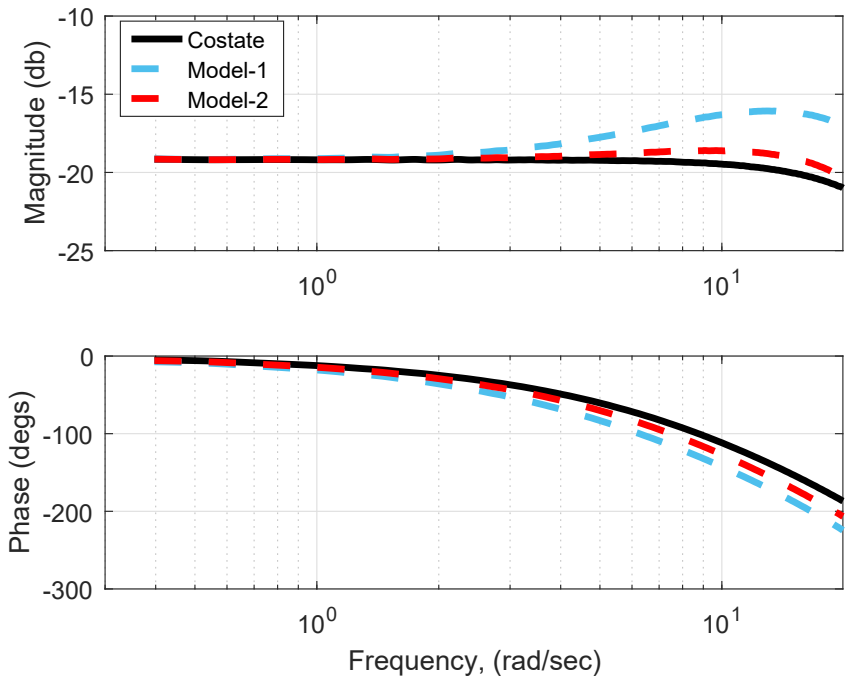

(b) Fore-to-aft loading (τ_2^{1c}) sweep

Figure 7.3: Comparison of off-rotor inflow predictions at fuselage aerodynamic reference point in hover

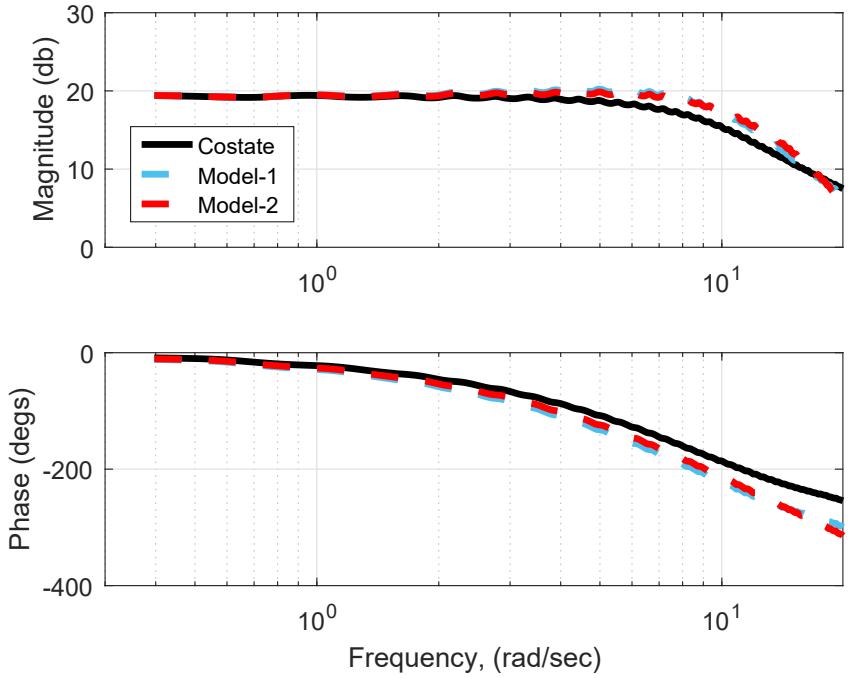

(a) Uniform loading (τ_1^{0c}) sweep

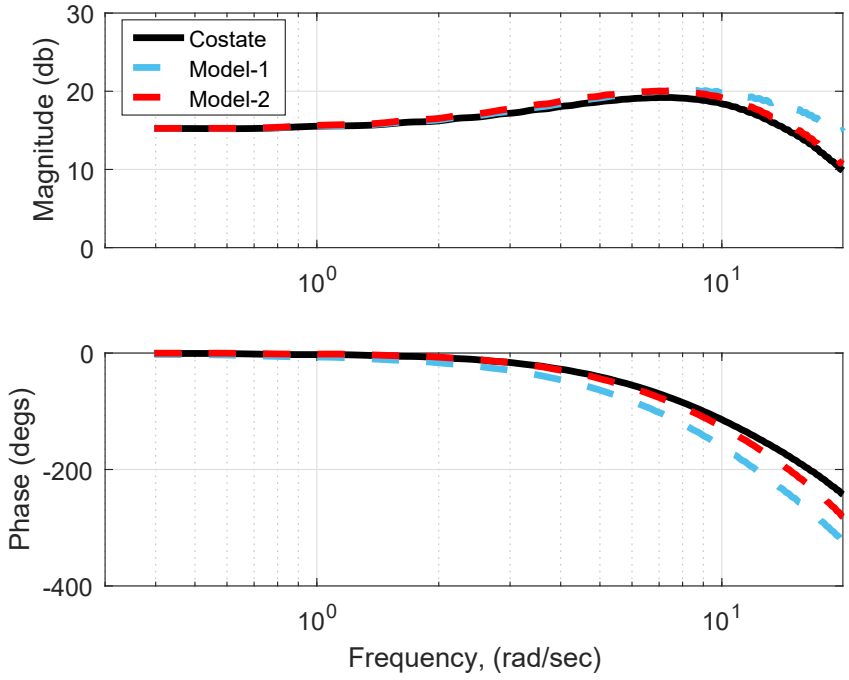

(b) Fore-to-aft loading (τ_2^{1c}) sweep

Figure 7.4: Comparison of off-rotor inflow predictions at horizontal tail aerodynamic center at $\mu = 0.10$

between the induced velocity at a selected point and loading perturbations, computed using Eq. (2.13) has stable dynamics, both Model–1 and Model–2 approximations neglect the effect of the pole cancellation of the costate dynamics, which introduces noticeable errors of increased magnitude and reduced phase at high frequencies.

In order to assess the differences between the truth model (Costate model) and the quasi-steady approximations, appropriate error metrics are needed. Coherence weighted cost function [63] and Maximum Unnoticeable Added Dynamics (MUAD) [64] error bound envelopes are widely used error metrics in the frequency domain. However, designated thresholds in these metrics are defined for body rates, attitudes, or accelerations, etc. Thresholds for error metrics are still not available for inflow dynamics. As such, the frequency domain quadratic error metric of Ref. [63] is used here only as a qualitative guide for assessing the inflow model fidelity. MUAD boundaries exemplify that pilots are more sensitive to modeling errors in a simulator over a certain range of frequencies, typically from 1 to 5 rad/s [64]. Therefore, the frequency domain quadratic error cost function (J) shown in Eq. (3.5) is evaluated in the frequency range of 1 to 5 rad/s for inflow comparisons.

Tables 7.1, 7.2, and 7.3 present cost functions of the inflow predictions at the fuselage aerodynamic reference point using the quasi-steady approximations in the inflow model for thrust coefficients of 0.0066, 0.0084, and 0.0102, respectively, at various advance ratios. Although Model–1 generally has cost functions larger than 100, the average cost functions of all advance ratios are close to 100 for uniform loading perturbations and below 100 for fore-to-aft loading perturbations. The Model–2 approximation generally has cost functions lower than 100 with some exceptions. The average cost functions of Model–2 are close to or less than 50. When fuselage aerodynamic reference point is outside the wake (typically for the advance ratio of 0.15 or higher), quasi-steady approximations match precisely with the Costate model. If the point of interest is outside the wake, the adjoint velocity v_C^* becomes zero while the adjoint velocity v_D^* is still non-zero. Since proposed approximations are only affecting v_C^*, every approximate model becomes identical to the Costate model.

Table 7.1: Off-rotor inflow prediction cost function comparison at the fuselage aerodynamic reference point with a C_T of 0.0066 for various advance ratios

	τ_1^{0c}		τ_2^{1c}	
μ	Model–1	Model–2	Model–1	Model–2
0.00	186.32	91.37	52.85	8.20
0.05	265.53	134.80	213.34	30.83
0.10	379.99	135.00	177.18	49.90
0.15	0.00	0.00	0.00	0.00
0.20	0.00	0.00	0.00	0.00
0.25	0.00	0.00	0.00	0.00
0.30	0.00	0.00	0.00	0.00
J_{avg}	118.83	51.60	63.34	12.70

Table 7.2: Off-rotor inflow prediction cost function comparison at the fuselage aerodynamic reference point with a C_T of 0.0084 for various advance ratios

	τ_1^{0c}		τ_2^{1c}	
μ	Model–1	Model–2	Model–1	Model–2
0.00	145.17	70.56	41.09	6.32
0.05	198.98	100.00	112.77	17.38
0.10	276.96	113.85	110.59	31.70
0.15	0.00	0.00	0.00	0.00
0.20	0.00	0.00	0.00	0.00
0.25	0.00	0.00	0.00	0.00
0.30	0.00	0.00	0.00	0.00
J_{avg}	88.73	40.63	37.78	7.91

Table 7.3: Off-rotor inflow prediction cost function comparison at the fuselage aerodynamic reference point with a C_T of 0.0102 for various advance ratios

	τ_1^{0c}		τ_2^{1c}	
μ	Model–1	Model–2	Model–1	Model–2
0.00	120.54	58.03	33.75	4.74
0.05	155.52	77.61	83.60	11.98
0.10	221.06	97.37	75.89	21.79
0.15	268.96	70.83	64.46	25.66
0.20	0.00	0.00	0.00	0.00
0.25	0.00	0.00	0.00	0.00
0.30	0.00	0.00	0.00	0.00
J_{avg}	109.44	43.41	36.82	9.17

Comparisons of off-rotor inflow predictions at the horizontal tail aerodynamic center are presented in Tables 7.4, 7.5, and 7.6 for different loading and advance ratio conditions. Although some of the cost functions exceed the value of 100 for both Model–1 and Model–2, they are generally close to 100. Moreover, the average cost function of Model–1 reduces as thrust coefficient increases. The average cost functions of Model–2 for uniform loading perturbations are below 20 for all thrust conditions. All average cost functions of Model–2 for fore-to-aft loading perturbations are closer to 100.

Table 7.4: Off-rotor inflow prediction cost function comparison at the horizontal tail aerodynamic center with a C_T of 0.0066 for various advance ratios

	τ_1^{0c}		τ_2^{1c}	
μ	Model–1	Model–2	Model–1	Model–2
0.00	0.00	0.00	0.00	0.00
0.05	2.28	31.72	9.75	3.56
0.10	64.24	26.99	37.83	3.04
0.15	129.89	30.25	199.86	273.83
0.20	138.75	12.89	208.13	132.89
0.25	104.43	5.27	106.48	48.01
0.30	59.44	3.89	39.29	116.12
J_{avg}	71.29	15.86	85.91	82.49

Table 7.5: Off-rotor inflow prediction cost function comparison at the horizontal tail aerodynamic center with a C_T of 0.0084 for various advance ratios

	τ_1^{0c}		τ_2^{1c}	
μ	Model–1	Model–2	Model–1	Model–2
0.00	0.00	0.00	0.00	0.00
0.05	3.88	48.03	7.56	2.66
0.10	32.97	12.10	16.61	1.00
0.15	88.82	28.48	97.09	119.49
0.20	95.72	15.66	135.55	256.47
0.25	78.58	7.29	87.47	152.93
0.30	47.44	4.74	38.06	167.57
J_{avg}	49.63	16.61	54.62	100.02

Table 7.6: Off-rotor inflow prediction cost function comparison at the horizontal tail aerodynamic center with a C_T of 0.0102 for various advance ratios

	τ_1^{0c}		τ_2^{1c}	
μ	Model–1	Model–2	Model–1	Model–2
0.00	0.00	0.00	0.00	0.00
0.05	5.25	60.17	6.28	2.10
0.10	17.22	4.76	9.56	1.12
0.15	63.86	23.84	48.76	34.54
0.20	72.39	16.67	107.23	303.73
0.25	61.26	8.60	69.62	223.08
0.30	40.70	5.38	38.21	199.67
J_{avg}	37.24	17.06	39.95	109.18

7.3 Impact of Inflow Model Approximations on Flight Simulation Model Fidelity

In order to use proper error metrics and evaluate the fidelity of the flight simulation models with quasi-steady approximations to the costate equation in the inflow model, a nonlinear longitudinal flight dynamic model of the UH-60 helicopter model is used. Here, vehicle response, which uses the Costate model for off-rotor inflow predictions, is considered as the truth model. The blade element main rotor with flapping dynamics and horizontal tail are modeled using the equations provided in Ref. [72]. The fuselage is represented by an equivalent flat plate drag area. The Howlett inflow [72] in the blade element main rotor model and inflow interference mechanism at the horizontal tail model are replaced by the velocity potential dynamic inflow model. Similar to the isolated rotor case, six odd numbered terms in the velocity potential expansion is used in the flight simulation model.

A frequency sweep with a frequency range between 0.4 to 20 radian per second is applied to either collective or longitudinal cyclic from trim at different advance ratios. The thrust coefficient is fixed at 0.0066. The simulation model fidelity is evaluated over the entire frequency range (0.4 to 20 rad/s). Tables 7.7 and 7.8 show cost function comparisons between Model–1 and Model–2 in vehicle longitudinal transient response due to collective and longitudinal cyclic inputs, respectively. Below the advance ratio of 0.25, simulations that use Model–1 and Model–2 have longitudinal dynamics that are indistinguishable from

the truth model. At the advance ratios of 0.25 and 0.30, Model–1 cost functions for pitch rate and attitude exceed 100 for an applied collective sweep, whereas cost functions of Model–2 predictions are below this threshold. Model–1 cost functions for pitch rate and pitch attitude responses due to longitudinal cyclic inputs are close to the acceptable threshold at the advance ratio of 0.30. At the same time, all other longitudinal cyclic input cases have cost functions below 100.

Table 7.7: Predicted longitudinal dynamic response cost function comparison with inflow model approximations and collective control input at various advance ratios

μ	Model	q	θ	u	w
0.05	Model–1	7.00	7.81	0.37	0.12
	Model–2	3.08	2.82	0.23	0.08
0.10	Model–1	7.61	7.99	3.42	1.09
	Model–2	2.06	1.93	1.07	0.20
0.20	Model–1	0.03	0.03	46.38	0.02
	Model–2	0.02	0.02	29.45	0.01
0.25	Model–1	181.66	221.85	24.91	58.46
	Model–2	78.64	81.27	8.28	14.87
0.30	Model–1	239.74	295.05	21.33	95.21
	Model–2	74.17	80.87	11.18	32.54
J_{avg}	Model–1	87.21	106.55	19.28	30.98
	Model–2	31.59	33.38	10.04	9.54

Figure 7.5 shows the helicopter pitch rate response at the advance ratio of 0.10. At this advance ratio, simulations with quasi-steady approximations have cost functions less than 10, which indicate indistinguishable differences in responses compared to the case with the Costate model.

The change in the off-rotor inflow velocity at the horizontal tail aerodynamic center and helicopter pitch rate for an applied collective sweep at the advance ratio of 0.25 are presented in Fig. 7.6. Initial off-rotor inflow dynamics of the quasi-steady approximation models are close to the Costate model (Fig. 7.6(a)). As input variations increase with time, discrepancies among the models start to appear in both off-rotor inflow velocity and

Table 7.8: Predicted longitudinal dynamic response cost function comparison with inflow model approximations and longitudinal cyclic control input at various advance ratios

μ	Model	q	θ	u	w
0.05	Model–1	0.14	0.13	0.03	0.05
	Model–2	0.11	0.11	0.08	0.07
0.10	Model–1	0.40	0.34	0.10	0.21
	Model–2	0.15	0.13	0.10	0.15
0.20	Model–1	0.05	0.08	0.88	0.08
	Model–2	0.00	0.00	0.45	0.00
0.25	Model–1	58.72	57.76	7.85	32.09
	Model–2	13.07	12.80	0.21	4.53
0.30	Model–1	105.52	103.78	24.89	66.33
	Model–2	35.03	31.27	13.86	24.39
J_{avg}	Model–1	32.97	32.42	6.75	19.75
	Model–2	9.67	8.86	2.94	5.83

pitch rate (Fig. 7.6(b)). Although changes in the inflow magnitude at the horizontal tail aerodynamic center and pitch rate are small, these small differences among the models still produce a relatively large error at high frequency range, as shown in Fig. 7.7. The Model–2 case shows a better correlation at higher frequencies compared to Model–1.

For flight dynamics analyses, the frequency of interest lies between 1 to 12 rad/s [63]. The MUAD error bound envelope in Fig. 7.8 shows that envelope boundaries enlarge towards the high frequency. In MUAD plots, vehicle response that uses the Costate model is considered as the truth model; hence, differences between the Costate case and quasi-steady approximations are plotted. For the longitudinal cyclic sweep case (Fig. 7.8(b)), simulations that use Model–1 and Model–2 are always inside the designated MUAD envelopes, whereas, for the collective sweep case (Fig. 7.8(a)), Model–1 crosses boundaries in both magnitude and phase plots at higher frequencies over a small range. On the other hand, Model–2 stays inside the envelope except where phase prediction slightly crosses the boundary over a tiny range of high frequency values (Fig. 7.8(a)).

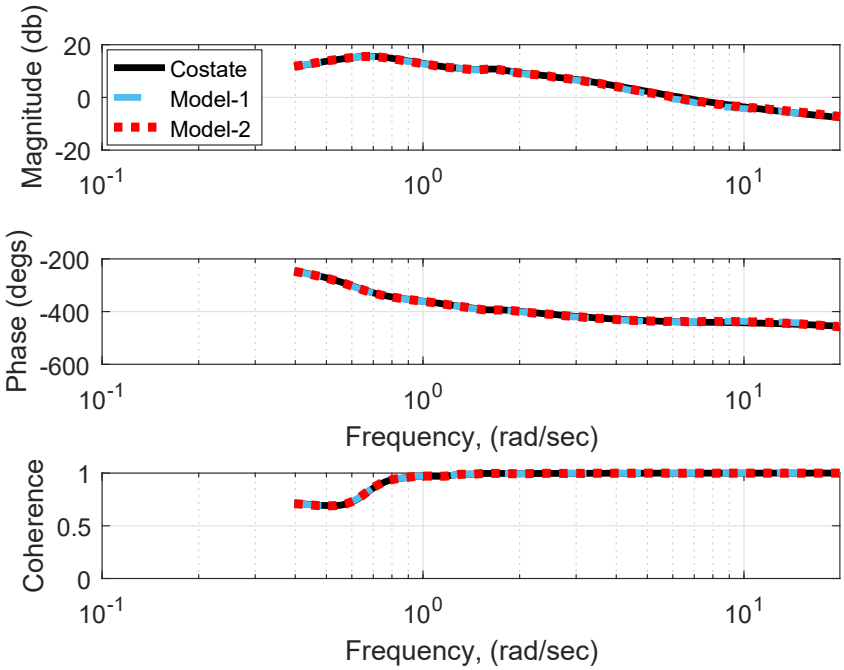

(a) Collective sweep

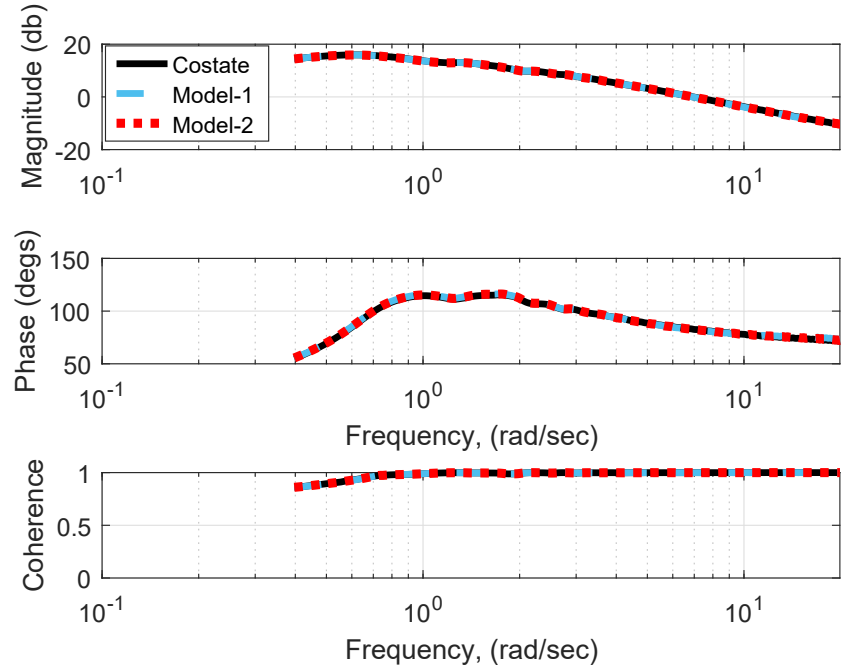

(b) Longitudinal cyclic sweep

Figure 7.5: Comparison of pitch rate responses at $\mu = 0.10$

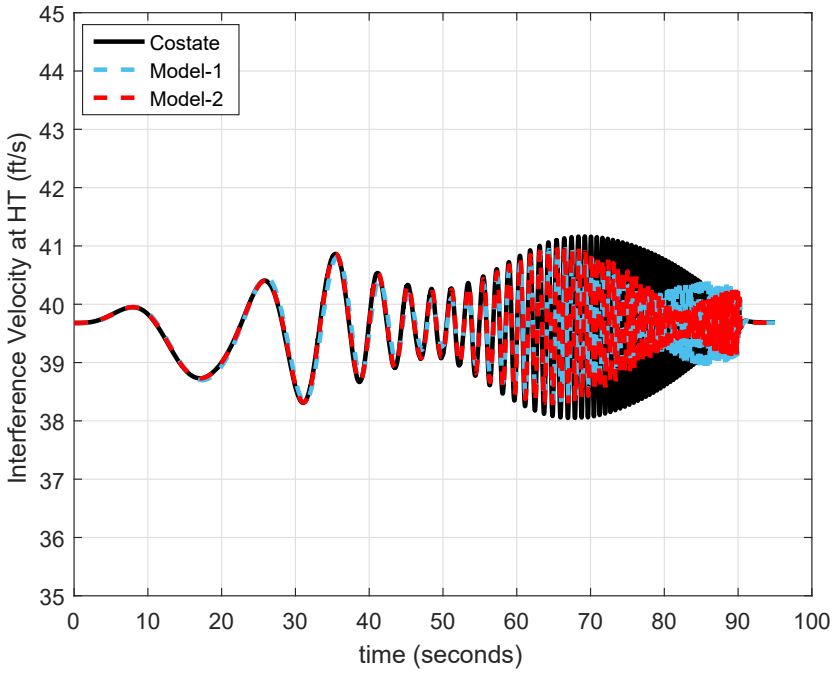

(a) Off-rotor inflow velocity at horizontal tail aerodynamic center

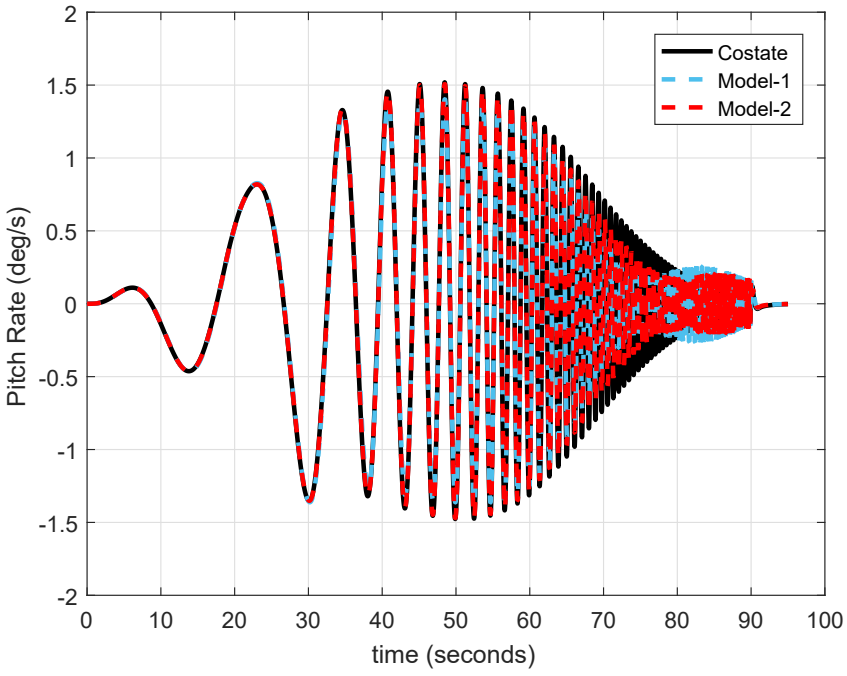

(b) Pitch rate

Figure 7.6: Comparison of off-rotor inflow prediction at horizontal tail and its effect on the pitch rate response at $\mu = 0.25$ due to collective sweep

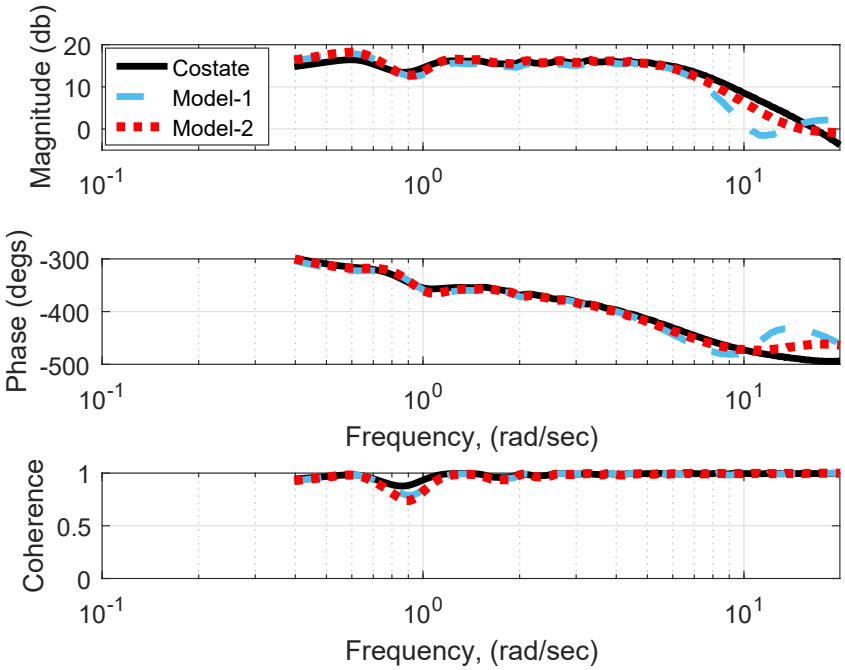

(a) Collective sweep

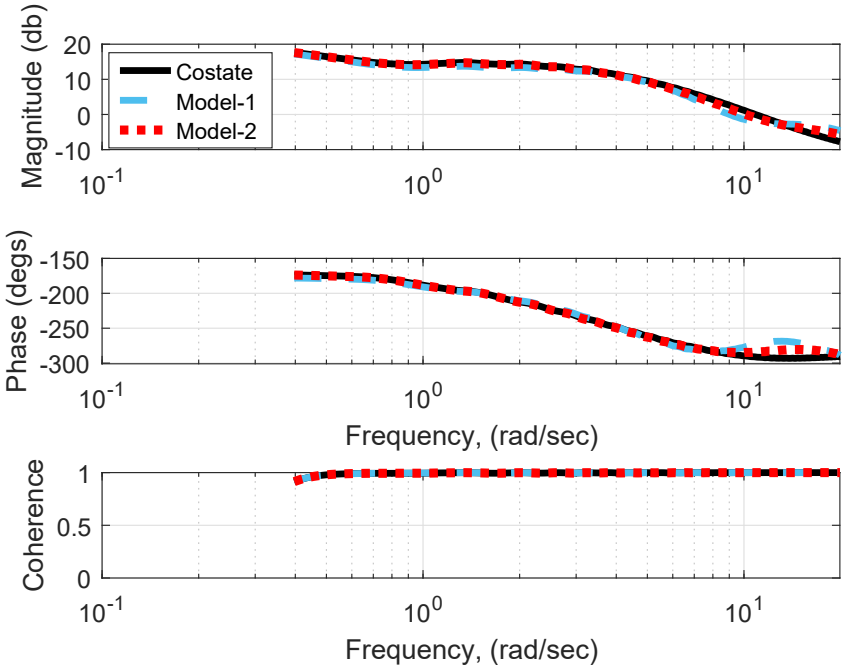

(b) Longitudinal cyclic sweep

Figure 7.7: Comparison of pitch rate responses at $\mu = 0.25$

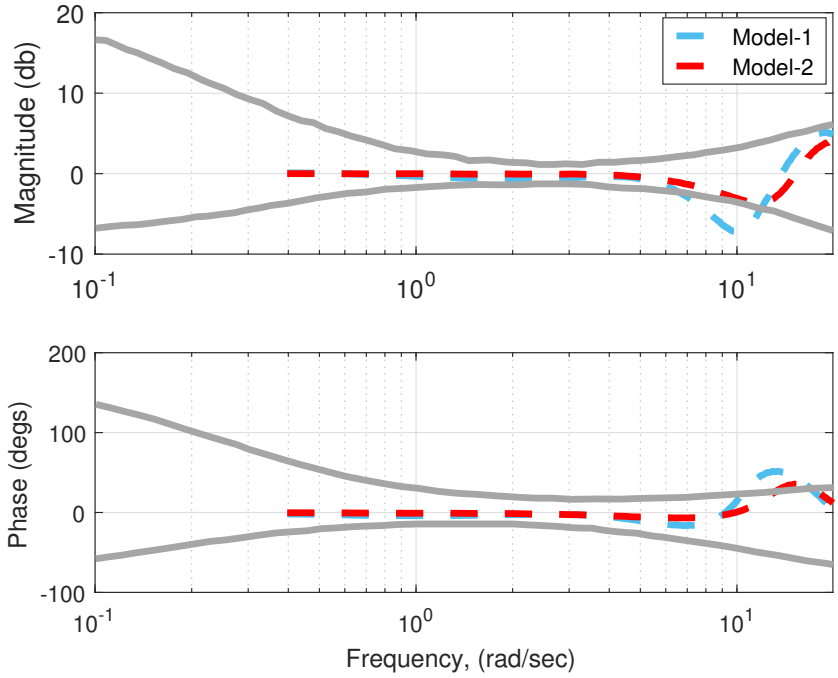

(a) Collective sweep

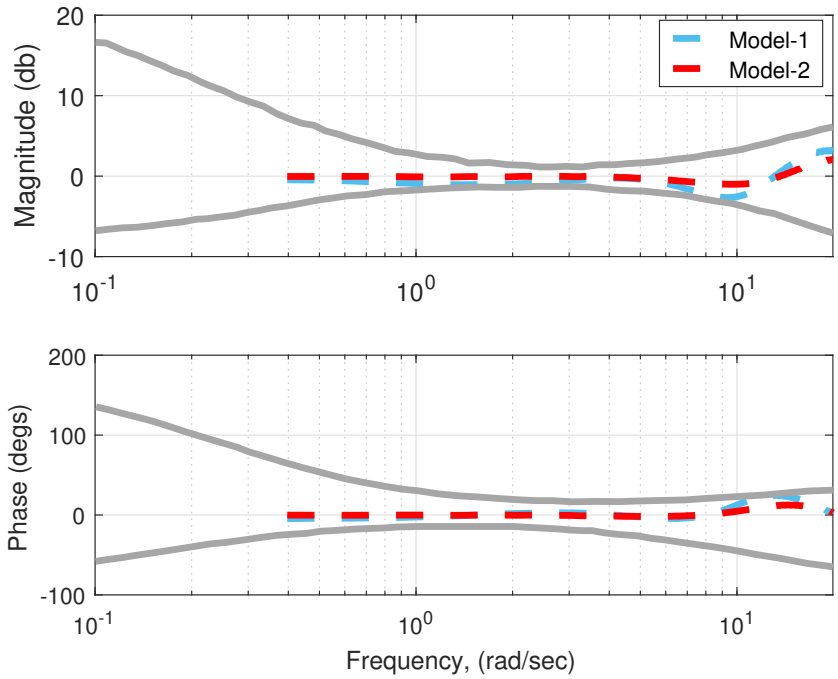

(b) Longitudinal cyclic sweep

Figure 7.8: Comparison of frequency response errors in pitch rate at $\mu = 0.25$, MUAD envelope

Next, instead of applying a frequency sweep, a doublet input is applied individually to either collective or longitudinal cyclic. Figure 7.9 shows the pitch rate response at the advance ratio of 0.10. Simulations with both Model–1 and Model–2 have good agreements with the Costate model for both collective and longitudinal inputs. At the advance ratio of 0.20, pitch rate response predictions of a doublet collective input agree well with each other, as shown in Fig. 7.10(a). For the longitudinal cyclic doublet input case (Fig. 7.10(b)), initial pitch rate response predictions that use the approximate inflow models closely follow the Costate model; however, small deviations are observed, which is thought to be due to integrated error in pitch acceleration over time. For all doublet input cases shown, Model–2 response predictions are seen to have higher fidelity compared to those using Model–1.

7.4 Removal of Backward Time Marching via Convolution Integral

In previous sections, quasi-steady approximations to costates and their effects on the inflow fidelity and flight simulation model fidelity are discussed. In this section, the adjoint equation is represented by a convolution integral to remove the backward time marching solution. The convolution integral can be transformed into a summation, which is more efficient than the time marching solution. The convolution integral is strictly valid for the linear systems. Linear inflow models are useful for some applications as nonlinear models are often linearized for analyses.

To represent the adjoint equation as a convolution integral, one should use a generic convolution integral structure accounting for an arbitrary starting time and initial condition. Equation (7.8) represents a convolution integral with an arbitrary starting time and initial condition [74].

$$\{x\}_t = e^{[A](t-t_0)}\{x\}_{t_{start}} + \int_{t_{start}}^{t} e^{[A]\tau}[B]u(t-\tau)d\tau \tag{7.8}$$

By replacing t_{start} with t_c, t with $t_c - t_0$, and x with Δ, the backward time marching

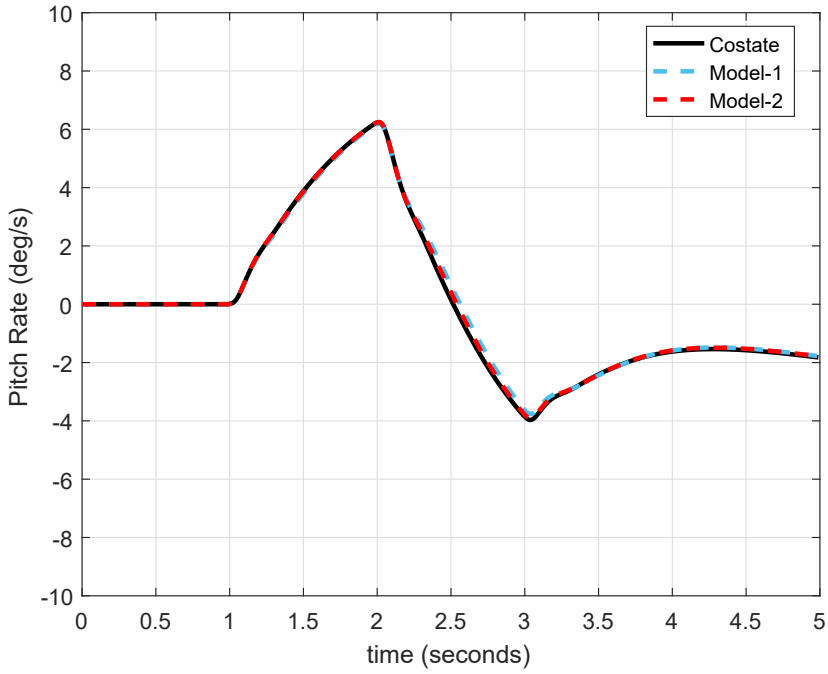

(a) Collective input with an amplitude of 1.5°

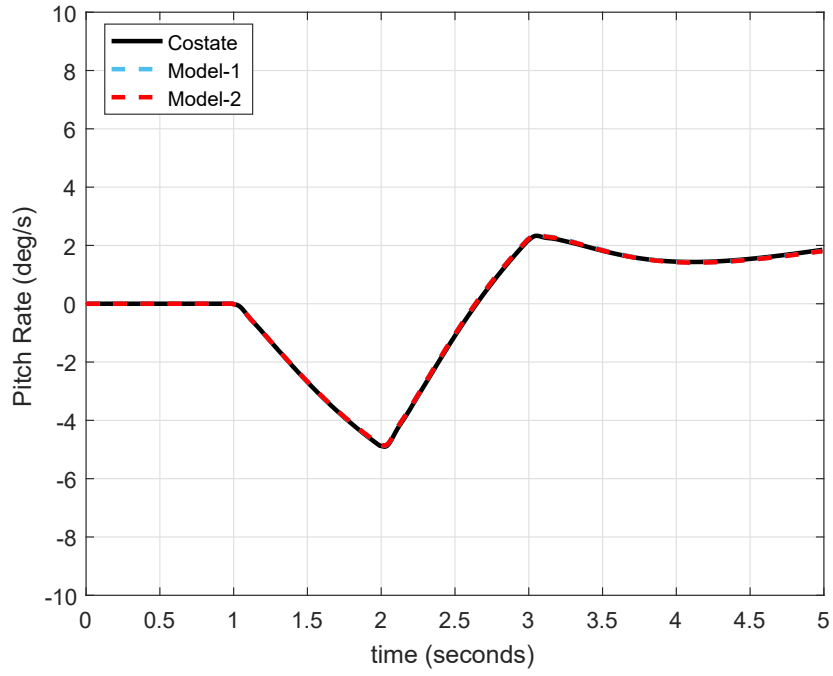

(b) Longitudinal cyclic input with an amplitude of 1.0°

Figure 7.9: Comparison of pitch rate responses at $\mu = 0.10$ due to doublet input

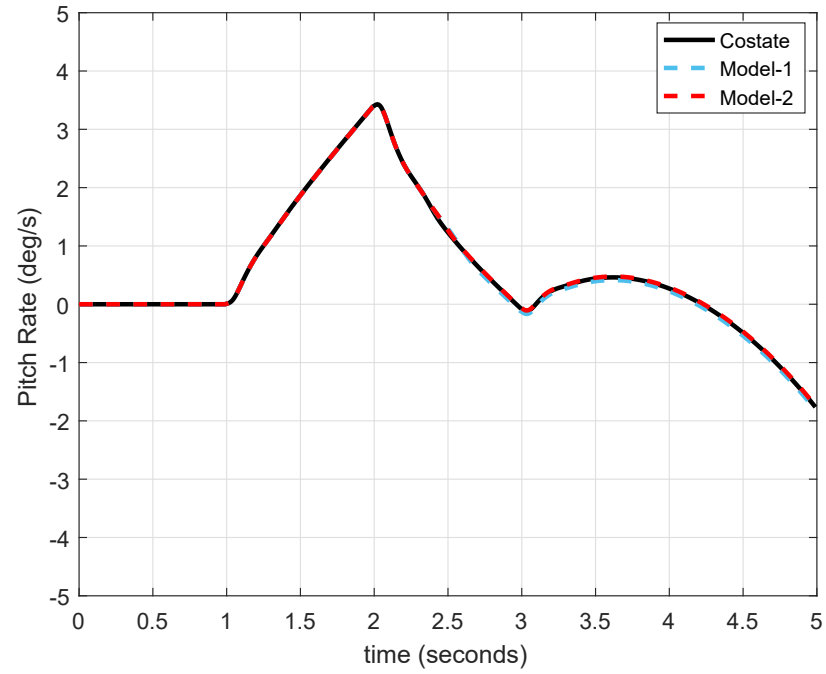

(a) Collective input with an amplitude of $0.5°$

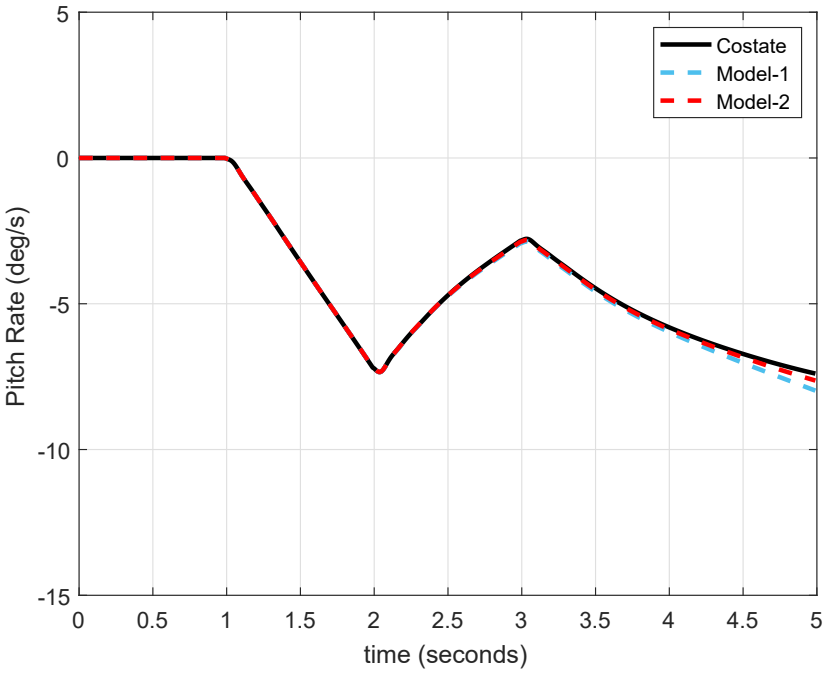

(b) Longitudinal cyclic input with an amplitude of $1.0°$

Figure 7.10: Comparison of pitch rate responses at $\mu = 0.20$ due to doublet input

solution is appropriately converted into the convolution integral.

$$\{\Delta\}_{t_c-t_0} = e^{[A](t_c-t_0)}\{\Delta\}_{t_c} + \int_{t_c}^{t_c-t_0} e^{[A]\varsigma}[B]\{\tau\}_{(t_c-t_0-\varsigma)}d\varsigma \tag{7.9}$$

In Eq. (7.9), t_c is the current time, t_0 is the time delay, $\{\Delta\}$ is the costates, and $\{\tau\}$ is the pressure coefficients. Note that dummy integration variable τ in Eq. (7.8) is replaced by ς to avoid confusion since pressure coefficients are also represented by the variable τ. It is essential to recognize that backward time marching starts from the current time (t_c) and decreases to $t_c - t_0$. Instead of a negative $d\varsigma$, one may use a positive quantity, δ. Besides, convolution integral in Eq. (7.9) can be represented as a summation by discretizing the integral, as shown in Eq. (7.10).

$$\{\Delta\}_{t_c-t_0} = e^{[A](t_c-t_0)}\{\Delta\}_{t_c} - \delta\sum_{k=1}^{N} e^{-[A]k\delta}[B]\{\tau\}_{(t_c-t_0-k\delta)} \tag{7.10}$$

In Eq. (7.10), N represents the number of time steps utilized to discretize the time from t_c to $t_c - t_0$. For typical simulations, backward time marching solution discretization uses the same time step as the forward time marching solution since pressure coefficients are known from the forward time marching solution. The system matrix ($[A]$) and input matrix ($[B]$) are found by modifying the linear adjoint equation provided in Eq. (7.11).

$$\begin{gathered} -[\tilde{M}]\{\overset{*}{\Delta}\}+[\tilde{D}][\tilde{L}]^{-1}[\tilde{M}]\{\Delta\} = [\tilde{D}][T]\{\tau\} \\ \{\overset{*}{\Delta}\} = [A]\{\Delta\} + [B]\{\tau\} \end{gathered} \tag{7.11}$$

where

$$[A] = [\tilde{M}]^{-1}[\tilde{D}][\tilde{L}]^{-1}[\tilde{M}] \qquad\qquad [B] = -[\tilde{M}]^{-1}[\tilde{D}][T]$$

For a linear model, $[A]$ and $[B]$ are calculated once at the beginning of the simulation

for a selected skew angle. In the current study, $[A]$ is diagonalized to obtain the state transition matrix ($e^{-[A]k\delta}$). Figures 7.11 and 7.12 show off-rotor inflow predictions at the UH-60 horizontal tail aerodynamic center due to a sinusoidal loading perturbation with a constant frequency. Off-rotor inflow predictions due to a sinusoidal fore-to-aft loading perturbation with a constant frequency are provided in Figs. 7.13 and 7.14. As seen, convolution integral solutions are identical to the backward time marching solutions of the adjoint equation for different loading perturbations and skew angles. The convolution integral is computationally more efficient than the backward time marching since the state transition matrix is only calculated once, and integration is represented by a simple summation. Therefore, instead of integrating backward in time at each time step, one can conveniently use the convolution integral for a faster solution.

Although the convolution integral solution does not apply to the nonlinear adjoint equation, one can still assume a quasi-linear adjoint equation to employ this approach. By linearizing the nonlinear adjoint equation (Eq. (2.11)), a quasi-linear adjoint equation can be obtained. This quasi-linear equation must be updated at each time step to account for changes in the rotor loading and flight conditions. Moreover, the system matrix ($[A]$), input matrix ($[B]$), and state transition matrix ($e^{-[A]k\delta}$) must be re-calculated at each time step. Because of these calculations, this approach is not necessarily better than the backward time marching solution since the state transition matrix computations involve several steps. However, predictions of this quasi-linear solution are still shown to demonstrate the applicability of the approach. For this case, $[A]$ and $[B]$ are calculated as follows: $[A] = \Omega[\tilde{M}]^{-1}[\tilde{D}][\tilde{V}_m][\tilde{L}]^{-1}[\tilde{M}]$, $[B] = -\Omega[\tilde{M}]^{-1}[\tilde{D}][T]$.

Figures 7.15 and 7.16 illustrate off-rotor inflow predictions at the horizontal tail due to sinusoidal perturbations of the uniform and fore-to-aft loading components, respectively, at the advance ratio of 0.05. Off-rotor inflow prediction due to uniform loading perturbation shows some differences between the quasi-linear and backward time marching solutions. During uniform loading perturbation, the mass flow parameter changes at each time step

because it is a direct function of the uniform inflow component. Because of this dependence (nonlinearity), predictions with the quasi-linear assumption have lower fidelity when uniform loading is perturbed. On the other hand, fore-to-aft loading perturbation case (Fig. 7.16) demonstrates good agreement since the effect of fore-to-aft loading on the uniform inflow component is smaller than the effect of uniform loading. Similar results are obtained at the advance ratio of 0.25 for both loading conditions, as shown in Figs. 7.17 and 7.18. Again, uniform inflow loading case exhibits some differences, while fore-to-aft loading case of the the quasi-linear solution has a good match with the backward time marching solution.

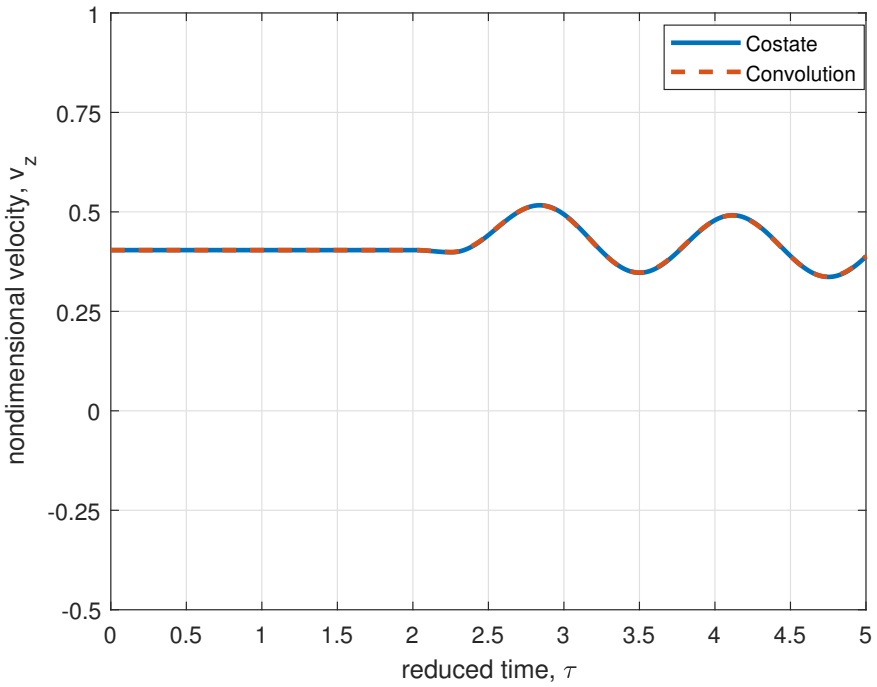

Figure 7.11: Off-rotor inflow predictions at horizontal tail aerodynamic center due to uniform loading perturbation, linear case, $\chi = 30$

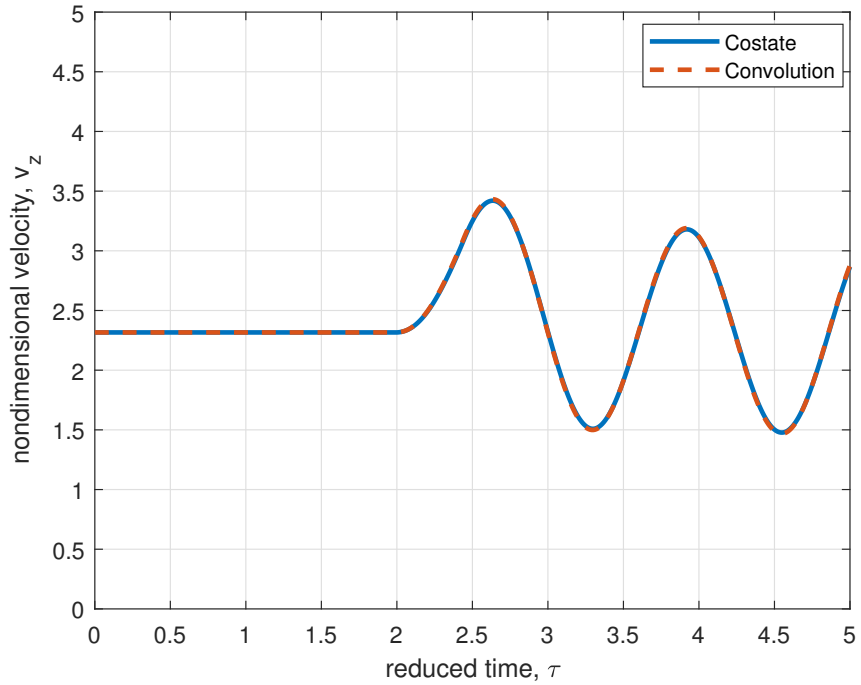

Figure 7.12: Off-rotor inflow predictions at horizontal tail aerodynamic center due to uniform loading perturbation, linear case, $\chi = 60$

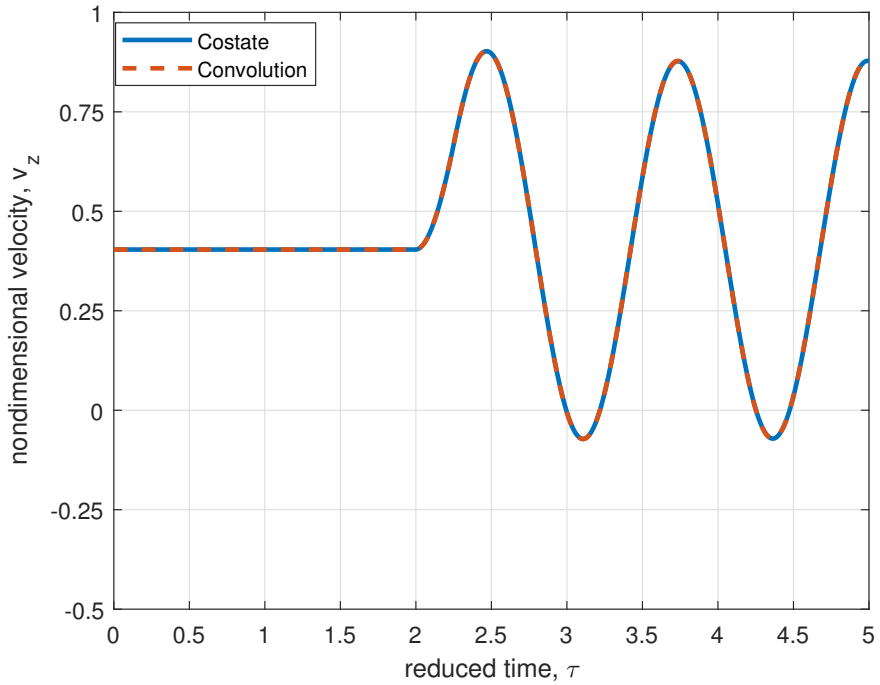

Figure 7.13: Off-rotor inflow predictions at horizontal tail aerodynamic center due to fore-to-aft loading perturbation, linear case, $\chi = 30$

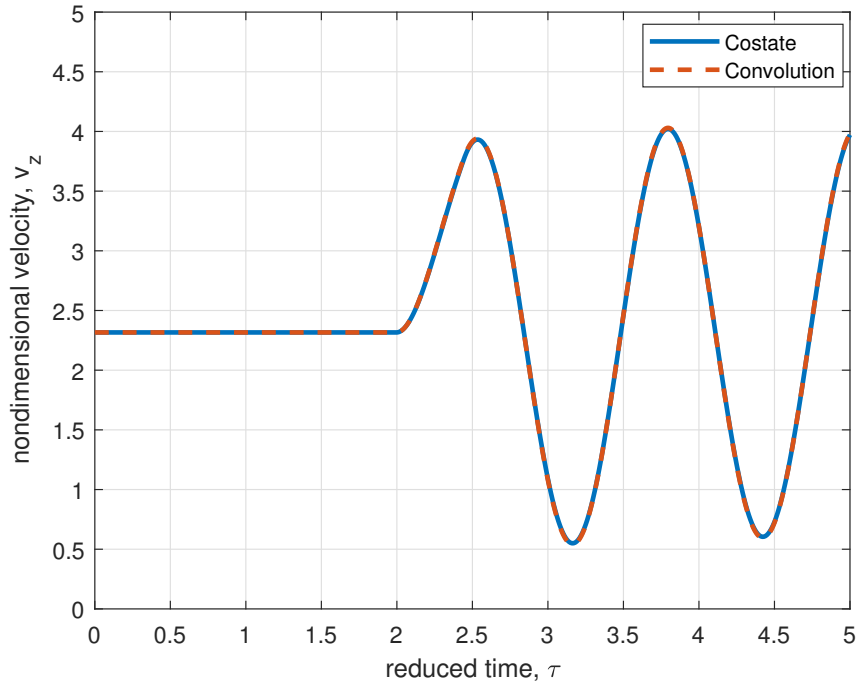

Figure 7.14: Off-rotor inflow predictions at horizontal tail aerodynamic center due to fore-to-aft loading perturbation, linear case, $\chi = 60$

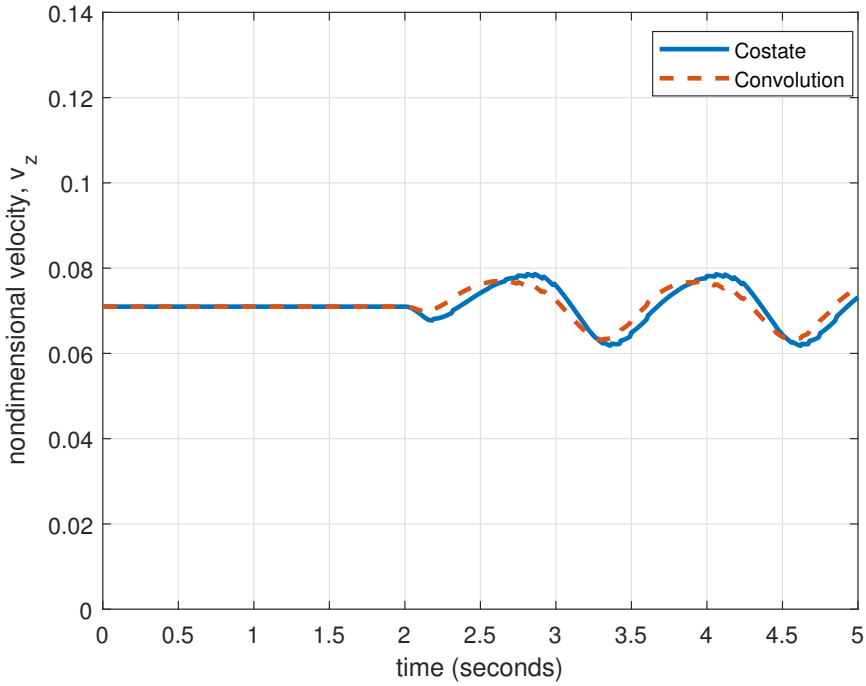

Figure 7.15: Off-rotor inflow predictions at horizontal tail aerodynamic center due to uniform loading perturbation, quasi-linear case, $\mu = 0.05$

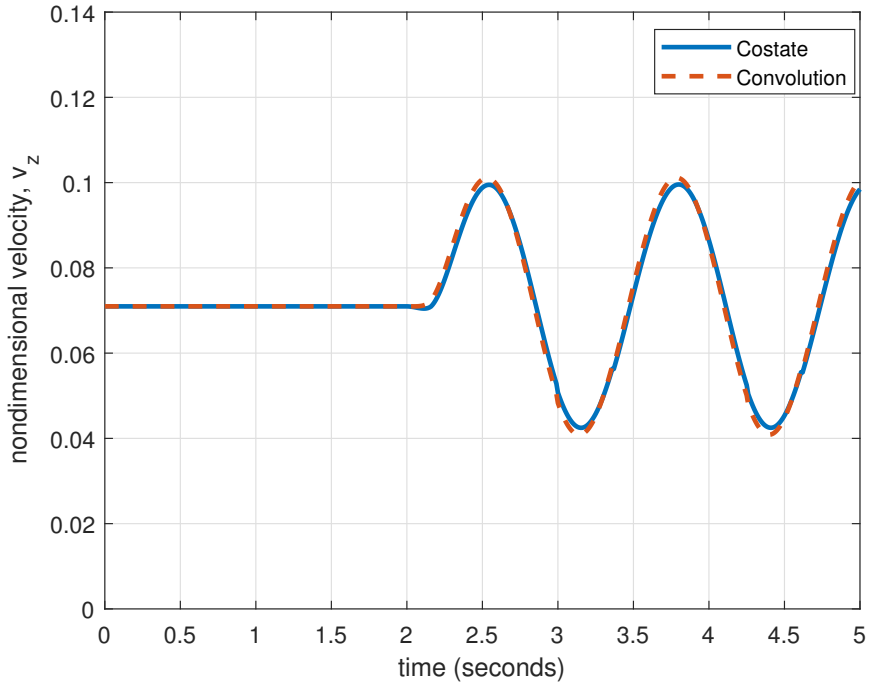

Figure 7.16: Off-rotor inflow predictions at horizontal tail aerodynamic center due to fore-to-aft loading perturbation, quasi-linear case, $\mu = 0.05$

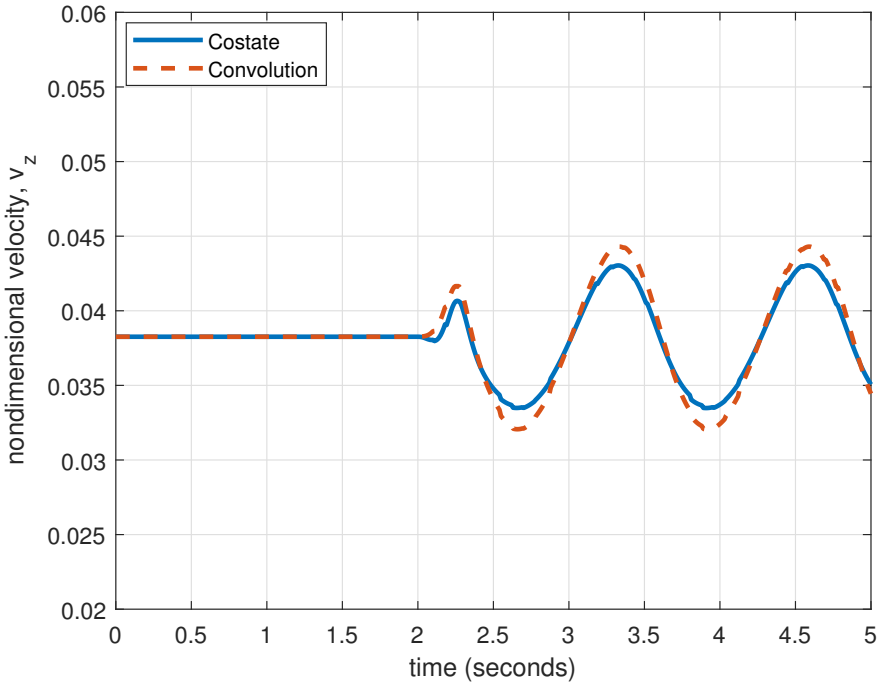

Figure 7.17: Off-rotor inflow predictions at horizontal tail aerodynamic center due to uniform loading perturbation, quasi-linear case, $\mu = 0.25$

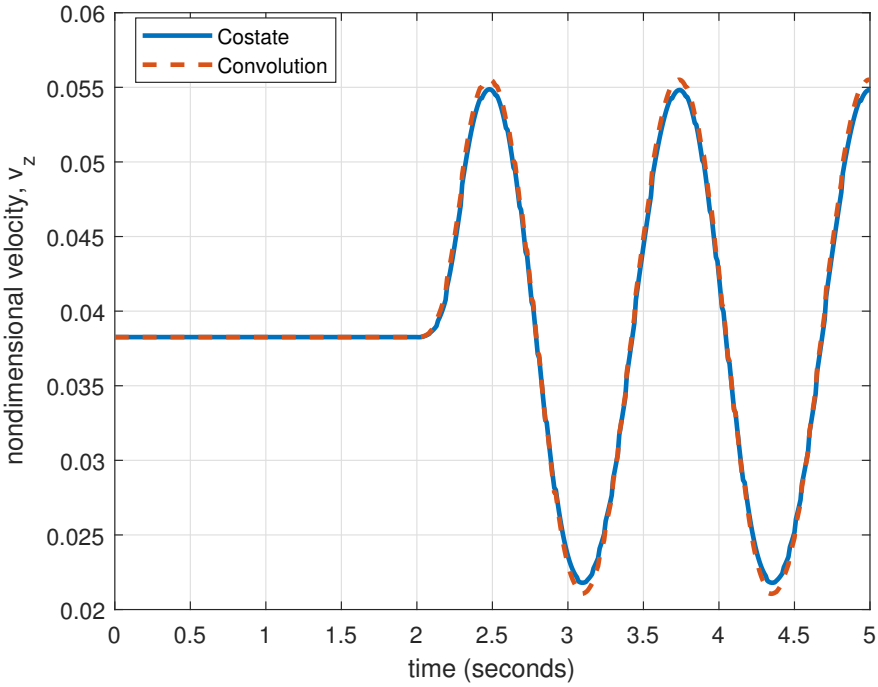

Figure 7.18: Off-rotor inflow predictions at horizontal tail aerodynamic center due to fore-to-aft loading perturbation, quasi-linear case, $\mu = 0.25$

CHAPTER 8
COMBINED MOMENTUM THEORY AND SIMPLE VORTEX THEORY INFLOW MODEL FOR MULTI-ROTOR CONFIGURATIONS

While previous chapters discuss the development and analysis of VPSIM and PPSIM so far, an attempt has been made in this chapter to develop a new multi-rotor inflow model by combining momentum theory with a simple vortex theory. The developed model, Combined Momentum Theory and Simple Vortex Theory (CMTSVT), captures the main interference effects while retaining the simplified modeling approach of the fundamental theories. In its current form, CMTSVT can only predict steady-state self-induced inflow and interference inflow of generic multi-rotor configurations. In this chapter, CMTSVT is described and then evaluated against the VPSIM for dual-rotor configurations. For the coaxial rotor configuration, GT-Hybrid and VVPM steady-state inflow predictions are also included.

8.1 Baseline Inflow Model (Without Interference)

The momentum theory inflow model, although simple, is still widely used for quick predictions of uniform inflow component of rotors in isolation. Using the proposed formula of Glauert [75], uniform inflow component (λ_0) is found by the following formula:

$$\lambda_0 = C_T/(2V_T) \tag{8.1}$$

where V_T is the net flow passing through the rotor calculated as $V_T = \sqrt{\mu^2 + (\lambda_f + \lambda_0)^2}$. Here, μ is the normalized inplane velocity parallel to the tip path plane, and λ_f is the normalized velocity perpendicular to it. Aerodynamic thrust coefficient is represented by C_T. The solution of Eq. (8.1) involves either fixed-point iteration or a root-finding algorithm since λ_0 appears on both sides of the equation.

In addition to the uniform component of inflow, the skew angle effect and contributions of aerodynamic hub moments should be added to achieve a more realistic flow representation. This representation is achieved by redistributing the uniform inflow over the rotor disk by the first harmonic inflow expansion as:

$$\lambda(\bar{r}, \psi) = \lambda_0 + \lambda_{1c}\bar{r}\cos(\psi) + \lambda_{1s}\bar{r}\sin(\psi) \tag{8.2}$$

In this model, the first harmonic inflow components are taken from the Pitt-Peters inflow model [10–12]. Disk angle of attack defined in the Pitt-Peters model is converted to the wake skew angle to arrive at a model with a more generic variable [19]. The longitudinal and lateral inflow components are calculated as:

$$\lambda_{1c} = \frac{15\pi}{64V_T}\tan\frac{\chi}{2}C_T - \frac{4\cos\chi}{V(1+\cos\chi)}C_M \tag{8.3}$$

$$\lambda_{1s} = -\frac{4}{V(1+\cos\chi)}C_L \tag{8.4}$$

where C_M and C_L are rotor aerodynamic pitch moment and roll moment coefficients, respectively. V is the mass flow parameter, and χ is the wake skew angle. Calculations of V and χ are provided by the following equations.

$$V = \frac{\mu^2 + (\lambda_f + \lambda_0)(\lambda_f + 2\lambda_0)}{V_T} \tag{8.5}$$

$$\chi = \tan^{-1}\frac{\mu}{\lambda_f + \lambda_0} \tag{8.6}$$

It is important to note that uniform and longitudinal inflow components are coupled in the Pitt-Peters model [10–12]. This coupling is neglected in this inflow model. Here, the original structure of the momentum theory inflow model introduced by Howlett [72] is retained to preserve the simple modeling approach.

8.2 Rotor-on-Rotor Interference Inflow Modifications

In multi-rotor inflow modeling, the total inflow on a rotor consists of self-induced inflow and interference inflow due to other rotors. By summing these inflow parts, the total inflow on a rotor can be described: $\lambda(\bar{r},\psi) = \lambda^S(\bar{r},\psi) + \lambda^I(\bar{r},\psi)$. Like the baseline inflow model introduced in chapter 8.1, inflow distribution of a rotor is approximated by uniform and the first harmonic inflow components. For the j^{th} rotor, the inflow distribution is expressed as:

$$\lambda^j(\bar{r},\psi) = (\lambda_0^{j,S} + \lambda_0^{j,I}) + (\lambda_{1c}^{j,S} + \lambda_{1c}^{j,I})\bar{r}\cos(\psi) + (\lambda_{1s}^{j,S} + \lambda_{1s}^{j,I})\bar{r}\sin(\psi) \tag{8.7}$$

In Eq. (8.7), superscript S and I refer to self-induced and interference inflow components, respectively. For multi-rotor configurations, total flow passing through each rotor must be corrected because of the interference inflow. It is essential to include this correction since the magnitude of the self-induced inflow can be significantly altered depending on the magnitude of the interference inflow. The self-induced uniform inflow of the j^{th} rotor is obtained from the following equation:

$$\lambda_0^j = C_T^j/(2V_T^j) \tag{8.8}$$

where

$$V_T^j = \sqrt{(\mu^j)^2 + (\lambda_f^j + \lambda_0^j)^2}$$

$$\lambda_0^j = \lambda_0^{j,S} + \lambda_0^{j,I}$$

Self-induced uniform inflow components of each rotor should be solved simultaneously until both self-induced and interference uniform inflow components converge. After obtaining the converged solutions, the first harmonic inflow components of the j^{th} rotor can be obtained from:

$$\lambda_{1c}^j = \lambda_{1c}^{j,S} + \lambda_{1c}^{j,I} \tag{8.9}$$

$$\lambda_{1s}^{j} = \lambda_{1s}^{j,S} + \lambda_{1s}^{j,I} \tag{8.10}$$

where

$$\lambda_{1c}^{j,S} = \frac{15\pi}{64V_T^j} \tan\frac{\chi^j}{2} C_T^j - \frac{4\cos\chi^j}{V^j(1+\cos\chi^j)} C_M^j$$

$$\lambda_{1s}^{j,S} = -\frac{4}{V^j(1+\cos\chi^j)} C_L^j$$

8.3 Interference Inflow Calculations

In this model, interference inflow is calculated using a simple vortex theory. In this theory, vortices are closely spaced, and they establish a cylinder (rigid wake) with a sheet of continuous vortices [76]. In his formulation, Heyson [76] divided the wake into two parts: outer wake and inner wake. The outer wake considers the wake due to blade tip vortices, while the inner wake takes into account the effect of shed trailing edge vortices. Here, interference inflow only due to the outer wake is considered. Reference [76] shows the detailed formulation of the theory. Heyson [76] showed that by using the Biot-Savart law, the induced velocities near a lifting rotor could be calculated as:

$$\lambda^I = -\frac{1}{4\pi}\int_0^{2\pi} F(\psi)\frac{1-(x\cos\psi + y\sin\psi) + R_c\sin\chi\cos\psi}{[R_c + (\cos\psi - x)\sin\chi + z\cos\psi]R_c}d\psi \tag{8.11}$$

where

$$F(\psi) = \gamma_0 + \gamma_{1c}\cos\psi + \gamma_{1s}\sin\psi$$

$$R_c = \sqrt{1 + x^2 + y^2 + z^2 - 2(x\cos\psi + y\sin\psi)}$$

In Eq. (8.11), x, y, z represent Cartesian coordinates normalized by rotor radius, $F(\psi)$ is the vorticity variation around the azimuth. Uniform (γ_0), cosine (γ_{1c}), and sine (γ_{1s}) parts

of the vorticity are related to C_T, C_M, and C_L using the following relations [19]:

$$\gamma_0 = \frac{C_T}{V_T(1-1.5\mu^2)} + \frac{3\mu C_L}{V_T(1-1.5\mu^2)}$$

$$\gamma_{1c} = -\frac{3C_M}{V_T} \tag{8.12}$$

$$\gamma_{1s} = -\frac{3C_L}{V_T(1-1.5\mu^2)} - \frac{1.5\mu C_T}{V_T(1-1.5\mu^2)}$$

Using Eqs. (8.11) and (8.12), interference inflow distribution at any rotor or lifting and non-lifting surfaces can be calculated. Then, uniform and the first harmonic inflow components are extracted using the following double integrals.

$$\lambda_0^I = \frac{1}{\pi}\int_0^{2\pi}\int_0^1 \lambda^I(\bar{r},\psi)\bar{r}\,d\bar{r}\,d\psi \tag{8.13}$$

$$\lambda_{1c}^I = \frac{4}{\pi}\int_0^{2\pi}\int_0^1 \lambda^I(\bar{r},\psi)\bar{r}^2\cos(\psi)\,d\bar{r}\,d\psi \tag{8.14}$$

$$\lambda_{1s}^I = \frac{4}{\pi}\int_0^{2\pi}\int_0^1 \lambda^I(\bar{r},\psi)\bar{r}^2\sin(\psi)\,d\bar{r}\,d\psi \tag{8.15}$$

For a multi-rotor system with N number of rotors, interference inflow calculation should be repeated for $(N-1)$ times to find total interference inflow on a single rotor. To obtain total interference inflow corresponding to every rotor, calculations should be repeated for $(N-1)\times N$ times. The following equation describes the indexing used to calculate total interference inflow components at the j^{th} rotor.

$$\{\lambda_0^{j,I},\ \lambda_{1c}^{j,I},\ \lambda_{1s}^{j,I}\} = \sum_{k=1,\ k\neq j}^{N}\{\lambda_0^{k,I},\ \lambda_{1c}^{k,I},\ \lambda_{1s}^{k,I}\} \tag{8.16}$$

It is important to recognize that self-induced uniform inflow and interference uniform

inflow components are directly coupled through Eqs. (8.8) and (8.13). Interference uniform inflow component modifies the wake skew angle (χ), the total flow passing through each rotor (V_T), and the mass flow parameter (V). Therefore, calculation of Eq. (8.13) is a must while Eqs. (8.14) and (8.15) are optional. These equations are optional because instead of extracting interference inflow components (λ_0^I, λ_{1c}^I, λ_{1s}^I), one may prefer to superimpose interference inflow ($\lambda^I(\bar{r}, \psi)$) directly at the aerodynamic calculation points. To find interference inflow ($\lambda^I(x, y, z)$) at the empennage, fuselage, or any other aerodynamic surface, Eqs. (8.11) and (8.12) can be used to find interference inflow contribution of each rotor.

The developed model, CMTSVT, is generic and applicable to any configuration since interference inflow calculation locations can be freely changed even during the simulation. This model provides a fast and simple approach to predict multi-rotor inflow at the expense of simplifying assumptions: rigid wake geometry and potential flow. On the other hand, identified multi-rotor inflow models are configuration specific and must be re-identified from the higher-order wake models whenever vehicle configuration is updated. Further, higher-order wake models may require more detailed rotor geometry to carry out simulations than the simpler models, and such detailed rotor geometry may not be available during the initial design stages involving design trade studies.

The CMTSVT is fast because Eq. (8.11) is an integral in closed form, which can be represented as a quadrature. For a dual-rotor configuration, the model converges to a steady-state solution in less than 0.5 second in MATLAB® that runs in a computer with an AMD Ryzen 5 1400 CPU and 8 GB RAM. Even for the initial implementation, the speed of CMTSVT is quite encouraging. The model can be extremely fast with more efficient implementation and better hardware. Furthermore, given the interference inflow calculation locations (x, y, z) and the wake skew angle (χ), Eq. (8.11) can be computed offline and represented as series of coefficients multiplied by the uniform (γ_0), cosine (γ_{1c}), and sine (γ_{1s}) parts of the vorticity. Like Eq. (8.11), extractions of uniform and the first harmonic inflow components (see Eqs. (8.13)–(8.15)) can be represented by summations, which will

further speed-up the model solution.

8.4 Evaluation of the CMTSVT

The assessment of CMTSVT consists of two parts: (1) CMTSVT model predictions are compared against the VPSIM predictions in hover for a dual-rotor configuration with varying longitudinal separation distance between the rotors, (2) CMTSVT predictions of the Harrington coaxial rotor configuration are compared against previously published results of VPSIM, GT-Hybrid, and VVPM (Ref. [42]) for various advance ratios. Reference [67] also includes CMTSVT inflow distributions in hover and at advance ratio of 0.10 for a quad-rotor configuration with partially overlapping rotors.

8.4.1 Effect of Longitudinal Separation Distance in a Dual-Rotor Configuration

Similar to the study conducted in chapter 5.1, the effect of the longitudinal separation distance is examined. The longitudinal separation distance between the Harrington rotors is gradually increased from 0.0 to 2.0 rotor radius. The thrust coefficient is set to 0.0035 for both rotors, while aerodynamic hub moments are set to 0.0. Figure 8.1 shows total uniform inflow predictions for various values of longitudinal separation distance between the upper and lower rotors. The developed model, CMTSVT, captures the uniform inflow trend of VPSIM at both rotors. On the other hand, neglecting the interference inflow gives rise to unrealistic inflow predictions, especially at the lower rotor with an overlap between the rotors. It should be noted that VPSIM simulations are carried out with 15 odd 15 even velocity potential states. Even with a simple representation, CMTSVT inflow predictions, although slightly larger, are in line with VPSIM results. These larger uniform inflow predictions might be related to the neglected inner wake in the interference inflow calculation. Another possibility might be the neglected radial vorticity distribution ($F(\psi)$).

Reference [51] provides alternative relations to Eq. (8.12) while assuming several different radial vorticity distributions. For future work, these alternative relations can be tested to achieve better correlations.

Next, longitudinal inflow predictions for various values of longitudinal separation distance between the rotors are illustrated in Fig. 8.2. Again, CMTSVT shows a good correlation with VPSIM in the predictions of upper and lower rotors longitudinal inflow components in hover. Without the inflow interference, the model predicts zero longitudinal inflow components for both rotors regardless of the longitudinal separation distance. From the results shown in Fig. 8.2, it is seen that the longitudinal inflow components can become as large as uniform inflow components at some separation distances. These may significantly affect the rotor loads, performance, and trim condition of the vehicle.

While uniform and first harmonic inflow components provide valuable information about the interference inflow, it is also crucial to check inflow distribution for a detailed understanding of the interference inflow. Figures 8.3 and 8.4 show the inflow distributions obtained by VPSIM and CMTSVT for the longitudinal separation distances of 1.0 and 1.5 rotor radius, respectively. The front region of the lower rotor is subject to a large downwash induced by the upper rotor. Likewise, the aft region of the upper rotor is subject to interference inflow caused by the lower rotor, although the magnitude of interference is smaller. It is why nonzero longitudinal interference components exist even in hover when rotors are longitudinally separated. The area of interference becomes smaller when the separation distance is increased from 1.0R to 1.5R, as expected. The predictions of inflow distributions using the CMTSVT and VPSIM are very similar.

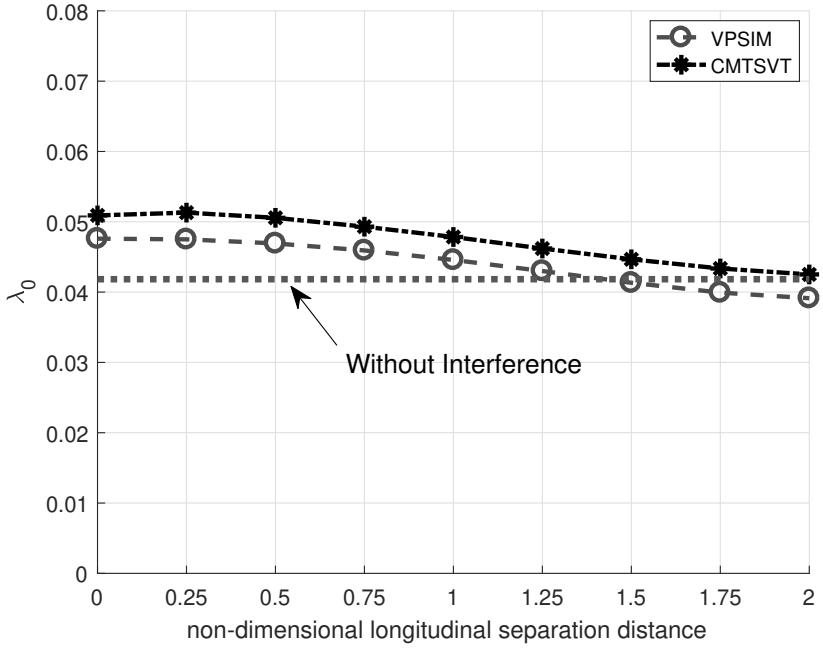

(a) Upper rotor

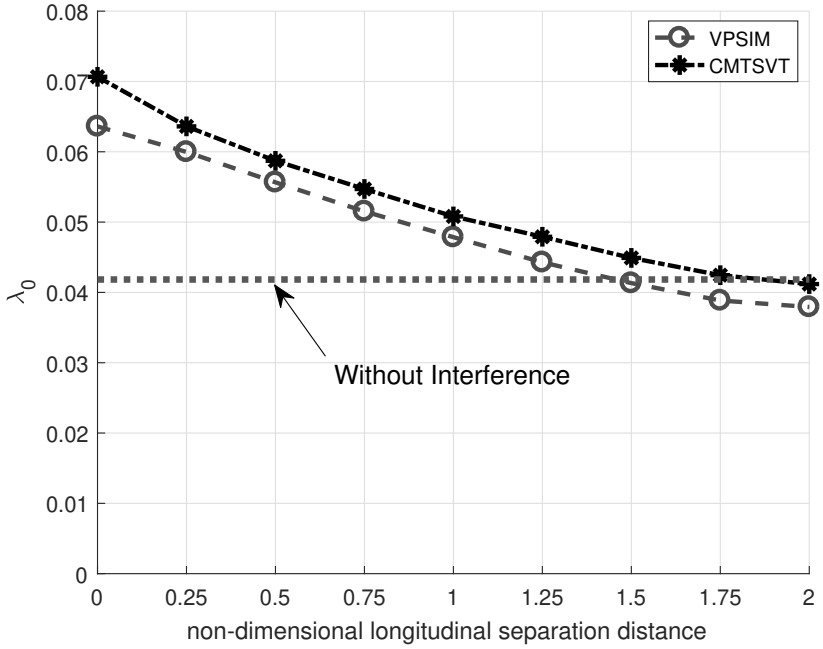

(b) Lower rotor

Figure 8.1: Comparison of CMTSVT and VPSIM uniform inflow predictions for various values of non-dimensional longitudinal separation distance (normalized by rotor radius) in hover

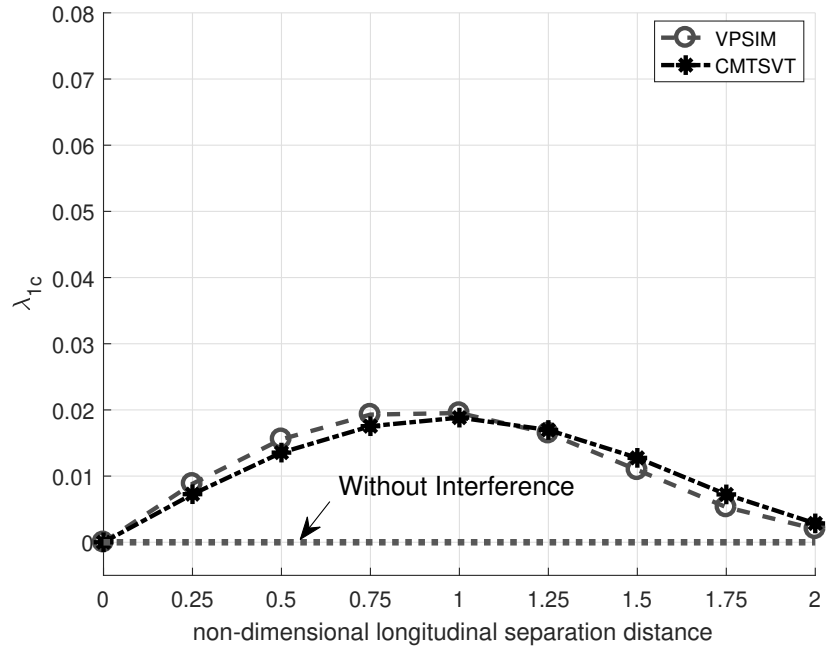

(a) Upper rotor

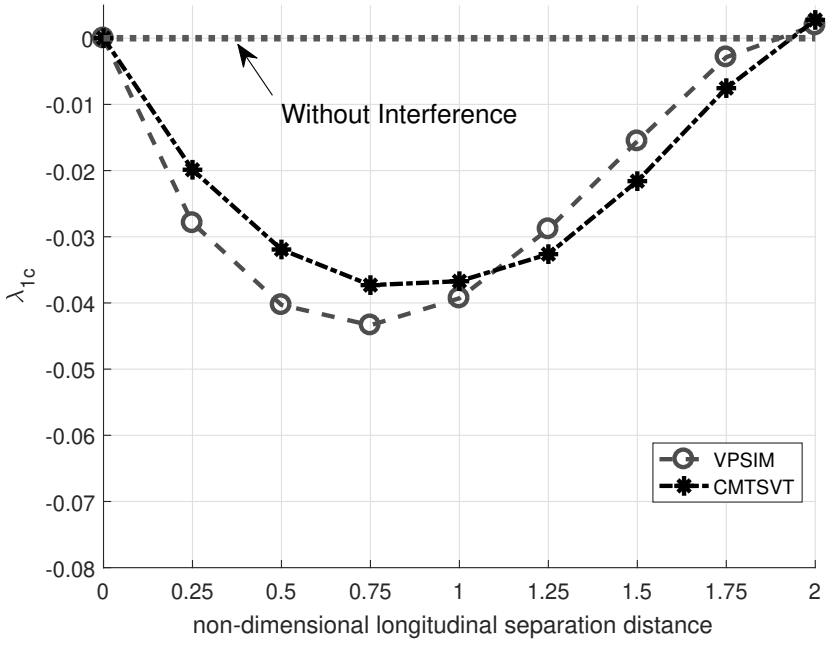

(b) Lower rotor

Figure 8.2: Comparison of CMTSVT and VPSIM longitudinal inflow predictions for various values of non-dimensional longitudinal separation distance (normalized by rotor radius) in hover

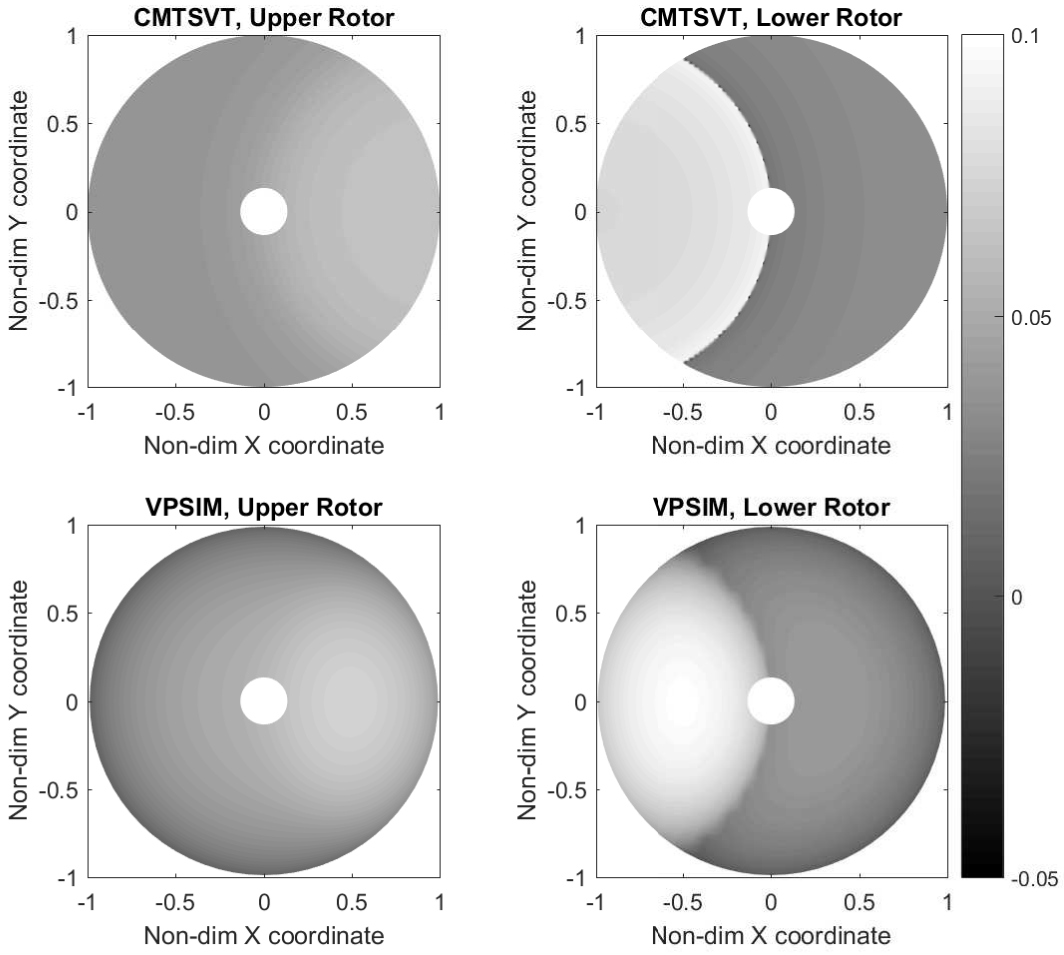

Figure 8.3: Comparison of CMTSVT and VPSIM inflow distributions for the longitudinal separation distance of 1.0R in hover

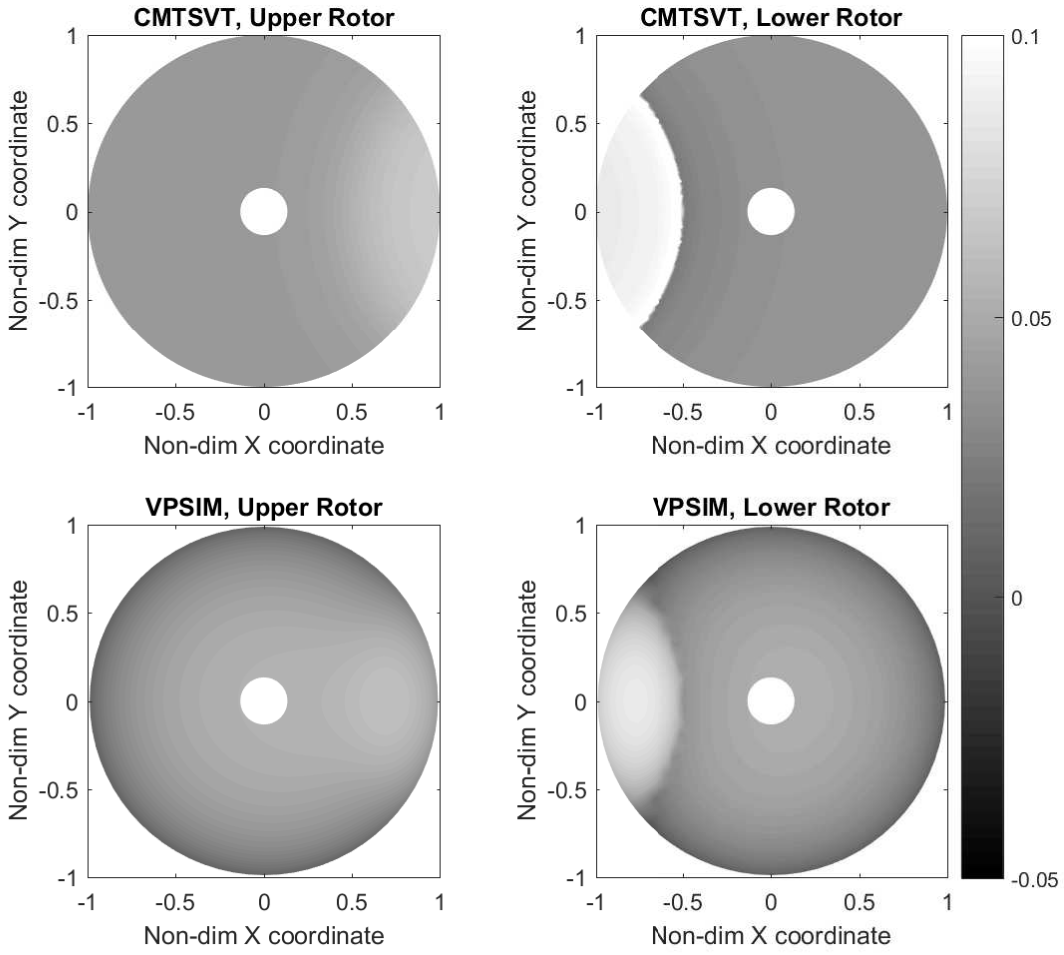

Figure 8.4: Comparison of CMTSVT and VPSIM inflow distributions for the longitudinal separation distance of 1.5R in hover

8.4.2 Coaxial Rotor Inflow Predictions

In this part, advance ratio is varied from 0 to 0.24 for inflow predictions of the Harrington coaxial rotor. The details of the simulation conditions are provided in Ref. [42], in which VPSIM was already validated against VVPM and GT-Hybrid. Here, CMTSVT coaxial rotor inflow predictions are compared against the GT-Hybrid, VVPM, and VPSIM. Besides, inflow predictions without rotor-on-rotor flow interference are also provided to gain further insight regarding interference inflow effects.

The uniform inflow predictions of CMTSVT and VPSIM are quite similar to each other at both rotors for every advance ratio case considered, as shown in Fig. 8.5. In hover, CMTSVT and VPSIM predictions have larger uniform inflow components at both rotors than the GT-Hybrid and VVPM uniform inflow predictions. CMTSVT and VPSIM assume a rigid cylindrical wake geometry and neglect real flow effects such as the wake contraction and diffusion. For example, Ref. [42] have shown that implementing the wake contraction effect into VPSIM results in much better uniform inflow predictions in hover. These real flow effects can also be introduced to CMTSVT for better hover correlation. As advance ratio becomes higher, differences between the multi-rotor inflow models and the inflow model without interference become smaller since the interference inflow magnitude decreases with speed as the area of interference becomes smaller at higher speeds. At low speeds, the effect of inflow interference is considerably high, especially for the lower rotor, and should be incorporated into inflow predictions.

Like the uniform inflow predictions, Fig. 8.6 shows that the longitudinal inflow component predictions of CMTSVT, GT-Hybrid, and VPSIM have good agreement, while the VVPM predictions are slightly higher for all advance ratio cases considered. The inflow model without rotor-on-rotor inflow interference considerably underestimates the longitudinal inflow components of both rotors at every forward flight case. These inflow predictions confirm that simple vortex theory interference inflow addition clearly improves the overall inflow correlation. The significance of rotor-on-rotor interference on the longitudi-

nal inflow component predictions can be seen at all speeds. Because of the inflow interference, larger longitudinal inflow components are predicted by VPSIM and CMTSVT at both rotors for all forward flight cases.

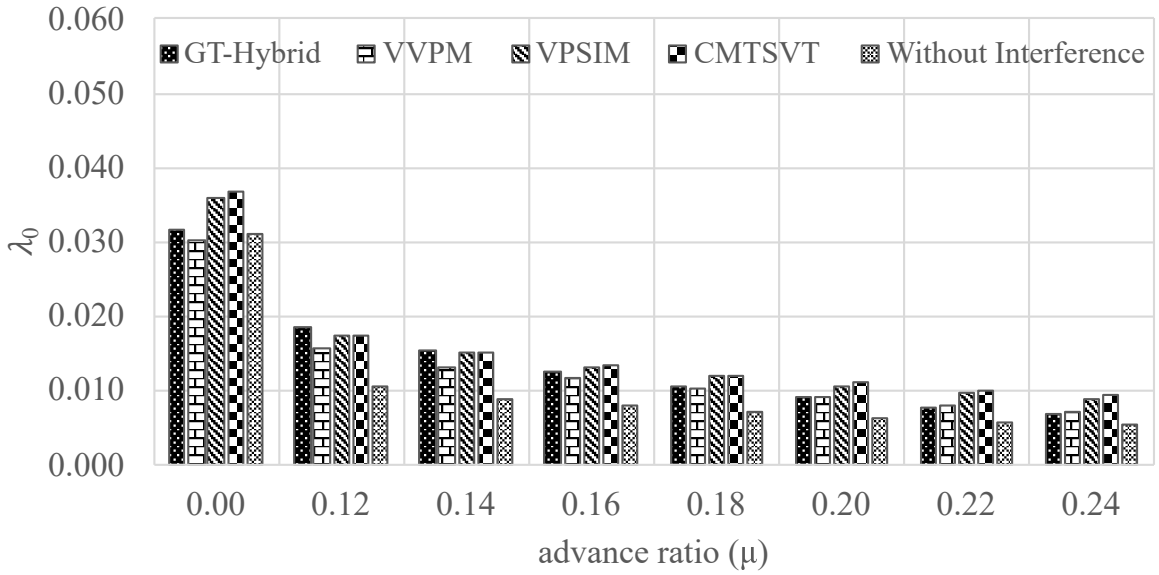

(a) Upper rotor

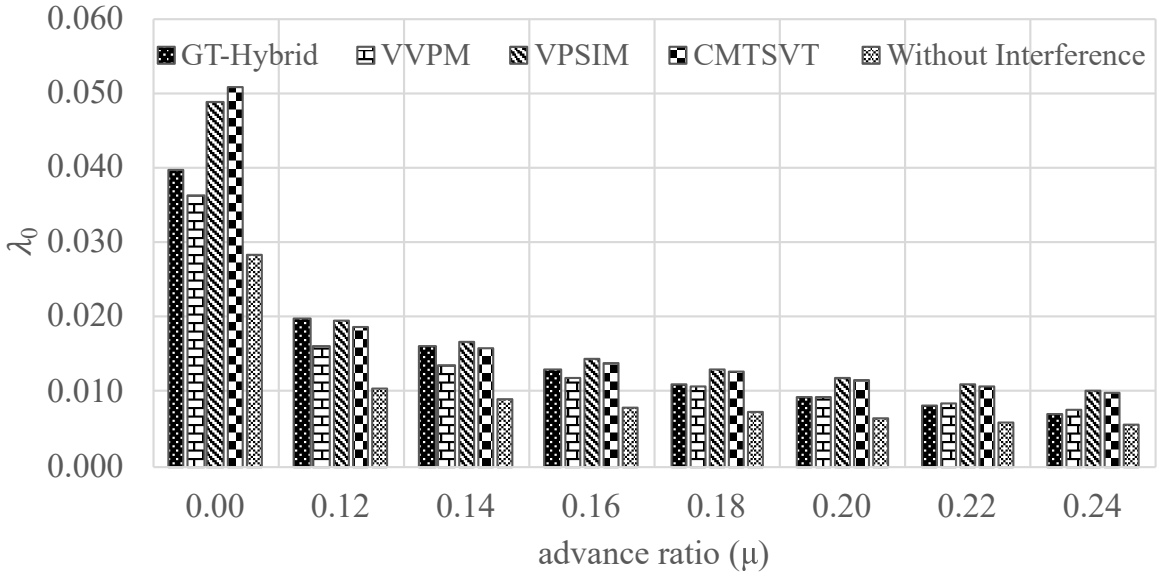

(b) Lower rotor

Figure 8.5: Comparison of GT-Hybrid, VVPM, VPSIM, and CMTSVT coaxial rotor uniform inflow predictions for various advance ratios

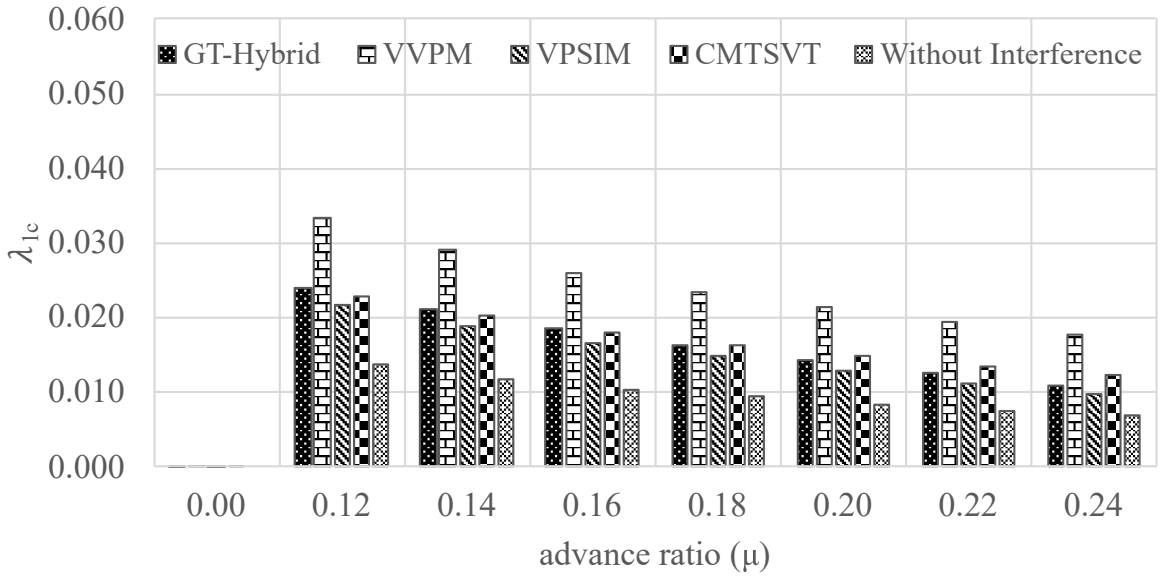

(a) Upper rotor

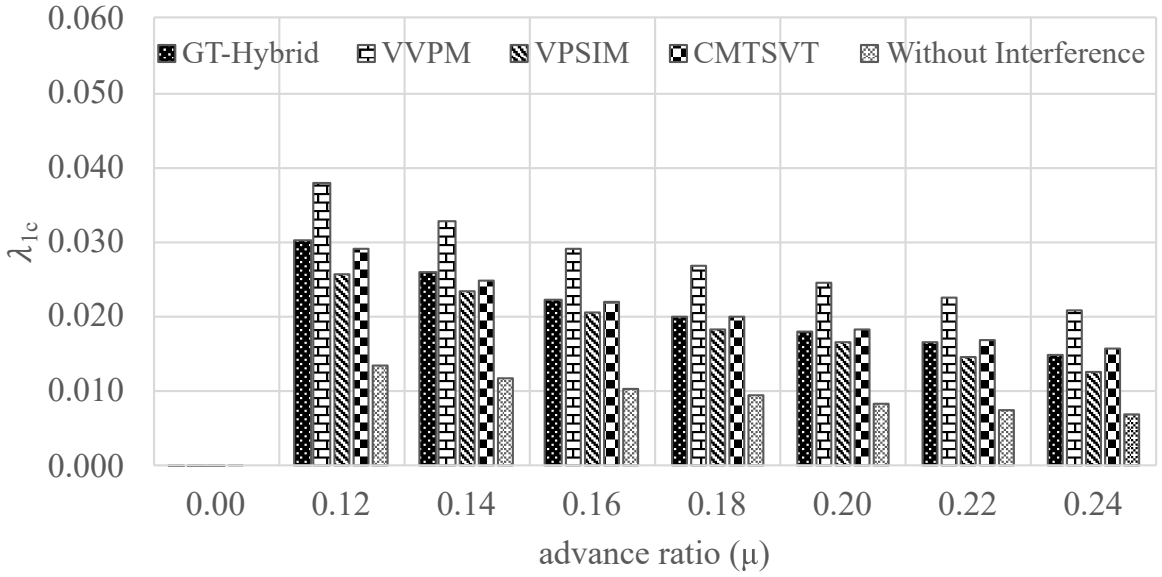

(b) Lower rotor

Figure 8.6: Comparison of GT-Hybrid, VVPM, VPSIM, and CMTSVT coaxial rotor longitudinal inflow predictions for various advance ratios

CHAPTER 9
SUMMARY, CONCLUSIONS, AND FUTURE WORK

9.1 Summary

In this dissertation, a finite state dynamic inflow model for generic multi-rotor configurations has been developed using the velocity potential superposition approach. Together with the recently developed multi-rotor pressure potential superposition inflow model, finite state multi-rotor dynamic inflow models are compared against a more comprehensive Viscous Vortex Particle Method (VVPM) for different configurations. Additional inflow comparison cases are also provided for VPSIM using the Combined Momentum Theory and Simple Vortex Theory (CMTSVT) inflow model. This study limits the number of rotors to two and inflow variations to uniform, fore-to-aft (longitudinal), and side-to-side (lateral) components for ease of comparison.

In chapter 2, the detailed formulation of the multi-rotor Velocity Potential Superposition Inflow Model (VPSIM) is provided. The mass flow parameter matrices and skew angles of the VPSIM are modified to account for mutual interference effects between the rotors. In addition to the VPSIM, formulation of the previously developed Pressure Potential Superposition Inflow Model (PPSIM) is summarized and common limitations, advantages, and disadvantages of the finite state multi-rotor dynamic inflow models are explained.

In chapter 3, inflow simulation and comparison methodologies are described. The truth model, Viscous Vortex Particle Method (VVPM), and procedures to simulate VVPM, VPSIM, and PPSIM are explained in detail. Equations for extracting the first harmonic inflow components in terms of Pitt-Peters and Peters-He states are provided. Then, methods for quantifying inflow responses are described to examine the quality of the matches between the VVPM and finite state multi-rotor dynamic inflow models.

In chapter 4, differences between two finite state multi-rotor dynamic inflow models, i.e., PPSIM and VPSIM, are pointed out, and connection between them are shown by comparing their inflow influence coefficient matrices for Harrington coaxial rotor. Then, the effect of the number of odd and even velocity potential states on inflow dynamics is studied in the frequency domain by exciting upper rotor pressure coefficients with a sinusoidal frequency sweep. Finally, PPSIM with different number of inflow states and VPSIM with different number of velocity potential states are compared against a high-fidelity numerical model known as the Viscous Vortex Particle Method (VVPM).

In chapter 5, baseline models are established for each multi-rotor dynamic inflow model to understand and pinpoint the differences among VPSIM, PPSIM, and VVPM. In particular, the effect of the longitudinal separation distance is studied using VPSIM and VVPM. Then, a detailed comparison study is carried out for a selected tandem rotor configuration using results of steady-state inflow, steady-state perturbation inflow, and unsteady inflow. Findings of this chapter support that VPSIM and PPSIM can capture some of the fundamental interference effects between the rotors for different configurations. Some of the differences between the finite state multi-rotor dynamic inflow models and VVPM are attributed to the missing real flow effects in the finite state multi-rotor dynamic inflow models. These missing effects are wake contraction/expansion, wake diffusion, wake distortion, wake roll-up, and swirl velocity.

In chapter 6, a new system identification methodology has been developed to incorporate real flow effects into the Velocity Potential Superposition Inflow Model (VPSIM). The real flow effects, such as due to wake contraction/expansion, wake distortion, wake diffusion, wake swirl, and wake roll-up, are included through modifications to inflow influence coefficient matrices and interference inflow terms of the VPSIM. This identification method effectively reduces the steady-state perturbation inflow differences between VPSIM and VVPM. From the results presented, it is seen that identified correction terms are relatively insensitive to changes in the rotor loadings. Besides, the usage of these identified

terms generally improves the unsteady inflow correlations between VPSIM and VVPM in the frequency domain. Lastly, identified terms with small magnitudes are removed to pinpoint significant missing real flow effects in the VPSIM.

In chapter 7, alternative methods for computing costates of the velocity potential finite state dynamic wake model are proposed based on quasi-steady approximations. The first approximation (Model–1) uses a quasi-steady representation of the costate equation in the computation of inflow velocities below the rotor. The second approximation (Model–2) uses, in addition to a quasi-steady representation of the costate equation, velocity potential states that are averaged over the wake propagation time for a selected location below the rotor. The proposed approximations remove the requirement of backward time integration, making the velocity potential finite state dynamic wake model feasible for integration into real-time flight dynamics simulations. The loss of fidelity arising from the proposed approximations is assessed by comparing inflow velocity predictions at two different locations below the rotor for various advance ratios and loading conditions for an isolated rotor. The loss of fidelity in the vehicle flight dynamics simulations arising from the approximations to the inflow model is further assessed using a nonlinear longitudinal flight dynamics model of the UH-60 helicopter.

In chapter 8, a new multi-rotor inflow model, which combines momentum theory with a simple vortex theory, is introduced. The developed model, Combined Momentum Theory and Simple Vortex Theory (CMTSVT), captures the fundamental interference effects while retaining the simplified modeling approach of the fundamental theories. Although the current formulation is only provided for the steady flow, the model can be extended to the unsteady flow regime by introducing time constants. Both self-induced and interference inflow time constants can be identified from the VPSIM, PPSIM, or any higher-order wake models, i.e., VVPM. The CMTSVT benefits from its modular structure and simplified modeling approach while capturing the fundamental interference effects. Although the developed model assumes rigid wake geometry and potential flow like VPSIM and PPSIM,

it is possible to improve this model by incorporating real flow effects.

9.2 Conclusions

The major contributions of this work are summarized as follows:

1. A new nonlinear finite state multi-rotor dynamic inflow model based on the superposition of velocity potentials of individual rotors is formulated for generic multi-rotor configurations.

2. VPSIM and previously developed PPSIM are evaluated against a higher-order wake model known as VVPM and shown to capture fundamental interference effects for different configurations.

3. A system identification methodology is developed to include missing real flow effects such as wake contraction/expansion, wake distortion, wake swirl, wake decay, and wake roll-up, which were neglected in the original VPSIM formulation.

4. Two quasi-steady approximations to the costates and a convolution integral solution are proposed to remove backward time marching solution of the costates, which are required in the calculation of the interference velocity below the rotor plane.

The following specific conclusions can be drawn from the results presented in this dissertation:

Chapter 4:

1. Comparison of VPSIM against PPSIM and VVPM shows that the superposition of velocity potentials is a feasible approach to take into account the effects of inflow interference.

2. VPSIM with even velocity potential state cases show magnitude drop at lower frequencies than the VPSIM with only odd velocity potential state cases at both upper

and lower rotors.

3. All VPSIM cases exhibit time delay at the lower rotor inflow response, whereas PPSIM does not consider this effect.

4. PPSIM, VPSIM, and VVPM present an overall good match with each other in uniform and fore-to-aft inflow predictions at both upper and lower rotors.

5. Inflow distributions of PPSIM and VPSIM converge to the inflow distribution of VVPM at both upper and lower rotors as the number of terms in the inflow expansion increases.

Chapter 5:

6. Finite state multi-rotor dynamic inflow models have ability to capture inflow interference effects for configurations with different separation distances.

7. Despite the fact that aerodynamic pitch moments of both rotors are set to zero, the longitudinal separation distance creates fore-to-aft inflow components with opposite signs in hover because of the partially overlapping interference area.

8. When rotors are separated longitudinally, fore-to-aft inflow component of the lower rotor becomes more sensitive to changes in the upper rotor thrust and aerodynamic pitch moment due to the partially overlapping interference area.

9. The frequency response plots show that VPSIM generally has better agreement with the VVPM compared to the PPSIM, especially for phase angle predictions. VPSIM captures the time delay effect associated with wake propagation, whereas there is no time delay in the wake estimated by the PPSIM. Therefore, phase angle predictions of the VPSIM match better with those of the VVPM over a broader range of frequencies, especially for the lower rotor.

10. From comparison studies, differences among the inflow models such as excessive upwash region in hover, wake distortion at low speed flight, and fore-to-aft to side-to-side inflow couplings due to swirl velocities are identified. Despite these differences, PPSIM and VPSIM correlate well with the VVPM at all flight conditions.

Chapter 6:

11. A new system identification methodology for the VPSIM is successfully developed to incorporate real flow effects into the VPSIM. The improved VPSIM shows a significantly better correlation with the VVPM than the original VPSIM for various flight conditions.

12. In hover, cosine-sine coupling due to the swirl velocity is found to be significant. This coupling is the main reason of the mismatch between the VVPM and VPSIM. As speed increases, the strength of cosine-sine coupling becomes weaker.

13. Identified correction terms are reasonably insensitive to changes in the initial rotor thrust sharing conditions. Instead of using table look-ups for all thrust sharing conditions, a second order curve-fitted correlations between the correction terms and wake skew functions are provided for more straightforward implementation.

14. Although correction terms are identified from the steady-state inflow perturbation results, the addition of these terms considerably improves the unsteady inflow correlations between the VPSIM and VVPM with a few exceptions.

15. The number of correction terms can be reduced by checking the gradient of the cost function with respect to each correction term. The number of correction terms is effectively reduced to half of the original number at the expense of a slight loss of accuracy.

Chapter 7:

16. At higher frequencies, the first approximation to the costate equation, which uses Eq. (7.5) for costate computation and is referred to as Model–1, gives rise to the fidelity loss for inflow predictions arising from high frequency rotor loading variations.

17. The loss of fidelity in the inflow predictions due to high frequency rotor loading variations arising from Model–1 approximation is somewhat reduced with the use of the second approximation to the costate equation, which uses Eq. (7.6) for costate computation and is referred to as Model–2.

18. Both Model–1 and Model–2 approximations retain inflow model fidelity over the typical frequency range of pilot control inputs.

19. If horizontal tail aerodynamic center is outside of the rotor wake or if dynamic pressure at the horizontal tail aerodynamic center is low, then the vehicle response is dominated by the variations in rotor loads. As such, for these cases, there is a slight loss of fidelity in the vehicle response due to collective or longitudinal cyclic control input with either Model–1 or Model–2 approximation to the inflow model.

20. When dynamic pressure at the horizontal tail aerodynamic center is high, for example, at the advance ratio of 0.2 or higher, both Model–1 and Model–2 approximations to the inflow model result in a noticeable loss of fidelity in vehicle response predictions, especially for control variations at the high frequency range.

21. When dynamic pressure at the horizontal tail aerodynamic center is not large, simulations with quasi-steady off-rotor inflow predictions show good correlations with the simulations of the Costate solution since main rotor forces and moments dominate the vehicle response.

Chapter 8:

22. A new multi-rotor inflow model is developed by combining momentum theory with a simple vortex theory (CMTSVT) for steady-state inflow predictions.

23. The developed model captures fundamental steady-state interference effects while retaining the simplified modeling approach.

24. The model can be used for early design stages involving performance and vehicle configuration trade studies of generic multi-rotor configurations.

9.3 Future Work

The following work is recommended to future researchers:

1. The effects of sideslip angle, climb rate, descend rate, and shaft-tilt angle on interference inflow predictions should be studied for multi-rotor configurations.

2. Effect of inflow interference on vortex ring state can be studied to determine operational limits of the multi-rotor configurations during descending flight.

3. Validation studies for the finite state multi-rotor dynamic inflow models can be further extended to other configurations with more than two rotors.

4. Although proposed quasi-steady approximations of costate equations are shown to retain fidelity in vehicle response predictions of a nonlinear longitudinal flight dynamics model, more work is needed for assessing the simulation model fidelity using full-flight vehicle simulations.

5. So far, VPSIM is validated against the VVPM. Additional validation studies for VPSIM can be carried out using available experimental data or other higher-order wake models.

6. It might be interesting to establish a sizing and performance analysis tools for multi-rotor configurations using VPSIM.

7. Despite the fact that VPSIM captures the time delay effect associated with the wake propagation, it showed some differences compared to the VVPM. In VPSIM, the time delay is computed by dividing the distance between the rotors by the total velocity passing from the rotor that is located above the other one. However, the wake starts to accelerate immediately after leaving the rotor, which is neglected in the VPSIM time delay computation. A new relation that takes into account this acceleration should be utilized for a better correlation with the VVPM or other higher-order wake models.

Appendices

APPENDIX A

ELLIPSOIDAL COORDINATE SYSTEM

The ellipsoidal coordinate system ($\nu,\ \eta,\ \psi$) is defined as:

$$\bar{x} = -\sqrt{1-\nu^2}\sqrt{1+\eta^2}cos(\psi) \tag{A.1}$$

$$\bar{y} = \sqrt{1-\nu^2}\sqrt{1+\eta^2}sin(\psi) \tag{A.2}$$

$$\bar{x} = -\nu\eta \tag{A.3}$$

where $\bar{x},\ \bar{y},\ \bar{z}$ are the Cartesian coordinates normalized with rotor radius. The values of $\nu,\ \eta,\ \psi$ cover entire 3-dimensional space if they are restricted to the following ranges:

$$-1 \leq \nu \leq 1 \tag{A.4}$$

$$0 \leq \eta \leq \infty \tag{A.5}$$

$$0 \leq \psi \leq 2\pi \tag{A.6}$$

Figure A.1 shows the ellipsoidal coordinate system viewed in the $\bar{x} - \bar{z}$ plane. While ν defines constant hyperboloid surfaces, η defines constant ellipsoid surfaces. Both families of surfaces are azimuthally symmetric about the $\bar{z}$-axis. When $\eta = 0$, surfaces represent the two faces of the disk, and ν changes sign across the disk. The inverse of Eqs. (A.1) through (A.3) is given as:

$$\nu = -\frac{sign(\bar{z})}{\sqrt{2}}\sqrt{(1-\bar{S}) + \sqrt{(1-\bar{S})^2 + 4\bar{z}^2}} \tag{A.7}$$

$$\eta = \frac{1}{\sqrt{2}}\sqrt{(\bar{S}-1) + \sqrt{(\bar{S}-1)^2 + 4\bar{z}^2}} \tag{A.8}$$

$$\psi = \tan^{-1}\left(\frac{-\bar{y}}{\bar{x}}\right) \tag{A.9}$$

where

$$\bar{S} = \bar{x}^2 + \bar{y}^2 + \bar{z}^2 \tag{A.10}$$

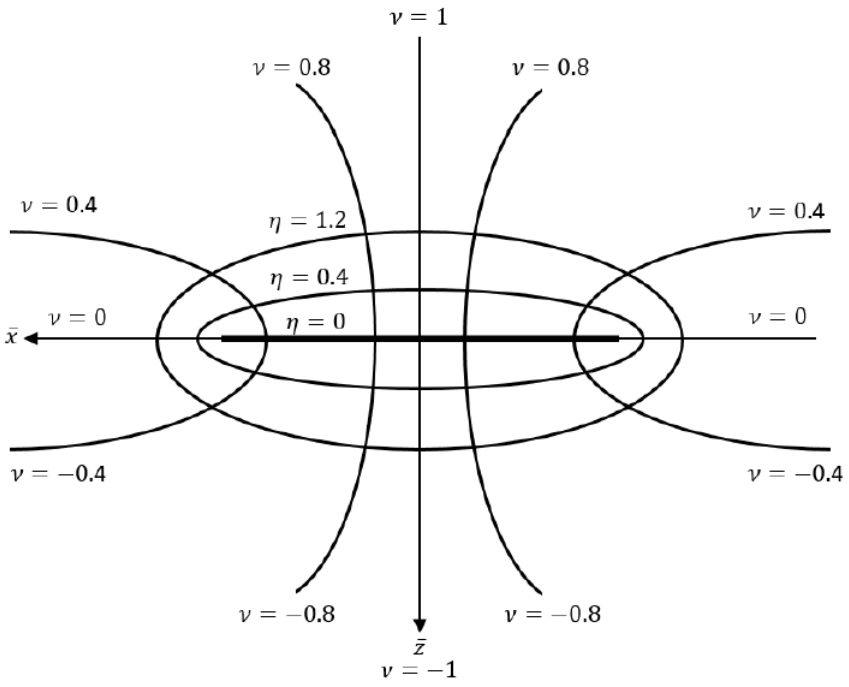

Figure A.1: Ellipsoidal coordinate system

The Laplace equation ($\vec{\nabla}^2\Phi = 0$) in the ellipsoidal coordinate system takes the following form:

$$\frac{\partial}{\partial\nu}\left[(1-\nu^2)\frac{\partial\Phi}{\partial\nu}\right] + \frac{\partial}{\partial\eta}\left[(1+\eta^2)\frac{\partial\Phi}{\partial\eta}\right] + \frac{\partial}{\partial\psi}\left[\frac{\nu^2+\eta^2}{(1-\nu^2)(1+\eta^2)}\frac{\partial\Phi}{\partial\psi}\right] = 0 \tag{A.11}$$

Analytical solution of the Eq. (A.11) is arrived at by applying the method of separation of variables. The Φ is expressed by multiplication of three separated parts, which are the only function of ν, η, or ψ, respectively.

$$\Phi(\nu,\eta,\psi) = V(\nu)N(\eta)W(\psi) \tag{A.12}$$

After substituting Eq. (A.12) into Eq. (A.11), the Laplace equation is separated into the following three equations:

$$\frac{\partial^2 W}{\partial \psi^2} + m^2 W = 0 \tag{A.13}$$

$$\frac{\partial}{\partial \nu}\left[(1-\nu^2)\frac{\partial V}{\partial \nu}\right] + \left[-\frac{m^2}{1-\nu^2} + n(n+1)\right] V = 0 \tag{A.14}$$

$$\frac{\partial}{\partial \eta}\left[(1+\eta^2)\frac{\partial N}{\partial \eta}\right] + \left[-\frac{m^2}{1+\eta^2} - n(n+1)\right] N = 0 \tag{A.15}$$

where m and n are the separation constants. Here, m and n are the harmonic number and radial mode number, respectively, in the finite state dynamic inflow model. It is recognized that Eqs. (A.14) and (A.15) are forms of Legendre's associated differential equation [77]. While $\bar{P}_n^m(\nu)$ and $\bar{Q}_n^m(\nu)$ are the general solutions of Eq. (A.14), $\bar{P}_n^m(i\eta)$ and $\bar{Q}_n^m(i\eta)$ are the general solutions of Eq. (A.15). The solutions related to $\bar{P}_n^m(i\eta)$ and $\bar{Q}_n^m(\nu)$ are excluded as they give rise to infinite pressure in the flow field.

APPENDIX B

NORMALIZED ASSOCIATED LEGENDRE FUNCTIONS

The normalized associated Legendre functions of the first and second kinds used in this dissertation are defined as:

$$\bar{P}_n^m(\nu) = (-1)^m \frac{P_n^m(\nu)}{\rho_n^m} \tag{B.1}$$

$$\bar{Q}_n^m(i\eta) = \frac{Q_n^m(i\eta)}{Q_n^m(i0)} \tag{B.2}$$

where

$$\rho_n^m = \sqrt{\int_0^1 (P_n^m(\nu))^2 d\nu} = \sqrt{\frac{1}{2n+1}\frac{(n+m)!}{(n-m)!}} \tag{B.3}$$

$$Q_n^m(i0) = \begin{cases} \frac{\pi}{2}(-1)^{m+n+1}(i)^{n+1}\frac{(n+m-1)!!}{(n-m)!!} & \text{if } m+n = even \\ (-1)^{m+n+1}(i)^{n+1}\frac{(n+m-1)!!}{(n-m)!!} & \text{if } m+n = odd \end{cases} \tag{B.4}$$

All required values of $\bar{P}_n^m(\nu)$ and $\bar{Q}_n^m(i\eta)$ are numerically calculated for desired harmonic number (m) and radial mode number (n) using the following recurrence relations:

$$\bar{P}_{n+1}^m(\nu) = \sqrt{\frac{(2n+3)(2n+1)}{(n+1)^2-m^2}}\left[\nu\bar{P}_n^m(\nu) - \sqrt{\frac{n^2-m^2}{4n^2-1}}\bar{P}_{n-1}^m(\nu)\right] \tag{B.5}$$

$$\bar{P}_{n+1}^m(\nu) = \sqrt{\frac{(2n+3)}{(n+m+1)(n+m)}}\left[\sqrt{\frac{(n-m+1)(n-m)}{2n-1}}\bar{P}_{n-1}^m(\nu) + \sqrt{1-\nu^2}\sqrt{2n+1}\bar{P}_n^{m-1}(\nu)\right] \tag{B.6}$$

$$\bar{P}_n^{m+1}(\nu) = \frac{1}{\sqrt{1-\nu^2}}\left[\sqrt{\frac{(2n+1)(n+m)}{(2n-1)(n+m+1)}}\bar{P}_{n-1}^m(\nu) - \frac{(n-m)}{\sqrt{(n+m+1)(n-m)}}\nu\bar{P}_n^m(\nu)\right] \tag{B.7}$$

$$\bar{Q}_{n+1}^m(i\eta) = \bar{Q}_{n-1}^m(i\eta) - (2n+1)K_n^m\eta\bar{Q}_n^m(i\eta) \tag{B.8}$$

$$\bar{Q}_n^{m+1}(i\eta) = \frac{1}{\sqrt{1+\eta^2}}\left[\bar{Q}_{n-1}^m(i\eta) - (n-m)K_n^m\eta\bar{Q}_n^m(i\eta)\right] \tag{B.9}$$

where

$$K_n^m = \left(\frac{\pi}{2}\right)^{(-1)^{n+m}} H_n^m \tag{B.10}$$

$$H_n^m = \frac{(n+m-1)!!(n-m-1)!!}{(n+m)!!(n-m)!!} \tag{B.11}$$

$$(i)!! = \begin{cases} (i)(i-2)(i-4)...(2) & \text{for } i\ even \\ (i)(i-2)(i-4)...(1) & \text{for } i\ odd \end{cases} \tag{B.12}$$

Special cases of double factorials are defined as:

$$(0)!! = 1, \qquad (-1)!! = 1, \qquad (-2)!! = \infty, \qquad (-3)!! = -1 \tag{B.13}$$

The recurrence relations for derivatives of $\bar{P}_n^m(\nu)$ and $\bar{Q}_n^m(i\eta)$ are given as:

$$(1-\nu^2)\frac{\partial\bar{P}_n^m(\nu)}{\partial\nu} = \sqrt{\frac{(2n+1)(n^2-m^2)}{2n-1}}\bar{P}_{n-1}^m(\nu) - n\nu\bar{P}_n^m(\nu) \tag{B.14}$$

$$(1-\nu^2)\frac{\partial\bar{P}_n^m(\nu)}{\partial\nu} = \sqrt{(n+m+1)(n-m)}\sqrt{1-\nu^2}\bar{P}_n^{m+1}(\nu) - m\nu\bar{P}_n^m(\nu) \tag{B.15}$$

$$(1+\eta^2)\frac{\partial\bar{Q}_n^m(i\eta)}{\partial\eta} = -\left[\frac{1}{K_n^m}\bar{Q}_{n+1}^m(i\eta) + (n+1)\eta\bar{Q}_n^m(i\eta)\right] \tag{B.16}$$

$$(1+\eta^2)\frac{\partial\bar{Q}_n^m(i\eta)}{\partial\eta} = \sqrt{1+\eta^2}\frac{Q_n^{m+1}(i0)}{Q_n^m(i0)}\bar{Q}_n^{m+1}(i\eta) + m\eta\bar{Q}_n^m(i\eta) \tag{B.17}$$

B.1 Orthogonality Integrals

$$\int_0^1 P_j^m(\nu)P_n^m(\nu)d\nu = \begin{cases} \delta_{jn} & \text{if } m+n=odd,\ m+j=odd \\ \delta_{jn} & \text{if } m+n=even,\ m+j=even \\ U_{jn}^m & \text{if } m+n=even,\ m+j=odd \end{cases} \tag{B.18}$$

where δ_{jn} is Kronecker delta, and U_{jn}^m is given as:

$$U_{jn}^m = \sqrt{\frac{H_n^m}{H_j^m}}\sqrt{\frac{(2j+1)(2n+1)}{(j+n+1)(j-1)}}(-1)^{\frac{j+n-2m-1}{2}} \tag{B.19}$$

B.2 Area Integrals

$$\int_0^1 P_j^m(\nu)P_n^m(\nu)\nu d\nu = \begin{cases} A_{jn}^m & \text{if } j+m=odd,\ m+n=odd \\ G_{jn}^m & \text{if } j+m=even,\ n+m=even \\ D_{jn}^m & \text{if } j+m=odd,\ n+m=even \end{cases} \tag{B.20}$$

where A_{jn}^m, G_{jn}^m, D_{jn}^m are given as:

$$A_{jn}^m = \frac{2}{\sqrt{H_n^m H_j^m}}\frac{\sqrt{(2n+1)(2j+1)}}{(n+j+2)(n+j)}\frac{(-1)^{\frac{n+j-2m}{2}}}{((j-n)^2-1)} \tag{B.21}$$

$$G_{jn}^m = \begin{cases} \sqrt{H_n^m H_j^m}\frac{\sqrt{(2n+1)(2j+1)}}{(n+j+2)(n+j)}\frac{(-1)^{\frac{n+j-2m}{2}}}{((j-n)^2-1)}\times & \\ (2m^2-n^2-j^2-n-j) & \text{if } j\neq 0,\ n\neq 0,\ m\neq 0 \\ 1/2 & \text{if } j=0,\ n=0,\ m=0 \end{cases} \tag{B.22}$$

$$D_{jn}^m = \begin{cases} \frac{1}{\sqrt{H_n^m H_j^m}}\frac{1}{\sqrt{(2j+1)(2n+1)}} & \text{if } j=n\pm 1 \\ 0 & \text{if } j\neq n\pm 1 \end{cases} \tag{B.23}$$

APPENDIX C

VPSIM MASS, DAMPING, AND INFLOW INFLUENCE COEFFICIENT MATRICES

The spatial part of the VPSIM velocity potential function, $\tilde{\Psi}_j^r$, and inflow matrices, $\tilde{M}$, $\tilde{D}$, $\tilde{L}$ are provided in this section.

$$\tilde{\Psi}_j^{rc} = \sigma_j^r \Phi_{j+1}^{rc} + \zeta_j^r \Phi_{j-1}^{rc} \tag{C.1}$$

$$\tilde{\Psi}_j^{rs} = \sigma_j^r \Phi_{j+1}^{rs} + \zeta_j^r \Phi_{j-1}^{rs} \tag{C.2}$$

$$\sigma_j^r = \frac{1}{K_j^r \sqrt{(2j+1)(2j+3)((j+1)^2 - r^2)}} \tag{C.3}$$

$$\zeta_j^r = \frac{1}{K_j^r \sqrt{(4j^2-1)(j^2-r^2)}}; \quad r \neq j \tag{C.4}$$

$$\Phi_j^{rc} = \bar{P}_j^r(\nu)\bar{Q}_j^r(i\eta)\cos(r\psi) \tag{C.5}$$

$$\Phi_j^{rs} = \bar{P}_j^r(\nu)\bar{Q}_j^r(i\eta)\sin(r\psi) \tag{C.6}$$

Equation (C.4) implies that the spatial part of the velocity potential function, $\tilde{\Psi}_j^r$ is only valid if $r \neq j$. When $r = j$, the following equations are used to avoid the singularity.

$$\tilde{\Psi}_r^{rc} = [\sigma_r^r \bar{P}_{r+1}^r(\nu)\bar{Q}_{r+1}^r(i\eta) + \bar{P}_{r-1}^r(\nu)\bar{Q}_{r-1}^r(i\eta)]\cos(r\psi) \tag{C.7}$$

$$\tilde{\Psi}_r^{rs} = [\sigma_r^r \bar{P}_{r+1}^r(\nu)\bar{Q}_{r+1}^r(i\eta) + \bar{P}_{r-1}^r(\nu)\bar{Q}_{r-1}^r(i\eta)]\sin(r\psi) \tag{C.8}$$

where

$$\bar{P}_{r-1}^r = \frac{2}{\pi}\sqrt{\frac{(2r)!!}{(2r+1)!!}}\frac{(1-\nu^2)^{r/2}}{(1+\nu)^r}\sum_{j=0}^{r-1}\frac{(r-1)!2^{r-j-1}(-1)^j}{(r-j-1)!(r+j)}(1-\nu)^j \tag{C.9}$$

$$\bar{Q}^r_{r-1} = \frac{1}{(1+\eta^2)^{m/2}} \tag{C.10}$$

Even with the Eq. (C.9), singularity still exists for the case $r = j = 0$. This singularity can be avoided by using the following expression.

$$\tilde{\Psi}^0_0 = \frac{2}{\pi}\nu\left[1 - \eta\tan^{-1}\left(\frac{1}{\eta}\right)\right] - \frac{2}{\pi}\ln \mid 1+\nu \mid -\frac{1}{\pi}\ln \mid 1+\eta^2 \mid +\frac{2}{\pi}\ln(Z_{max}) \tag{C.11}$$

where Z_{max} is a large number that represents the radius of integration along the free-stream direction, ξ.

C.1 Mass Matrix

$$\tilde{M}^{rm}_{jn} = \frac{2}{\sqrt{H^m_n H^r_j}} \frac{(-1)^{\frac{n+j-2m}{2}}\sqrt{(2n+1)(2j+1)}}{(n+j)(n+j+2)[(n-j)^2-1]} \tag{C.12}$$

$$r = m; \qquad j + r = \text{odd}; \qquad n + m = \text{odd}$$

$$\tilde{M}^{rm}_{jn} = \frac{1}{\sqrt{H^m_n H^r_j}\sqrt{(2n+1)(2j+1)}} \tag{C.13}$$

$$r = m; \qquad j = n \pm 1; \qquad j + r = \text{odd}; \qquad n + m = \text{even}$$

$$r = m; \qquad j = n \pm 1; \qquad j + r = \text{even}; \qquad n + m = \text{odd}$$

$$\tilde{M}^{rm}_{jn} = \frac{8}{\pi^2\sqrt{H^m_n H^r_j}} \frac{(-1)^{\frac{n+j-2m+2}{2}}\sqrt{(2n+1)(2j+1)}}{(n+j)(n+j+2)[(n-j)^2-1]} \tag{C.14}$$

$$r = m; \qquad j + r = \text{even}; \qquad n + m = \text{even}$$

$$\tilde{M}^{rm}_{jn} = 0 \tag{C.15}$$

$$r \neq m$$

C.2 Damping Matrix

$$\tilde{D}_{jn}^{rm} = \frac{1}{K_n^m}\delta_{jn} \tag{C.16}$$

$$r = m; \qquad j + r = \text{odd}; \qquad n + m = \text{odd}$$

$$r = m; \qquad j + r = \text{even}; \qquad n + m = \text{even}$$

$$\tilde{D}_{jn}^{rm} = \frac{2}{\pi\sqrt{H_n^m H_j^r}} \frac{\sqrt{(2n+1)(2j+1)}}{(j+n+1)(j-n)} (-1)^{\frac{j+3n-1}{2}} \tag{C.17}$$

$$r = m; \qquad j + r = \text{odd}; \qquad n + m = \text{even}$$

$$r = m; \qquad j + r = \text{even}; \qquad n + m = \text{odd}$$

$$\tilde{D}_{jn}^{rm} = 0 \tag{C.18}$$

$$r \neq m$$

C.3 Inflow Influence Coefficient Matrix

$$\left(\tilde{L}_{jn}^{0mc}\right) = X^m \left(\Gamma_{jn}^{0m}\right) \tag{C.19}$$

$$\left(\tilde{L}_{jn}^{rmc}\right) = \left(X^{|m-r|} + (-1)^l X^{|m+r|}\right) \left(\Gamma_{jn}^{rm}\right) \tag{C.20}$$

$$\left(\tilde{L}_{jn}^{rms}\right) = \left(X^{|m-r|} - (-1)^l X^{|m+r|}\right) \left(\Gamma_{jn}^{rm}\right) \tag{C.21}$$

where wake skew function, X, l, and Γ are given as:

$$X = \tan\left(\frac{\chi}{2}\right), \qquad l = \min(r, m) \tag{C.22}$$

$$\Gamma_{jn}^{rm} = \frac{\text{sign}(r-m)}{\sqrt{K_n^m K_j^r}\sqrt{(2n+1)(2j+1)}}\delta_{j(n\pm1)} \tag{C.23}$$

$$r+m = \text{odd}; \qquad j+r = \text{odd}; \qquad n+m = \text{odd}$$

$$r+m = \text{odd}; \qquad j+r = \text{even}; \qquad n+m = \text{even}$$

$$\Gamma_{jn}^{rm} = \frac{2}{\sqrt{H_n^m H_j^r}} \frac{(-1)^{\frac{n+j-2r}{2}}\sqrt{(2n+1)(2j+1)}}{(n+j)(n+j+2)[(n-j)^2-1]} \tag{C.24}$$

$$r+m = \text{even}; \qquad j+r = \text{odd}; \qquad n+m = \text{even}$$

$$\Gamma_{jn}^{rm} = \frac{8}{\pi^2\sqrt{H_n^m H_j^r}} \frac{(-1)^{\frac{n+j-2r+2}{2}}\sqrt{(2n+1)(2j+1)}}{(n+j)(n+j+2)[(n-j)^2-1]} \tag{C.25}$$

$$r+m = \text{even}; \qquad j+r = \text{even}; \qquad n+m = \text{even}$$

$$\Gamma_{jn}^{rm} = \frac{4\text{sign}(r-m)}{\pi\sqrt{H_n^m H_j^r}} \frac{(-1)^{\frac{3n+j+2m-2r}{2}}\sqrt{(2n+1)(2j+1)}}{(n+j)(n+j+2)[(n-j)^2-1]} \tag{C.26}$$

$$r+m = \text{odd}; \qquad j+r = \text{odd}; \qquad n+m = \text{even}$$

$$r+m = \text{odd}; \qquad j+r = \text{even}; \qquad n+m = \text{odd}$$

$$\Gamma_{jn}^{rm} = \frac{1}{\sqrt{H_n^m H_j^r}\sqrt{(2n+1)(2j+1)}}\delta_{j(n\pm1)} \tag{C.27}$$

$$r+m = \text{even}; \qquad j+r = \text{odd}; \qquad n+m = \text{even}$$

$$r+m = \text{even}; \qquad j+r = \text{even}; \qquad n+m = \text{odd}$$

$$\Gamma_{00}^{00} = \left(\frac{4}{\pi^2}\sum_{n=1}^{N_{max}}\frac{1}{n}\right) + \frac{1}{2} \tag{C.28}$$

$$r = j = m = n = 0$$

where N_{max} is the maximum harmonic number.

APPENDIX D

PPSIM APPARENT MASS AND INFLOW INFLUENCE COEFFICIENT MATRICES

Elements in PPSIM apparent mass matrix ($[M]$) and inflow influence coefficient matrix ($[L]$) involve calculations in multiple coordinate systems. Multi-rotor configurations consist of more than two rotors can be partitioned into a set of dual-rotor systems to simplify analyses. As such, interference effects on a rotor due to other rotors can be identified individually. For example, when quad-rotors are considered, PPSIM $[M]$ and $[L]$ will have the following form:

$$[M] = \begin{bmatrix} M_{11} & M_{12} & M_{13} & M_{14} \\ M_{21} & M_{22} & M_{23} & M_{24} \\ M_{31} & M_{32} & M_{33} & M_{34} \\ M_{41} & M_{42} & M_{43} & M_{44} \end{bmatrix} \qquad [L] = \begin{bmatrix} L_{11} & L_{12} & L_{13} & L_{14} \\ L_{21} & L_{22} & L_{23} & L_{24} \\ L_{31} & L_{32} & L_{33} & L_{34} \\ L_{41} & L_{42} & L_{43} & L_{44} \end{bmatrix}$$

where diagonal terms consider self-induced effects, and off-diagonal terms include wake interference effects among the rotors. After partitioning the multi-rotor configuration into the set of dual-rotor systems, the coordinate system can be generalized using the *receiving rotor* and *active rotor* concept. Figure D.1 shows a generic coordinate system for the receiving and active rotors used to calculate elements in PPSIM $[M]$ and $[L]$. Two rotors are separated along the vertical ($\bar{h}$), longitudinal ($\bar{d}$), and lateral ($\bar{l}$) directions. These distances are normalized by the receiving rotor radius.

In Eqs. (D.1) through (D.6), subscripts *R* and *A* represent the coordinate system of the receiving rotor and active rotor, respectively. For example, elements in $[L_{14}]$ are computed by treating rotor 1 as the receiving rotor and rotor 4 as the active rotor. Similarly, elements in $[L_{41}]$ are computed by treating rotor 4 as the receiving rotor and rotor 1 as the active

rotor.

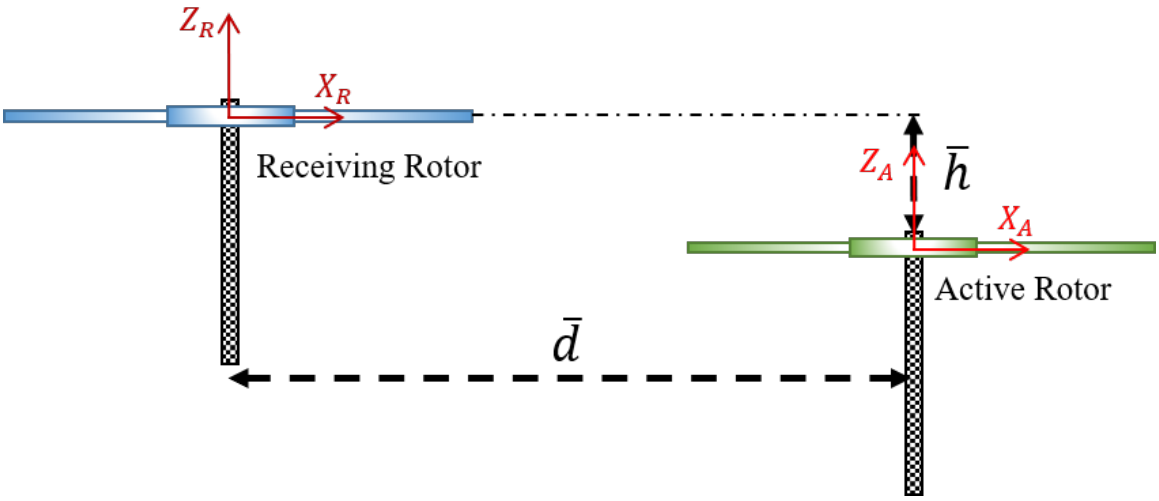

(a) Side view

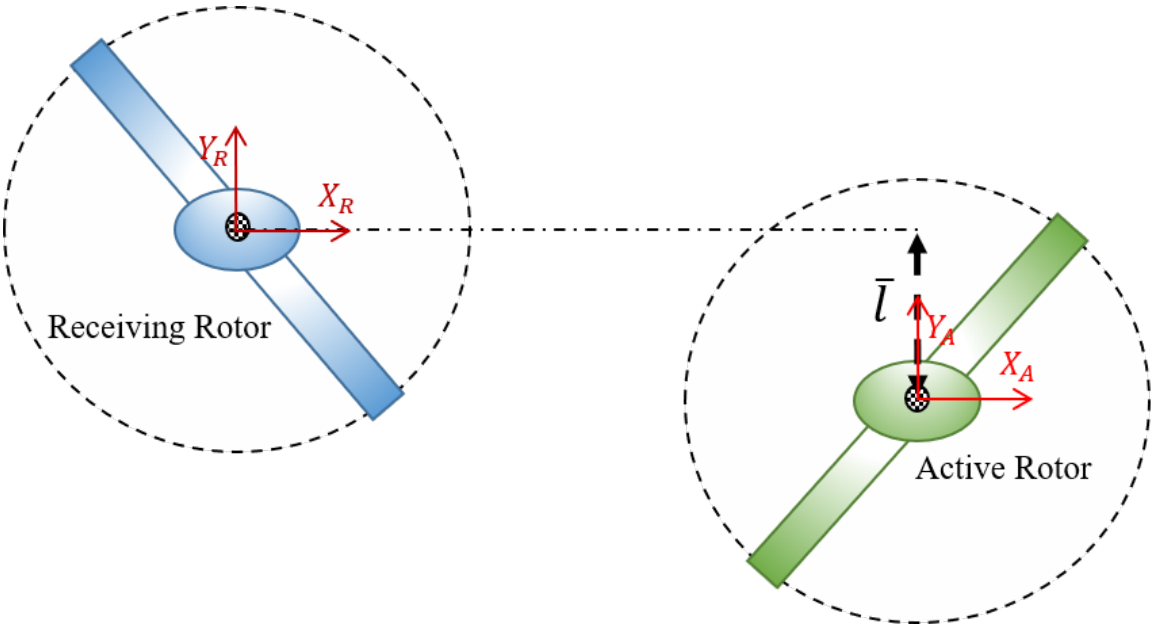

(b) Top view

Figure D.1: Reference coordinate system used to compute PPSIM $[M]$ and $[L]$

The $[M]$ is defined as the inverse of linear operator E ($[M] = [E]^{-1}$). Thus, it is possible to numerically integrate operator $[E]$ instead of $[M]$. Elements in $[E_{RA}]$ are calculated using Eqs. (D.1) through (D.3).

$$E^{0m}_{jn,\cos} = \frac{1}{2\pi}\int_0^{2\pi}\int_0^1 \nu_R \bar{P}^0_j(\nu_R)\frac{\partial(\bar{P}^m_n(\nu_A)\bar{Q}^m_n(\eta_A)\cos(m\psi_A))}{\partial \bar{z}_R} d\nu_R d\psi_R \tag{D.1}$$

$$E^{rm}_{jn,\cos} = \frac{1}{\pi}\int_0^{2\pi}\int_0^1 \nu_R \bar{P}^r_j(\nu_R)\cos(r\psi_R)\frac{\partial(\bar{P}^m_n(\nu_A)\bar{Q}^m_n(\eta_A)\cos(m\psi_A))}{\partial \bar{z}_R} d\nu_R d\psi_R \tag{D.2}$$

$$E^{rm}_{jn,\sin} = \frac{1}{\pi}\int_0^{2\pi}\int_0^1 \nu_R \bar{P}^r_j(\nu_R)\sin(r\psi_R)\frac{\partial(\bar{P}^m_n(\nu_A)\bar{Q}^m_n(\eta_A)\sin(m\psi_A))}{\partial \bar{z}_R} d\nu_R d\psi_R \tag{D.3}$$

Similarly, elements in $[L_{RA}]$ are obtained using Eqs. (D.4) through (D.6).

$$L^{0m}_{jn,\cos} = \frac{1}{2\pi}\int_0^{2\pi}\int_0^1 \nu_R \bar{P}^0_j(\nu_R)\int_0^\infty \frac{\partial(\bar{P}^m_n(\nu_A)\bar{Q}^m_n(\eta_A)\cos(m\psi_A))}{\partial \bar{z}_R} d\xi_A d\nu_R d\psi_R \tag{D.4}$$

$$L^{rm}_{jn,\cos} = \frac{1}{\pi}\int_0^{2\pi}\int_0^1 \nu_R \bar{P}^r_j(\nu_R)\cos(r\psi_R)\int_0^\infty \frac{\partial(\bar{P}^m_n(\nu_A)\bar{Q}^m_n(\eta_A)\cos(m\psi_A))}{\partial \bar{z}_R} d\xi_A d\nu_R d\psi_R \tag{D.5}$$

$$L^{rm}_{jn,\sin} = \frac{1}{\pi}\int_0^{2\pi}\int_0^1 \nu_R \bar{P}^r_j(\nu_R)\sin(r\psi_R)\int_0^\infty \frac{\partial(\bar{P}^m_n(\nu_A)\bar{Q}^m_n(\eta_A)\sin(m\psi_A))}{\partial \bar{z}_R} d\xi_A d\nu_R d\psi_R \tag{D.6}$$

Table D.1: Precalculated elements in off-diagonal blocks of three-state PPSIM apparent mass matrix ($[M_{12}]$, $[M_{21}]$) for different configurations

Elements	Coax[a]	TR-CI[b]	TR-CII[c]	CH-47
$M_{12}(1,1)$	1.117	-14.229	-98.137	-11.565
$M_{12}(1,2)$	0.000	3.164	77.865	4.020
$M_{12}(2,1)$	0.000	-6.326	-155.832	-8.040
$M_{12}(2,2)$	0.994	-2.883	145.085	0.590
$M_{12}(3,3)$	0.994	1195.786	-93.190	19.027
$M_{21}(1,1)$	1.117	-14.229	-98.083	-11.566
$M_{21}(1,2)$	0.000	-3.164	-77.820	-4.020
$M_{21}(2,1)$	0.000	6.326	155.756	8.040
$M_{21}(2,2)$	0.994	-2.883	145.021	0.590
$M_{21}(3,3)$	0.994	1191.524	-93.155	19.029

[a] Coaxial Harrington Rotor 1
[b] Tandem Rotor Configuration I: ($\bar{d} = 1.5, \bar{l} = 0.0,\ \bar{h} = 0.19$)
[c] Tandem Rotor Configuration II: ($\bar{d} = 2.0, \bar{l} = 0.0,\ \bar{h} = 0.19$)

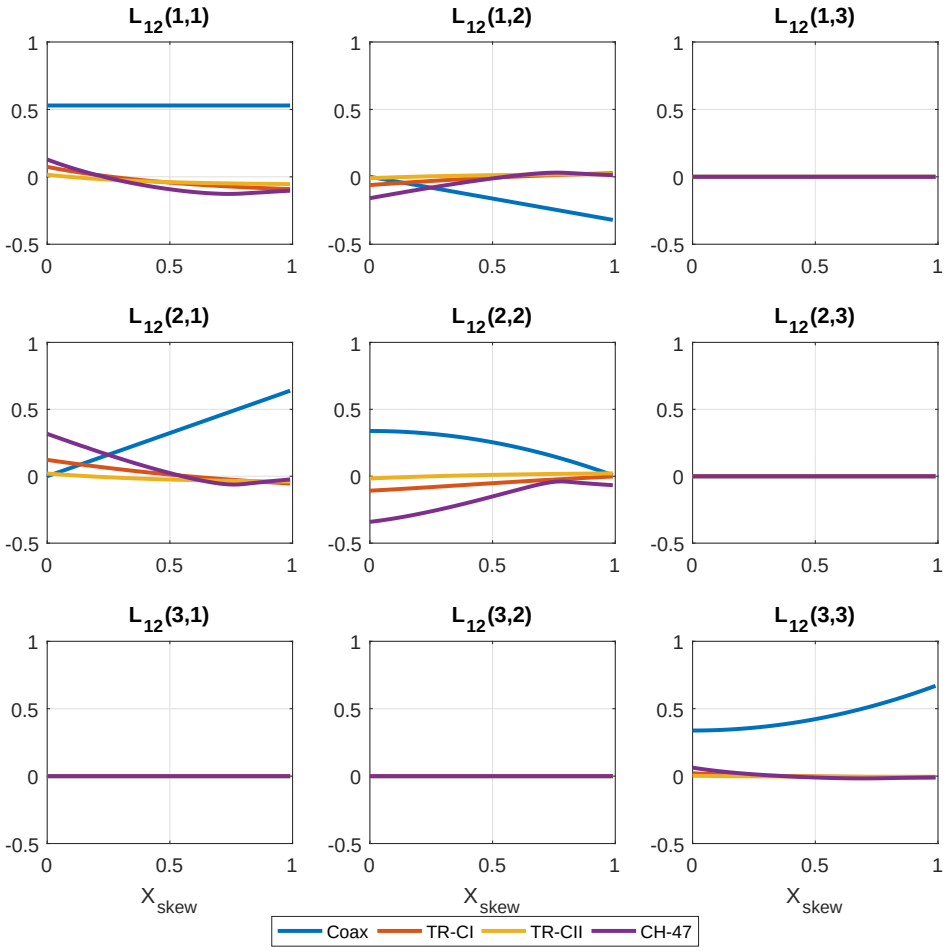

Figure D.2: Precalculated elements in three-state PPSIM $[L_{12}]$ corresponding to different multi-rotor configurations (Coax: Coaxial Harrington Rotor 1, TR-CI: Tandem rotor configuration I , TR-CII: Tandem rotor configuration II)

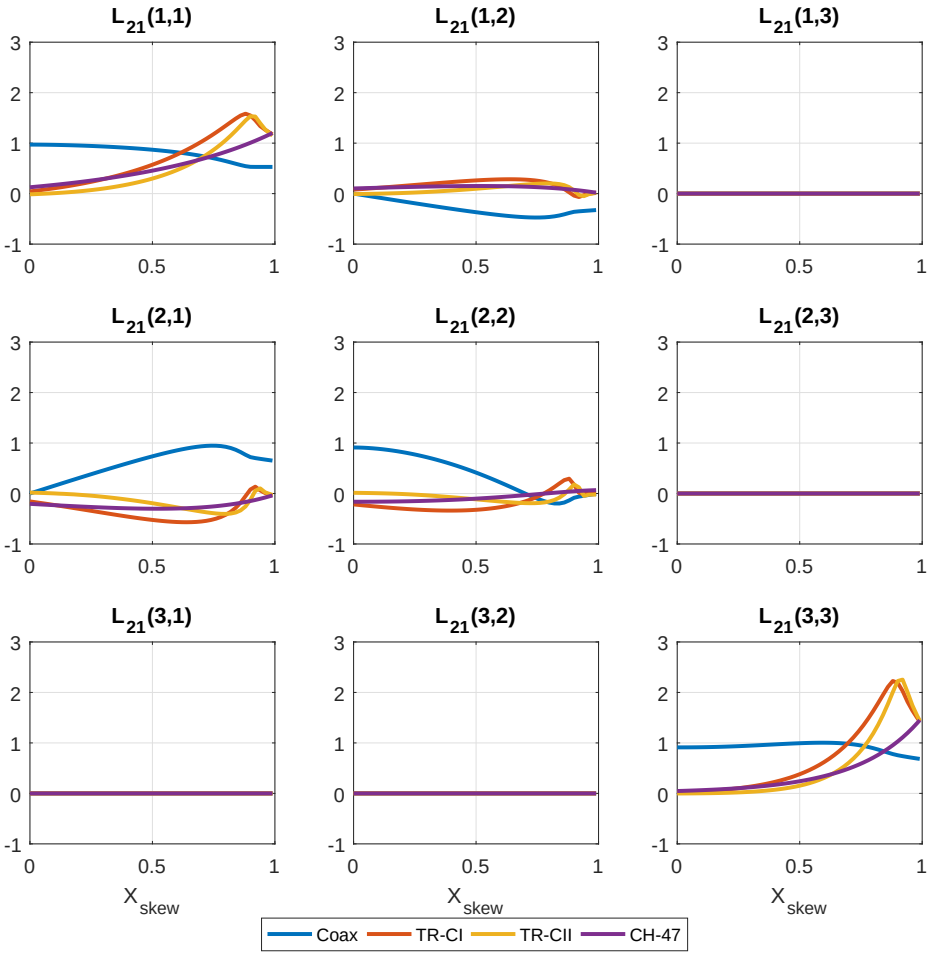

Figure D.3: Precalculated elements in three-state PPSIM $[L_{21}]$ corresponding to different multi-rotor configurations (Coax: Coaxial Harrington Rotor 1, TR-CI: Tandem rotor configuration I , TR-CII: Tandem rotor configuration II)

REFERENCES

[1] Carpenter, P. J. and Friedovich, B., "Effect of a Rapid Blade Pitch Increase on the Thrust and Induced Velocity Response of a Full Scale Helicopter Rotor," NACA TN 3044, 1953.

[2] Chen, R. and Hindson, W. S., "Influence of Dynamic Inflow on the Helicopter Vertical Response," NASA Technical Memorandum 88327, Jun. 1986.

[3] Ormiston, R. A. and Peters, D. A., "Hingeless Helicopter Rotor Response with Nonuniform Inflow and Elastic Blade Bending," *Journal of Aircraft*, vol. 9(10), Apr. 1972.

[4] Peters, D. A., "Hingeless Rotor Frequency Response with Unsteady Inflow," in *Proceedings of the American Helicopter Society/NASA-Ames Specialist's Meeting on Rotorcraft Dynamics*, 1974.

[5] Chen, R. T. N., "A Survey of Non-Uniform Inflow Model for Rotorcraft Flight Dynamics and Control Applications," NASA TM 102219, 1989.

[6] He, C. and Zhao, J., "A Real Time Finite State Induced Flow Model Augmented with High Fidelity Viscous Vortex Particle Simulation," in *Proceedings of the 64th Annual Forum of the American Helicopter Society*, Montréal, Québec, Canada, May 2008.

[7] He, C. and Zhao, J., "Modeling Rotor Wake Dynamics with Viscous Vortex Particle Method," *AIAA Journal*, vol. 47(4), Apr. 2009.

[8] Rajmohan, N., "Application of Hybrid Methodology to Rotors in Steady and Maneuvering Flight," Ph.D. dissertation, Georgia Institute of Technology, Aug. 2010.

[9] Marpu, R. P., Sankar, L. N., Makinen, S. M., Egolf, T. A., Baeder, J. D., and Wasikowski, M., "Physics-Based Modeling of Maneuver Loads for Rotor and Hub Design," *Journal of Aircraft*, vol. 51(2), pp. 377–389, Apr. 2014.

[10] Pitt, D. M. and Peters, D. A., "Theoretical Prediction of Dynamic-Inflow Derivatives," in *Proceedings of the 6th European Rotorcraft and Powered Lift Aircraft Forum*, Bristol, England, Sep. 1980.

[11] Pitt, D. M. and Peters, D. A., "Rotor Dynamic Inflow Derivatives and Time Constants from Various Inflow Models," in *Proceedings of the 9th European Rotorcraft Forum*, Stresa, Italy, Sep. 1983.

[12] Peters, D. A. and HaQuang, N., "Technical Note: Dynamic Inflow for Practical Applications," *Journal of the American Helicopter Society*, vol. 33(4), Oct. 1988.

[13] He, C., "Development and Application of a Generalized Dynamic Wake Theory for Lifting Rotors," Ph.D. dissertation, Georgia Institute of Technology, Jul. 1989.

[14] He, C. and Peters, D., "An Aeroelastic Analysis with a Generalized Dynamic Wake," in *Proceedings of the American Helicopter Society International Technical Specialist's Meeting on Rotorcraft Basic Research*, Atlanta, Georgia, Mar. 1991.

[15] Peters, D. A., Barwey, D., and Su, A., "An Integrated Airloads-Inflow Model for Use in Rotor Aeroelasticity and Control Analysis," *Mathematical and Computer Modelling*, vol. 19(3–4), Feb. 1994.

[16] *FLIGHTLAB X-Analysis User Manual*, Advanced Rotorcraft Technology, Inc., Sunnyvale, California, Sep. 2018.

[17] *Rotorcraft Comprehensive Analysis System User's Manual*, US Army Research, Development, and Engineering Command, Moffett Field, California, Aug. 2012.

[18] Zhao, J., Prasad, J. V. R, and Peters, D. A., "Rotor Dynamic Wake Distortion Model for Helicopter Maneuvering Flight," *Journal of the American Helicopter Society*, vol. 49(4), pp. 414–424, Oct. 2004.

[19] Zhao, J., "Dynamic Wake Distortion Model for Helicopter Maneuvering Flight," Ph.D. dissertation, Georgia Institute of Technology, Mar. 2005.

[20] Chen, C., "Development of a Simplified Inflow Model for a Helicopter Rotor in Descent Flight," Ph.D. dissertation, Georgia Institute of Technology, Aug. 2006.

[21] He, C., Lee, C. S., and Chen, W., "Technical Note: Finite State Induced Flow Model in Vortex Ring State," *Journal of the American Helicopter Society*, vol. 45(4), Sep. 2000.

[22] Peters, D. A. and He, C., "Technical Note: Modification of Mass-Flow Parameter to Allow Smooth Transition Between Helicopter and Windmill States," *Journal of the American Helicopter Society*, vol. 51, Jul. 2006.

[23] Prasad, J. V. R., Nowak, M., and Xin, H., "Finite State Inflow Models for a Coaxial Rotor in Hover," in *Proceedings of the 38th European Rotorcraft Forum*, Amsterdam, the Netherlands, Sep. 2012.

[24] Nowak, M., Prasad, J. V. R., and Peters, D., "Development of a Finite State Model for a Coaxial Rotor in Forward Flight," in *Proceedings of the 70th Annual Forum of the American Helicopter Society*, Montréal, Québec, Canada, May 2014.

[25] Nowak, M., Prasad, J. V. R., Xin, H., and Peters, D. A., "A Potential Flow Model for Coaxial Rotors in Forward Flight," in *Proceedings of the 39th European Rotorcraft Forum*, Moscow, Russia, Sep. 2013.

[26] Prasad, J. V. R., Kong, Y.-B., and Peters, D. A., "Analytical Methods for Modeling Inflow Dynamics of a Coaxial Rotor System," in *Proceedings of the 42nd European Rotorcraft Forum*, Lille, France, Sep. 2016.

[27] Kong, Y.-B., Prasad, J. V. R., Sankar, L. N., and Kim, J, "Finite State Coaxial Rotor Inflow Model Improvements via System Identification," in *Proceedings of the 72nd Annual Forum of the American Helicopter Society, West Palm Beach, Florida*, May 2016.

[28] Kong, Y.-B., Prasad, J. V. R., Sankar, L. N., and Peters, D. A., "Finite State Coaxial Rotor Inflow Model System Identification Using Perturbation Approach," in *Proceedings of the 5th Asian/Australian Rotorcraft Forum*, Singapore, Nov. 2016.

[29] Kong, Y.-B., Prasad, J. V. R., and Peters, D. A., "Development of a Finite State Dynamic Inflow Model for Coaxial Rotor Using Analytical Methods," in *Proceedings of the 73rd Annual Forum of the American Helicopter Society*, Fort Worth, Texas, May 2017.

[30] Kong, Y.-B., "Development of a Finite State Coaxial Rotor Dynamic Inflow Model," Ph.D. dissertation, Georgia Institute of Technology, Aug. 2018.

[31] Kong, Y.-B., Prasad, J. V. R., Sankar, L. N., and He, C., "Finite State Inflow Flow Model for Coaxial Rotor Configuration," *Journal of the American Helicopter Society*, vol. 65(3), Jul. 2020.

[32] Kong, Y.-B., Prasad, J. V. R., and He, C., "Finite State Coaxial Rotor Inflow Model Enhancements Using VVPM-Extracted Influence Coefficients," *Journal of the American Helicopter Society*, vol. 65(2), Apr. 2020.

[33] Kim, H. W. and Brown, R. E., "A Comparison of Coaxial and Conventional Rotor Performance," *Journal of the American Helicopter Society*, vol. 55(1), Jan. 2010.

[34] Bagai, A. and Leishman, J. G., "Free-Wake Analysis of Tandem, Tilt-Rotor and Coaxial Rotor Configurations," *Journal of the American Helicopter Society*, vol. 41(3), pp. 196–207, Jul. 1996.

[35] Bagai, A., Leishman, J. G., and Ananthan, S., "Free-Vortex Wake Predictions of the Vortex Ring State for Single-Rotor and Multi-Rotor Configurations," in *Proceedings of the 58th Annual Forum of the American Helicopter Society*, Montréal, Québec, Canada, Jun. 2002.

[36] Wachspress, D. A. and Quackenbush, T. R., "Impact of Rotor Design on Coaxial Rotor Performance, Wake Geometry and Noise," in *Proceedings of the 62nd Annual Forum of the American Helicopter Society*, Phoenix, Arizona, May 2006.

[37] Egolf, T. A., Reed, E., Rajmohan, N., and Sankar, L. N., "A Hybrid CFD Method for Coaxial Rotor Performance Prediction in Forward Flight," in *Proceedings of the American Helicopter Society Aeromechanics Specialist's Conference*, San Francisco, California, Jan. 2010.

[38] Kim, J., Sankar, L. N., and Prasad, J. V. R., "Application of a Navier-Stokes Free Wake Hybrid Methodology to the Harrington Coaxial Rotor," in *Proceedings of the American Helicopter Society Aeromechanics Specialist's Conference on Aeromechanics Design for Vertical Lift*, San Francisco, California, Jan. 2016.

[39] Chen, P.-W., Sankar, L. N., and Prasad, J. V. R., "A Hybrid Navier Stokes–Free Wake Method for Modeling Tandem Rotors," in *Proceedings of the 7th Asian/Australian Rotorcraft Forum*, Jeju Island, Korea, 2018.

[40] Chen, P.-W., Sankar, L. N., Prasad, J. V. R., Schatzman, N., and Rajagopalan, R. G., "Extraction of Dynamic Inflow Models for Coaxial and Tandem Rotors from CFD Simulations," in *Proceedings of the 75th Annual Forum of the Vertical Flight Society*, Philadelphia, Pennsylvania, May 2019.

[41] Chen, P.-W., Shukla, D., Sankar, L. N., Komerath, N., and Prasad, J. V. R., "Rotor Wake and Inflow Characteristics of Multi-Rotor Drone Configurations," in *Proceedings of the 45th European Rotorcraft Forum*, Warsaw, Poland, Sep. 2019.

[42] Chen, P.-W., Guner, F., Sankar, L. N., Prasad, J. V. R., and He, C., "Calibration of Velocity Potential Superposition Inflow Model Using Computational Fluid Dynamics Data," in *Proceedings of the Vertical Flight Society Aeromechanics for Advanced Vertical Flight Technical Meeting*, San Jose, California, Jan. 2020.

[43] Lee, J., Yee, K., and Oh, S., "Numerical Investigation of Dual Rotors Using a Time-Marching Free-Wake Method," in *Proceedings of the 64th Annual Forum of the American Helicopter Society*, Montréal, Québec, Canada, May 2008.

[44] Lee, J., Oh, S., Yee, K., and Kim, D. K., "Numerical Investigation on Overlap Effects of Tandem Rotors in Forward Flight," *Int'l Journal of Aeronautical & Space Sciences*, vol. 10(2), 2009.

[45] Lakshminarayan, V. K. and Baeder, J. D., "High-Resolution Computational Investigation of Trimmed Coaxial Rotor Aerodynamics in Hover," *Journal of the American Helicopter Society*, vol. 54(4), Jul. 2009.

[46] Zhao, J. and He, C., "Real-Time Simulation of Coaxial Rotor Configurations with Combined Finite State Dynamic Wake and VPM," in *Proceedings of the 70th Annual Forum of the American Helicopter Society*, Montréal, Québec, Canada, May 2014.

[47] Xin, H., Goss, J., and Parkes, C., "Development of a Three-State Rotor Interference Model and Application to Coaxial Rotor Inflow Modeling," in *Proceedings of the American Helicopter Society 5th Decennial Aeromechanics Specialist's Conference*, San Francisco, California, Jan. 2014.

[48] Hackett, W. E., Garnett, T. S., and Borek, B. V., "Mathematical Model of the CH-47B Helicopter Capable of Real-Time Simulation of the Full Flight Envelope," NASA CR 166458, Jul. 1983.

[49] Rand, O., Khromov, V., Hersey, S., Celi, R., Juhasz, O., and Tischler, M. B., "Linear Inflow Model Extraction from High-Fidelity Aerodynamic Models for Flight Dynamics Applications," in *Proceedings of the 71st Annual Forum of the American Helicopter Society*, Virginia Beach, Virginia, May 2015.

[50] Rand, O. and Khromov, V., "Free-Wake Based Dynamic Inflow Model for Hover, Forward, and Maneuvering Flight," *Journal of the American Helicopter Society*, vol. 63(1), pp. 1–16, Jan. 2018.

[51] Rand, O. and Khromov, V., "Parametric Study of Dynamic Inflow for Single and Coaxial Rotor Systems," *Journal of the American Helicopter Society*, vol. 63(4), Oct. 2018.

[52] Keller, J. D., McKillip Jr., R. M., Wachspress, D. A., Tischler, M. B., and Juhasz, O., "A Free Wake Linear Inflow Model Extraction Procedure for Rotorcraft Analysis," in *Proceedings of the 73rd Annual Forum of the American Helicopter Society*, Fort Worth, Texas, May 2017.

[53] Keller, J. D., McKillip Jr., R. M., Wachspress, D. A., Tischler, M. B., and Juhasz, O., "Linearized Inflow and Interference Models from High Fidelity Free Wake Analysis for Modern Rotorcraft Configurations," in *Proceedings of the 75th Annual Forum of the Vertical Flight Society*, Philadelphia, Pennsylvania, May 2019.

[54] He, C., Syal, M., Tischler, M. B., and Juhasz, O., "State-Space Inflow Model Identification from Viscous Vortex Particle Method for Advanced Rotorcraft Configurations," in *Proceedings of the 73rd Annual Forum of the American Helicopter Society*, Fort Worth, Texas, May 2017.

[55] He, C., Gladfelter, M., Chang, C., Tischler, M. B., and Juhasz, O., "VPM-Derived State Space Inflow Model for Multi-Rotor Air Vehicle Modeling and Simulation," in *Proceedings of the 75th Annual Forum of the Vertical Flight Society*, Philadelphia, Pennsylvania, May 2019.

[56] Kong, Y.-B., Prasad, J. V. R., and Peters, D. A., "Analysis of a Finite State Multi-Rotor Dynamic Inflow Model," in *Proceedings of the 43rd European Rotorcraft Forum*, Milan, Italy, Sep. 2017.

[57] Morillo, J. A., "A Fully Three-Dimensional Unsteady Inflow Model from a Galerkin Approach," Ph.D. dissertation, Washington University in St. Louis, Dec. 2001.

[58] Huang, J., "Potential-Flow Inflow Model Including Wake Distortion and Contraction," Ph.D. dissertation, Washington University in St. Louis, May 2015.

[59] Fei, Z, "A Rigorous Solution for Finite-State Inflow Throughout the Flowfield," Ph.D. dissertation, Washington University in St. Louis, May 2013.

[60] Guner, F., Kong, Y.-B., Prasad, J. V. R., Peters, D. A., and He, C., "Development of Finite State Inflow Models for Multi-Rotor Configurations Using Analytical Approach," in *Proceedings of the 74th Annual Forum of the Vertical Flight Society*, Phoenix, Arizona, May 2018.

[61] Guner, F., Prasad, J. V. R., Sankar, L. N., Peters, D. A., and He, C., "Correlation of Finite State Multi-Rotor Dynamic Inflow Models with a High Fidelity Viscous Vortex Particle Method," in *Proceedings of the 44th European Rotorcraft Forum*, Delft, the Netherlands, Sep. 2018.

[62] Peters, D. and He, C., "Correlation of Measured Induced Velocities with a Finite-State Wake Model," *Journal of the American Helicopter Society*, vol. 36(3), Jul. 1991.

[63] Tischler, M. B. and Remple, R. K., *Aircraft and Rotorcraft System Identification: Engineering Methods with Flight-Test Examples*, 2nd. Reston, Virginia: AIAA Education Series, AIAA, 2012.

[64] Anonymous, "Department of Defense Interface Standard, Flying Qualities of Piloted Aircraft," MIL-STD-1797A Notice 3, 2004.

[65] Neal, T. and Smith, R., "An In-Flight Investigation to Develop Control System Design Critera for Fighter Airplanes," AFFDL-TR-70-74 Volume 1, 1970.

[66] Harrington, R., "Full Scale Tunnel Investigation of the Static Thrust Performance of a Coaxial Helicopter Rotor," NACA TN 2318, Mar. 1951.

[67] Guner, F. and Prasad, J. V. R., "Combined Momentum and Simple Vortex Theory Inflow Model for Multi-Rotor Configurations," in *Proceedings of the Vertical Flight Society's 9th Biennial Autonomous VTOL Technical Meeting*, Virtual, Jan. 2021.

[68] Guner, F., Prasad, J. V. R., He, C., and Miller, D. G., "Tandem Rotor Inflow Modeling and its Effect on Vehicle Dynamics," in *Proceedings of the 75th Annual Forum of the Vertical Flight Society*, Philadelphia, Pennsylvania, May 2019.

[69] Guner, F., Miller, D. G., and Prasad, J. V. R., "Understanding the Effect of Rotor-to-Rotor Interference on CH-47D Helicopter Dynamics," in *Proceedings of the 76th Annual Forum of the Vertical Flight Society*, Virtual, Oct. 2020.

[70] Mettler, B., Tischler, M., and Kanade, T., "System Identification Modeling of a Model-Scale Helicopter," Carnegie Mellon University, Pittsburgh, Pennsylvania, Tech. Rep. CMU-RI-TR-00-03, 2000.

[71] He, C. and Lee, J., "Rotorcraft Simulation Model Enhancement to Support Land and Sea-Based Testing and Operational Analysis," Advanced Rotorcraft Technology, Inc., Mountain View, California, ART Technical Report: ART-97-TR0006, Jun. 1997.

[72] Howlett, J. J., "UH-60A Black Hawk Engineering Simulation Program: Volume I - Mathematical Model," NASA CR 166309, Dec. 1981.

[73] Kim, J., He, C., Saberi, H., and Peters, D. A., "Integration of Finite State Dynamic Wake Model for Rotor Interference with Comprehensive Rotorcraft Analysis," in *Proceedings of the 75th Annual Forum of the Vertical Flight Society*, Philadelphia, Pennsylvania, May 2019.

[74] Ogata, K., *Modern Control Engineering*, 5th edition. United Kingdom: Prentice Hall, 2010, p. 667.

[75] Glauert, H. A., "A General Theory of the Autogyro," British A. R. C. R & M No. 1111, 1926.

[76] Heyson, H. H., "Equations for the Induced Velocities Near A Lifting Rotor with Nonuniform Azimuthwise Vorticity Distribution," NASA TN D-394, Aug. 1960.

[77] Lebedev, N. N., *Special Functions and Their Applications*. Englewood Cliffs, N.J.: Prentice Hall, 1965, pp. 192–193, Rev. English ed. translated and edited by Richard, A. S.

VITA

Feyyaz Guner was born in March 1990 in Samsun, Turkey. He received his Bachelor of Science degree with high honors in Aerospace Engineering from the Middle East Technical University (METU) in June 2014. After graduation, Feyyaz was employed as a modeling and simulation engineer by a local simulator company in Ankara, and he developed real-time helicopter math models for level-D full flight simulators. While working as a full-time engineer, he continued to engage in graduate school and received a Master of Science degree in Aerospace Engineering from the METU in September 2016. Feyyaz left his job to pursue a Doctor of Philosophy (Ph.D.) degree and joined the Daniel Guggenheim School of Aerospace Engineering at the Georgia Institute of Technology in May 2017. During his Ph.D. studies, Feyyaz developed novel multi-rotor inflow models for advanced rotorcraft configurations and presented his work at multiple conferences. Also, he was part of the NATO AVT-296: Rotorcraft Flight Simulation Model Fidelity Improvement and Assessment Group, where a group of scientists from the allied countries discussed and documented methods for improving fidelity of rotorcraft simulation models. As a result of his contribution to the vertical lift community, Feyyaz was recognized by the Vertical Flight Society with the award of Dr. E. Roberts Wood Scholarship in 2019. He is a member of the Vertical Flight Society since 2015.